LAND SURFACE MODELING OF ENERGY-BALANCE COMPONENTS: MODEL VALIDATION AND SCALING EFFECTS

By

VENKATARAMANA RAO SRIDHAR

Bachelor of Engineering
College of Agricultural Engineering
Tamil Nadu Agricultural University
Coimbatore, Tamil Nadu, India
1991

Master of Engineering
Irrigation Engineering and Management
School of Civil Engineering
Asian Institute of Technology
Bangkok, Thailand
1994

Submitted to the Faculty of the
Graduate College of the
Oklahoma State University
in partial fulfillment of
the requirements for
the Degree of
DOCTOR OF PHILOSOPHY
August, 2001

LAND SURFACE MODELING OF ENERGY-BALANCE COMPONENTS: MODEL VALIDATION AND SCALING EFFECTS

Thesis Approved:

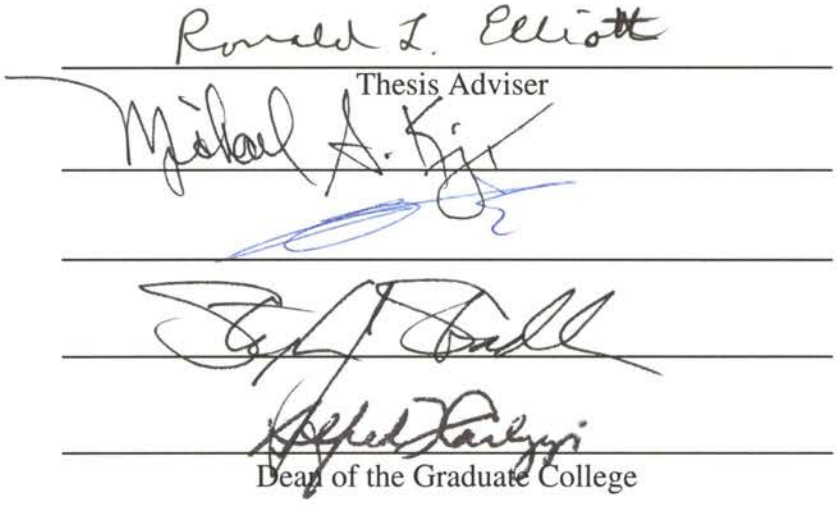

Thesis Adviser

Dean of the Graduate College

ACKNOWLEDGEMENTS

I would like to express immense thanks to my major adviser Dr. Ronald L. Elliott for his guidance, support and encouragement throughout my study at OSU. His dedication to work, in-depth understanding of issues and sincerity has taught me a lot and inspired me greatly. Dr. Elliott 's contribution towards my completion of this research is acknowledged with a great sense of gratitude and his professional and personal framework will have a great positive impact in carrying me forward successfully. I also extend my appreciation to my other committee members, Dr. Stephen J. Stadler, Dr. Fei Chen and Dr. Michael A. Kizer for their advice and encouragement. Special thanks to Dr. Fei Chen for his invaluable contribution with regard to model training for two successive summers. I would like to extend my appreciation to Dr. C.T. Haan who was on my committee until his retirement and I treasure his advice.

This research was made possible by EPSCoR grants from the National Aeronautics and Space Administration (Cooperative Agreement Number NCC5-171) and the National Science Foundation (Project Number EPS9550478). I would also like to acknowledge the assistance of the Oklahoma Mesonet and the Oklahoma Agricultural Experiment Station.

Appreciation is extended to Dr. Jerry Brotzge and Derek Arndt who provided the OASIS and the Oklahoma Mesonet data for this study. I thank Dr. Daniel Itenfisu, Mark Gregory and Pete Earls for extending a helping hand whenever I sought for it. I wish to

express my thanks to Dr. Norm Elliott, USDA-ARS for providing me with the FRAGSTAT software. The support and help that I received over the last few years at OSU from many friends is tremendous. Kudos to Barbara T., Jana, Gloria, Marge and Hope (for the administrative support), Drs. Hamilton and Senay (well-wisher and soccer-fan) and Ron Tejral (for taking pictures at Mesonet sites).

Finally and above all, I thank my parents, brothers (and family) and my wife for their support during all these years. They are with me guiding physically, emotionally and more importantly spiritually that gave me endurance, courage and faith in all my efforts.

TABLE OF CONTENTS

LIST OF TABLES

LIST OF FIGURES

CHAPTER 1

INTRODUCTION

Background

Modeling the processes related to land-atmosphere interaction over a large area is recognized as a complex and unresolved issue. Energy and water exchanges occur continuously at the interface between the land surface and the lower atmosphere. These exchanges are in the form of fluxes of radiant energy, latent heat and sensible heat. While there have been significant efforts in data collection and model development, validation and application, a number of issues are yet to be resolved. This is partly due to the multi-disciplinary nature of land-atmosphere modeling, which involves at least, hydrological, biophysical, and atmospheric science disciplines.

Scaling is an important issue that underlies modeling efforts. Models developed to estimate the surface energy and mass balance components at a point scale may tend to perform not as well when applied to larger areas. The land-atmosphere interaction process is often viewed from a relatively large-area perspective (i.e., predicting phenomena at regional to continental to global scales). Modeling the land surface processes plays an important role in large-scale atmospheric models (e.g., Mintz, 1981; Rowntree, 1983; Avissar and Pielke, 1989; Chen and Dudhia, 2001). Accurate partitioning of energy balance components improves regional weather and also global climate simulations. This necessitates the combined efforts of both hydrologists and

atmospheric scientists to deal with the land surface and the atmosphere as an interactively coupled system.

The problems of land surface heterogeneity within modeling grid cells have long been recognized. Traditionally the lumped model concept, where the spatially variable inputs and parameters are assumed to be homogeneous, has been in wide use. But many studies (e.g., Avissar and Pielke, 1989; Entekhabi and Eagleson, 1989; Avissar, 1992; Famiglietti and Wood, 1994; Wood, 1994; Hu and Islam, 1997) have revealed that the accuracy of the model response is very much dominated by sub-grid scale parameterizations of inputs and parameters. The distributed modeling approach, which accounts for spatial variability of input variables and parameters, can be adopted for large areas should this be supported by better (physically-based) models and high-resolution data sets. This approach could lead to improved predictions and reduced uncertainties in large-scale simulations. There are unanswered questions about the scale required for modeling a particular process, and the associated tradeoffs in data requirements and the accuracy in the model output.

There are a number of soil-vegetation-atmosphere models available for use and their characteristics in terms of model physics, number of parameters, time step, number of users and level of acceptance vary considerably. The well-tested NOAH-OSU LSM (National Centers for Environmental Prediction / Air Force/Office of Hydrology / Oregon State University / Land Surface Model) is chosen for this study. This LSM has been coupled to two mesoscale models, the NCEP operational Eta and the PSU/MM5 (Penn State University/fifth –generation Mesoscale Model) models (Marshall, 1998; Chen and Dudhia, 2001), and is well recognized by the land surface modeling community.

Objectives

The overall objective of this research is to examine the effects of different spatial scales of input data on modeled net radiation, latent, sensible and ground heat fluxes, and thereby understand the resolution needed for the realistic modeling of large-scale land atmosphere interaction. This is the specific focus of Chapter 5 of the dissertation. In support of this objective, there are two additional components of the study:

1. To evaluate the available techniques for estimating downwelling longwave radiation, to investigate possible improvements and/or simplifications to those techniques, and to incorporate nighttime as well as daytime conditions. This work is the subject of Chapter 3 and was undertaken because the land surface model requires downwelling longwave radiation as one of its inputs, which is not readily available from observations.
2. To validate the land surface model using the net radiation, latent, sensible and ground heat flux measurements from the Oklahoma Atmospheric Surface-layer Instrumentation System. Model validation was deemed to be an important precursor to the scaling analysis and is the focus of Chapter 4.

Scope of the study

Oklahoma was chosen as the geographic setting for this study because of: (1) its natural variability in climate ranging from the sub-humid east to the semi-arid west; (2) the availability of a unique combination of soil, land use, vegetation, weather, and surface flux data sets; and (3) the recent history of large-scale experiments in this region. For the longwave radiation and model validation analyses, a diversity of Oklahoma sites was used and the study period encompassed all seasons of the year. Due to the complexity in

data acquisition and handling for large areas, the area for the scaling study was identified using statistical analysis of land use and soil data. The scaling analysis then focused on two specific "cells" reflecting extremes in spatial heterogeneity/homogeneity, with a summertime study period of approximately five weeks that fall within the SGP97 (Southern Great Plains 97) experiment period.

CHAPTER 2

DESCRIPTION OF THE LAND SURFACE MODEL

The land surface model utilized in this study was originally developed at Oregon State University (Pan and Mahrt, 1987) and then gradually enhanced over the next decade. These enhancements have come primarily from work at the National Centers for Environmental Prediction, the Air Force and the NOAA Office of Hydrology. The evolving model has recently been dubbed the "NOAH-OSU LSM", and this identifier or simply "LSM" will be used to refer to the model herein. Dr. Fei Chen at the National Center for Atmospheric Research provided a working version of the model and associated user training.

This chapter contains a brief overview of the LSM, followed by a more detailed description of the components addressing soil hydrology and soil thermodynamics. An abbreviated description of the LSM is also contained in Chapter 4.

Overview

A schematic representation of the LSM is shown in Figure 2-1. Originally, the LSM consisted of the diurnally-dependent Penman potential evaporation approach of Mahrt and Ek (1984), the multi-layer soil model of Mahrt and Pan (1984) and the primitive canopy model of Pan and Mahrt (1987). Later NCEP/Office of Hydrology extended the improvements by including (1) a fairly complex canopy resistance

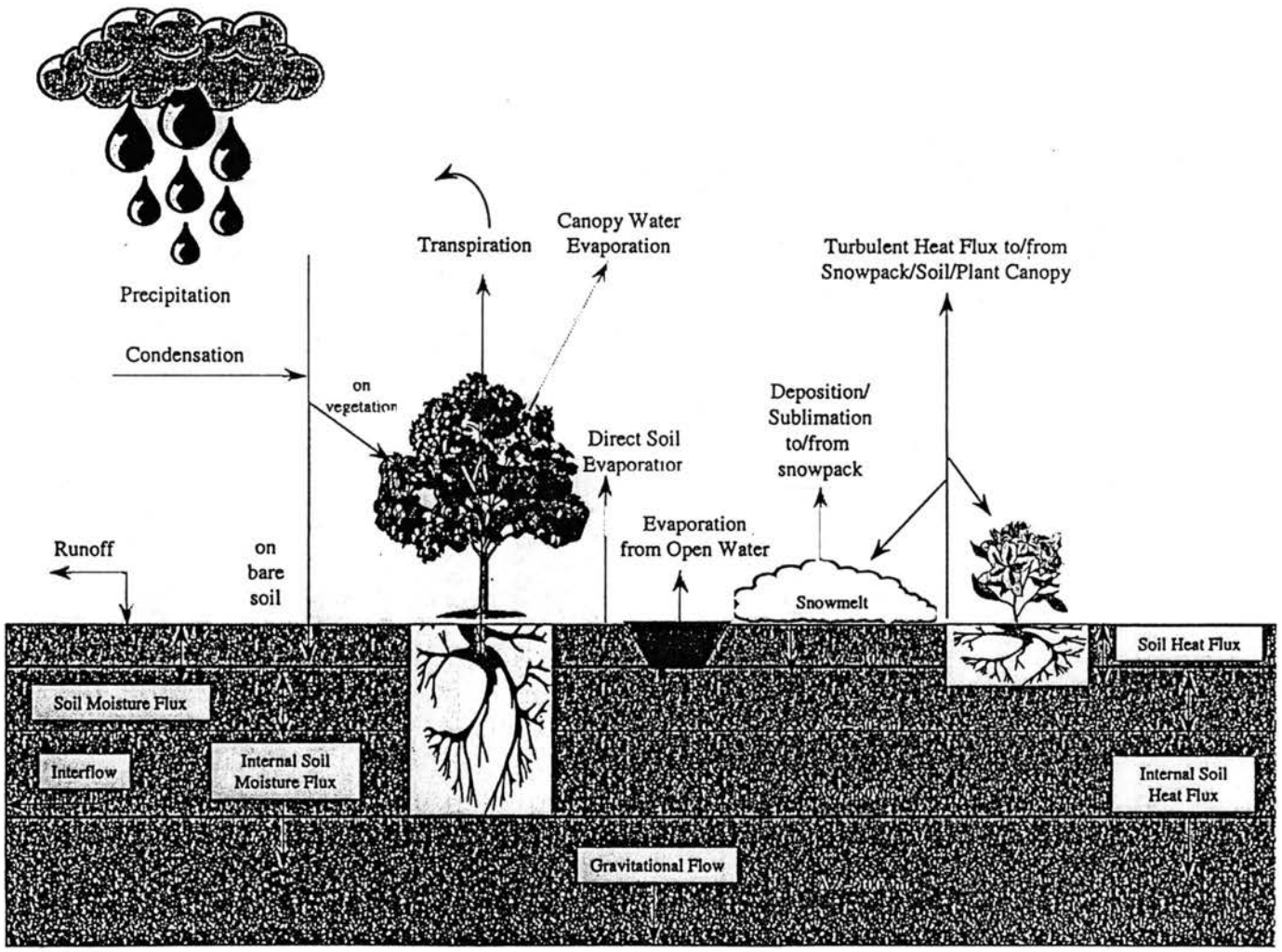

Figure 2-1. Schematic diagram of the NOAH-OSU Land Surface Model (from Chen and Dudia, 2001).

approach; (2) the bare soil evaporation approach of Noilhan and Planton (1989); (3) the surface runoff scheme of Schaake et al. (1996); (4) a higher-order time integration scheme by Kalnay and Kanamitsu (1988); and (5) refinements to the snowmelt algorithm and the treatment of soil thermal and hydraulic properties. Chen et al. (1996) modified the LSM to incorporate an explicit canopy resistance formulation used by Jacquemin and Noilhan (1990).

The LSM has one canopy layer and four soil layers with thicknesses of 0.1, 0.3, 0.6 and 1.0 m (total soil depth of 2 m) from the ground surface to the bottom, respectively. The four-level soil layer configuration is adopted in the LSM for capturing the daily, weekly and seasonal evolution of soil moisture and mitigating the possible truncation error in discretization. The lower 1 m acts as a reservoir with gravity drainage at the bottom, and the upper 1 m of soil serves as the root zone depth. From the standpoint of model input, the LSM requires soil and vegetation types and meteorological forcing variables (as the model is used here in an uncoupled fashion). The model soil and vegetation-related parameters are given in Appendix A. Prognostic variables include soil moisture and temperature in the soil layers, water intercepted on the canopy and snow accumulated on the ground. Model simulations also provide estimates of surface energy balance components (net radiation, surface skin temperature, latent, sensible, and ground heat fluxes).

Soil Hydrology

The prognostic equation for the volumetric soil water content (θ) in the hydrology of the LSM is given by:

$$\frac{\partial \theta}{\partial t} = \frac{\partial}{\partial z}\left(D\frac{\partial \theta}{\partial z}\right) + \frac{\partial K}{\partial z} + F_\theta \tag{2-1}$$

where D and K are the soil water diffusivity ($m^2\ s^{-1}$) and hydraulic conductivity ($m\ s^{-1}$), respectively, and both are functions of θ; t and z are time (s) and the vertical distance (m) from the soil surface downward (i.e., the depth), respectively; and F_θ represents sources and sinks (i.e., precipitation, evaporation and runoff). This diffusive form of the relationship is known as Richard's equation and is derived from Darcy's Law for movement of water in soils (with the assumption of a rigid, isotropic, homogeneous, and one dimensional vertical flow domain) (Hanks and Ashcroft, 1986). The soil water diffusivity (D) is given by

$$D = K(\theta)\left[\frac{\partial \psi}{\partial \theta}\right] \tag{2-2}$$

where ψ is the matric potential, which is a measure of the holding strength of the soil particles to water (i.e., suction or negative pressure). Cosby et al. (1984) computed K and ψ using the empirical functions

$$K(\theta) = K_s\left[\frac{\theta}{\theta_s}\right]^{2b+3} \tag{2-3}$$

and

$$\psi(\theta) = \frac{\psi_s}{\left(\frac{\theta}{\theta_s}\right)^b} \tag{2-4}$$

where K_s, ψ_s, θ_s and b are the saturated hydraulic conductivity, saturated soil water tension, saturation value of volumetric water content, and a curve-fitting parameter respectively. They all depend on the soil type.

K and D are highly non-linear functions of soil moisture and in particular when the soil is dry, they can change very rapidly by several orders of magnitude, for a small variation in soil moisture. As the soil-water parameterization is very sensitive to the diurnal partitioning of surface energy into latent and sensible heat (Cuenca et al., 1996), Chen and Dudhia (2001) suggested the investigation of alternative soil hydraulic parameterization schemes that would effectively accommodate the dynamic relationship between hydraulic conductivity and soil moisture.

Expanding the source and sink term (F_θ) and integrating equation (2-1) over four soil layers, as used in the MM5 model, yields:

$$d_{z1}\frac{\partial\theta_1}{\partial t} = -D\left(\frac{\partial\theta}{\partial z}\right)_{z1} - K_{z1} + P_d - R - E_{dir} - E_{t1} \tag{2-5}$$

$$d_{z2}\frac{\partial\theta_2}{\partial t} = D\left(\frac{\partial\theta}{\partial z}\right)_{z1} - D\left(\frac{\partial\theta}{\partial z}\right)_{z2} + K_{z1} - K_{z2} - E_{t2} \tag{2-6}$$

$$d_{z3}\frac{\partial\theta_3}{\partial t} = D\left(\frac{\partial\theta}{\partial z}\right)_{z2} - D\left(\frac{\partial\theta}{\partial z}\right)_{z3} + K_{z2} - K_{z3} - E_{t3} \tag{2-7}$$

$$d_{z4}\frac{\partial\theta_4}{\partial t} = D\left(\frac{\partial\theta}{\partial z}\right)_{z3} + K_{z3} - K_{z4} \tag{2-8}$$

where d_{zi} is the i–th soil layer thickness, P_d is the precipitation not intercepted by the canopy, R is the surface runoff, and E_{ti} is the canopy transpiration taken by the canopy root in the i-th layer within the root-zone layers. The soil water flux at the bottom of the model domain (i.e., drainage) is determined from the gravitational percolation term K_{z4}, and by assuming the hydraulic diffusivity to be zero at the bottom of the soil model.

Surface runoff is addressed in the LSM using the Simple Water Balance (SWB) model approach given by Schaake et al. (1996). The SWB model is a two-reservoir hydrological model that has been well calibrated for large river basins. It takes into

account the spatial heterogeneity of rainfall, soil moisture, and runoff. The excess of precipitation that is not infiltrated into the soil is termed surface runoff ($R = P_d - I_{max}$), where the maximum infiltration, I_{max}, is given as:

$$I_{\max} = P_d \frac{D_x\left(1-e^{(-kdt\delta i)}\right)}{P_d + D_x\left(1-e^{(-kdt\delta i)}\right)} \tag{2-9}$$

$$D_x = \sum_{i=1}^{4} \Delta Z_i(\theta_s - \theta_i) \tag{2-10}$$

$$k_{dt} = k_{dt.ref} \frac{K_s}{K_{ref}} \tag{2-11}$$

δ_i is the conversion of the current model time step δ_t (in seconds) into daily values ($\delta_i = \delta_t/86400$), K_s is the saturated hydraulic conductivity which depends on soil texture, D_x is soil moisture deficit, θ_s is the volumetric water content at saturation point, θ_i is the actual volumetric water content, k_{dt} is a runoff parameter, and $k_{dtref} = 3.0$ and $K_{ref} = 2 \times 10^{-6}$ m s^{-1}. Chen and Dudhia (2001) suggested the calibration of these parameters over various basins with different precipitation characteristics.

The total evaporation, E, as formulated in the LSM, is the sum of 1) the direct evaporation from the top shallow soil layer, E_{dir}, 2) evaporation of precipitation intercepted by the canopy, E_c, and 3) transpiration through canopy and roots, E_t.

$$E = E_{dir} + E_t + E_c \tag{2-12}$$

The simple linear expression for bare soil evaporation is:

$$E_{dir} = \left(1-\sigma_f\right)\left(\frac{\theta-\theta_w}{\theta_{ref}-\theta_w}\right)E_p \tag{2-13}$$

where θ_w and θ_{ref} are the soil wilting point and field capacity (dimensionless), σ_f is the green vegetation fraction (dimensionless) which is critical for the partitioning of total evaporation between bare-soil direct evaporation and canopy transpiration, and E_p is the potential evaporation (ms^{-1}), calculated by a Penman-based energy balance and given by:

$$Ep = \frac{\Delta(Rn - G) + \rho\lambda C_h |u_a|(q^* - q)}{1 + \Delta} \tag{2-14}$$

where Δ is the local derivative of saturation specific humidity (q^*) with respect to temperature (dimensionless), R_n and G are the surface net radiation and ground heat flux ($W\ m^{-2}$), u_a is the surface layer wind speed ($m\ s^{-1}$), q is specific humidity and ρ, λ and C_h are the air density ($Kg\ m^{-3}$), latent heat of vaporization ($J\ kg^{-1}$), and surface exchange coefficient ($m\ s^{-1}$), respectively.

Evaporation of rainfall intercepted by the canopy is governed by:

$$E_c = \sigma_f E_p \left(\frac{W_c}{S}\right)^n \tag{2-15}$$

where W_c is the canopy intercepted water content (mm), S is the maximum allowed value for W_c (specified here as 0.5 mm), and n = 0.5. W_c is determined by a budget equation:

$$\frac{\partial W_c}{\partial t} = \sigma_f P - D - E_c \tag{2-16}$$

where P is the total precipitation ($kg\ m^{-2}\ s^{-1}$), and D is the drip or precipitation that reaches the ground (mm). This implies that P_d in equation (2-5) is computed by:

$$P_d = (1 - \sigma_f)P + D \tag{2-17}$$

It is worthwhile to note that after significant rainfall, then W_c reaches S, and the time tendency in equation (2-16) reduces to zero and $P_d \approx P$. In other words, additional rainfall drips off the canopy and reaches the ground (except the small amount lost to E_c)

E_t is determined by:

$$E_t = \sigma_f E_p B_c \left[1 - \left(\frac{W_c}{S} \right)^n \right] \tag{2-18}$$

where B_c (dimensionless) is a function of canopy resistance and is expressed as:

$$B_c = \frac{1 + \frac{\Delta}{R_r}}{1 + R_c C_h + \frac{\Delta}{R_r}} \tag{2-19}$$

where R_r (dimensionless) is a function of surface air temperature, surface pressure and C_h (m s^{-1}), and R_c is the canopy resistance (s m^{-1}). Details on C_h, R_r and Δ are given by Ek and Mahrt (1991). R_c is calculated using the formulation of Jacquemin and Noilhan (1990):

$$R_C = \frac{R_{c\min}}{LAI \, F_1 F_2 F_3 F_4} \tag{2-20}$$

where

$$F1 = \frac{R_{c\min} / R_{c\max} + f}{1 + f} \tag{2-21}$$

$$f = 0.55 \frac{R_g}{R_{gl}} \frac{2}{LAI} \tag{2-22}$$

$$F_2 = \frac{1}{1 + h_s [q_s(T_a) - q_a]} \tag{2-23}$$

$$F_3 = 1 - 0.0016 (T_{ref} - T_a)^2 \tag{2-24}$$

$$F_4 = \sum_{i=1}^{3} \frac{(\theta_i - \theta_w) d_{zi}}{(\theta_{ref} - \theta_w)(d_{z1} + d_{z2})} \tag{2-25}$$

F_1, F_2, F_3 and F_4 are all subject to 0 and 1 as lower and upper bounds and they represent the effects of solar radiation, vapor pressure deficit, air temperature and soil moisture,

respectively. LAI is the leaf area index, R_{cmin} is the minimum stomatal resistance, and R_{cmax} is the cuticular resistance of the leaves and is specified as 5000 s m^{-1} as in Dickinson et al. (1993). R_{gl} (limiting value of photosynthetically active solar radiation) is 100 W m^{-2} and R_g is determined from radiation physics (Jacquemin and Noilhan, 1990); $q_s(T_a)$ is the saturated water vapor mixing ratio at the air temperature T_a and q_a is the actual specific humidity. The parameter T_{ref} is 298 K (Noilhan and Planton, 1989). The soil moisture stress function, F_4, embodies a linear relationship in soil moisture stress between the field capacity θ_{ref} and the wilting point θ_w, and is only integrated in the root-zone which encompasses the first three soil layers in the current formulation.

Soil Thermodynamics

One of the primary functions of the coupled land surface model is to provide the near-surface layer of an atmospheric model with sensible and latent heat fluxes, as well as surface skin temperature to compute upward longwave radiation. The surface skin temperature is determined following Mahrt and Ek [1984] by applying a single linearized surface energy balance equation:

$$T_{skin} = \frac{R_n - \lambda E - G}{\rho C_p C_h |U_a|} + T_a \tag{2-26}$$

where R_n is the net radiation (W m^{-2}), G is the ground heat flux (W m^{-2}), λE is the latent heat flux (W m^{-2}), C_p is the air heat capacity (J m^{-3} K^{-1}), U_a is the surface layer wind speed (m s^{-1}), and T_a is the near-surface air temperature (K). Equation (2-26) expands the sensible heat flux (H) term such that the relationship can be expressed in terms of T_{skin}. As the skin is treated as an infinitesimally thin layer, and has no thermal inertia (heat capacity) of its own, the skin temperature may be very sensitive to forcing (especially

radiation) errors. This expression has to be solved iteratively due to the implicit relationship, as some of the terms on the right hand side of the equation also contain skin temperature. The ground heat flux is governed by the diffusion equation for soil temperature (T):

$$C(\theta)\frac{\partial T}{\partial t} = \frac{\partial}{\partial z}\left(K_t(\theta)\frac{\partial T}{\partial z} \right) \tag{2-27}$$

where C is the volumetric heat capacity (J m^{-3} K^{-1}) and K_t is the thermal conductivity (W m^{-1} K^{-1}), and both are functions of θ; θ is fraction of unit soil volume occupied by water; and t and z are time (s) and the vertical distance (m) from the soil surface downward (i.e., the depth), respectively.

C and K_t are formulated as functions of volumetric water content, θ, and are given by:

$$C(\theta) = \theta C_{water} + (1-\theta_s)C_{soil} + (\theta_s - \theta)C_{air} \tag{2-28}$$

$$K_t(\theta) = \begin{cases} 420e^{-(2.7+Pf)}, 0 \le P_f \le 5.1 \\ 0.1744, P_f > 5.1 \,\&\, P_f < 0 \end{cases} \tag{2-29}$$

$$P_f = \log\left[\psi_s \left(\theta_s / \theta \right)^b \right] \tag{2-30}$$

The volumetric heat capacities are C_{water} = 4.2 x 10^6 J m^{-3} K^{-1}, C_{soil} = 1.26 x 10^6 J m^{-3} K^{-1}, and C_{air} = 1004 J m^{-3} K^{-1}. θ_s and ψ_s are maximum soil moisture (porosity) and saturated soil potential (suction), respectively, and both depend on the soil texture (Cosby et al., 1984). The K_t relationship used in the LSM, as suggested by McCumber and Pielke (1981), has been used in many land surface models (e.g., Noilhan and Planton, 1989; Viterbo and Beljaars, 1995). However, Peters-Lidard et al. (1998) showed that this approach tends to overestimate (underestimate) K_t during wet (dry) periods, and the

surface heat fluxes are sensitive to the treatment of thermal conductivity. In the LSM, K_t is capped at 1.9 W m^{-1} K^{-1}. Chen and Dudhia (2001) suggested that several thermal conductivity formulations are needed to arrive at the best approach.

Expanding equation (2-27) for the i^{th} soil layer yields:

$$\Delta z_i C_i \frac{\partial T_i}{\partial t} = \left(K_t \frac{\partial T}{\partial z} \right)_{z_i+1} - \left(K_t \frac{\partial T}{\partial z} \right)_{z_i} \tag{2-31}$$

where Δz_i is the thickness (m) of the i-th soil layer. The prediction of T_i is performed using the fully implicit Crank-Nicholson scheme. In the top layer the last term in equation (6) represents the surface ground heat flux and is computed using the surface skin temperature. The gradient at the lower boundary, assumed to be 3 m below the ground surface, is computed from a specified constant boundary temperature and is taken as the mean annual near-surface air temperature.

CHAPTER 3

VALIDATION OF A SIMPLE DOWNWELLING LONGWAVE RADIATION SCHEME FOR BOTH DAYTIME AND NIGHTTIME CONDITIONS

Abstract

This chapter addresses the refinement and testing of a simple downwelling longwave radiation model. Oklahoma Atmospheric Surface-layer Instrumentation System (OASIS) radiation data in combination with Oklahoma Mesonet weather data were used to evaluate various techniques for estimating downwelling longwave radiation, for daytime and nighttime as well as clear and cloudy skies. The Brutsaert (1975) equation, which requires near-surface temperature and vapor pressure data, was chosen for further investigation. A simple regression calibration was performed for Brutsaert's leading coefficient using hourly data from four OASIS sites. The calibrated equation was applied to five independent OASIS sites and the hourly predictions of downwelling longwave radiation showed good agreement with the measurements. The mean bias error ranged between –3.95 and 4.24 Wm^{-2}, and the root mean square error was approximately 20 Wm^{-2} in all five cases. Comparisons to a more complex longwave radiation formulation that explicitly considers cloudiness were also quite favorable. The significance of this downwelling longwave radiation scheme is that it is simple and seasonally invariant and predicts well during both daytime and nighttime conditions.

Introduction

A thorough understanding of the factors controlling the surface energy balance is of paramount importance in effectively estimating evapotranspiration, soil moisture, global climate change, and other phenomena. Accurate partitioning of energy balance components also improves regional weather predictions and global climate simulations. Downwelling longwave radiation plays a significant role in investigations of the energy balance, and longwave radiation is a key component of the radiation budget found in land surface models (Chen et al., 1996; Hatzianastassiou et al., 1999). Longwave radiation is also an important component in sea ice modeling studies (Guest, 1998). When shortwave components are relatively small in magnitude due to clouds, the season of the year, or other factors, the accuracy in the measurement or computation of downwelling longwave radiation becomes relatively more important.

As downwelling longwave radiation is more difficult and expensive to measure than shortwave radiation (Esbensen and Kushnir, 1981; Francis, 1997; Hatzianastassiou et al., 1999), it is frequently estimated from weather variables that are easier to measure such as air temperature and vapor pressure (Morill et al., 1999). Various techniques have been developed to estimate downwelling longwave radiation for daytime clear and cloudy skies, and no single technique has emerged as the most appropriate one to use. The focus in this study was to evaluate several of the available techniques, to investigate possible improvements and/or simplifications to those techniques, and to incorporate nighttime as well as daytime conditions. The goal was to identify a simple and reliable technique that could be used to estimate downwelling longwave radiation for input to a land surface model.

Models for longwave radiation

The general equation for calculating downwelling longwave radiation (LW_{in}) for clear sky conditions is given as

$$LW_{in} = \varepsilon_c \sigma T^4 \tag{3-1}$$

where ε_c is the effective clear-sky atmospheric emissivity (dimensionless), σ is the Stefan- Boltzmann constant (5.675×10^{-8} J m^{-2} K^{-4} s^{-1}), and T is the air temperature (K). Though the amount of downwelling longwave radiation is dependent upon the atmospheric emissivity and temperature, due to the difficulties associated in specifying them, parameterizing the longwave downwelling radiation based upon near-surface measurements of temperature and/or vapor pressure becomes critical. Many studies (Brunt, 1932; Swinbank, 1963; Idso and Jackson, 1969; Aase and Idso, 1978; Hatfield et al., 1983) suggested that atmospheric emittance can be related to either vapor pressure only or vapor pressure and air temperature at screen height. These studies primarily resulted in deriving location-specific atmospheric emittance formulations utilizing local empirical coefficients. This leads to a natural concern about the transferability of these estimations.

Brutsaert (1975) analytically derived an equation to compute downward longwave radiation at ground level under clear skies and nearly standard atmospheric conditions:

$$LW_{in} = 1.24\left(\frac{10e_d}{T}\right)^{1/7} \sigma T^4 \tag{3-2}$$

where T is the air temperature (K), e_d is the vapor pressure (kPa) at screen height and LW_{in} has the units of Wm^{-2}. Using expressions by Idso (1981) and Anderson (1954) for

clear-sky atmospheric emittance, downwelling longwave radiation can be given respectively as

$$LW_{in} = \left(0.7 + \frac{59.5}{10^5} e_d \exp\left(\frac{1500}{T}\right)\right)\sigma T^4 \tag{3-3}$$

$$LW_{in} = \left(0.68 + 0.036\sqrt{10e_d}\right)\sigma T^4 \tag{3-4}$$

Though these three equations are prominent for clear sky conditions, they do not explicitly consider clouds and their effect on the total effective emissivity of the sky. Crawford and Duchon (1999) generalized the effect of clouds by introducing a cloud fraction term, *clf*, defined as

$$clf = 1 - s \tag{3-5}$$

in which s is the ratio of the measured solar irradiance to the clear-sky irradiance. They also considered equation (3-2) and suggested seasonal adjustments to the leading coefficient ranging from 1.28 in January to 1.16 in July. Thus the Crawford and Duchon (1999) downwelling longwave radiation equation is

$$LW_{in} = \left\{ clf + (1 - clf)\left(1.22 + 0.06\sin\left[(m + 2)\frac{\pi}{6} \right]\left(\frac{e_d}{T} \right)^{\frac{1}{7}} \right) \right\}\sigma T^4 \tag{3-6}$$

where m is the numerical month (e.g., January = 1), T is the air temperature (K) and e_d is the vapor pressure (millibars). The estimation of cloud fraction in equation (3-6) requires solar irradiance measurements during the daytime, and some means of estimating cloud fraction for nighttime conditions. The sinusoidal variation as shown in equation (3-6)

results in the largest value for the leading coefficient in winter and the smallest in summer.

Culf and Gash (1993) recommended 1.31 instead of 1.24 for Brutsaert's leading coefficient in equation (3-2) during dry seasons in Niger, and a reduced coefficient during wet seasons. Traditional longwave models such as Swinbank (1963) and Idso and Jackson (1969), which use only temperature for their emittance calculation, tend to be location specific and inadequate in their estimation (Hatfield et al., 1983). These authors also suggested that inclusion of a water vapor term leads to improvements in the longwave estimation such that the error is less than 5% for clear skies. The recently developed satellite-based longwave radiation scheme by Diak et al. (2000) included cloudy conditions, but the empiricism in the scheme and the 10-km pixel size of the Geostationary Operational Environmental Satellite (GOES) cloud product could result in some uncertainties.

Data

The Oklahoma Mesonet (Brock et al., 1995; Elliott et al., 1994), a system of 114 automated measurement stations across Oklahoma, provides the platform for the Oklahoma Atmospheric Surface-layer Instrumentation System (OASIS) project (Brotzge et al., 1999). The OASIS project was designed to enhance the Mesonet's capability to measure boundary layer fluxes of sensible, latent, and ground heat, as well as the radiation balance, and is believed to represent the most extensive flux measurement network in the world.

At ten OASIS "super-sites," a Kipp & Zonen CNR1 four-component net radiometer is used to measure incoming and outgoing shortwave and longwave radiation.

The integrated design of the CNR1 incorporates an upward-facing, ISO-class (International Organization for Standardization), thermopile pyranometer and pyrgeometer, and a complementary downward-facing pyranometer and pyrgeometer. The body of the CNR1 houses a PT-100 RTD (Platinum Resistance Temperature Detector) temperature sensor for accurate instrument body temperature measurements. The sensitivity of all four sensors is trimmed and calibrated to a single identical sensitivity coefficient, during manufacturing.

Downwelling longwave radiation data were measured at a height of 2 m, and hourly averages were calculated from 5-minute average observations for this study. Mesonet dewpoint temperature (which was used to derive vapor pressure) and air temperature were measured at a 1.5-m height and also averaged over one hour. The Mesonet's Li-Cor Model 200 silicon-cell pyranometers were used to measure solar irradiance (at a height of 1.8 m) for the calculation of cloud fraction (equation 3-5). As opposed to the CNR1, this instrument is available at all Mesonet sites and therefore more suitable for any operational method requiring solar irradiance data. OASIS and Mesonet data from nine sites as shown in Figure 3-1 and listed in Table 3-1 were used in this study.

Model selection and calibration

Equations (3-2), (3-3) and (3-4) were used in their original form to observe their performance for both clear and cloudy sky conditions during all hours of the day. That is, model estimates were compared to observed data (daytime and nighttime) on an hourly basis for a seven-month period (June, 1999 through December, 1999). The results are shown in Table 3-2. Considering all three methods and all nine sites, the root mean

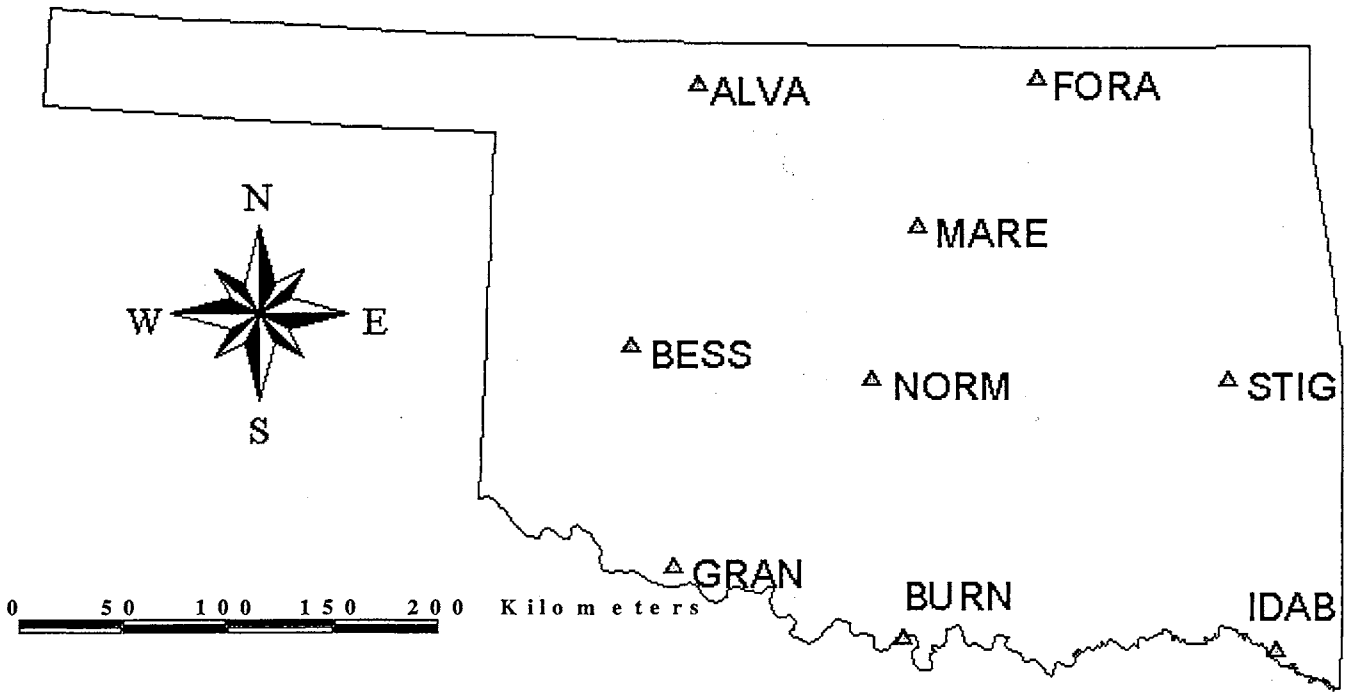

Figure 3-1. Location of Oklahoma Atmospheric Surface-layer Instrumentation System (OASIS) sites.

Table 3-1. Oklahoma Atmospheric Surface-layer Instrumentation System (OASIS) sites used in this study.

Site	Latitude(deg)	Longitude(deg)	Approx.no.of hourly observations
ALVA	36.7797	-98.6717	7540
BESS	35.4017	-99.0589	7787
BURN	33.8939	-97.2692	8106
FORA	36.8403	-96.4278	8015
GRAN	34.2392	-98.7397	7418
IDAB	33.8303	-94.8806	7811
MARE	36.0644	-97.2128	7910
NORM	35.2556	-97.4836	7884
STIG	35.2653	-95.1814	5887

Table 3-2. Comparison of 3 clear-sky downwelling longwave radiation schemes to observed hourly data.

Site	Mean Bias Error (W/m2)			Root Mean Square Error (W/m^2)			Mean Absolute Error (W/m^2)			Mean Percent Error (%)		
	Eqn. 3-2	Eqn. 3-3	Eqn. 3-4	Eqn. 3-2	Eqn. 3-3	Eqn. 3-4	Eqn. 3-2	Eqn. 3-3	Eqn. 3-4	Eqn. 3-2	Eqn. 3-3	Eqn. 3-4
ALVA	-23.52	-6.67	-17.34	41.42	32.34	37.33	33.11	24.41	28.65	9.43	6.77	7.84
BESS	-15.77	2.54	-8.69	39.98	36.79	38.21	22.83	19.87	19.92	8.33	7.66	7.58
BURN	-16.79	2.39	-12.63	27.21	21.84	24.45	20.47	16.12	17.87	5.76	4.38	4.82
FORA	-17.47	2.75	-13.30	30.47	24.73	27.47	22.45	19.22	19.48	6.58	5.37	5.45
GRAN	-19.82	-3.19	-10.72	39.15	31.86	35.59	30.39	23.76	26.60	8.57	6.58	7.30
IDAB	-15.12	5.58	-13.70	26.73	22.36	25.42	20.08	17.71	19.37	5.67	4.80	5.26
MARE	-17.05	3.32	-11.99	41.03	37.30	39.08	21.80	18.40	19.03	6.22	5.02	5.17
NORM	-18.45	0.75	-14.10	29.68	23.29	26.95	21.39	17.17	18.80	5.96	4.68	5.05
STIG	-17.81	1.74	-13.94	28.75	22.95	26.23	21.64	17.44	19.59	6.09	4.77	5.32

$$MBE = \frac{\sum_{i=1}^{n}(P-O)}{n}; \qquad RMSE = \sqrt{\frac{\left[\sum_{i=1}^{n}(P-O)^2\right]}{n}}; \qquad MAE = \frac{\sum_{i=1}^{n}(|P-O|)}{n}; \qquad MPE = \left(\frac{1}{n}\sum_{i=1}^{n}\frac{|(P-O)|}{|O|}\right)\times 100;$$

P is the predicted value, O is the observed value and n is the sample size.

square error (RMSE) ranged between about 20 and 40 W m^{-2}, with no one of the methods appearing to be clearly superior in its ability to predict observed downwelling longwave radiation. Equation (3-3) resulted in the smallest errors, but it can be seen from the mean bias error (MBE) that equations (3-2) and (3-4) had a strong negative bias for all of the sites, suggesting that an adjusted calibration could significantly improve model predictions. The range of about 20 to 30 W m^{-2} in mean absolute error (MAE) and 5 to 8 percent in mean percent error (MPE) in equations (3-2), (3) and (4) also implied that all of these models were performing similarly. Equation (3-2) was selected as the focus for this effort because it was analytically derived and widely used, because the magnitude and sign of its errors seemed quite consistent from site to site, and because the presence of the leading coefficient (1.24) simplified the calibration process.

Equation (3-2) was calibrated for four sites (ALVA, FORA, GRAN and IDAB) individually, using simple linear regression (intercept equal to zero). The resulting leading coefficients for the four sites ranged from 1.30 to 1.32 as shown in Table 3-3. The MBE was significantly reduced for all sites, and also for most sites the RMSE decreased, with a slight increase only at IDAB. The simple averaging of the four coefficients resulted in a value of 1.31, which represents different geographic locations and climatic conditions within Oklahoma. While ALVA and FORA are situated in the northern part of the state (west and east with an elevation of 450 m and 330 m respectively), GRAN and IDAB are located in the southern part of the state (again, west and east with an elevation of 342 m and 110 m respectively). The mean annual temperature of ALVA and FORA is slightly lower (about 14 °C) than that of GRAN and IDAB (about 17 °C).

Table 3-3. Regression calibration of Brutsaert's leading coefficient in equation (3-2).

Site	ALVA	FORA	GRAN	IDAB
Mean Obs. LW_{in} (W/m^2)	335.99	337.08	337.93	360.37
Mean Bias Error (W/m^2)	-2.57	-2.66	-2.28	-2.52
Root Mean Square Error (W/m^2)	22.42	24.21	23.17	29.86
Mean Percent Error (%)	5.59	5.64	5.33	6.51
Mean Absolute Error (W/m^2)	18.47	19.14	17.99	22.99
Leading Coeff.	1.323	1.304	1.308	1.300

Average leading coefficient: 1.31

The downwelling longwave radiation equation of Brutsaert (equation 3-2) then becomes:

$$LW_{in} = 1.31\left(\frac{10e_d}{T}\right)^{1/7}\sigma T^4 \tag{3-7}$$

The significance of equation (3-7) is that the leading coefficient is fixed for all seasons and skies, and for both daytime and nighttime conditions. It should also be noted that the leading coefficient obtained in this method agrees with the results of Culf and Gash (1993).

The performance of equation (3-7) was compared to that of equation (3-6) using data independent from the calibration dataset discussed above. As equation (3-6) included a complex cloud fraction computation and seasonal variations, it was considered to be desirable to compare with equation (3-7). In order to calculate the cloud fraction in equation (3-6), both measured and clear-sky solar irradiance must be known. The Mesonet pyranometer provided the observed values of incoming shortwave radiation, and the clear- sky solar irradiance was computed following the procedures described *in* Crawford and Duchon (1999). The transmission coefficients for Rayleigh scattering, absorption by permanent gases and water vapor, and absorption and scattering by aerosols were calculated first. Using these transmission coefficients, the effective solar constant and the solar zenith angle, clear-sky solar irradiance was determined. For nighttime conditions, the ratio of the measured solar irradiance to clear-sky irradiance was linearly interpolated by using the values near sunset and sunrise.

Results and Discussion

Validation of calibrated model

The performance of equation (3-7) was validated using an independent dataset obtained from five OASIS sites (BESS, BURN, MARE, NORM and STIG) for a one-year period (June, 1999 through May, 2000). Figures (3-2a-e) are equal-value plots illustrating the comparison for these sites over the one-year period. Figure 3-3 compares the time series of observed and modeled (equation 3-7) downwelling longwave radiation for the BURN site over the one-year period; time series plots for the other sites are very similar as shown in Appendix B. It can be seen that the model performed well over an extended period of time. As shown in Table 3-4, the MBE ranged between –3.95 and 4.24 Wm^{-2}, and the RMSE was approximately 20 Wm^{-2} in all five cases. The sites that were used for this validation represent different regions of the state and fall under different climatic regimes. The predictions using equation (3-7) consistently agreed well with the measurements, suggesting that the scheme could be used for any site in this region and for any season of the year.

Comparison of calibrated model with cloud-fraction longwave model

Equation (3-7) compared very favorably with equation (3-6), as shown in Table 3-5. The values of both MBE and RMSE were comparable for the two models. It is important to note that this model comparison was carried out for a limited period of time (85 days) from June 1 through August 25, 1999 in equation (3-6) and equation (3-7). The four sites used were those with data available beginning on June 1. By using a summer time period for the comparison, the number of nighttime hours is reduced and the

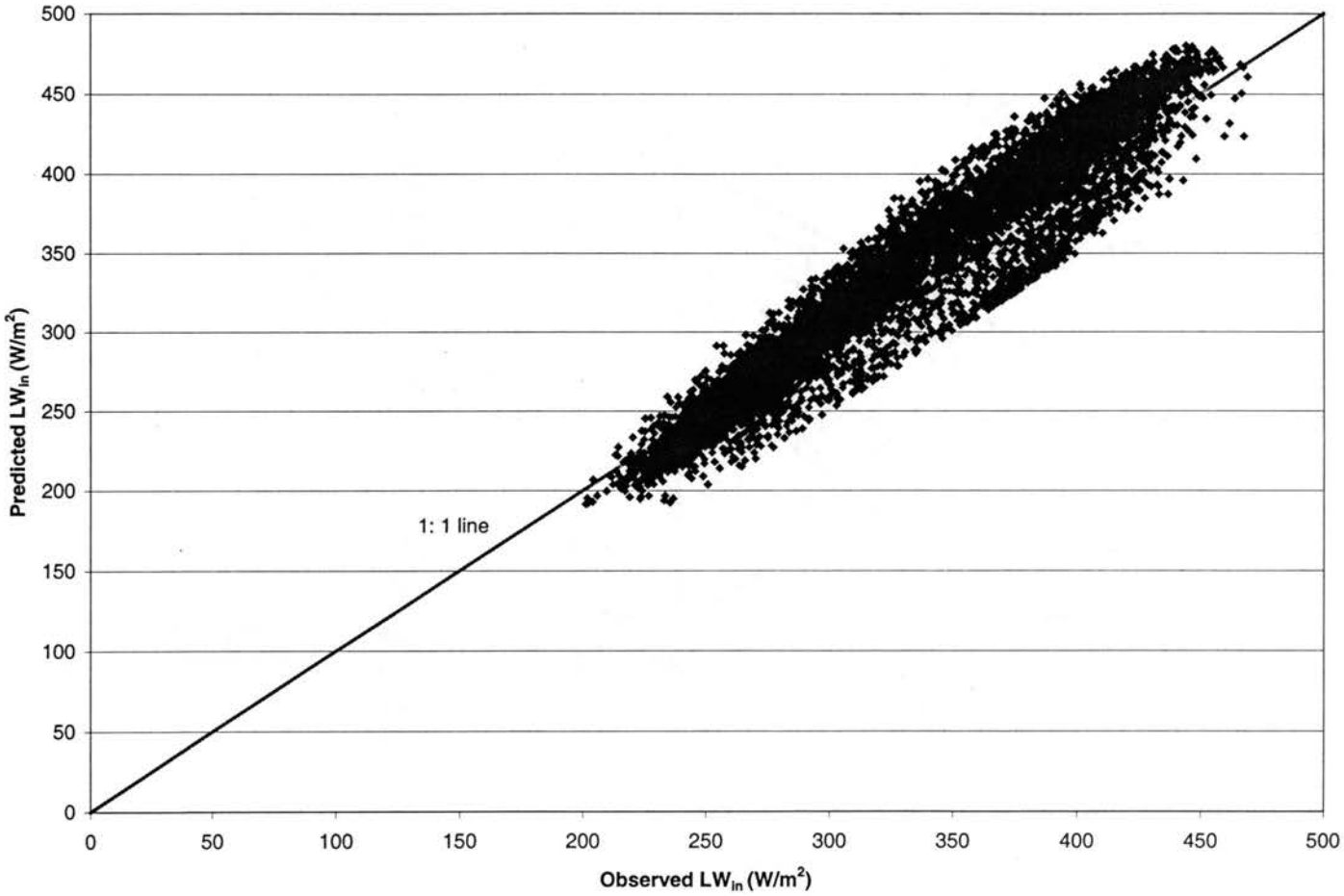

Figure 3-2a. Comparison of hourly observed and predicted downwelling longwave radiation for the BESS site.

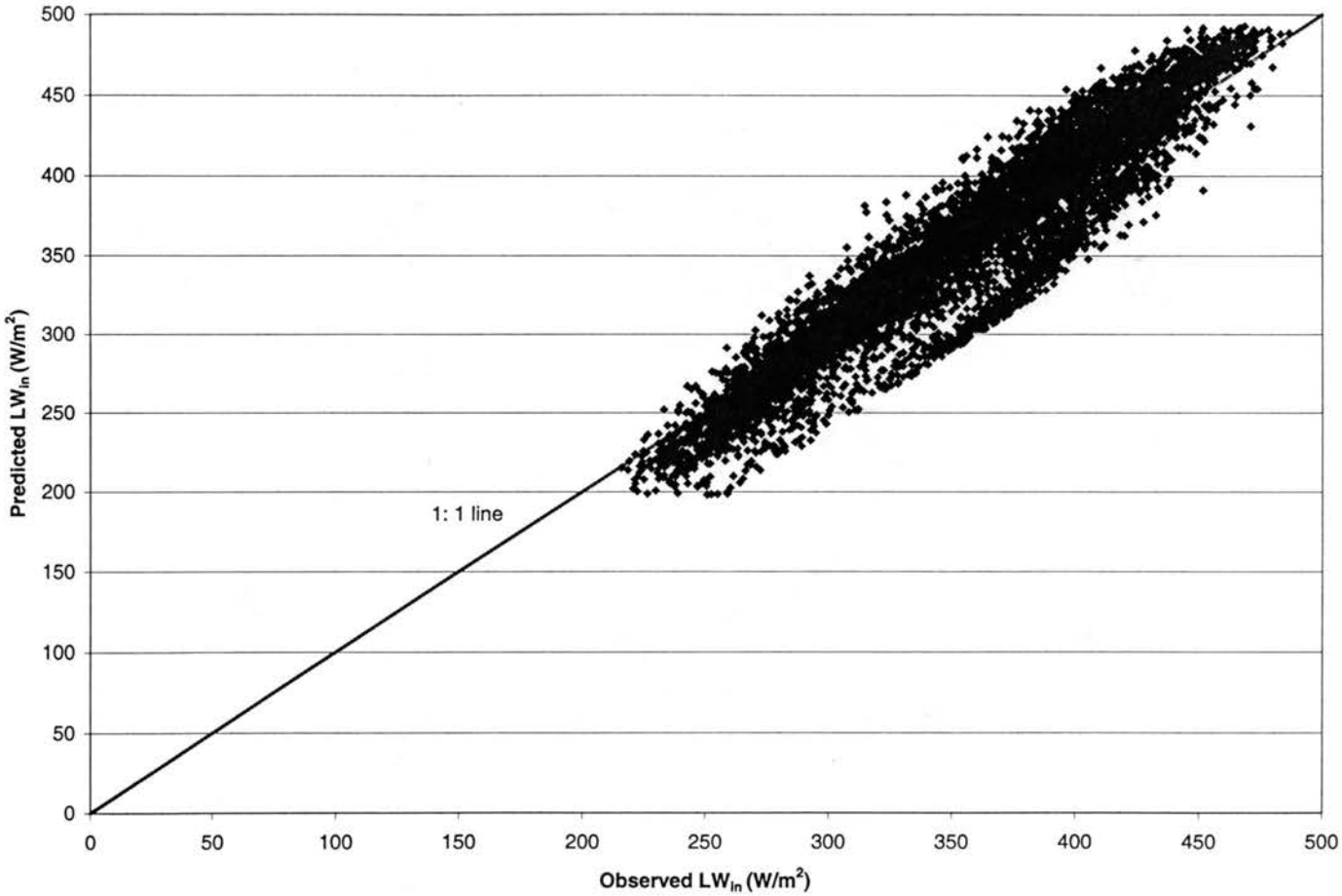

Figure 3-2b. Comparison of hourly observed and predicted downwelling longwave radiation for the BURN site.

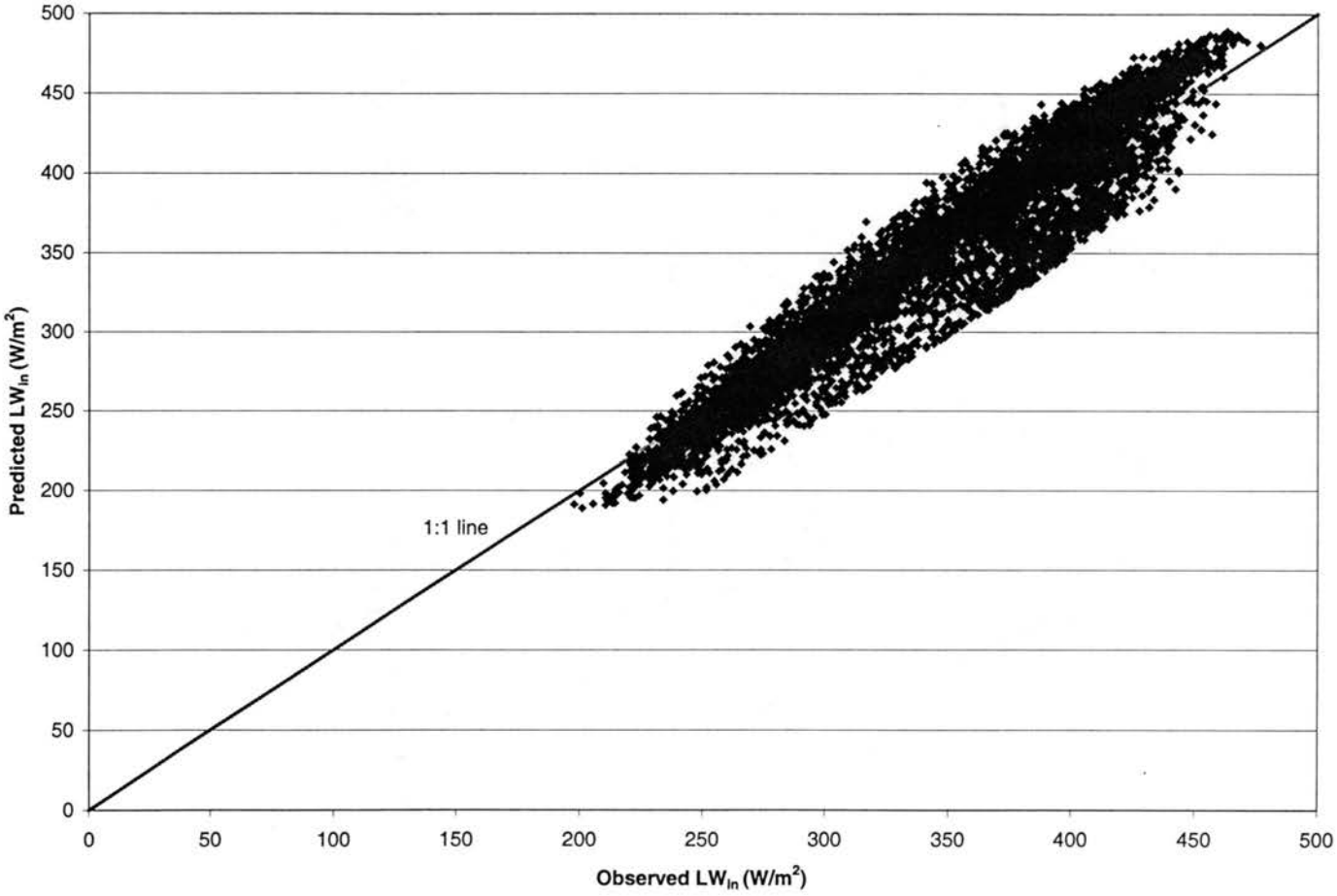

Figure 3-2c. Comparison of hourly observed and predicted downwelling longwave radiation for the MARE site.

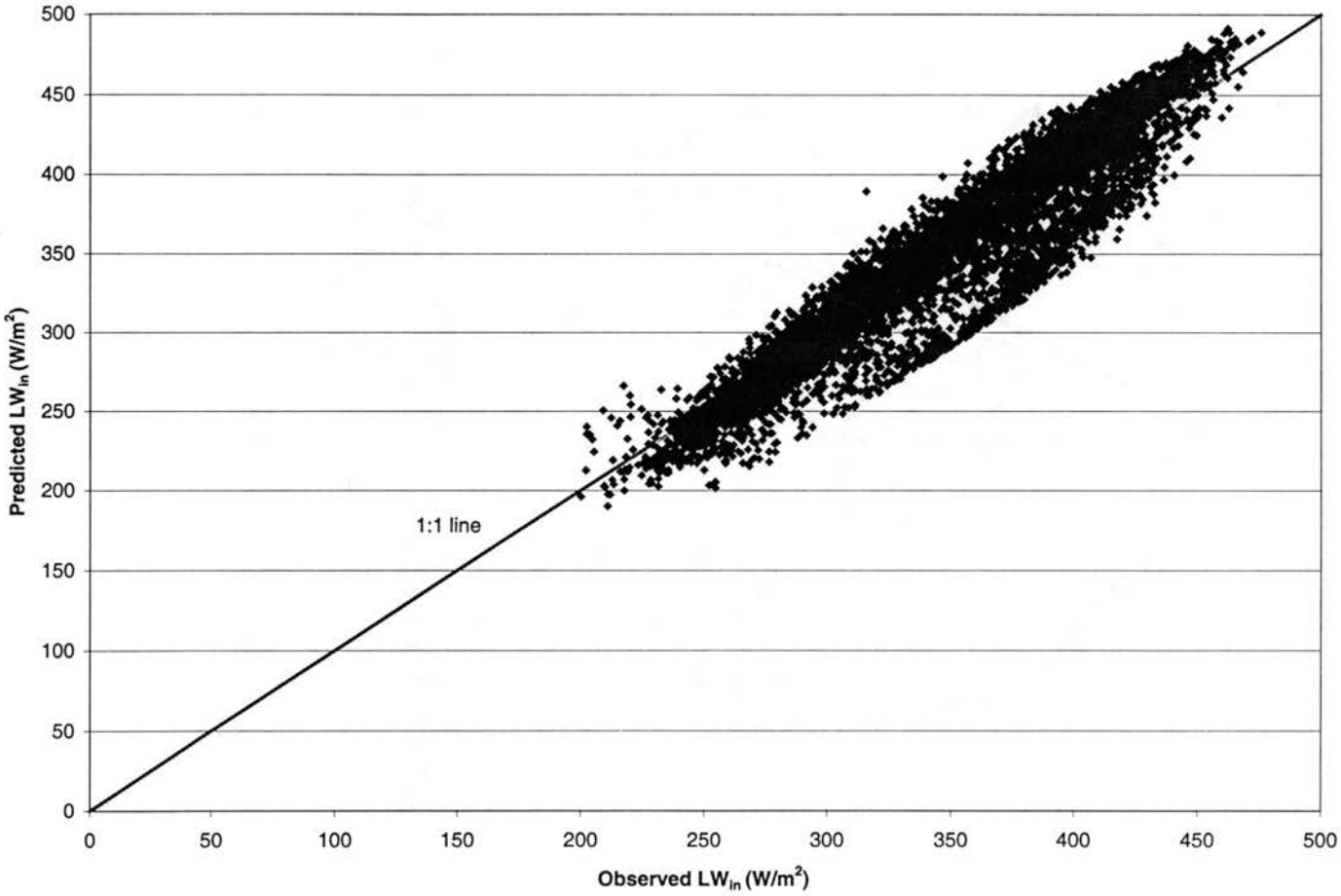

Figure 3-2d. Comparison of hourly observed and predicted downwelling longwave radiation for the NORM site.

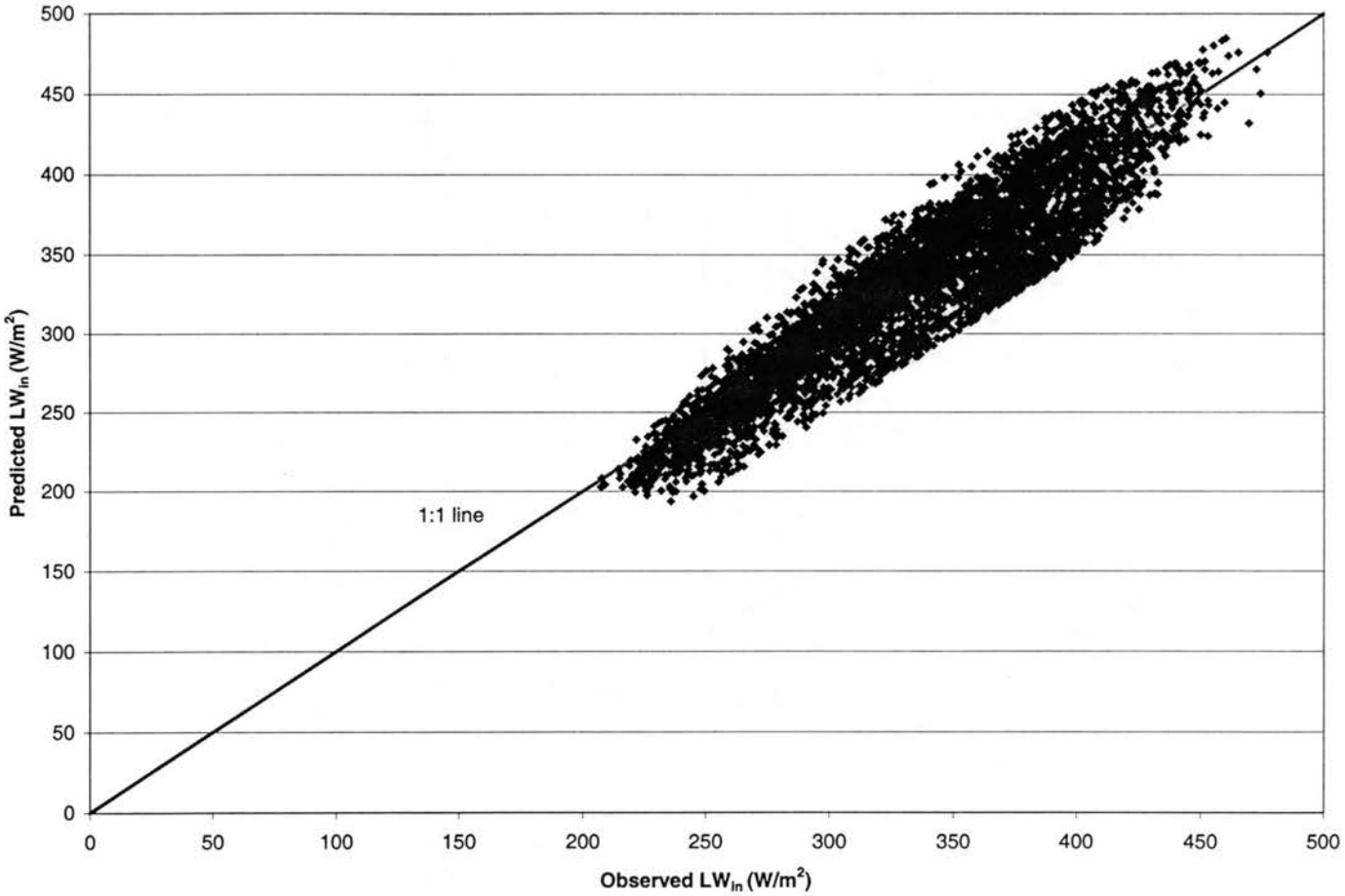

Figure 3-2e. Comparison of hourly observed and predicted downwelling longwave radiation for the STIG site.

Figure 3-3. Comparison of hourly observed and predicted downwelling longwave radiation for the BURN site.

Table 3-4. Validation of equation (3-7) using hourly data for June 1, 1999 though May 31, 2000.

Site	BESS	BURN	MARE	NORM	STIG
Mean Obs. LW_{in} (W/m^2)	334.21	354.69	342.74	347.20	332.50
Mean Bias Error (W/m^2)	4.24	-0.13	0.67	-0.36	-3.95
Root Mean Square Error (W/m^2)	21.81	22.68	21.50	22.08	22.24
Mean Percent Error (%)	5.23	5.07	5.03	4.97	5.38
Mean Absolute Error (W/m^2)	17.72	17.87	17.40	17.36	18.01

Table 3-5. Comparison of equations (3-6) and (3-7) to hourly observed data for June 1 though August 25, 1999.

Site	Mean Bias Error (W/m^2)		Root Mean Square Error (W/m^2)		Mean Absolute Error (W/m^2)		Mean Percent Error (%)		No. of Observations
	Eqn. 6	Eqn. 7	Eqn. 6	Eqn. 7	Eqn. 6	Eqn. 7	Eqn. 6	Eqn. 7	
BESS	-10.33	10.07	29.08	27.37	21.17	22.71	5.19	5.63	1858
BURN	-6.94	13.46	21.30	23.31	16.59	19.35	3.98	4.73	1855
MARE	-9.24	13.40	17.65	22.26	14.66	19.69	3.54	4.83	1596
NORM	-11.95	10.53	27.01	24.17	21.05	20.28	5.11	5.02	1842

uncertainties in interpolating the cloud factor in equation (3-6) should be minimized. The linear interpolation scheme was used between 18:00 and 7:00 CDT.

Even though equation (3-7) uses only temperature and vapor pressure as inputs, and does not require solar irradiance or "cloudiness" data, it predicts downwelling longwave radiation nearly as accurately as the more complex estimation method. The RMSE using equation (3-7) was approximately 25 W m^{-2} for the four sites in Table 3-5. The MBE was about 10 W m^{-2} and the mean percent error was about 5 percent and very close to the predictions by equation (3-6).

Based on these results from Oklahoma, it appears that the downwelling longwave radiation estimated by equation (3-7) is accurate enough to be used as the input for land surface models. This relatively simple equation performed well at a variety of sites and under both daytime and nighttime conditions. The mean absolute errors of approximately 20 W m^{-2} are less than 10% of measured downwelling longwave radiation, and rather insignificant compared to total surface radiation forcing.

Summary

A modified form of Brutsaert's (1975) equation has been developed to estimate downwelling longwave radiation for input to land surface models. The equation requires near-surface measurements of temperature and vapor pressure, and can be used under all sky conditions (day and night; clear and cloudy). The results show good agreement with measured data from several Oklahoma sites. It also compared very well with a more complex estimation method. The expression can be used reliably for climatologically similar locations where measurements of downwelling longwave radiation are not available.

CHAPTER 4

VALIDATION OF THE NOAH-OSU LAND SURFACE MODEL USING SURFACE FLUX MEASUREMENTS IN OKLAHOMA

Abstract

Oklahoma Atmospheric Surface-layer Instrumentation System (OASIS) measurements of net radiation (R_n), latent heat flux (LH), sensible heat flux (SH) and ground heat flux (GH) were used to validate the NOAH-OSU LSM (NOAH-Oregon State University Land Surface Model). A one-year study period was used. R_n, LH, SH and GH data from seven sites were screened based on an energy balance closure criterion (daily/hourly sum of the flux components within the range of –10 W m^{-2} to +10 W m^{-2}). The vegetation fraction used in the model was computed using both the Gutman-Ignatov (G-I) and the Carlson-Ripley (C-R) schemes. The simulated surface energy balance components were found to be sensitive to the choice of vegetation scheme, however the G-I approach was used for the validation study as it is widely used and linear in its form. The daily aggregated model outputs showed that the predicted R_n had a positive bias of 0.8 MJ m^{-2} d^{-1} and an RMSE of 1.6 MJ m^{-2} d^{-1} when averaged over all seven sites. The seven-site average bias in LH was about 0.9 MJ m^{-2} d^{-1} with an RMSE of 2.5 MJ m^{-2} d^{-1}. The bias in SH and GH was low and positive with an RMSE of about 2.2 MJ m^{-2} d^{-1} in SH estimation. The hourly average output showed similar results, with the exception that GH had a negative bias. The overall performance of the NOAH-OSU LSM was good for a diverse set of Oklahoma conditions.

Introduction

A strong coupling exists between land surface hydrologic processes and climate. Energy and water exchanges occur continuously at the interface between land surfaces and the lower atmosphere. The energy and water balances are linked by the conversion of thermal and radiative energy to latent heat. Realistic modeling of the processes of land-atmosphere interaction over a large area is being advanced by the realization that it should be addressed from both hydrologic and atmospheric science perspectives. Modeling of land surface processes plays an important role, not only in large-scale atmospheric models including general circulation models (GCMs), but also in regional and mesoscale atmospheric models (Mintz, 1981; Rowntree, 1983; Avissar and Pielke, 1989; Chen and Dudhia, 2001).

It is understood that the atmospheric and soil – vegetation systems are dynamically coupled through the physical processes which produce transport of thermal energy and water mass across the land surface (Eagleson, 1978; Entekhabi, 1996). Many studies have demonstrated the interaction between the atmosphere and the land surface and the significant role played by soil moisture in regional weather predictions (e.g., Yan and Anthes, 1988; Pielke, 1989; Avissar, 1992; Hipps et al., 1994; Chen and Brutsaert, 1995; Betts et al., 1996; Chen et al., 1996; Entekhabi et al., 1996; Henderson-Sellers, 1996; Betts et al., 1997; Sellers et al., 1997; Braud, 1998; Robock et al., 1998; Dirmeyer, 1999; Fennessy and Shukla, 1999; Silberstein et al., 1999; Dirmeyer et al., 2000). Recently, Rodriguez-Iturbe (2000) asserted that "the interplay between climate, soil and vegetation cannot be one of general and universal characteristics". The near-surface processes that include evapotranspiration and evaporation from bare soil and wet vegetation contribute to the surface energy partition and subsequent evolution of the

convective boundary layer (CBL). Studies that analyzed the feedback mechanism between precipitation and evaporation include Mintz (1984), Benjamin and Carlson (1986), Lanicci et al. (1987), Oglesby (1991) and Betts et al. (1996). Generally they suggested that more surface evaporation leads to more precipitation, causing greater persistence of wet and dry spells. As Eagleson (1986) suggested, the issue of global scale hydrology has reoriented the attention of hydrologists in considering the atmosphere and the land surface as an interactively coupled system. Physically based modeling is an important tool for studying the coupled system.

The purpose of this part of the present study was to validate the extended Oregon State University Land Surface Model (hereafter referred to as "NOAH-OSU LSM" or "NOAH LSM"), using surface flux measurements available from various sites in Oklahoma. This model has been coupled to the NCEP operational Eta and PSU/MM5 mesoscale models (Marshall, 1998; Chen and Dudhia, 2001) and is in wide use by the land surface research community. It is important to quantify model accuracy using measured data. This investigation was supported by the availability of unparalleled spatially distributed data from the Oklahoma Mesonet (Brock et al., 1995; Elliott et al., 1994), the Oklahoma Atmospheric Surface-layer Instrumentation System (OASIS) project (Brotzge et al., 1999) and extensive soil and landuse databases. These unique data provide an incentive for using a study area such as Oklahoma to carry out this validation task.

Model Description

Overview

Pan and Mahrt (1987) developed the original LSM that is the focus of this study. Chen et al. (1996) modified the model to incorporate an explicit canopy resistance formulation used by Jacquemin and Noilhan (1990). Originally, the LSM incorporated the diurnally-dependent Penman potential evaporation approach of Mahrt and Ek (1984), the multi-layer soil model of Mahrt and Pan (1984) and the primitive canopy model of Pan and Mahrt (1987). Later the NCEP/Office of Hydrology extended the improvements by including: (1) a fairly complex canopy resistance approach; (2) the bare soil evaporation approach of Noilhan and Planton (1989); (3) the surface runoff scheme of Schaake et al. (1996); (4) a higher-order time integration scheme by Kalnay and Kanamitsu (1988); and (5) refinements to the snowmelt algorithm and the treatment of soil thermal and hydraulic properties.

The LSM has one canopy layer and four soil layers with thicknesses of 0.1, 0.3, 0.6 and 1.0 m (total soil depth of 2 m) from the ground surface to the bottom, respectively. The four-level soil layer configuration is adopted in the LSM for capturing the daily, weekly and seasonal evolution of soil moisture and mitigating the possible truncation error in discretization. The lower 1 m acts as a reservoir with gravity drainage at the bottom, and the upper 1 m of soil serves as the root zone depth. From the standpoint of model input, the LSM requires soil and vegetation types and meteorological forcing variables (as the model is used here in an uncoupled fashion). Prognostic variables include soil moisture and temperature in the soil layers, water intercepted on the

canopy and snow accumulated on the ground. Model simulations also provide estimates of surface energy balance components (net radiation and latent, sensible, and ground heat fluxes).

Soil Hydrology

The prognostic equation for the volumetric soil water content (θ) in the hydrology model is given by:

$$\frac{\partial \theta}{\partial t} = \frac{\partial}{\partial z}\left(D\frac{\partial \theta}{\partial z}\right) + \frac{\partial K}{\partial z} + F_\theta \tag{4-1}$$

where D and K are the soil water diffusivity ($m^2\ s^{-1}$) and hydraulic conductivity ($m\ s^{-1}$), respectively, and both are functions of θ; t and z are time (s) and the vertical distance (m) from the soil surface downward (i.e., the depth), respectively; and F_θ represents sources and sinks (i.e., precipitation, evaporation and runoff). This diffusive form of the relationship is known as Richard's equation and is derived from Darcy's Law for movement of water in soils (with the assumption of a rigid, isotropic, homogeneous, and one dimensional vertical flow domain) (Hanks and Ashcroft, 1986). K and D are highly non-linear functions of soil moisture and in particular when the soil is dry, they can change several orders of magnitude for a small variation in soil moisture. As the soil-related parameterization is very sensitive to the diurnal partitioning of surface energy into latent and sensible heat (Cuenca et al., 1996), Chen and Dudhia (2001) suggested the investigation of alternative soil hydraulic parameterization schemes that would reflect the relationship between hydraulic conductivity and soil water content.

Surface runoff is addressed in the LSM using the Simple Water Balance (SWB) model approach given by Schaake et al. (1996). The SWB model is a two-reservoir

hydrological model that has been well calibrated for large river basins. It takes into account the spatial heterogeneity of rainfall, soil moisture, and runoff. The total evaporation is the sum of the direct evaporation from the top shallow soil layer, evaporation of precipitation intercepted by the canopy, and transpiration through the canopy via water uptake by roots. The bare soil evaporation scheme is governed by soil wilting point and field capacity, green vegetation fraction cover, and a Penman-based energy balance approach for potential evaporation. Evaporation of rainfall intercepted by the canopy is a function of the canopy intercepted water content, which depends upon the total precipitation and the precipitation that reaches the ground. The canopy transpiration is determined by:

$$E_t = \sigma_f E_p B_c \left[1 - \left(\frac{W_c}{S} \right)^n \right] \tag{4-2}$$

where E_t is canopy transpiration (m s^{-1}), σ_f is the green vegetation fraction (dimensionless), E_p is potential evaporation (m s^{-1}), W_c is the canopy intercepted water content (mm), S is the maximum allowed value for W_c (specified here as 0.5 mm), and n = 0.5 (dimensionless). B_c is a function of canopy resistance and is expressed as:

$$B_c = \frac{1 + \frac{\Delta}{R_r}}{1 + R_c C_h + \frac{\Delta}{R_r}} \tag{4-3}$$

where C_h is the surface exchange coefficient for heat and moisture (m s^{-1}), Δ is the slope of the saturation-specific humidity curve (dimensionless), R_r is a function of surface air temperature, surface pressure and C_h (dimensionless), and R_c is the canopy resistance (s

m^{-1}). Details on C_h, R_r and Δ are given by Ek and Mahrt (1991) and R_c is discussed by Jacquemin and Noilhan (1990).

Soil Thermodynamics

One of the primary functions of the coupled land surface model is to provide the near-surface layer of an atmospheric model with sensible and latent heat fluxes, and surface skin temperature to compute upward longwave radiation. The surface skin temperature is determined following Mahrt and Ek (1984) by applying a single linearized surface energy balance equation, given by:

$$T_{skin} = \frac{R_n - \lambda E - G}{\rho C_p C_h |U_a|} + T_a \tag{4-4}$$

where R_n is the net radiation (W m^{-2}), λE is the latent heat flux (W m^{-2}), G is the ground heat flux (W m^{-2}), ρ is the air density (Kg m^{-3}), C_p is the air heat capacity (J m^{-3} K^{-1}), C_h is the surface exchange coefficient for heat and moisture (dimensionless), U_a is the surface layer wind speed (m s^{-1}), and T_a is the near-surface air temperature (K). Equation (4-4) is the surface energy balance expression, with the sensible heat flux (H) term expanded such that the relationship can be expressed in terms of T_{skin}. As the skin is treated as an infinitesimally thin layer, and has no thermal inertia (heat capacity) of its own, the skin temperature may be very sensitive to forcing (especially radiation) errors. This expression has to be solved iteratively due to the implicit relationship, as some of the terms on the right hand side of the equation also contain skin temperature. The ground heat flux is governed by the diffusion equation for soil temperature (T):

$$C(\theta)\frac{\partial T}{\partial t} = \frac{\partial}{\partial z}\left(K_t(\theta)\frac{\partial T}{\partial z} \right) \tag{4-5}$$

where C is the volumetric heat capacity (J m^{-3} K^{-1}) and K_t is the thermal conductivity (W m^{-1} K^{-1}), and both are functions of θ; θ is fraction of unit soil volume occupied by water; and t and z are time (s) and the vertical distance (m) from the soil surface downward (i.e., the depth), respectively. The K_t relationship used in the LSM, as suggested by McCumber and Pielke (1981), has been used in many land surface models (e.g., Noilhan and Planton, 1989; Viterbo and Beljaars, 1995). However, Peters-Lidard et al. (1998) showed that this approach tends to overestimate (underestimate) K_t during wet (dry) periods, and the surface heat fluxes are sensitive to the treatment of thermal conductivity. In the LSM, K_t is capped at 1.9 W m^{-1} K^{-1}. Chen and Dudhia (2001) suggested that several thermal conductivity formulations are needed to arrive at the best approach.

Expanding equation (4-5) for the i^{th} soil layer yields:

$$\Delta z_i C_i \frac{\partial T_i}{\partial t} = \left(K_t \frac{\partial T}{\partial z} \right)_{z_i+1} - \left(K_t \frac{\partial T}{\partial z} \right)_{z_i} \tag{4-6}$$

where Δz_i is the thickness (m) of the i-th soil layer. The prediction of T_i is performed using the fully implicit Crank-Nicholson scheme. In the top layer the last term in equation (4-6) represents the surface ground heat flux and is computed using the surface skin temperature. The gradient at the lower boundary, assumed to be 3 m below the ground surface, is computed from a specified constant boundary temperature and is taken as the mean annual near-surface air temperature.

Previous studies using the LSM

Comparing against five months of the First International Satellite Land Surface Climatology Project (ISLSCP) Field Experiment (FIFE) observations, the performance of the modified LSM was superior to that of the simple bucket and fairly complex

Simplified Simple Biosphere (SSiB) models (Chen et al., 1996; Chen and Mitchell, 1999). The NOAH-LSM simulated the long-term observed diurnal variation of sensible heat fluxes and surface skin temperature very well, and captured the diurnal and seasonal evolution in evaporation and soil moisture. The NCEP implemented this NOAH-LSM in its operational Eta model in February 1996 under the support of the NOAA GCIP program (Marshall, 1998; Chen and Dudhia, 2001). Various studies (Betts et al., 1997; Chen et al., 1997; Yucel et al., 1998) showed that "the coupled Eta/NOAH-OSU LSM system indeed improved the short-range prediction of surface heat fluxes, near-surface sensible variables, boundary layer and precipitation" (Chen and Dudhia, 2001). Marshall (1998) studied the performance of this LSM in an uncoupled mode for Oklahoma conditions and found that the model overestimated net radiation and underestimated ground heat flux. He further suggested that the excess available energy resulted in an inappropriate estimation of latent and sensible heat flux. Marshall's (1998) study was limited to one site, and latent and sensible heat fluxes were estimated using Bowen ratio and aerodynamic approaches. As this NOAH-LSM is relatively simple (based on number of parameters), efficient (simulates with adequate accuracy) and similar to the LSM used in the NCEP's operational global and regional models, it has been implemented in the MM5 model (Chen and Dudhia, 2001).

Field Instrumentation and Data

Mesonet

The Oklahoma Mesonet (Elliott et al., 1994; Brock et al., 1995), a dense network of 114 automated measurement stations across Oklahoma, provided the forcing data that were used in this investigation. Each Mesonet station measures a number of

meteorological and hydrological variables. The Mesonet data used in this study were 5-minute averages that were again averaged over one-hour intervals. The variables used were air temperature (K), specific humidity (Kg Kg^{-1}), wind speed (m s^{-1}), pressure (Pa), precipitation (kg m^{-2} s^{-1}) and solar radiation (W m^{-2}). It should be noted that air temperature in degree K and specific humidity were derived quantities using the original Mesonet variables. Other data used for initial conditions were soil temperature (K) at 5 cm, 25 cm, and 60 cm and the two-year average of 1.5 m air temperature (K) for estimating soil temperature at 3 m. The scheme as shown in Chapter 3 was used for estimating downwelling longwave radiation. The scheme uses near-surface vapor pressure and air temperature data. The soil data for all the sites were also available from the Mesonet.

OASIS

The Oklahoma Mesonet also provides the platform for the Oklahoma Atmospheric Surface-layer Instrumentation System (OASIS) project (Brotzge et al., 1999; Brotzge, 2000). Instruments have been added at approximately 90 Mesonet stations, enabling routine surface energy budget measurements. These measurements include net radiation (R_n), sensible heat flux (SH) and ground heat flux (GH). Latent heat flux (LH) is estimated as the residual of the energy balance. Also, 10 of the 90 "Standard" sites are designated as "Super" sites and they have additional instrumentation to verify the simpler standard instrumentation. The OASIS data used in this study were from seven Super sites and included 5-minute averages of R_n, LH, SH and GH. Hourly averages were then computed. These data spanned a one-year period from 1 June 1999

through 31 May 2000. The locations of the seven sites are shown in Figure 4-1 and the soil and vegetation types are given in Table 4-1.

At each Super site a Kipp & Zonen CNR1 four-component net radiometer is used to measure incoming and outgoing shortwave and longwave radiation. The design of the CNR1 includes an upward-facing, ISO-class, thermopile pyranometer and pyrgeometer, and a complementary downward-facing pyranometer and pyrgeometer in an integrated fashion. The body of the CNR1 houses a PT-100 RTD temperature sensor for measuring the instrument body temperature precisely. During manufacturing, the sensitivity of all four sensors is trimmed and calibrated to a single identical sensitivity coefficient.

The latent and sensible heat flux measurements are done using a sonic anemometer and Krypton KH20 hygrometer. The Campbell Scientific CSAT3 sonic anemometer is mounted at the OASIS sites to measure wind speed and air temperature using sound wave (sonic) theory. By measuring the speed of sound between two points, the fluctuations of wind and temperature can be calculated. The sonic anemometer itself measures an average u (east-west), w (north-south), and v (vertical) wind speed and mean temperature (T) at a frequency of 8 Hz (8 times per second). Covariances of v and T are calculated within the datalogger program and then used to obtain 5-minute means of sensible heat flux. The Krypton hygrometer is mounted within 10 cm of the sonic anemometer and the amount of absorption of Krypton between two points is proportional to the specific humidity (q) of the air. The covariance of v and q is used to compute latent heat flux.

Two REBS HFT3.1 heat flux plates are buried 5 cm below the soil surface at each OASIS site. The plates have a horizontal separation of 1 m. Each plate has been

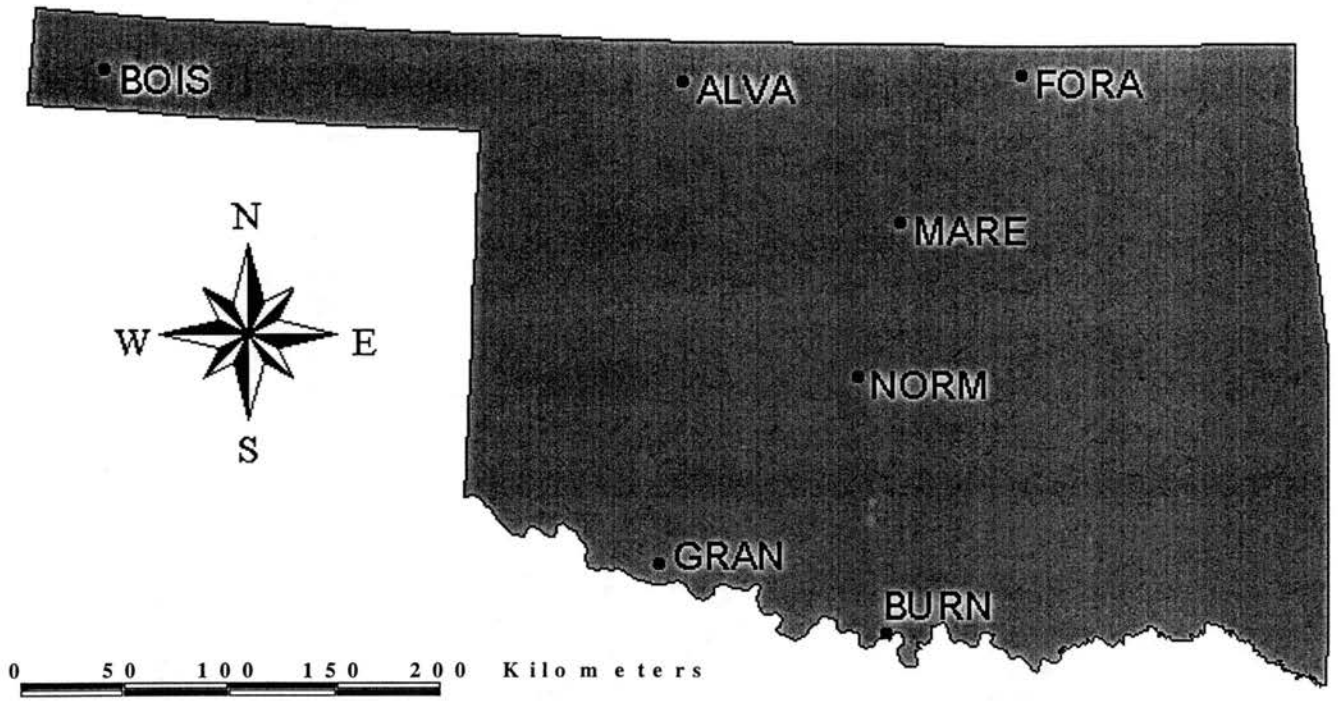

Figure 4-1. Location of Oklahoma Atmospheric Surface-layer Instrumentation System (OASIS) sites used in this study.

Table 4-1. OASIS sites' soil and vegetation types

Site	Soil Type	Vegetation Types							
		Dominant Species # 1		Dominant Species # 2		Dominant Species # 3		Dominant Species # 4	
		Common name	Scientific name	Common name	Scientific name	Common name	Scientific name	Common name	Scientific name
ALVA	Clay loam	Wheat	Triticum aestivum						
BOIS	Clay loam	Bluegrama	Bouteloua gracillis	Hairy grama	Bouteloua hirsuta	Sweet clover	Melilotus officinalis	Sideouts grama	Bouteloua curtipendula
BURN	Loamy sand	Japanese Brome	Bromus Japonicus	Hairy vetch	Vicia villosa	Bermudagrass	Cynodon dactylon	Downey brome	Bromus tectorum
FORA	Sandy loam	Leadplant	Amorpha canescens	Little bluestem	Schizachyrium scoparium	Indiangrass	Sorghastrum nutans	Scribner panicum	Panicum oligosanthes
GRAN	Clay loam	O.W. bluestem	Bothriocloa ischaemum	Yellow sweet clover	Melilotus officinalis	Prairie acacia	Acacia angustissima	Western ragweed	Ambrosia psilostachya
MARE	Sandy clay loam	Silver bluestem	Bothriochloa saccharoides	Little bluestem	Schizachyrium scoparium	Bermudagrass	Cynodon dactylon	Sessile-leaved tickclover	Desmodium sessilifolium
NORM	Silt loam	Goldenrod	Solidago canadensis	Silver bluestem	Bothriochloa saccharoides	Western ragweed	Anbrosia psilostachya	Large hop	Trifolium campestre

individually calibrated. Two REBS Platinum Resistance Temperature Detectors (PRTDs) are buried between 0 and 5 cm of the soil surface. A combination approach that includes both ground heat flux (measured at 5 cm) and heat storage is used to estimate the ground heat flux at the surface. Brotzge (2000) provided a detailed discussion of the instrumentation at the OASIS sites including the quality of the data and source of errors in the measurements.

Green Vegetation Fraction

Canopy conductance depends on leaf water potential (in addition to vapor pressure deficit and temperature) and is a function of soil moisture potential and stress. In addition to variables such as vegetation type, density, height, leaf area index, etc., the unstressed or maximum canopy conductance is expected to vary as a function of canopy greenness and incident photosynthetically active radiation (PAR). The green vegetation fraction (f_g) is defined as the fractional area of the vegetation occupying each grid-cell wherein mid-day downward solar radiation is intercepted by photosynthetically active green canopy. Vegetation indices derived from spectral reflectances seem to have a linear relationship with the ratio of unstressed canopy conductance to incident flux of PAR. That is, as the greenness of vegetation increases, the ratio of unstressed canopy conductance to incident flux of PAR increases (Sellers et al., 1997).

Gutman and Ignatov (1998) suggested that evapotranspiration (also photosynthesis) is controlled by green vegetation fraction and by green leaf area index. The green vegetation fraction acts as a fundamental weighting coefficient in partitioning the total evaporation into soil evaporation, evaporation of canopy intercepted precipitation and transpiration in the LSM (Chen and Dudhia, 2001). Gutman and

Ignatov (1998) derived an expression for green vegetation fraction using the Normalized Difference Vegetation Index (NDVI) as

$$f_g = \frac{(NDVI - NDVI_{\min})}{(NDVI_{\max} - NDVI_{\min})} \tag{4-7}$$

In equation (4-7) bare soil NDVI ($NDVI_{min}$) and dense vegetation NDVI ($NDVI_{max}$) are prescribed as 0.04 and 0.52 respectively and they correspond to seasonally and geographically invariant constants for desert and evergreen clusters.

Carlson and Ripley (1997) defined a scaled NDVI (N^*) and derived a similar expression for N^* as

$$N^* = \frac{(NDVI - NDVI_o)}{(NDVI_s - NDVI_o)} \tag{4-8}$$

where $NDVI_o$ and $NDVI_s$ correspond to the values of NDVI for bare soil (LAI=0) and a surface with a fractional green vegetation cover of 100%, respectively. They also suggested adopting a value of full-cover NDVI about 0.05 below the largest values of NDVI in the image. Choudhury et al. (1994) and Gillies and Carlson (1995) independently obtained an identical square root relation between N^* and green vegetation fraction, f_g as,

$$f_g \approx N^{*2} \tag{4-9}$$

In equation (4-8) the selection of a bare soil value of NDVI results in some uncertainty. The values of f_g obtained using equations (4-7) and (4-9) differ because of the form of the equations and also the assumed upper and lower bounds on NDVI. Because f_g serves as a weighting coefficient for the partitioning of canopy evaporation and bare soil evaporation, the effect of these alternative formulations was evaluated. Each value of NDVI was obtained from Advanced Very High Resolution Radiometer (AVHRR)

satellite images and represented the 1 km pixel area that included the OASIS site. The temporal variation in f_g for two of the study sites is shown in Figure 4-2, and the difference between the two schemes is apparent. When necessary, f_g was truncated at a value of 1.0. The model sensitivity to the f_g derived based on these two different formulations is discussed in the subsequent section.

Results and Discussion

Sensitivity to Green Vegetation Fraction

Prior to the validation analysis, the sensitivity of the model to each of the Gutman-Ignatov (G-I) and Carlson-Ripley (C-R) green vegetation fraction schemes was tested. The simulated surface energy balance components (i.e., net radiation (R_n), latent heat flux (LH), sensible heat flux (SH) and ground heat flux (GH)) using G-I and C-R green vegetation fractions were compared for four of the OASIS sites (BOIS, BURN, MARE and NORM). The results are shown only for BOIS and BURN (Figures 4-3 – 4-6) because the other two sites showed similar results. The short grass at BOIS has less dense cover and the corresponding peak green vegetation fraction reaches only 0.64 in the G-I scheme whereas it reaches the maximum of 1.0 for a summer month in the C-R scheme. For both BOIS and BURN (warm season grass), the green vegetation fraction by the C-R scheme was higher than that by the G-I scheme.

The simulated R_n using G-I and C-R green vegetation fraction for BOIS and BURN showed a slight positive bias towards the C-R method as observed from the equal-value plots shown in Figure 4-3. This indicated that the R_n was insensitive to the two green vegetation fraction schemes. Figure 4-4 shows that the estimated LH for BOIS and BURN had a similar positive bias for the C-R method. Model results for SH (Figure 4-5)

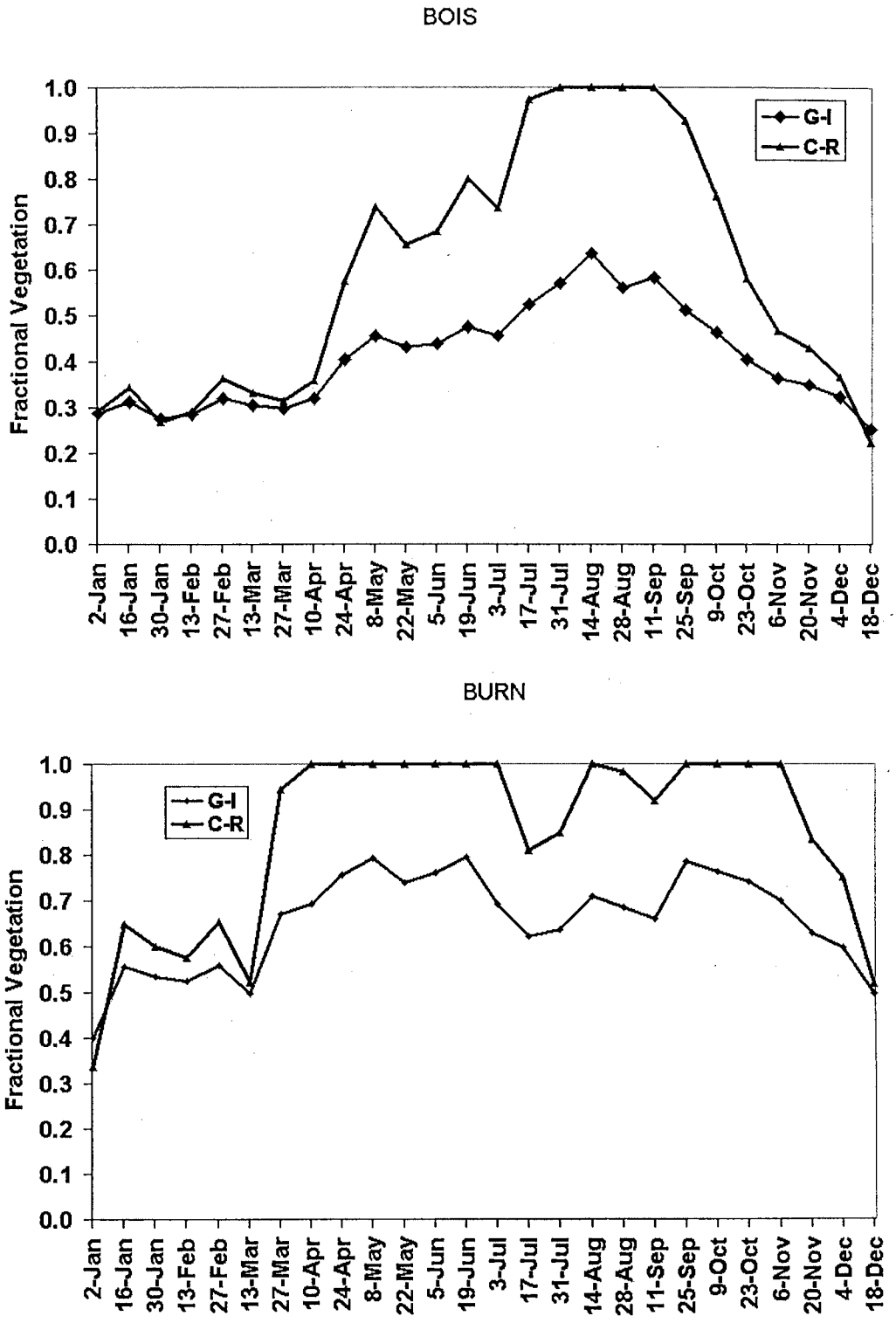

Figure 4-2. Green vegetation fraction as derived by the Gutman-Ignatov (G-I) and Carlson-Ripley (C-R) schemes for BOIS and BURN

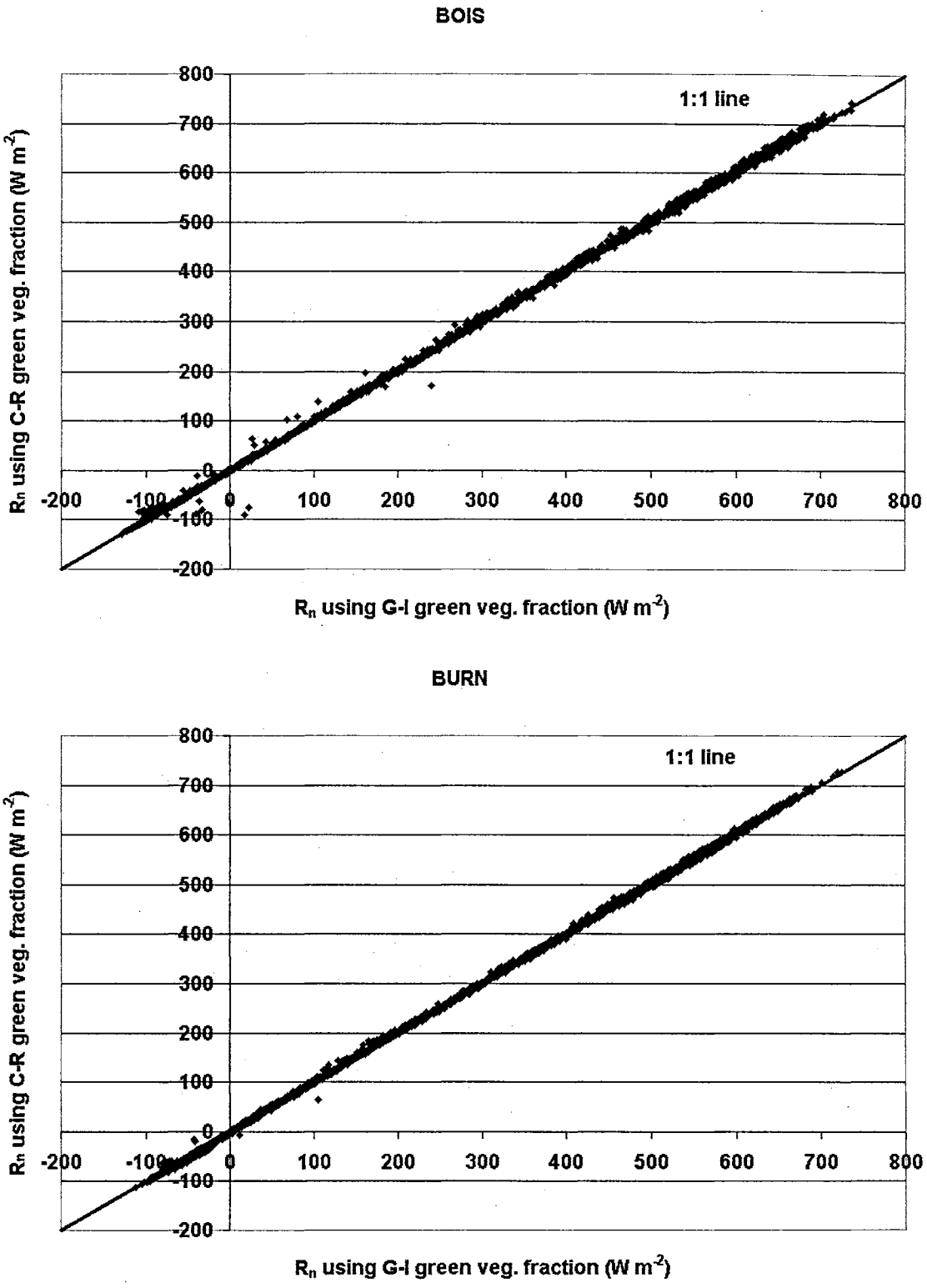

Figure 4-3. Sensitivity of the modeled net radiation using G-I and C-R green vegetation fraction methods.

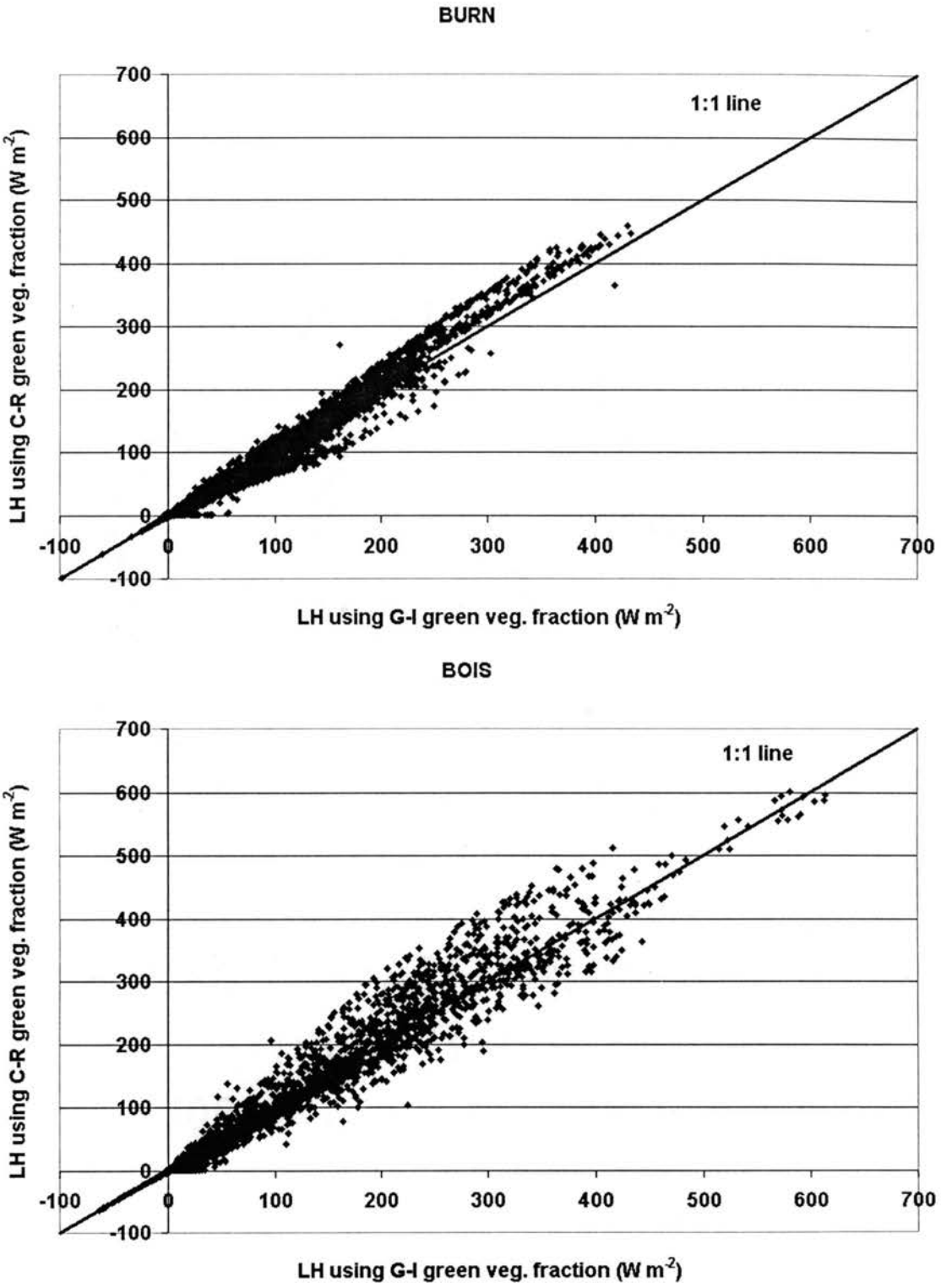

Figure 4-4. Sensitivity of the modeled latent heat flux using G-I and C-R green vegetation fraction methods.

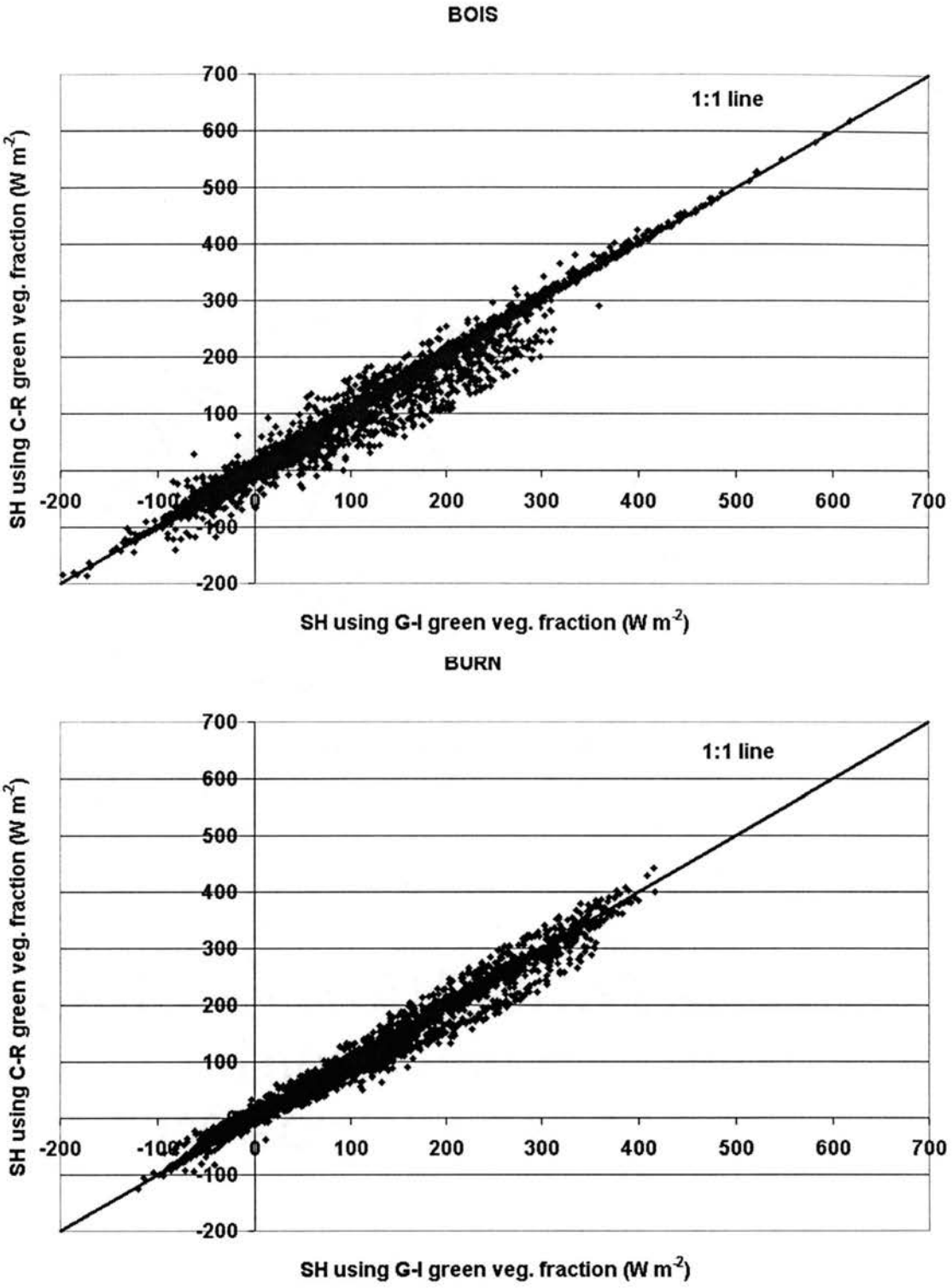

Figure 4-5. Sensitivity of the modeled sensible heat flux using G-I and C-R green vegetation fraction methods.

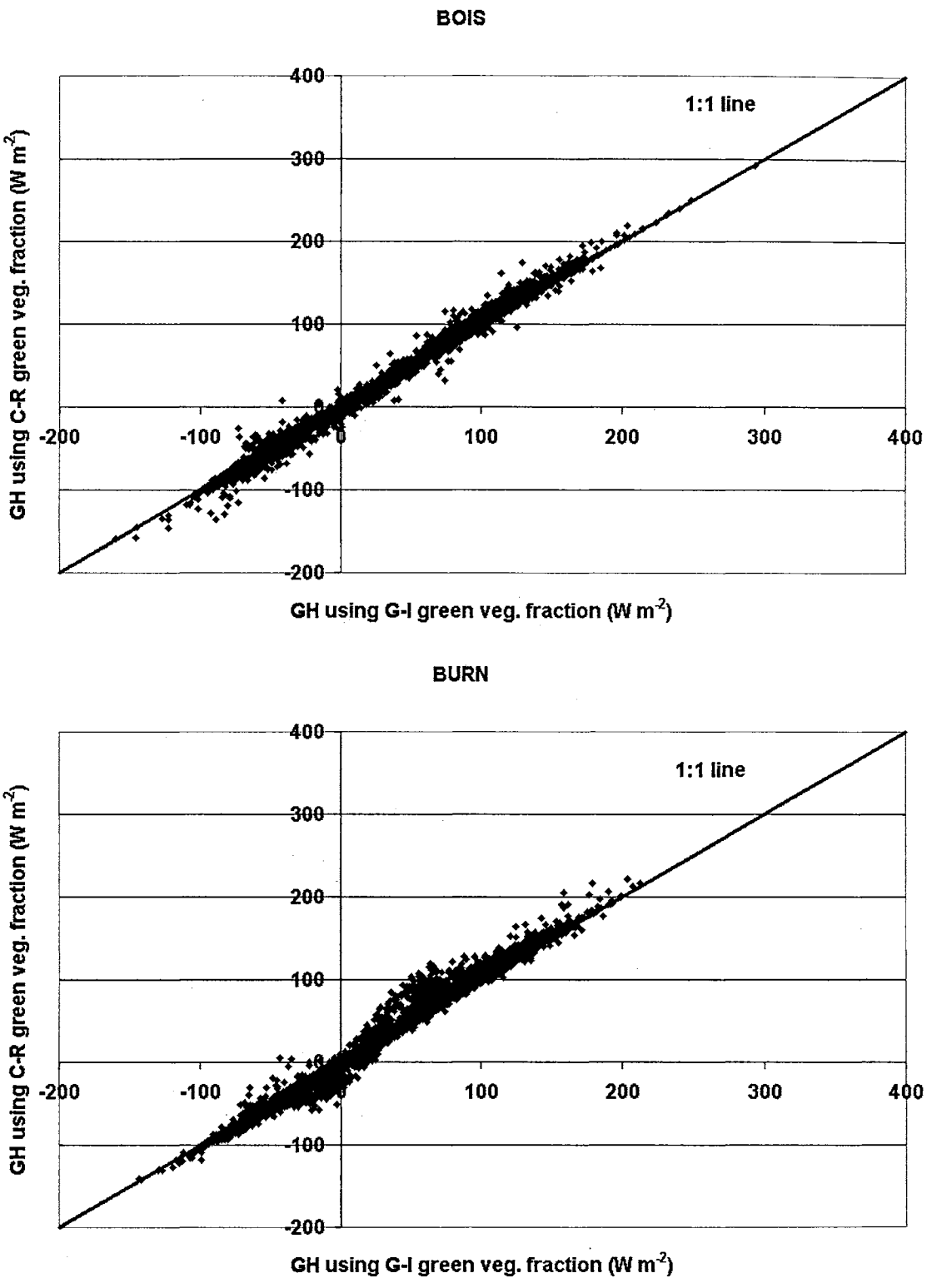

Figure 4-6. Sensitivity of the modeled ground heat flux using G-I and C-R green vegetation fraction methods.

and GH (Figure 4-6) were also somewhat sensitive to the choice of the vegetation scheme. The model sensitivity to the green vegetation fraction was tested for other sites also and similar results were observed.

Figures (4-7)-(4-8) show the sensitivity of the model to green vegetation fraction at BOIS and BURN for relatively wet and dry soil conditions. It can be seen that the two green vegetation fraction methods exhibited distinct patterns during wet and dry soil conditions. When the soil was relatively wet (high soil volumetric water content) due to rain, both the methods resulted in similar LH estimation. However, model estimated LH during dry periods (low soil volumetric water content) showed positive bias towards the C-R method as it had higher green vegetation fraction.

The geographical locations of these Oklahoma sites (ALVA, BOIS, BURN, FORA, GRAN, MARE and NORM) are sufficiently widespread that they have different vegetation pattern and cover as shown in Table 4-1. For all sites, simulated R_n and GH were rather insensitive to the two different green vegetation fraction schemes, while LH and SH exhibited some sensitivity to that choice. All further analysis was carried out with only the G-I green vegetation fraction scheme, which is widely used and linear in its form.

Daily Comparisons

Using daily aggregations of the hourly results, the outputs of uncoupled LSM simulations were compared with OASIS measurements for a one-year period from June 1999 through May 2000. For all seven sites R_n, LH, SH and GH flux measurements were compared with the model simulations. Only those field measurements with good energy-balance closure were chosen for this study. The criterion used was that the daily sum

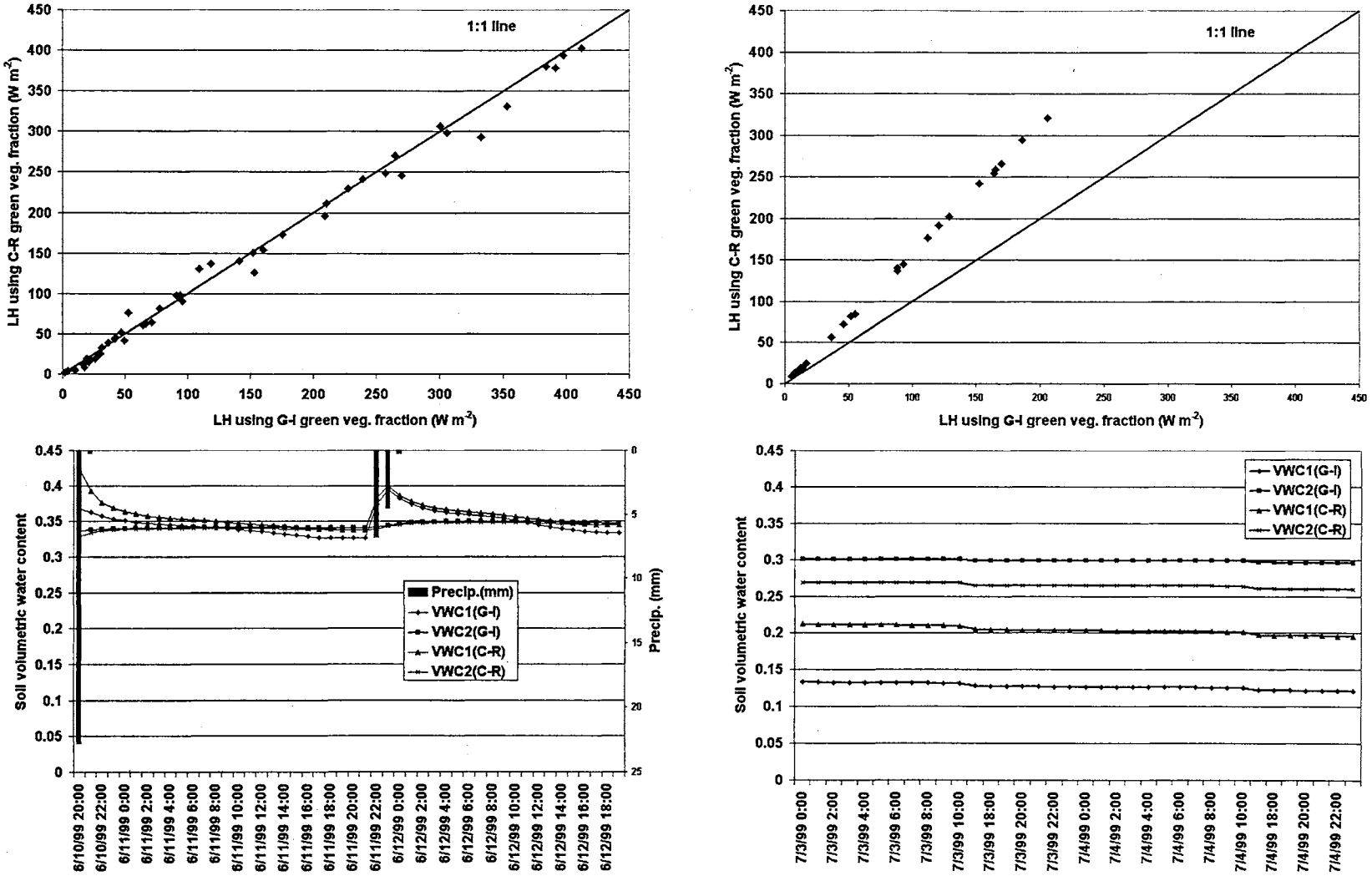

Figure 4-7. Sensitivity of the model to green vegetation fraction at BOIS for relatively wet and dry soil conditions (VWC1- Top soil layer volumetric water content; VWC2-Root zone volumetric water content).

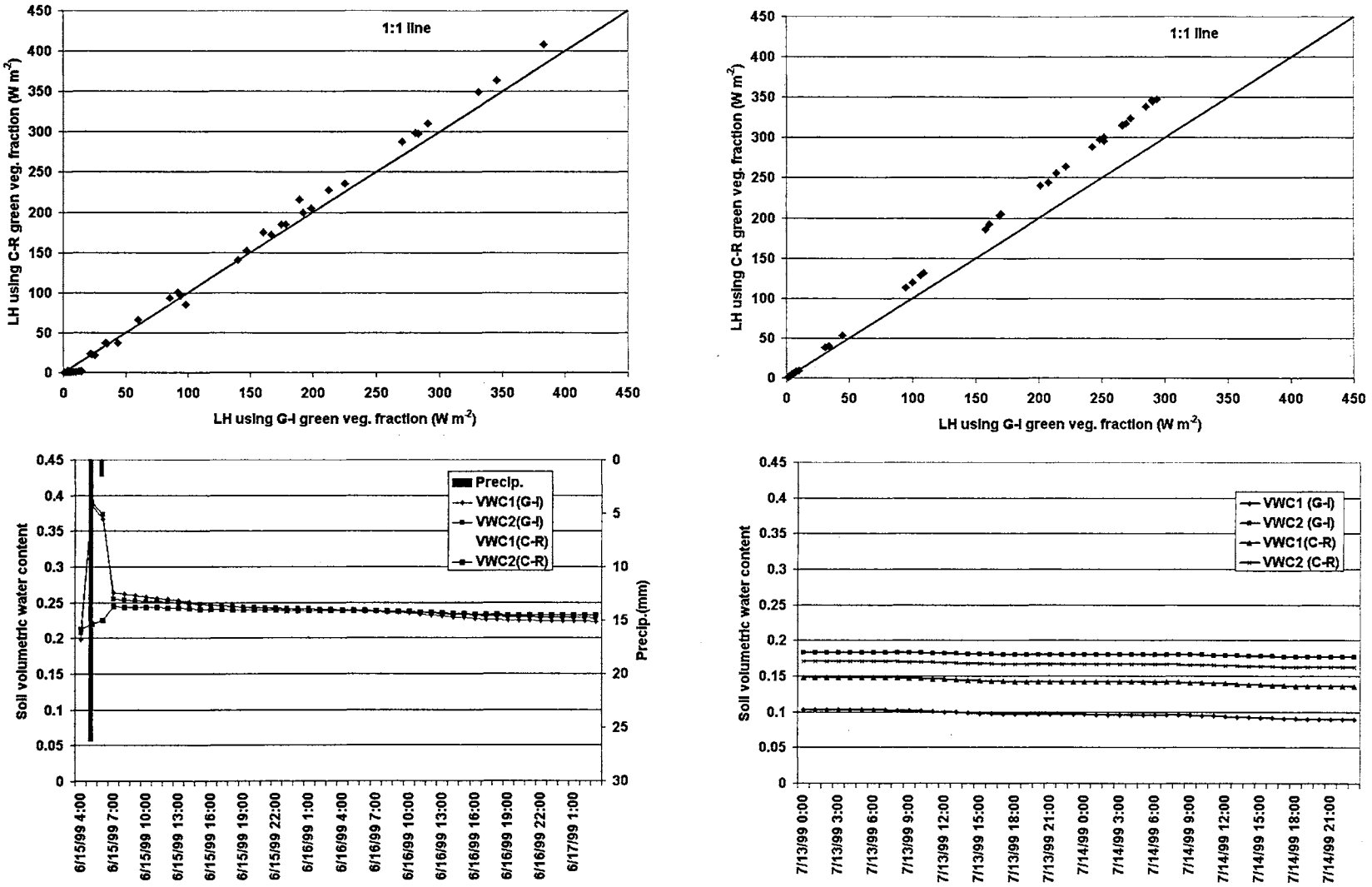

Figure 4-8. Sensitivity of the model to green vegetation fraction at BURN for relatively wet and dry soil conditions (VWC1- Top soil layer volumetric water content; VWC2-Root zone volumetric water content).

(R_n-LH-SH-GH) was to be within the range of -10 W m^{-2} to +10 W m^{-2}. This reduced the number of records to a certain extent but the filtered data provided a more valid comparison to model results. In other words, judgments of model accuracy should not be based on measured data that are internally inconsistent.

Figures 4-9 – 4-12 compare daily average observed and modeled net radiation, latent heat flux, sensible heat flux and ground heat flux for four of the sites (ALVA, BOIS, BURN and NORM). Appendix C contains these equal-value plots for all seven of the sites. One note of caution is that the time scale on the horizontal axis is not continuous (due to the above-described filtering based on energy-balance closure).

Table 4-2a shows daily averaged Mean Bias Error (MBE) and Root Mean Square Error (RMSE) for all seven study sites. There was a slight bias of about 0.8 MJ m^{-2} d^{-1} in net radiation when averaged over all sites and an RMSE of about 1.6 MJ m^{-2} d^{-1} (Figure 4-9). NORM had the highest positive bias of about 3.4 MJ m^{-2} d^{-1} and GRAN had the lowest negative bias of about –0.6 MJ m^{-2} d^{-1}. These discrepancies in net radiation may be partially due to the uncertainty in the downwelling longwave radiation estimation procedure. ALVA, BOIS, BURN and MARE showed a slight overestimation of R_n, especially during summer and spring months, and NORM showed a still higher estimation (NORM had limited data). FORA and GRAN showed a slight underestimation of R_n except during winter. It could be beneficial to investigate the LSM physics for the partitioning of incoming radiant energy, and to examine the parameterizations involving green vegetation fraction, rooting depth, albedo and minimum stomatal resistance. The model structure with its current version could accommodate only a single soil texture even though it has four soil layers in its

configuration. This could be an important factor when partitioning the energy as well as mass balance components. The energy balance in the LSM is formulated in such a way that excess net radiation is redistributed into latent, sensible and ground heat fluxes as shown in the equation below.

$$R_n = LH + SH + G \tag{4-10}$$

Thus, predicting net radiation becomes crucial in order to accurately quantify the sensible and latent heat fluxes.

The positive bias in daily LH (MBE of about 0.9 MJ m^{-2} d^{-1} when averaged over seven sites) is shown in Table 4-2a. The average RMSE was approximately 2.5 MJ m^{-2} d^{-1}. The time series plots of observed and modeled LH are shown in Figure 4-10. As with R_n, it was observed that the LH for the NORM site was higher than for the other sites. This could be again partially due to the limited number of days used in the comparisons for NORM, and the fact that more of those days were during the summer months (when other sites showed a high positive bias). As pointed out earlier, most of the excess energy from the modeled R_n can be directed into LH and was seen at those sites where R_n was overestimated such as ALVA, BOIS, BURN and MARE. This is because the LSM first computed potential evaporation and then actual evaporation, which was used to determine the skin temperature at equilibrium state, and subsequently SH was computed. As the LSM computed LH first, it tended to distribute excess energy to that term.

For SH, the seven-site average of MBE showed that the model had a negative bias of about –0.3 MJ m^{-2} d^{-1} and the average RMSE was about 2.2 MJ m^{-2} d^{-1} (Table 4-2b). The magnitude of the site-by-site bias in SH estimation was smaller than that for R_n and

LH, as shown in Table 4-2a,b. The time series plots as shown in Figure 4-11 gave ample indication that SH estimations tended to be the complement of LH simulations (meaning the available energy is partitioned into LH and SH depending on the surface vegetation and other parameterizations). The positive bias in daily averaged GH for all but FORA and NORM was also relatively low, i.e., about 0.2 MJ m^{-2} d^{-1}. The overall RMSE was about 0.7 MJ m^{-2} d^{-1} (Figure 4-12). Betts et al. (1997) and Marshall (1998) suggested that the GH estimations were sensitive to model errors in R_n computation. The mean absolute errors (MAE) for LH and SH each tended to be greater than that for R_n.

Hourly Comparisons

The performance of the LSM was also analyzed using hourly data (Table 4-3a,b). The graphic representation of the hourly results for FORA, GRAN and MARE is shown in Figures 4-13 – 4-16. Appendix C (Figures (C-8) – (C14)) shows for each of the seven sites, the equal-value plots for all four energy-balance components. As in the daily data analysis, field data with good hourly energy-balance closure were chosen with the criterion that the hourly sum (Rn-LH-SH-GH) was within the range of -10 W m^{-2} to +10 W m^{-2}. As this criterion was applied to both daily and hourly data sets separately, it should be remembered that this resulted in different data sets (i.e., not all hourly data that met the criterion were from days that met the daily criterion). The net radiation plots in Figure 4-13 suggested that model hourly estimates were not biased significantly. The hourly average of R_n for BOIS had a high negative bias of about –9 W m^{-2} while NORM showed a high positive bias of about 22 W m^{-2}. The average of all seven sites' hourly averaged net radiation showed a very low positive bias of about 1.4 W m^{-2} and an RMSE of approximately 60 W m^{-2}. Given the fact that the simulation was carried out for a one-

Table 4-2 (a). Statistics of daily averaged Net Radiation (R_n) and Latent Heat (LH) flux for June '99 – May '00.

Site	R_n			LH			Days
	MBE	RMSE	MAE	MBE	RMSE	MAE	
	(MJ m^{-2} d^{-1})	(MJ m^{-2} d^{-1})	(MJ m^{-2} d^{-1})	(MJ m^{-2} d^{-1})	(MJ m^{-2} d^{-1})	(MJ m^{-2} d^{-1})	
ALVA	0.921	1.300	1.164	1.109	1.768	1.293	13
BOIS	0.755	1.311	1.045	0.140	1.002	0.813	38
BURN	0.647	1.457	1.199	0.915	1.313	1.044	87
FORA	-0.265	1.005	0.767	-1.280	2.478	1.839	9
GRAN	-0.561	0.994	0.769	-1.052	3.018	2.577	61
MARE	0.956	1.502	1.298	2.491	2.991	2.491	49
NORM	3.397	3.608	3.458	3.955	5.184	4.350	17
Mean	0.836	1.597	1.386	0.897	2.537	2.058	

Table 4-2 (b). Statistics of daily averaged Sensible Heat (SH) and Ground Heat (GH) flux for June '99 – May '00.

Site	SH			GH			Days
	MBE	RMSE	MAE	MBE	RMSE	MAE	
	(MJ m^{-2} d^{-1})	(MJ m^{-2} d^{-1})	(MJ m^{-2} d^{-1})	(MJ m^{-2} d^{-1})	(MJ m^{-2} d^{-1})	(MJ m^{-2} d^{-1})	
ALVA	-0.285	2.128	1.838	0.260	0.401	0.292	13
BOIS	0.396	1.601	1.326	0.150	0.545	0.434	38
BURN	-0.429	1.068	0.805	0.185	0.711	0.523	87
FORA	0.238	2.993	2.514	0.495	1.071	0.873	9
GRAN	0.310	3.164	2.779	0.237	0.607	0.514	61
MARE	-1.609	2.069	1.712	0.127	0.804	0.608	49
NORM	-0.572	2.446	2.272	-0.243	0.791	0.693	17
Mean	-0.279	2.210	1.892	0.173	0.704	0.563	

$$MBE = \frac{\sum_{i=1}^{n}(P-O)}{n}; \qquad RMSE = \sqrt{\frac{\left[\sum_{i=1}^{n}(P-O)^2\right]}{n}}; \qquad MAE = \frac{\sum_{i=1}^{n}(|P-O|)}{n};$$

P-Predicted; O-Observed; n-total records.

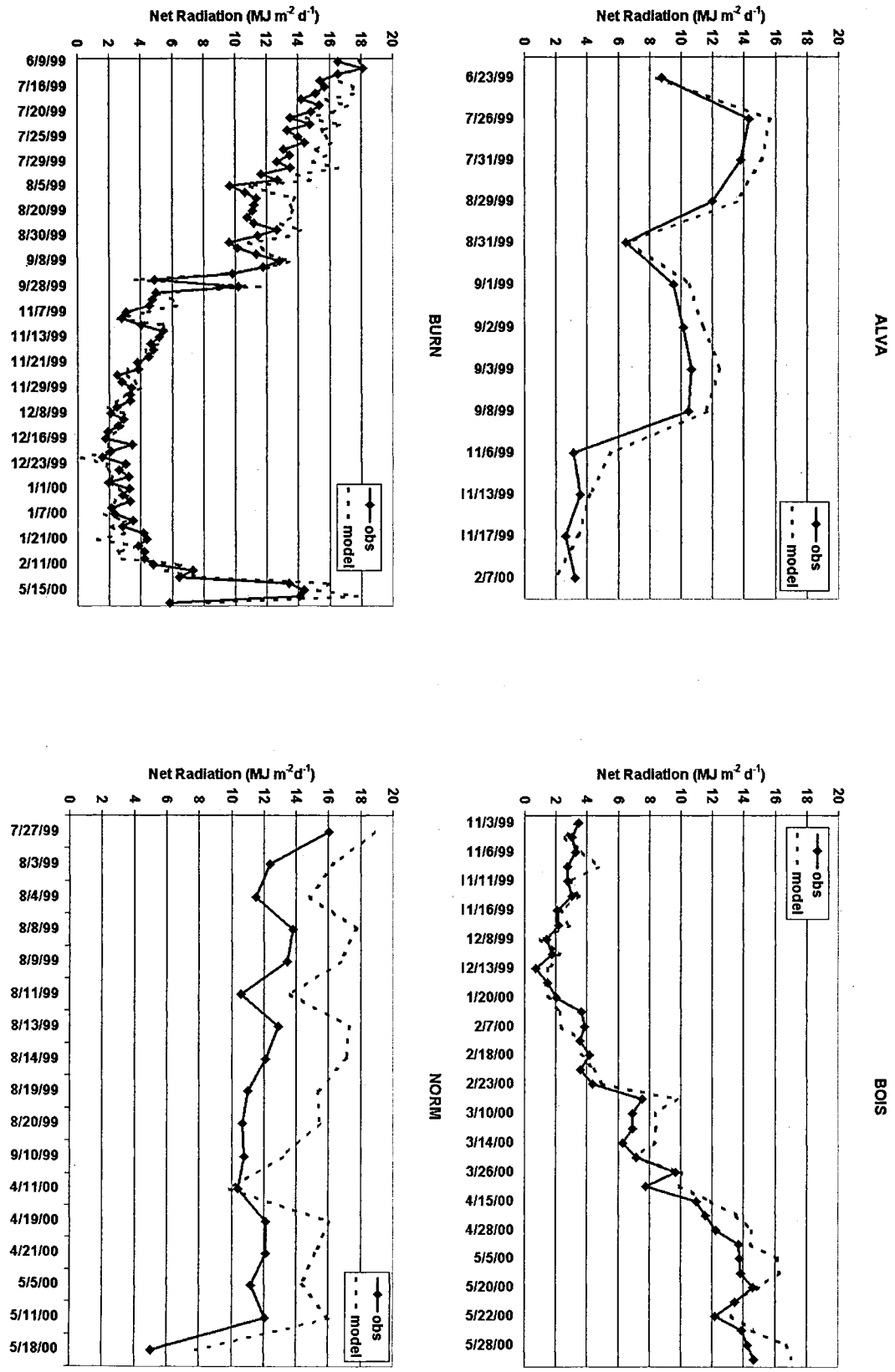

Figure 4-9. Comparison of daily average observed and modeled net radiation.

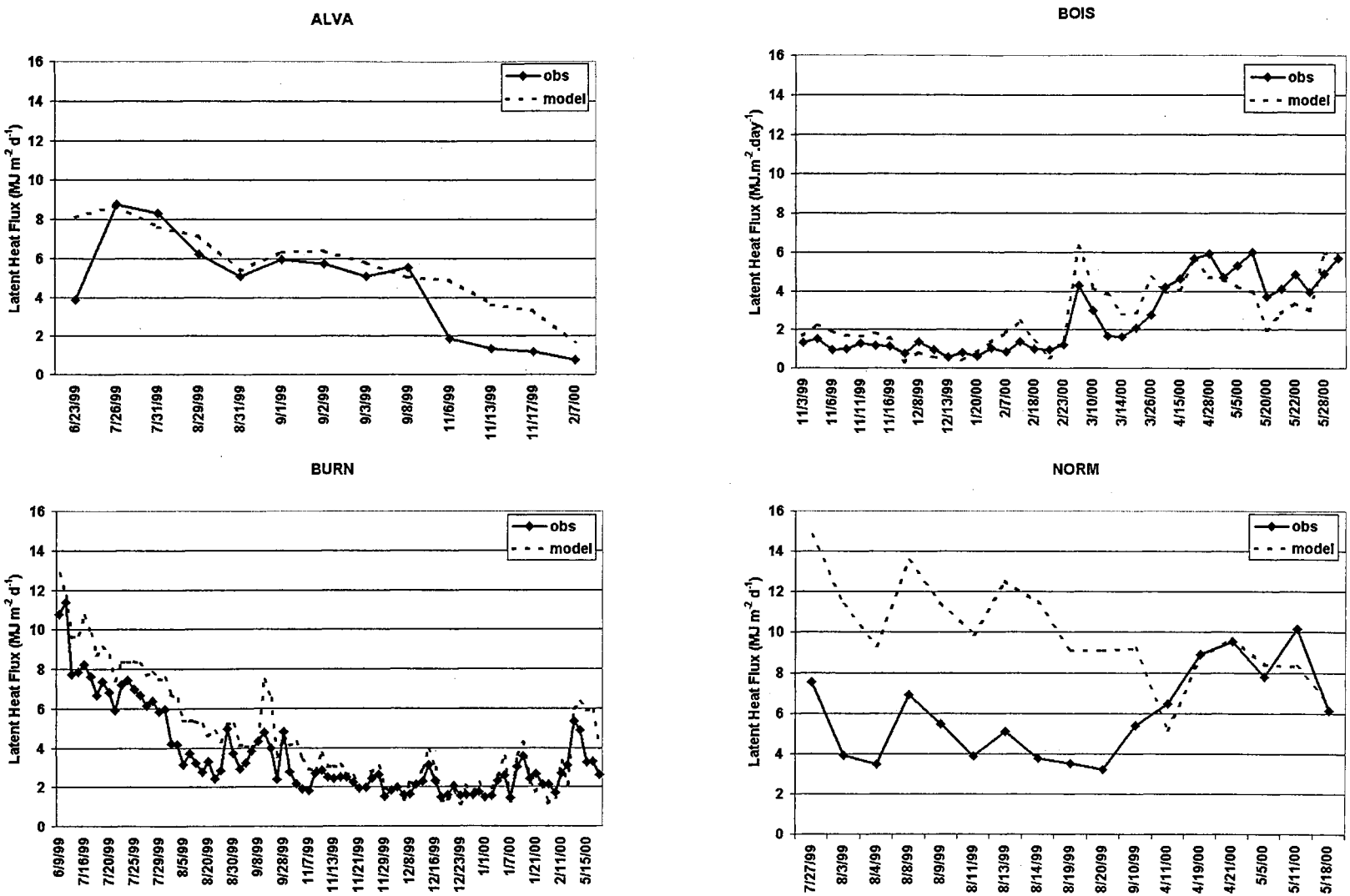

Figure 4-10. Comparison of daily average observed and modeled latent heat flux.

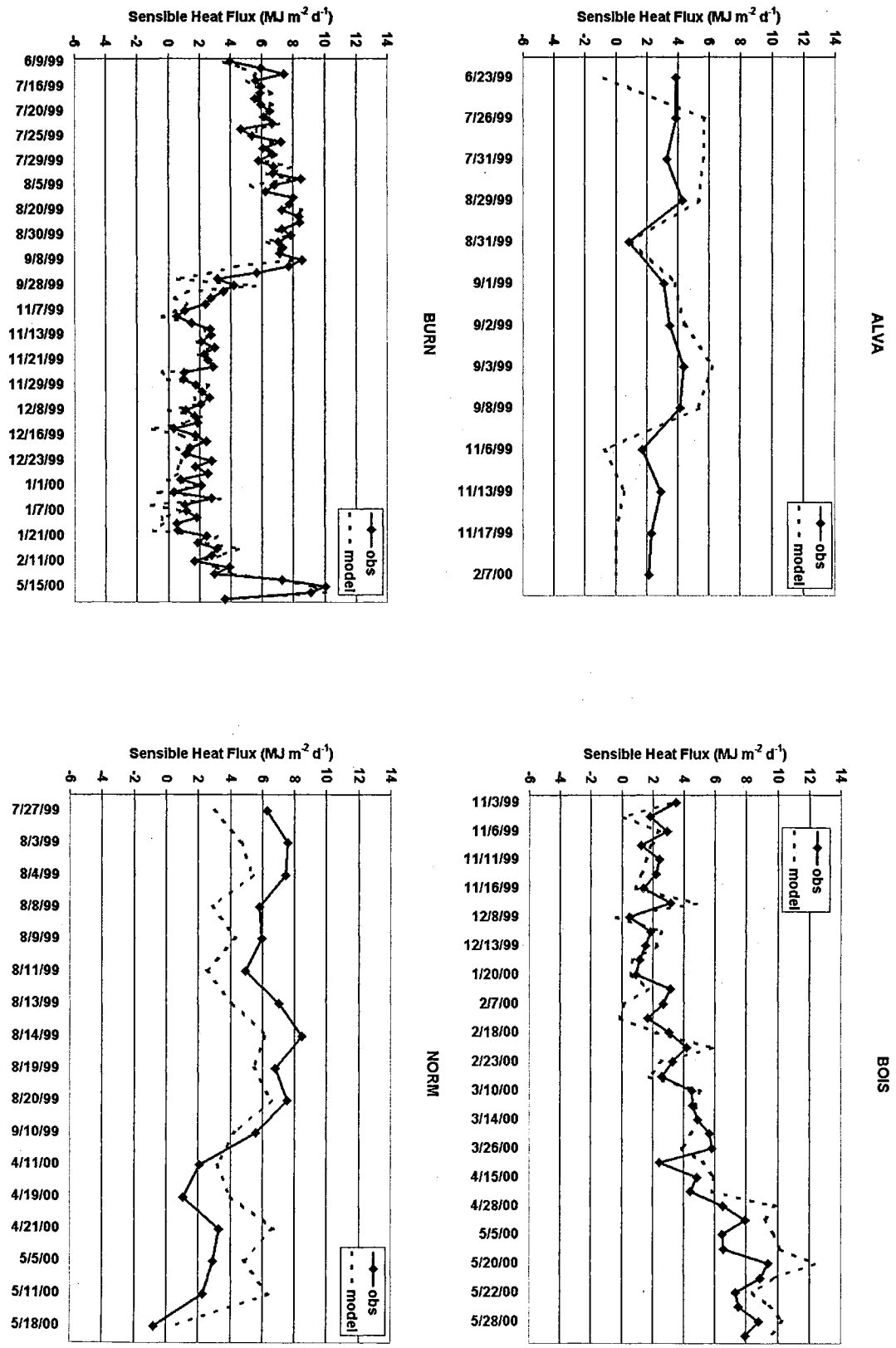

Figure 4-11. Comparison of daily average observed and modeled sensible heat flux.

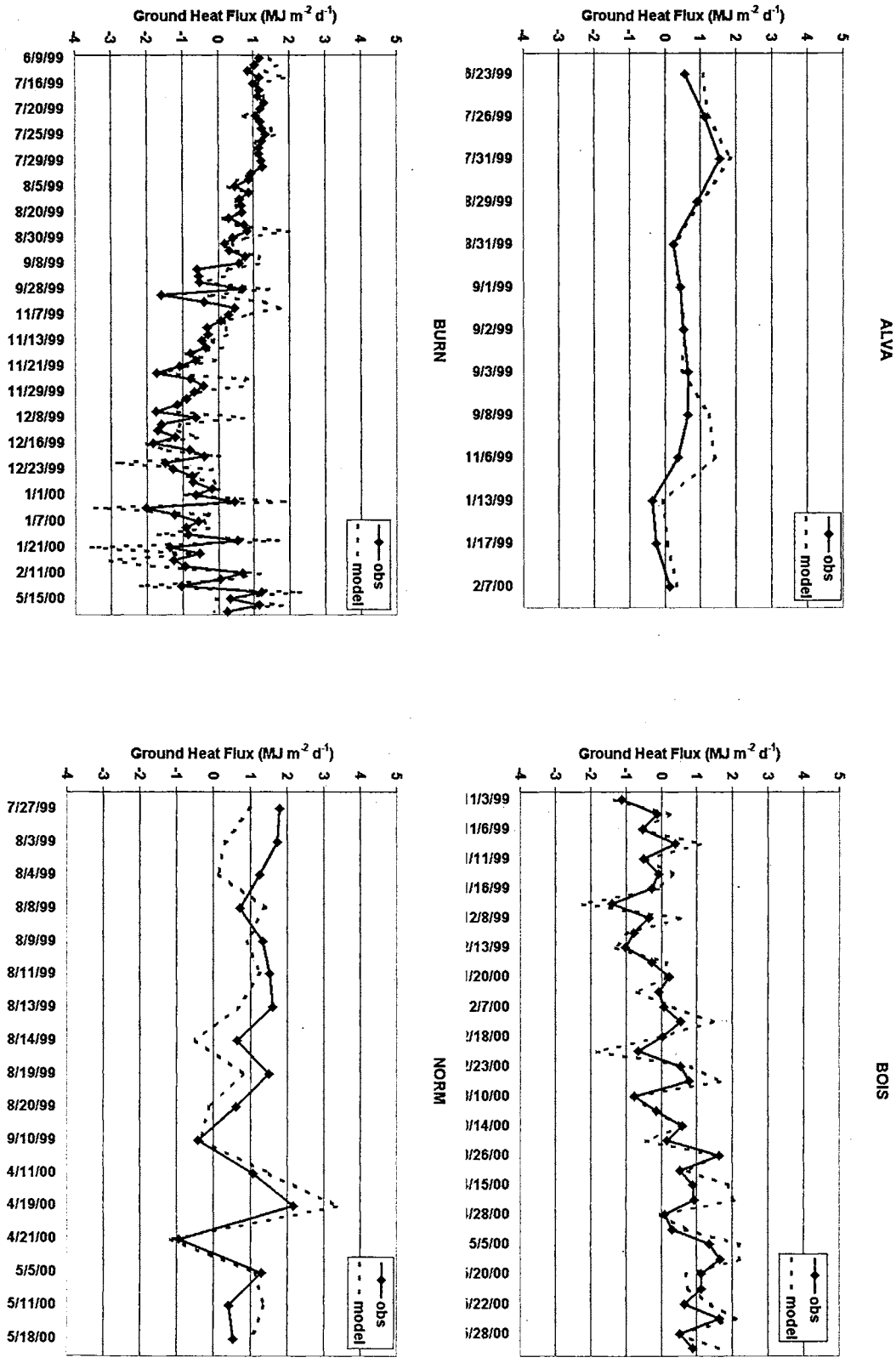

Figure 4-12. Comparison of daily average observed and modeled ground heat flux.

year period, including all seasons, an RMS error of about 60 W m^{-2} in R_n simulation is relatively insignificant. The site bias for hourly LH ranged from – 3 to 22 W m^{-2} and RMSE ranged between 16 and 52 W m^{-2} (Figure 4-14). NORM showed a high positive bias of 22 W m^{-2} and BOIS had the least positive bias of 1.1 W m^{-2}. FORA and GRAN had a negative bias of –3 W m^{-2} as shown in Table 4-3a.

Conversely, from Table 4-3b it can be seen that the model overestimated SH at FORA and GRAN. The hourly averaged SH for all seven sites was –0.18 W m^{-2} with an average RMSE of approximately 42 W m^{-2} (Figure 4-15). The range was about –11 to 12 W m^{-2} and 37 to 50 W m^{-2} for MBE and RMSE, respectively. ALVA results indicated a high negative bias of –11 W m^{-2} and FORA had a high positive bias of about 13 W m^{-2}. The GH simulations showed that FORA had a high negative bias of about –12 W m^{-2} as seen in Figure 4-16 and the average of all seven sites yielded a negative bias of 5 W m^{-2}. The average RMSE was 28 W m^{-2}. This was low when compared with the bias and RMSE of the other energy balance components. With the exception of GH, the trends in the hourly and daily component estimates were observed to be very similar for all sites. Analysis of the hourly energy-balance components provided results that were similar to the daily analysis. That is, the "sink" terms of the energy budget (LH and SH) tended to be predicted less accurately than the "source" terms (R_n and GH).

Summary and Conclusions

Modeling land surface processes plays an important role in understanding the interaction between the land surface and the atmosphere. Energy and water balances at the land surface should impact mesoscale, regional and general circulation models. There have been persistent efforts to develop and refine physically based land surface models.

Table 4-3 (a). Statistics of hourly averaged Net Radiation (R_n) and Latent Heat (LH) flux for June '99 – May '00.

Site	R_n			LH			Hours
	MBE	RMSE	MAE	MBE	RMSE	MAE	
	($W\ m^{-2}$)	($W\ m^{-2}$)	($W\ m^{-2}$)	($W\ m^{-2}$)	($W\ m^{-2}$)	($W\ m^{-2}$)	
ALVA	2.068	47.588	30.603	9.430	26.557	16.614	552
BOIS	-9.305	55.625	38.597	1.109	16.066	6.924	1272
BURN	1.238	61.254	39.891	4.342	20.232	11.220	1685
FORA	-4.291	55.667	31.854	-3.159	39.961	20.050	629
GRAN	-3.168	58.442	36.417	-3.374	36.450	19.706	1433
MARE	1.417	58.402	35.920	8.062	31.686	17.914	1323
NORM	22.042	71.755	41.385	22.881	52.606	27.226	961
Mean	1.429	58.390	36.381	5.613	31.937	17.093	

Table 4-3 (b). Statistics of hourly averaged Sensible Heat (SH) and Ground Heat (GH) flux for June '99 – May '00.

Site	SH			GH			Hours
	MBE	RMSE	MAE	MBE	RMSE	MAE	
	($W\ m^{-2}$)	($W\ m^{-2}$)	($W\ m^{-2}$)	($W\ m^{-2}$)	($W\ m^{-2}$)	($W\ m^{-2}$)	
ALVA	-11.008	37.211	22.818	1.741	29.362	17.435	552
BOIS	-4.833	39.423	26.112	-6.073	25.856	19.743	1272
BURN	-0.723	38.657	25.276	-4.862	28.132	20.399	1685
FORA	12.815	50.407	34.799	-11.996	36.670	27.458	629
GRAN	9.671	47.572	32.950	-9.058	25.144	19.004	1433
MARE	-4.535	42.764	28.237	-4.355	32.084	21.674	1323
NORM	-2.639	39.619	23.159	3.275	24.964	15.876	961
Mean	-0.179	42.236	27.622	-4.475	28.887	20.227	

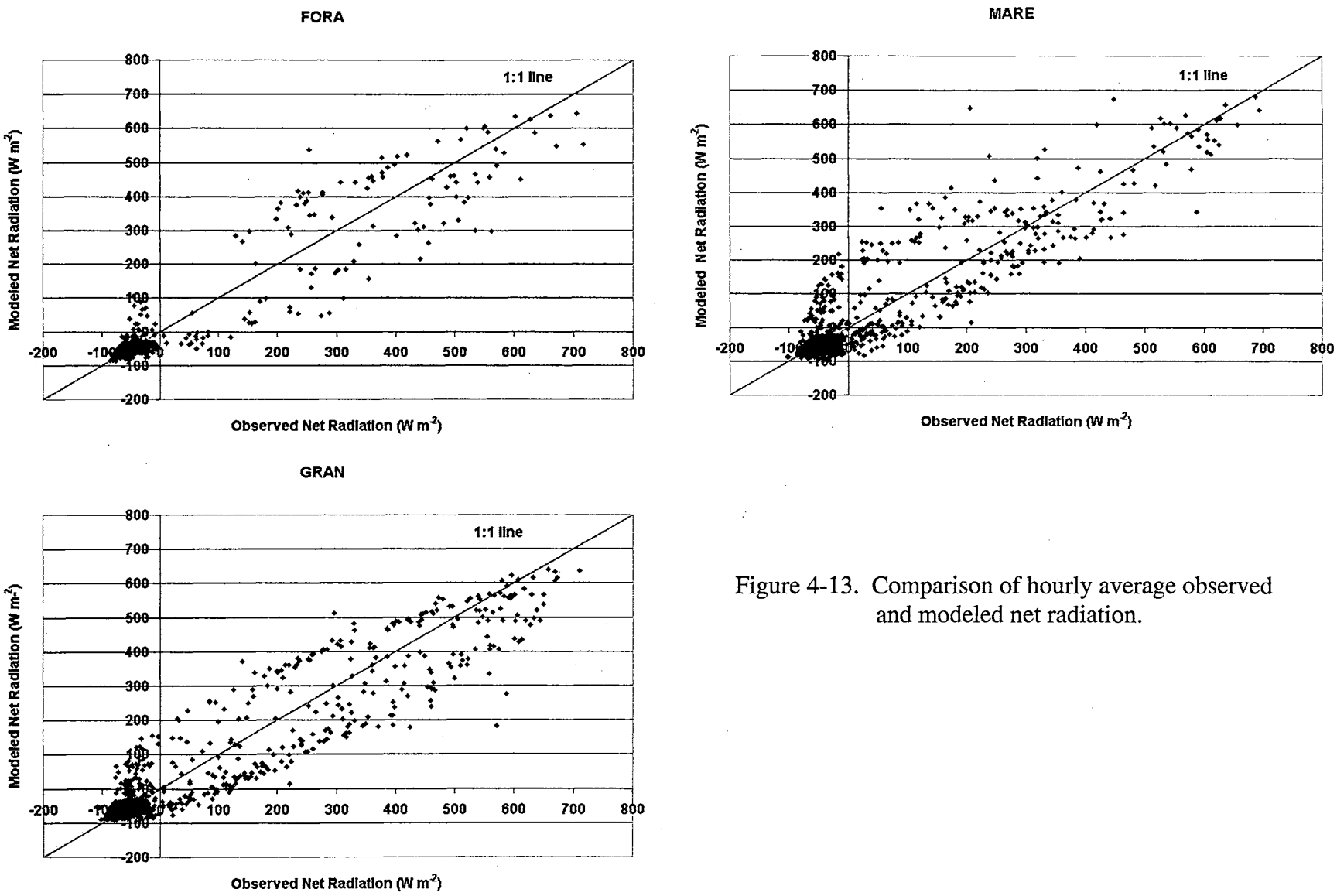

Figure 4-13. Comparison of hourly average observed and modeled net radiation.

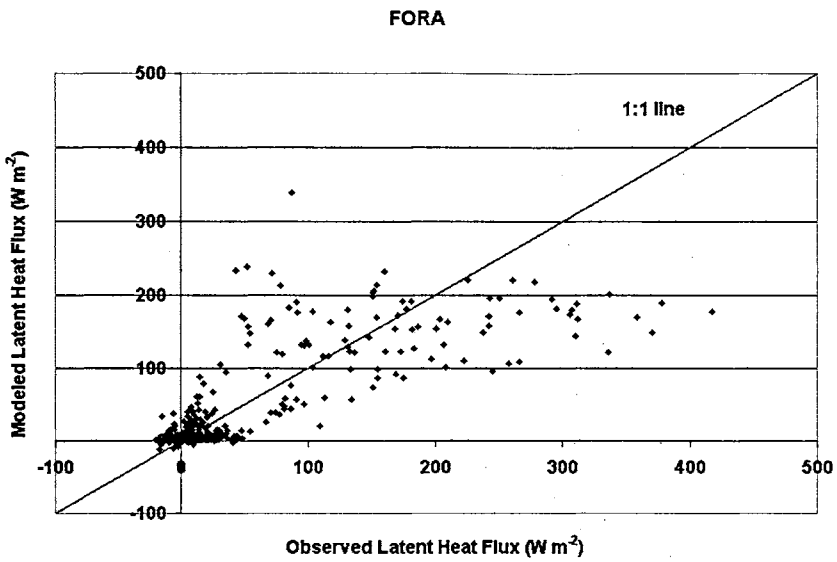

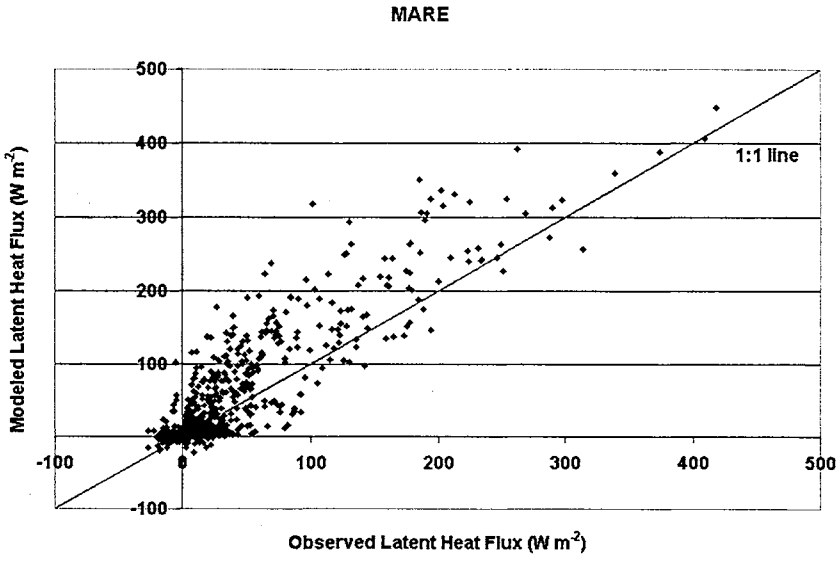

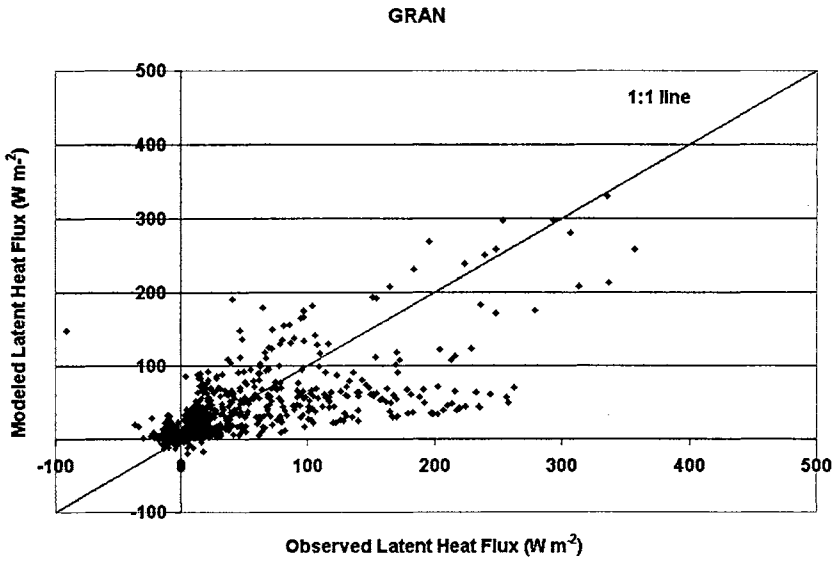

Figure 4-14. Comparison of hourly average observed and modeled latent heat flux.

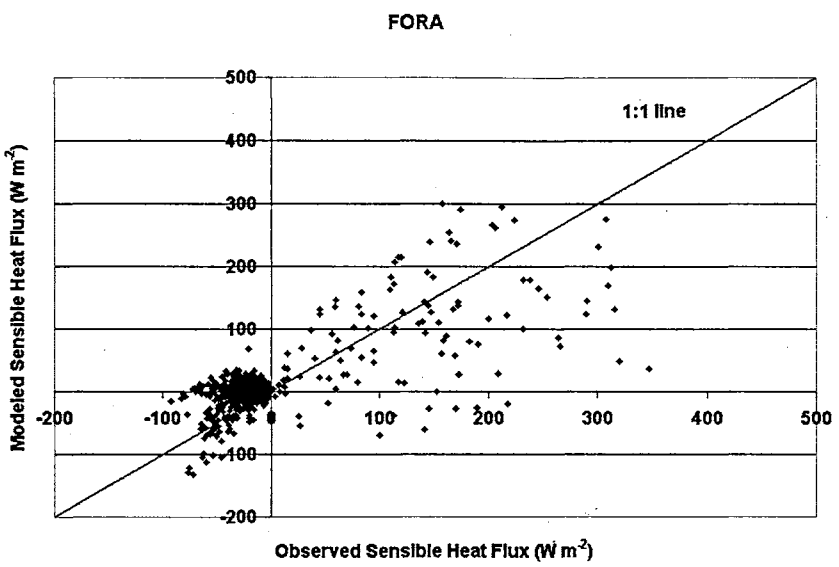

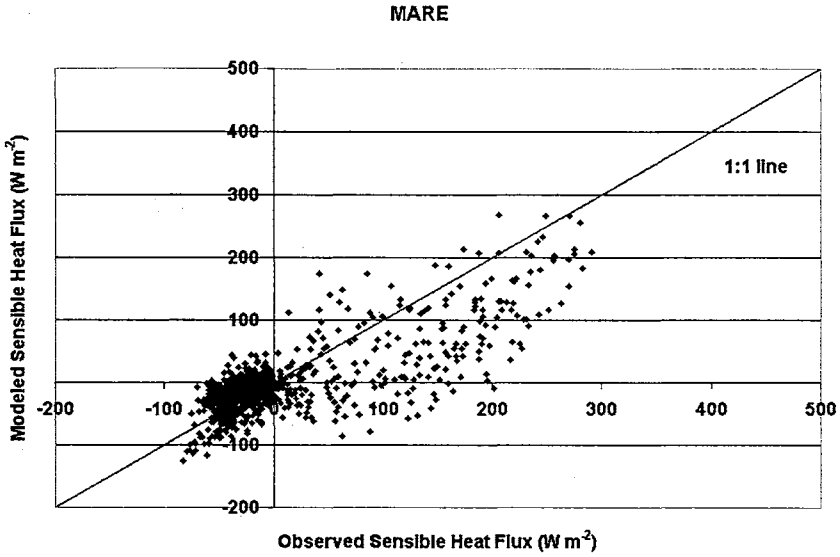

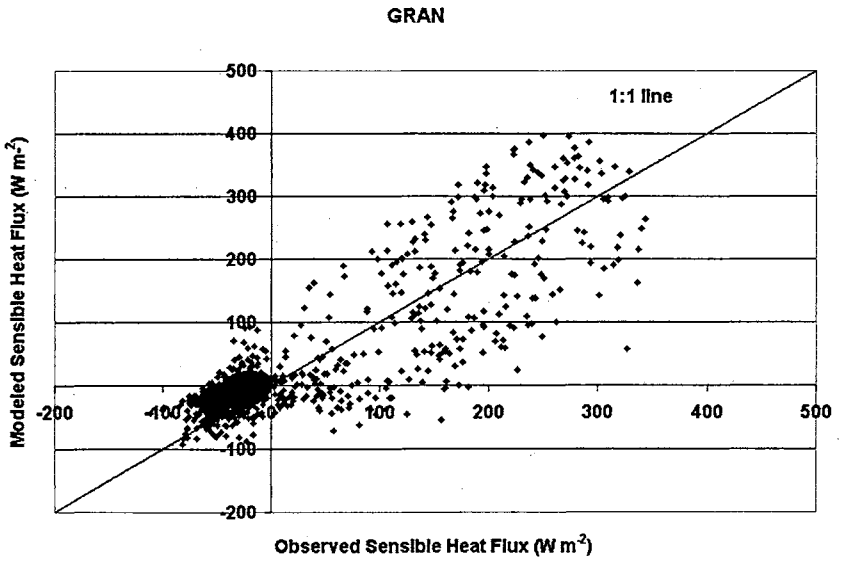

Figure 4-15. Comparison of hourly average observed and modeled sensible heat flux.

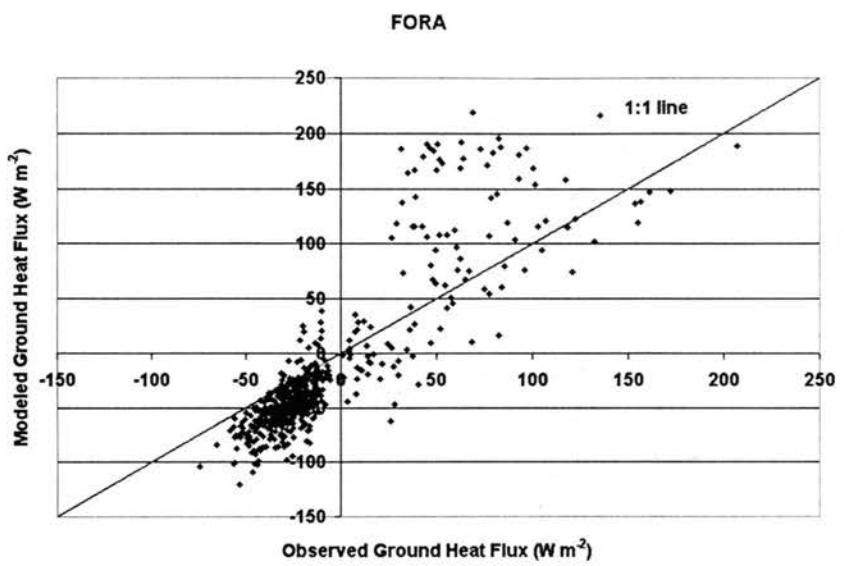

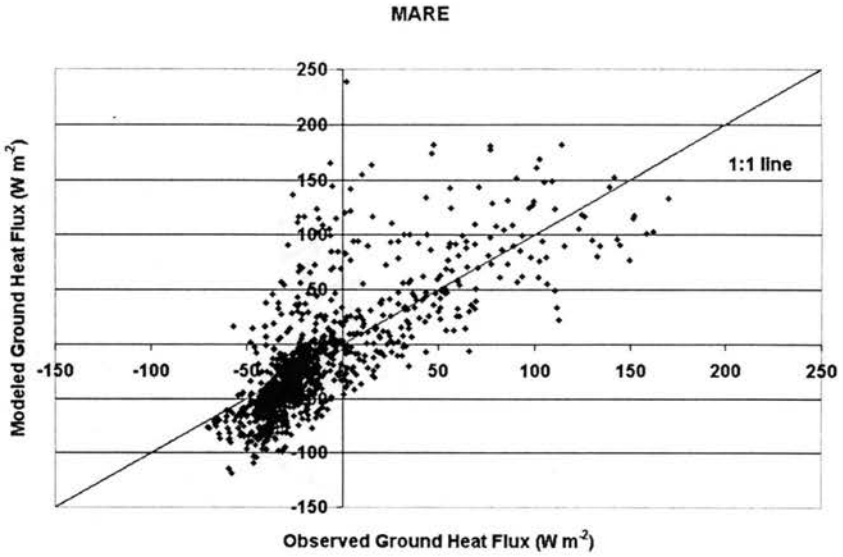

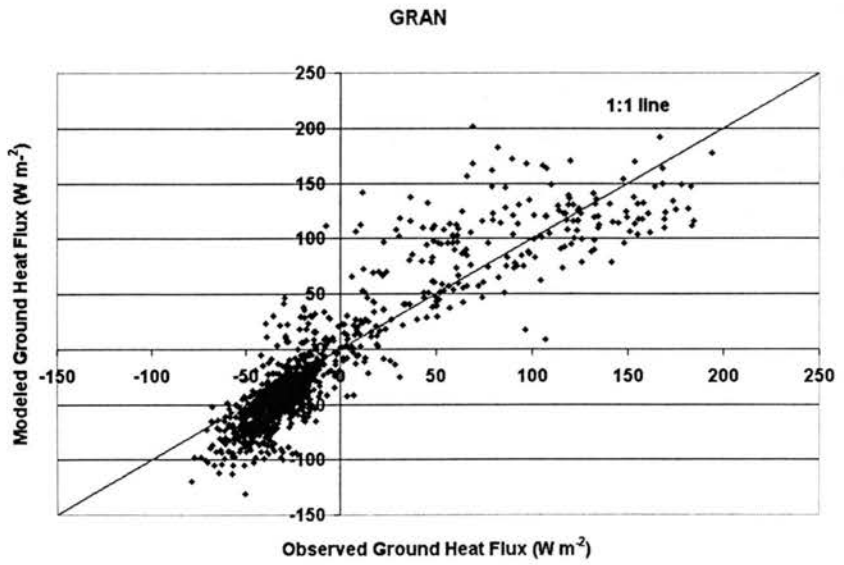

Figure 4-16. Comparison of hourly average observed and modeled ground heat flux.

Quantifying the accuracy of such models using long periods of measurements becomes crucial.

The purpose of this study was to validate the NOAH-OSU Land Surface Model using measurements from the Oklahoma Mesonet and the Oklahoma Atmospheric Surface-layer Instrumentation System (OASIS) project. Through the work of others, the original Oregon State University Land Surface Model (OSU LSM) was extended by incorporating a complex canopy resistance approach along with other improvements. This extended model is used in a coupled fashion with the NCEP Eta and PSU/MM5 operational mesoscale models.

The Oklahoma Mesonet, comprising a network of 114 automated weather stations, provided the meteorological forcing data for this study. The OASIS project used the Mesonet as its foundation and supported the development of 10 "Super" sites. These Mesonet sites are equipped with additional instrumentation for measuring surface energy components (R_n, LH, SH and GH). Seven Super sites were the focus of this validation study. Hourly averages of Mesonet and OASIS data were compiled for the period 1 June 1999 though 31 May 2000. The field data set was filtered for good energy balance closure using the criterion that the daily (hourly) sum (R_n-LH-SH-GH) was within the range of -10 W m^{-2} to $+10$ W m^{-2}.

In order to provide green vegetation fraction data for the LSM, the Gutman-Ignatov (1998) and Carlson-Ripley (1997) schemes for computing green vegetation fraction from observed NDVI data were studied. The two schemes estimated significantly different green vegetation fractions, which translated into some sensitivity in

the estimates of LH and SH. The Gutman-Ignatov (1998) scheme was selected for the remainder of the study as it is in wide use and linear in its form.

Validation of the NOAH – OSU LSM using OASIS surface energy measurements from seven sites (ALVA, BOIS, BURN, FORA, GRAN, MARE and NORM) was carried out for daily and hourly time intervals. Based on the daily average values, it was observed that the model tended to slightly overestimate R_n with both the MBE and RMSE at about 0.8 MJ m^{-2} d^{-1} and 1.6 MJ m^{-2} d^{-1}, respectively. The seven-site daily average bias in LH was 0.9 MJ m^{-2} d^{-1}, with an RMSE of 2.5 MJ m^{-2} d^{-1}. NORM had a relatively high bias in both R_n and LH, perhaps due to a limited data set dominated by summer days. Model estimates of SH had a slight negative bias with an RMSE of 2.2 MJ m^{-2} d^{-1}. The mean bias error in GH was low when compared with the estimation of the other energy balance components. The mean absolute errors for LH and SH were observed to be greater than those for R_n. The model distributes any excess R_n into latent, sensible and ground heat fluxes. It was observed that excess energy was predominantly assigned to LH as opposed to SH and this was due to the model computation of LH first and subsequent estimation of SH in the formulation.

In the hourly analysis, it appeared that the model tended to slightly overestimate R_n as the average MBE was about 1.4 W m^{-2} and the RMSE was 58 W m^{-2}. The hourly average LH showed a positive bias of about 5.6 W m^{-2} and an RMSE of 32 W m^{-2}. Both SH and GH showed a slight negative bias for most of the sites with an RMSE of 42 W m^{-2} and 29 Wm^{-2}, respectively. Thus the trends observed in hourly and daily estimates for all the energy balance components were similar except for GH, which had a slight positive bias for the daily analysis.

The overall performance of the NOAH-OSU LSM was observed to be reasonably good when tested for Oklahoma conditions. As with any model, the user must judge the accuracy based on the particular application. It could be beneficial to investigate refinements to the model physics and vegetation parameterization (green vegetation fraction, rooting depth, albedo and minimum stomatal resistance). Incorporating vertical heterogeneity in soil texture as opposed to the use of single top layer soil texture in the model might improve the partitioning of LH and SH. The estimated downwelling longwave radiation is another potential source of model uncertainty.

CHAPTER 5

SCALING EFFECTS ON MODELED SURFACE ENERGY-BALANCE COMPONENTS USING THE NOAH-OSU LAND SURFACE MODEL

Abstract

Accurate modeling of the hydrologic processes that influence land-atmosphere exchange phenomena is crucial for better weather prediction. This is widely recognized as an issue to be addressed from both hydrological and atmospheric science perspectives. As surface exchange processes are highly non-linear and heterogeneous in space and time, it is important to know the appropriate scale for the reasonable prediction of them. The study region was chosen from the Southern Great Plains 1997 (SGP97) Hydrology Experiment. A statistical procedure was followed to select two cells, each 20 km x 20 km, representing the most homogeneous and the most heterogeneous surface conditions (based on soil and vegetation), recognizing that these areas might not represent the typical variability when considered at regional or continental scales. Three scales of study (200 m, 2 km and 20 km) were considered in order to investigate the impacts of the aggregation of input data on the model output. Simulations were performed using the NOAH-OSU (Oregon State University) Land Surface Model (LSM). Green vegetation fraction was computed from Normalized Difference Vegetation Index data using two different approaches, but the model results were insensitive to this choice. Model results of net radiation, latent, sensible and ground heat fluxes were compared for the three

scales. For the heterogeneous area, the model output at the 20-km resolution showed some differences when compared with the 200-m and 2-km resolutions. This was more pronounced in latent and sensible heat estimation than in net radiation and ground heat flux estimation. The scaling effects were much less for the relatively homogeneous land area. The results suggested that considering sub-grid scale heterogeneity can be important for realistic modeling of surface exchange processes.

Introduction

Realistic modeling of land-atmosphere interaction over a large area is being advanced by the realization that it should be addressed from both hydrological and atmospheric science perspectives. It is understood that the atmospheric and soil-vegetation systems are dynamically coupled through the physical processes which produce transport of thermal energy and water mass across the land surface (Eagleson, 1978). The issue of global scale hydrology has reoriented the attention of hydrologists in considering the atmosphere and the land surface as an interactively coupled system (Eagleson, 1986).

The large-scale processes influencing the terrestrial water balance (e.g., infiltration and the partitioning of net radiation into sensible and latent heat fluxes and soil heat flux), are highly non-linear and also heterogeneous both in space and time due to the natural variability in soil, land use, vegetation and weather. Studies have shown that the complex land-atmosphere models often contain overly simplified parameterization of land surface hydrology, thereby resulting in inaccurate representation of the real situation (Wood et al., 1992; Sivapalan and Woods, 1995). The issue of scale interaction has

emerged as one of the crucial problems for the parameterization of general circulation models (GCMs) due to the strong interconnection between land and atmospheric processes. In order to address this issue, the understanding of the scaling properties of water and energy fluxes with their corresponding storage term (soil moisture) becomes significant (Wood, 1994).

Many times, soil moisture and evapotranspiration are either assumed to have lesser significance or are misrepresented, resulting in simplification of these processes in large-scale hydrological studies. For instance, some land surface modelers fail to consider soil moisture and its related processes within their models as physically based, and instead parameterize it as an index to be used for evapotranspiration and runoff calculations rather than representative of the actual mass of moisture in the soil (Robock et al., 1998). Evapotranspiration and runoff may not be sufficiently dependent upon the soil moisture even in the simple monthly water balance simulation of land surface models (Koster and Milly, 1997). Hence when these results are linked to GCMs, the corresponding model responses can be grossly inaccurate.

To date, understanding the effects of land surface heterogeneity at the sub-GCM grid scale level is an unfinished task due to the associated challenges. Traditionally the lumped model concept, where the spatially variable inputs and parameters are assumed to be homogeneous, has been widely used even in many large-scale water balance studies. But the accuracy of the model response is very much dominated by sub-grid scale parameterizations of inputs and parameters (Avissar and Pielke, 1989; Famiglietti and Wood, 1994; Wood, 1994; Hu and Islam, 1997). If the model is process based, and if the

resolution of the model grid is increased, some of these modeling problems can be addressed successfully. This would probably be the most accurate approach but not always practical due to limitations in computing as well as data availability (Avissar and Pielke, 1989). However, with the advent of high-speed computers, the problem of voluminous data handling and processing can be overcome whereas the number and measurements is still a problem. Oklahoma offers the best chance to address the problem as the Mesonet provides high-resolution weather data both spatially and temporally. As part of the realistic modeling of spatially variable water and energy balance processes, one needs to understand sub-grid scale heterogeneity and its impact on model results.

This study will provide some insight into the effects of parameterization of land surface heterogeneity on the quantification of surface energy-balance components (namely net radiation and latent, sensible and ground heat fluxes). This will be done at various scales using a distributed modeling approach. The overall objective is to examine the effects of different spatial scales of input data on modeled fluxes, and thereby better understand the resolution needed for the realistic modeling of large-scale land-atmosphere interaction.

Scaling concepts

The term scale refers to the characteristic length (or time) of a process, observation or model. Models and theories developed in darcian scale (point scale) may be applied to larger scale predictions. Similarly large-area models and data are used for small-area predictions. This transfer of information across scales is called scaling and the problems associated with it are scale issues (Bloschl and Sivapalan, 1995). DeCoursey

(1996) defines scaling as the transcending concepts that link processes at different levels of space and time.

Typical hydrological modeling scales (Dooge, 1982, 1986) in space are: local scale (1 m), hillslope (reach) scale (100 m), catchment scale (10 km) and regional scale (1000 km). Typical hydrological time scales are: event scale (1 day), seasonal scale (1 yr) and the long-term scale (100 yrs). There is additional terminology related to scaling such as upscaling and downscaling. For example, if we consider the problem of estimating catchment rainfall from one or more rain gauge(s), upscaling rainfall from a dm^2 scale to a km^2 scale involves distributing the point precipitation over the catchment and then aggregating the spatial distribution of rainfall into one single value. Conversely, downscaling involves disaggregating and singling out (Bloschl and Sivapalan, 1995).

A major complication in parameter specification is the fact that these parameters vary from point to point because of the spatial variability always present in nature. One of the merits of distributed models usually claimed is that the parameters have some physical relevance and hence they should be measurable in the field. Jensen and Mantoglou (1992) believed that a theoretically justified model would provide more confident predictions and therefore the incentive to use physically-based models would increase in the future. On the other hand Meentemeyer (1989) states that: *"much of the cherished detail of the reductionist sciences may not be needed, and indeed cannot be used, in broad scale modeling"*. Another perspective is that a model that is suitable at a plot scale cannot be used to simulate a region if the simulator does not represent all relevant phenomena existing at the larger scale. For instance, scaling up of a soil-plant

model in space and time involves the incorporation of additional phenomena that are not incorporated at the small scale (Luxmoore et.al., 1991) This has been termed phenomena-added modeling. Examples of such additional phenomena include topographic effects in watersheds and successional processes of forest communities.

Representing soil-vegetation-atmosphere transfer (SVAT) at larger scales is extremely difficult due to the problems of spatial heterogeneity. Thus the question of extrapolation of non-linear hydrological processes to large scales remains largely unanswered. As scaling embodies such concepts as process descriptions, cartographic considerations or pattern analysis, and spatial and temporal variability, simple integration or aggregation of values at one level to achieve estimates at a more encompassing level of consideration may not be acceptable (DeCoursey, 1996). Dooge (1986) observes:

To predict catchment behavior reliably we must either solve extremely complex physically based models which take full account of the spatial variability of various parameters or else derive realistic models on the catchment scale in which the global effect of these spatially variable properties is parameterized in some way. The former approach requires extremely sophisticated models and exceedingly expensive computers to have any hope of success. The latter approach requires the discovery of hydrologic laws at the catchment scale that represent more than mere data fitting.

A phenomenon termed 'coarse-graining in hydrological observations' occurs with the transformation of a nonstationary hydrological process at a finer scale to a stationary hydrologic process at a larger scale (Kavvas, 1999). With the loss of some information, however, Kavvas (1999) stated that a simple expression that includes sub-grid scale heterogeneity for large scales could be used successfully. Various studies have shown that upscaled hydrologic equations preserve heterogeneity at field scales (Chen et al.,

1994a, 1994b; Kavvas and Karakas, 1996) and thus can be applied successfully for regional scale land surface simulations (Kavvas et al., 1998).

While studies in the last few years have been consistently aimed at narrowing the gap in the understanding of land-atmosphere interactions, Wood's (1991) statement is still valid:

The inadequate representation (of land-atmospheric interactions) *reflects the recognition that the well-known physical relationships, which are well described at small scales, result in different relationships when represented at the scales used in climate models. Understanding this transition in the mathematical relationships with increased space-time scales appears to be very difficult, and has led to different approaches; at one extreme, the famous 'bucket' model where the land-surface is a simple one layer storage without vegetation; the other extreme may be Seller's Simple Biosphere Model (SiB) where one big leaf covers the climate model grid.*

Land surface model

There are several land surface models that are being used to simulate the hydrologic processes governing biosphere-atmosphere interrelationships. Each of them has distinct features with respect to model physics, parameters (including distributed or lumped), time step, extent of testing and validation, and number of users. This study used the NOAH- OSU (Oregon State University) Land Surface Model (LSM), which has been widely recognized by the land-surface research community and which is coupled to the NCEP operational Eta and PSU/MM5 mesoscale models. The LSM simulation of seasonal and diurnal variation in evaporation, soil moisture, sensible heat flux and surface skin temperature agrees well with field observations and its performance appears to be better than many land surface models (Chen et al., 1996). Various studies (Betts et al., 1997; Chen et al., 1997; Yucel et al., 1998, Chen and Dudhia, 2001) showed that the coupled Eta/OSULSM system indeed improved the short-range prediction of surface heat

fluxes, near-surface sensible variables, planetary boundary layer and precipitation. Marshall (1998) studied the performance of this LSM in an uncoupled mode for Oklahoma conditions and found that the model overestimated net radiation and underestimated ground heat flux and the study was limited to one site, and latent and sensible heat fluxes were estimated using Bowen ratio and aerodynamic approaches. Validation study of this LSM using Oklahoma Atmospheric Surface-layer Instrumentation System (OASIS) measurements is in Chapter 4.

The energy balance in the model is formulated as shown in equation (5-1). Net radiation (as the "source" term in the energy balance) is directed into latent, sensible and ground heat fluxes:

$$R_n = LH + SH + GH \tag{5-1}$$

Each of these surface energy-balance components is computed using physically-based formulations. A more detailed description of the model can be found in Chen and Dudhia (2001).

Study area and data

Study area description

This research utilized the study area for the Southern Great Plains 1997 (SGP97) Hydrology Experiment. SGP97 focused on the central section of Oklahoma from Comanche and Stephens counties in the south to Grant and Kay counties in the north, covering a soil moisture mapping area of about 50 km x 280 km (SGP97 Hydrology Experimental Plan, 1997; Famiglietti et al., 1999; Jackson et al., 1999). SGP97 took

advantage of the availability of the Oklahoma Mesonet (Brock et al., 1995), and was built upon the success of the Little Washita 1992 experiment (Jackson and Schiebe, 1993; Jackson et al., 1995; Rodriguez-Iturbe et al., 1996) in demonstrating the viability of L-band radiometry for remotely sensing surface moisture. The insight gained from the Little Washita 1992 experiment and the emerging research needs associated with the GEWEX Continental-scale International Project (SGP97 Hydrology Experimental Plan, 1997; Schneider and Fisher, 1997; International GEWEX Project Office, 1998) formed the basis of the scientific objectives of SGP97. The main objective was understanding soil moisture dynamics in space and time using remotely sensed and field measurements. The schematic representation of the study area is shown in Figure 5-1.

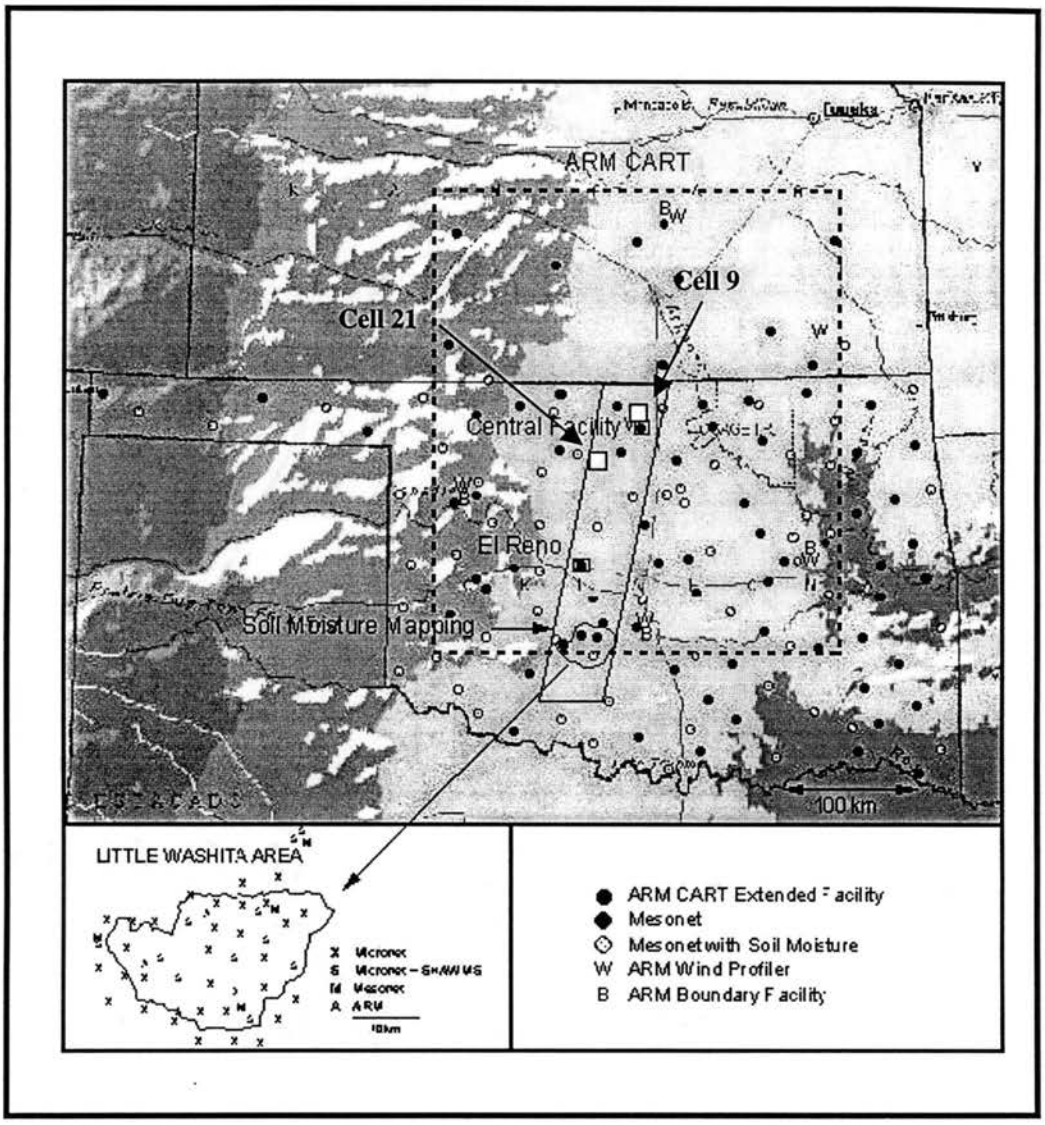

Figure 5-1. Location map of Southern Great Plains 97 (SGP97) and the study area.

Soil and vegetation data

The GIS (Geographic Information Systems) soil data for this study was available from the MIADS (Map Information Analysis and Display System) of the USDA Natural Resources Conservation Service. Soil surveys conducted for the individual counties had been merged to create a seamless statewide data set in gridded format. The resolution of the MIADS soil data was 200 m (4 ha).

Land-use-class information, derived from Landsat Thematic Mapper (TM) data, was available for the SGP97 study area. These 30-m resolution land-use data were aggregated (using a majority filter) in order to match the spatial resolution of the 200-m soil data.

The Conterminous U.S. Advanced Very High Resolution Radiometer (AVHRR) satellite data provided measurements of Normalized Difference Vegetation Index (NDVI) with a 1-km resolution. A time series of biweekly composite NDVI data sets was obtained from the USGS EROS Data Center. The model soil and vegetation parameters are shown in Table 5-1.

Identification of the homogeneous and the heterogeneous cell

Due to the difficulties associated with handling and processing the huge volume of 200-m resolution data, a representative subset of the SGP97 study area was selected for the scaling analysis. A simple statistical analysis of the combined soil and land use data was performed to identify the most homogeneous and the most heterogeneous 20-km cells within the SGP97 area. Seventy cells, each 20 km x 20 km, were analyzed using FRAGSTATS (McGarigal and Marks, 1995).

Table 5-1. List of vegetation and soil parameters used in the land surface model.

Vegetation parameters	Soil parameters
Albedo	Porosity
Roughness length	Air dry soil moisture content
Shade factor	Saturation soil suction
Root depth	Saturation soil conductivity/diffusivity
Minimum stomatal resistance	Soil conductivity/diffusivity coefficient
A parameter in the radiation stress function	Field capacity
A parameter in the vapor pressure deficit function	Wilting point
	Soil quartz content

Landscape indices were computed to find the fragmentation as shown in Table 5-2. A total of 9 soil classes and 13 land-use classes were present in the 28,000 km^2 area. "Patches" in the landscape represent homogeneous, discrete areas with the smallest area being 4 ha, in this study. The indices considered in the analysis included the number of patches, the largest patch index (the area of the largest patch in the landscape divided by total landscape area), patch density (number of patches in the landscape divided by total landscape area), diversity index (sum of the proportional abundance of each patch type multiplied by that proportion; it increases as the number of different patch types increases), evenness index (sum of the proportional abundance of each patch type multiplied by that proportion divided by the logarithm of the number of patch types), interspersion/juxtaposition index (the observed interspersion over the maximum possible interspersion for the given number of patch types), and the contagion index (observed contagion over the maximum possible contagion for the given number of patch types).

An analysis of the various indices led to the identification of Cell 21 as the most heterogeneous and Cell 9 as the most homogeneous of the 70 cells. These two cells were selected for further study. It is important to mention that these areas were defined within the SGP97 region and do not necessarily represent the degree of heterogeneity and homogeneity that might be seen at continental or even regional scales.

Cell 21 was situated in the west-central part of SGP97 (Figure 5-1) and its Universal Transverse Mercator (UTM) coordinates were (553000,3998000) and (573000,4018000) for the southwest and northeast corners, respectively.

Table 5-2. Landscape indices for the heterogeneous cell (#21) and the homogeneous cell (#9).

LANDSCAPE INDICES	*Cell 21*	*Cell 9*
Number of patches:	2455	1414
Largest Patch Index(%):	3.76	27.33
Patch Density (#/100 ha):	6.51	3.6
Shannon's Diversity Index:	3.28	1.94
Simpson's Diversity Index:	0.94	0.69
Modified Simpson's Diversity Index:	2.78	1.18
Shannon's Evenness Index:	0.73	0.46
Simpson's Evenness Index:	0.95	0.7
Modified Simpson's Evenness Index:	0.62	0.28
Interspersion/Juxtaposition Index (%)	65.58	50.49
Contagion Index (%):	39.57	61.06

The variability in soil and land use in this 20 x 20 km grid was very high. As shown in Figure 5-2a, at the 200-m resolution, Cell 21 contained 13 vegetation classes with pastureland (42%) and wheat (33%) as predominant types. The soil as shown in Figure 5-3a consisted of 9 different textures, the major ones being sand (23%), silt loam (18%), loamy sand (16%) and sandy loam (12%). Cell 9 was located in the northeast part of SGP97 (Figure 5-1) and its UTM coordinates were (613000,4058000) and (633000,4078000) for the southwest and northeast corners, respectively. This cell primarily consisted of wheat (59%) and pastureland (24%) as shown in Figure 5-4a. Silt loam occupied 83 % of the cell area with several other textures having minor presence (Figure 5-5a).

Aggregation of the input data

The high resolution data (200 m) were used to develop the input data sets for two coarser resolutions, i.e., 2 km and 20 km. These scales increase by a factor of 10 in each case and were chosen in order to represent the scales that might be of interest for current and (especially) future operational weather modeling. Also, the 20-km scale should eventually be relevant to global climate modeling, as GCM grid cells continue to decrease in size.

The soil and land use types were each aggregated using a majority filter on 100 of the 200-m cells (in the case of the 2-km resolution) and on 10,000 of the 200-m cells (in the case of the 20-km resolution). As shown in Figure 5-2b, land use types for Cell 21 were reduced to five classes at the 2-km resolution as compared to 13 classes at the 200-m resolution. Similarly, Figure 5-3b shows that the number of soil types was reduced

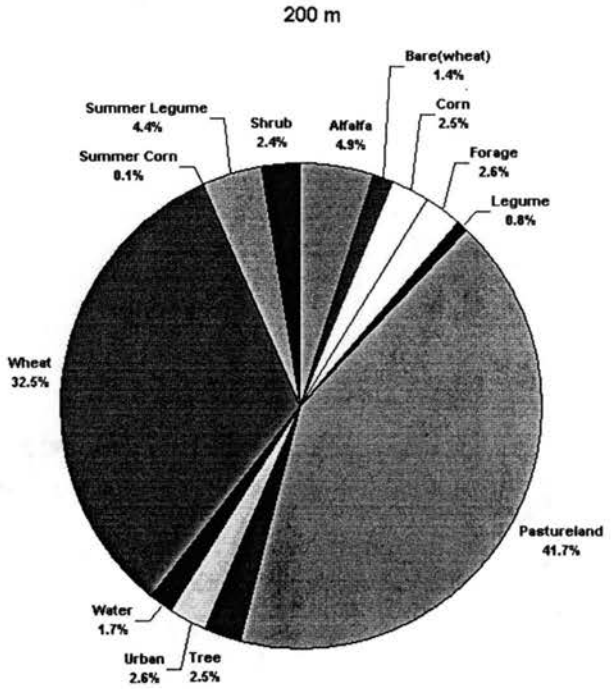

Figure 5-2a. Land use types of the heterogeneous area (Cell 21) at 200-m resolution.

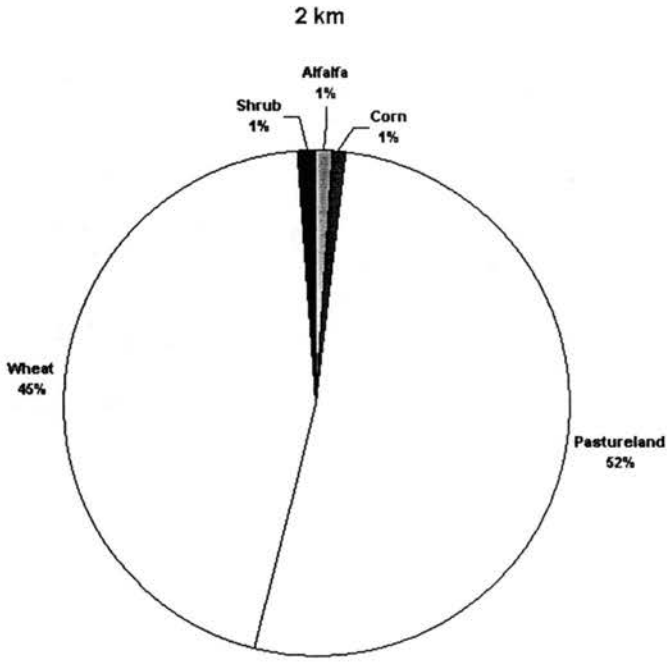

Figure 5-2b. Land use types of the heterogeneous area (Cell 21) at 2-km resolution.

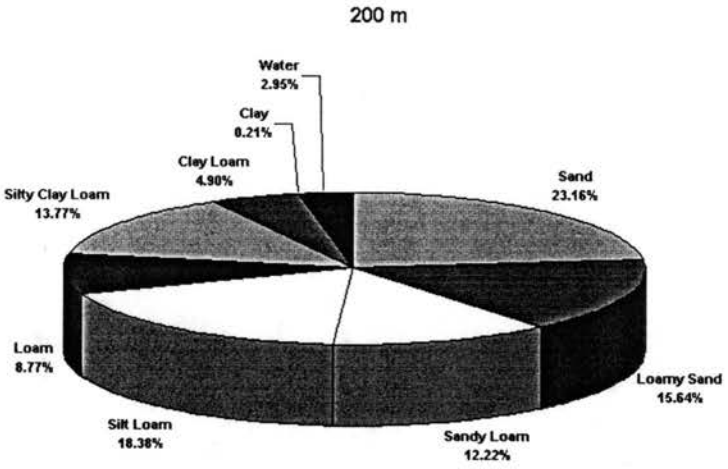

Figure 5-3a. Soil types of the heterogeneous area (Cell 21) at 200-m resolution.

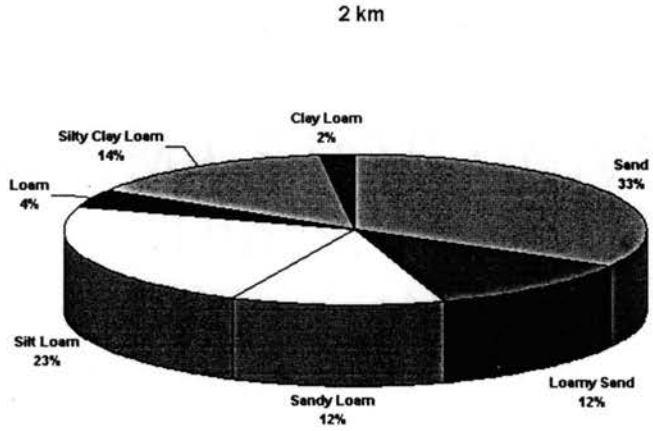

Figure 5-3b. Soil types of the heterogeneous area (Cell 21) at 2-km resolution.

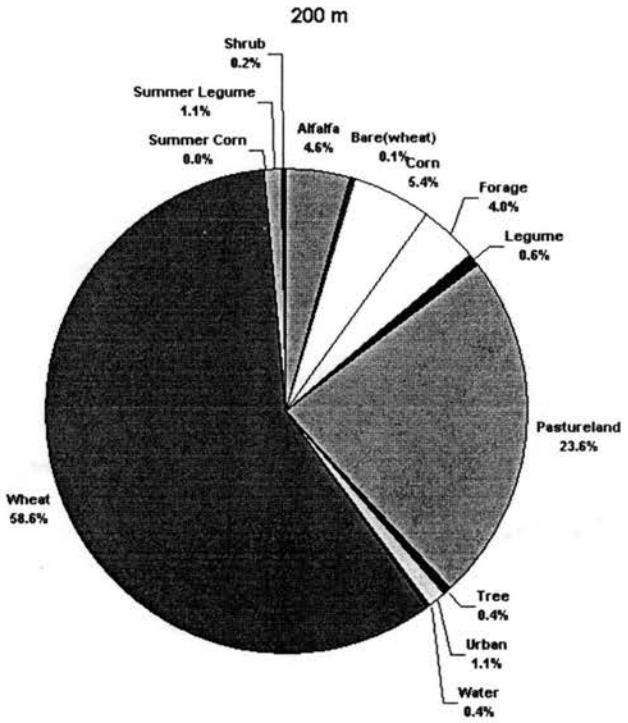

Figure 5-4a. Land use types of the homogeneous area (Cell 9) at 200-m resolution.

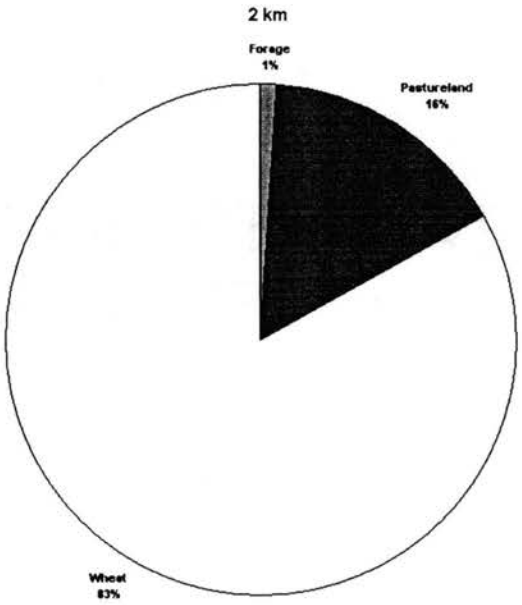

Figure 5-4b. Land use types of the homogeneous area (Cell 9) at 2-km resolution.

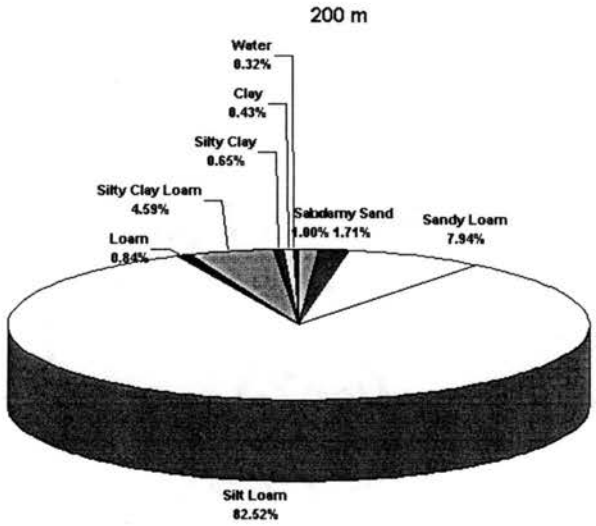

Figure 5-5a. Soil types of the homogeneous area (Cell 9) at 200-m resolution.

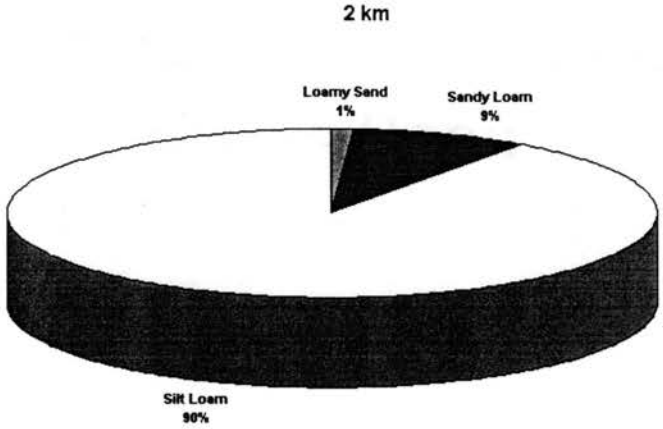

Figure 5-5b. Soil types of the homogeneous area (Cell 9) at 2-km resolution.

from nine to seven. The difference is even more dramatic for the homogeneous cell (Cell9). As evident from Figure 5-4b, land use at the 2-km resolution was reduced from 13 classes to only three (with 83% wheat). Similarly, only three soil types remained in Cell 9 at the 2-km resolution, with 90% silt loam (Figure 5-5b). So, the clear distinction between the heterogeneous (#21) and homogeneous (#9) cells was still evident after the aggregation to 2 km.

Area-averaged and dominant-landuse-based NDVI for green vegetation fraction

The land surface model requires green vegetation fraction as a key input. Using GIS, "area-averaged" NDVI was computed and it is simply the numerical average of the NDVI values over the given area. For instance, averages of 4 and 400 numerical values of NDVI (1-km resolution) were computed to obtain a cell-average NDVI value for 2 km and 20 km, respectively. An alternative approach ties the NDVI value for a given area to the dominant land use in that area. "Dominant-land use-based" NDVI was computed by first applying a majority filter on 100 and 10000 land use "pixels" (200-m resolution) in GIS for 2 km and 20 km, respectively. Then an average was taken of the NDVI values for all pixels with that majority land use. As opposed to the area-average, this approach was more likely to result in an NDVI value that is consistent with the single vegetation type assigned to a modeling area.

From both the area-averaged and dominant-landuse-based NDVI data, vegetation fraction (f_g) was computed using the Gutman-Ignatov (1998) method:

$$f_g = \frac{(NDVI - NDVI_{\min})}{(NDVI_{\max} - NDVI_{\min})} \tag{5-2}$$

Bare soil NDVI ($NDVI_{min}$) and dense vegetation NDVI ($NDVI_{max}$) are defined as 0.04 and 0.52 respectively and they correspond to seasonally and geographically invariant

constants for desert and evergreen clusters. As NDVI was available from the biweekly composite images, the computed vegetation fraction based on NDVI was then linearly interpolated on a daily basis. The vegetation fractions derived based on area-averaged based NDVI and dominant-landuse-based NDVI are referred to herein as the area-averaged vegetation fraction and the dominant-landuse-based vegetation fraction, respectively.

Weather data

The Oklahoma Mesonet, an automated network of 114 stations (Elliott et al., 1994; Brock et al., 1995) provided meteorological data. The Mesonet sites used for this study included LAHO (Lat: 36° 23′ 3″ N, Long: 98° 6′ 41″ W, elev: 395 m) and MEDF (lat:36° 47′ 31″ N, long: 97° 44′ 44″ W, elev: 330 m). These sites were assigned to Cell 21 and Cell 9, respectively based on the nearest neighbor approach. The data from the Oklahoma Mesonet consisted of 5-minute averages which were then averaged over one-hour intervals. The variables used were air temperature (K), specific humidity (Kg Kg^{-1}), wind speed (m s^{-1}), pressure (Pa), precipitation (kg $m^{-2}s^{-1}$) and solar radiation (W m^{-2}). It should be noted that air temperature in degree K and specific humidity were derived quantities using the original Mesonet variables. Longwave downwelling radiation was estimated using the scheme discussed in Chapter 3. This longwave radiation scheme uses near-surface vapor pressure and air temperature data.

The model simulations were carried out over a five-month period (from 1 March 1997 through 31 July 1997). It should be noted that simulation from March through May was considered as the model 'spin-up' period before the SGP97 duration of June-July. The model was run on an hourly time step, and the results were aggregated daily. Though

the model was run continuously for a five-month period, due to the huge volume of output generated at the 200-m resolution, the model was coded to write the output at the 200-m resolution only for selected days. The days were chosen to fall within the SGP97 period. Nine days with relatively high solar radiation were chosen as "clear days" (18,25,27, and 30 June; 3,6,14,22, and 23 July), while four days with relatively low solar radiation were considered as "cloudy days" (23 June; 11,15, and 20 July). For the 2-km and the 20-km resolutions, simulation results were obtained throughout the study period.

Results and Discussion

Model sensitivity to the area-averaged and dominant-landuse-based vegetation fraction

The impact of the area-averaged versus dominant-landuse-based vegetation fraction on the model results is discussed briefly here. The sensitivity of the model to the two approaches was analyzed for both the cells, by comparing the model estimated surface energy-balance components, i.e., net radiation, latent, sensible and ground heat (GH) fluxes. There was virtually no difference in the model output resulting from these two vegetation fractions. This was consistent for both clear and cloudy days. The results of this analysis are tabulated in Appendix D (Table (D-1)–(D-2)). The differences in NDVI values were not large enough to cause appreciable differences in the computed vegetation fraction.

Model output

The hourly model simulations of surface energy-balance components were aggregated on a daily basis. Then, the numerical average over the domain was computed for comparing the results across the three scales, i.e., 200 m, 2 km and 20 km. The spatial

representations of the model output for Cell 21 and Cell 9 for 18 June 97 are shown in Figures (5-6) – (5-13). Appendix D (Figures (D-1) – (D-16) contains the output for one additional clear day and one cloudy day.

Tables (5-3) and (5-4) summarize the numerical model output. Maximum, minimum and average values are shown for each study day. It was observed that the range of the cell-by-cell model output was greater at the 200-m resolution than at the 2-km resolution, for all of the components. In other words, the range of the lower-resolution model output always fell within the range of the high-resolution output, indicating that the variability in the output was reduced at coarser scales.

Time series comparison of the model output for the three scales

Figure 5-14 shows the time series plot of all four surface energy-balance components at 200 m, 2 km and 20 km for Cell 21. The time period is June 15 through July 25. As shown in Figure 5-14a, the discrete series of domain average net radiation for 200 m (13 days) agreed very well with the continuous time series for both the 2-km and 20-km resolutions. This indicated that, in spite of the aggregation of input variables from 200 m to 2 km and 20 km, the model estimates of net radiation were very closely matched across these scales. This is perhaps to be expected because net radiation is dominated by the magnitude of incoming solar radiation and is only minimally influenced by vegetation and soil parameters (i.e., the albedo). It should be remembered that weather data from a single site were applied at all three scales for the entire domain of Cell 21. The 200-m and 2- km output for latent heat flux matched very closely while the 20-km output did show some deviations (Figure 5-14b). Figure 5-14c suggested that the sensible heat flux estimations at 20 km were higher than for the other two resolutions, and the

Table 5-3. Daily average modeled energy-balance components for the heterogeneous area (Cell 21) at three scales of input aggregation.

Type of Day	Date		R_n (MJ $m^{-2} d^{-1}$)			LH (MJ $m^{-2} d^{-1}$)			SH (MJ $m^{-2} d^{-1}$)			GH (MJ $m^{-2} d^{-1}$)		
			200 m	2 km	20 km	200 m	2 km	20 km	200 m	2 km	20 km	200 m	2 km	20 km
Clear - day	18-Jun-97	MAX	20.24	19.55		17.49	15.98		16.82	7.99		3.26	3.11	
		MIN	15.10	17.76		0.33	8.46		0.91	1.06		0.05	1.70	
		AVE	18.39	18.31	18.39	13.18	13.26	12.83	3.05	2.85	2.89	2.16	2.20	2.67
	25-Jun-97	MAX	18.09	17.39		15.15	13.29		15.18	8.12		2.79	2.12	
		MIN	13.70	15.82		0.40	7.15		1.82	2.28		0.02	1.11	
		AVE	16.33	16.29	16.21	10.85	10.88	9.94	4.15	3.99	4.67	1.33	1.42	1.61
	27-Jun-97	MAX	15.79	15.19		12.67	11.85		13.47	7.25		1.27	1.13	
		MIN	11.95	13.82		0.14	6.81		2.04	2.12		0.01	0.42	
		AVE	14.28	14.21	14.22	10.01	10.07	9.42	3.56	3.41	3.73	0.72	0.73	1.07
	30-Jun-97	MAX	20.53	19.73		16.03	14.85		17.60	9.60		2.77	2.48	
		MIN	15.83	17.92		0.61	7.65		2.43	2.62		0.05	1.37	
		AVE	18.58	18.41	18.45	11.92	11.88	10.45	4.87	4.78	5.85	1.78	1.75	2.15
	03-Jul-97	MAX	20.61	19.79		16.81	15.06		17.26	10.99		1.71	1.17	
		MIN	15.65	17.74		0.62	7.37		2.36	3.68		0.00	0.27	
		AVE	18.55	18.51	18.33	11.89	11.75	9.88	6.21	6.16	7.59	0.46	0.61	0.87
	06-Jul-97	MAX	18.06	17.21		14.25	12.39		14.80	9.45		2.21	2.11	
		MIN	13.48	14.91		0.44	3.98		2.48	2.87		0.04	1.10	
		AVE	16.15	16.04	15.91	9.98	9.90	8.17	4.84	4.72	6.09	1.33	1.42	1.65
	14-Jul-97	MAX	20.24	19.29		14.85	12.93		17.08	10.16		2.54	1.96	
		MIN	15.53	17.46		0.62	7.17		3.86	4.40		0.03	0.97	
		AVE	18.11	17.96	17.77	10.43	10.26	7.96	6.44	6.49	8.47	1.23	1.21	1.33

Table 5-3. Daily average modeled energy-balance components for the heterogeneous area (Cell 21) at three scales of input aggregation (contd.)

Type of Day	Date		R_n (MJ $m^{-2} d^{-1}$)			LH (MJ $m^{-2} d^{-1}$)			SH (MJ $m^{-2} d^{-1}$)			GH (MJ $m^{-2} d^{-1}$)		
			200 m	2 km	20 km	200 m	2 km	20 km	200 m	2 km	20 km	200 m	2 km	20 km
Clear - day	22-Jul-97	MAX	18.29	17.63		12.86	12.45		14.74	6.13		3.24	3.18	
		MIN	13.49	16.05		0.29	8.32		2.26	2.41		0.05	1.41	
		AVE	16.45	16.40	16.39	10.89	10.95	9.78	3.57	3.34	3.78	1.99	2.11	2.84
	23-Jul-97	MAX	18.23	17.50		13.49	13.23		14.62	6.38		3.34	2.95	
		MIN	13.29	15.94		0.37	8.17		1.57	1.83		0.04	1.40	
		AVE	16.44	16.37	16.29	11.39	11.41	9.94	3.16	2.97	3.65	1.89	1.99	2.71
Cloudy - day	23-Jun-97	MAX	11.61	11.25		9.79	9.72		10.22	3.94		0.71	0.49	
		MIN	8.95	10.04		0.13	7.25		0.51	0.72		-0.12	-0.11	
		AVE	10.37	10.28	10.35	8.52	8.64	8.00	1.56	1.50	1.75	0.32	0.17	0.63
	11-Jul-97	MAX	9.62	9.26		7.89	8.31		7.95	3.17		1.30	0.91	
		MIN	7.16	8.27		0.16	5.52		0.44	0.39		-0.36	-0.18	
		AVE	8.51	8.46	8.43	6.83	6.78	5.88	1.20	1.21	1.65	0.48	0.48	0.90
	15-Jul-97	MAX	7.02	6.63		7.35	7.12		5.43	2.32		0.27	-0.26	
		MIN	5.03	5.82		0.27	4.80		-0.54	-0.27		-1.09	-0.76	
		AVE	6.07	6.06	5.91	6.04	6.01	4.89	0.64	0.59	1.41	-0.61	-0.54	-0.40
	20-Jul-97	MAX	9.03	8.76		7.39	7.56		7.09	2.04		1.97	1.93	
		MIN	6.35	7.87		0.13	4.93		0.22	-0.09		0.02	0.63	
		AVE	8.05	8.02	8.06	6.11	6.18	5.47	0.76	0.58	0.64	1.18	1.25	1.95

Table 5-4. Daily average modeled energy-balance components for the homogeneous area (Cell 9) at three scales of input aggregation.

Type of Day	Date		R_n (MJ $m^{-2} d^{-1}$)			LH (MJ $m^{-2} d^{-1}$)			SH (MJ $m^{-2} d^{-1}$)			GH (MJ $m^{-2} d^{-1}$)		
			200 m	2 km	20 km	200 m	2 km	20 km	200 m	2 km	20 km	200 m	2 km	20 km
Clear - day	18-Jun-97	MAX	17.00	15.36		16.25	12.19		8.79	3.29		2.87	2.24	
		MIN	12.44	14.74		3.57	9.29		0.03	1.26		0.06	1.64	
		AVE	15.01	14.91	14.85	10.78	10.54	10.30	2.44	2.60	2.75	1.80	1.78	1.80
	25-Jun-97	MAX	16.33	14.80		15.17	10.16		10.22	5.29		1.83	1.24	
		MIN	12.37	14.25		2.39	7.72		0.46	3.67		0.01	0.82	
		AVE	14.41	14.40	14.30	8.76	8.70	8.60	4.80	4.78	4.88	0.85	0.92	0.82
	27-Jun-97	MAX	19.63	17.70		16.62	13.22		10.92	5.29		2.33	1.72	
		MIN	14.80	17.10		3.86	10.58		1.62	3.25		0.03	1.01	
		AVE	17.40	17.30	17.23	11.95	11.72	11.45	4.32	4.48	4.68	1.14	1.11	1.11
	30-Jun-97	MAX	18.64	16.92		15.36	14.59		9.67	2.68		3.27	2.12	
		MIN	13.95	16.31		4.21	11.97		0.55	0.73		0.06	1.41	
		AVE	16.58	16.49	16.41	12.92	12.97	12.41	1.95	1.92	2.30	1.70	1.60	1.69
	03-Jul-97	MAX	20.37	18.55		17.60	15.35		11.16	5.64		0.84	0.42	
		MIN	15.25	17.83		4.09	12.10		1.18	3.01		-0.05	0.07	
		AVE	18.09	18.04	17.89	13.57	13.26	12.93	4.47	4.67	4.94	0.06	0.10	0.02
	06-Jul-97	MAX	19.51	17.80		15.95	13.31		10.86	5.19		2.04	1.45	
		MIN	14.76	17.14		4.26	10.91		2.26	3.31		0.03	0.95	
		AVE	17.39	17.27	17.22	11.57	11.44	11.18	4.78	4.78	5.02	1.04	1.05	1.02
	14-Jul-97	MAX	18.91	17.16		16.26	12.01		13.87	6.79		1.41	0.83	
		MIN	14.67	16.62		1.54	9.25		1.68	4.58		0.01	0.40	
		AVE	16.81	16.72	16.67	10.42	10.39	10.27	5.85	5.85	5.90	0.55	0.49	0.51

Table 5-4. Daily average modeled energy-balance components for the homogeneous area (Cell 9) at three scales of input aggregation (contd.)

	Date		R_n (MJ $m^{-2} d^{-1}$)			LH (MJ $m^{-2} d^{-1}$)			SH (MJ $m^{-2} d^{-1}$)			GH (MJ $m^{-2} d^{-1}$)		
			200 m	2 km	20 km	200 m	2 km	20 km	200 m	2 km	20 km	200 m	2 km	20 km
Clear - day	22-Jul-97	MAX	20.18	18.48		13.75	12.89		11.66	4.95		3.48	2.47	
		MIN	15.09	17.91		3.36	11.08		3.45	3.53		0.05	1.68	
		AVE	18.11	18.02	17.96	11.69	11.53	11.33	4.62	4.66	4.84	1.80	1.83	1.78
	23-Jul-97	MAX	20.43	18.73		13.81	13.66		12.38	5.12		2.75	2.08	
		MIN	15.16	18.18		2.73	11.49		3.47	3.77		0.05	1.29	
		AVE	18.39	18.31	18.24	12.23	12.09	11.89	4.70	4.76	4.92	1.46	1.45	1.44
Cloudy - day	23-Jun-97	MAX	10.46	9.18		10.03	7.97		6.90	2.46		0.17	-0.18	
		MIN	7.97	8.91		2.65	6.79		-0.43	1.38		-0.51	-0.36	
		AVE	9.08	9.00	9.02	7.38	7.41	7.43	1.89	1.91	1.80	-0.17	-0.31	-0.21
	11-Jul-97	MAX	7.93	7.03		7.53	6.80		4.80	0.78		0.71	0.46	
		MIN	5.99	6.84		1.47	5.76		-0.40	-0.09		0.01	0.18	
		AVE	6.90	6.89	6.86	6.50	6.51	6.62	0.10	0.16	-0.02	0.29	0.22	0.25
	15-Jul-97	MAX	9.99	8.96		10.03	7.36		7.01	2.54		0.88	0.60	
		MIN	7.35	8.65		0.75	5.62		-0.56	1.16		0.01	0.26	
		AVE	8.72	8.70	8.66	6.56	6.61	6.59	1.86	1.78	1.81	0.29	0.32	0.25
	20-Jul-97	MAX	9.67	8.70		7.85	7.45		3.97	0.64		1.86	1.34	
		MIN	6.92	8.46		2.92	6.86		0.01	0.21		0.02	0.83	
		AVE	8.55	8.51	8.50	7.16	7.17	7.17	0.50	0.47	0.49	0.89	0.87	0.83

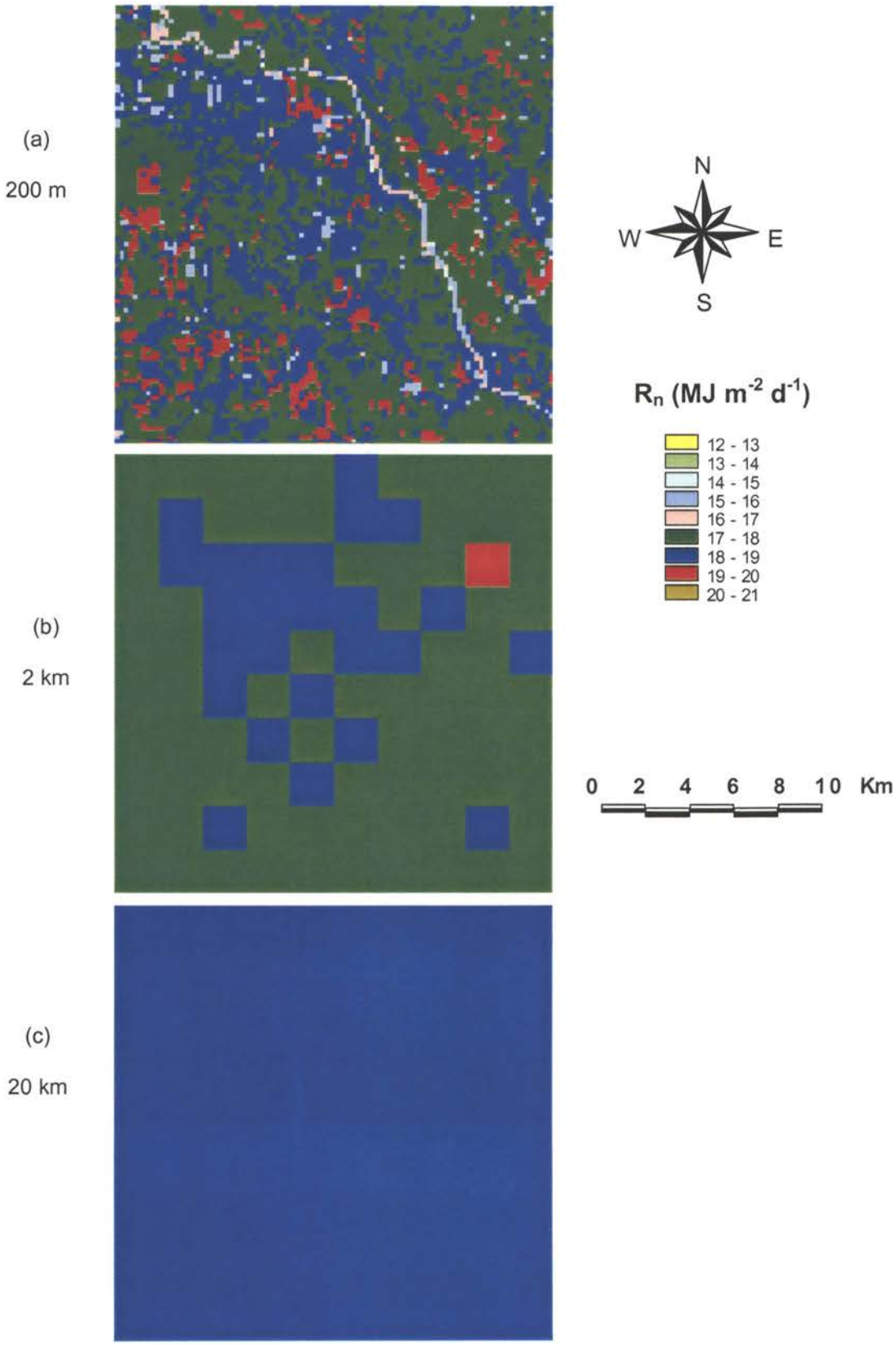

Figure 5-6. Scale comparisons of modeled net radiation (R_n) for the heterogeneous area (Cell 21) for 18 June 97.

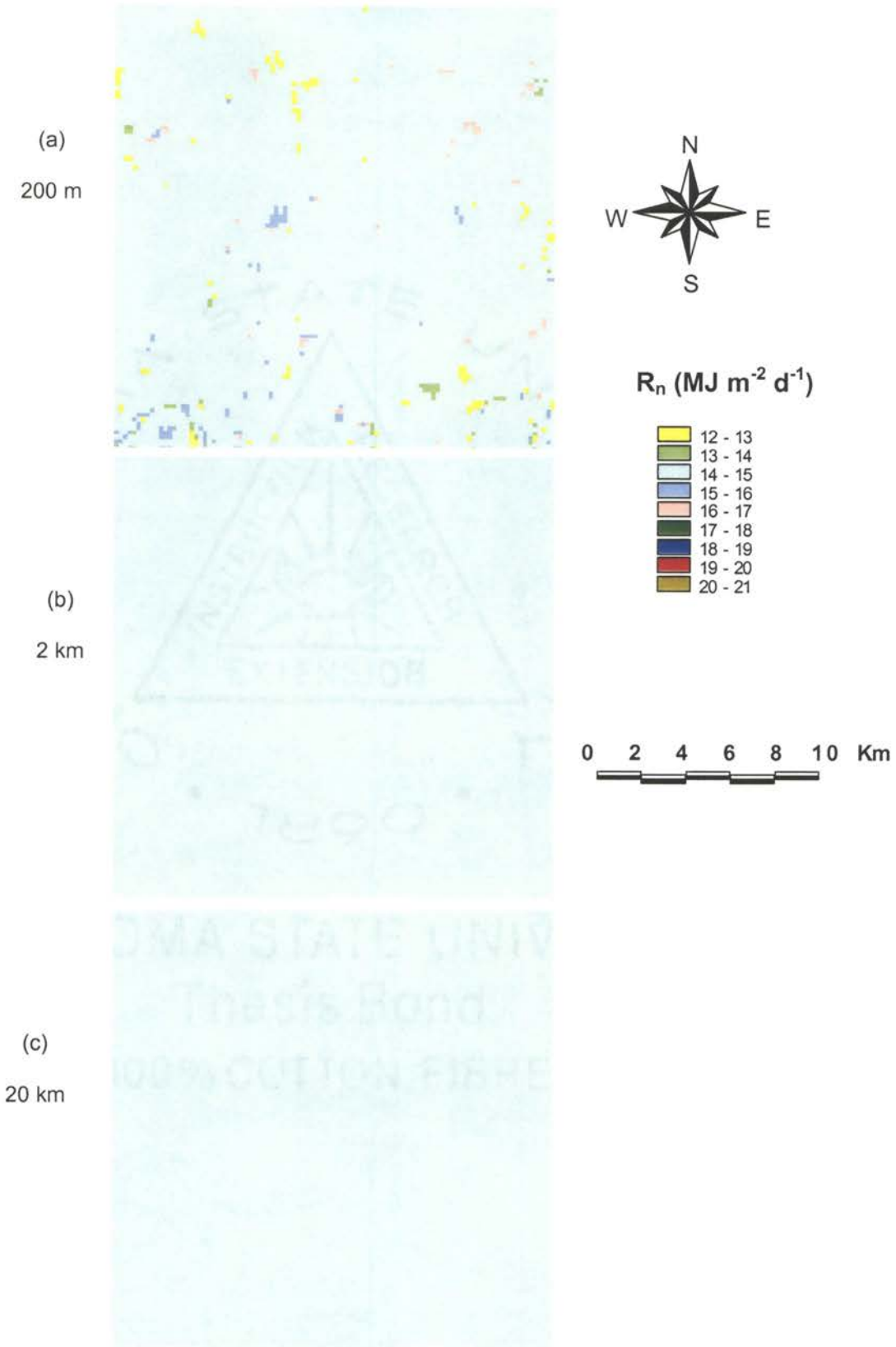

Figure 5-7. Scale comparisons of modeled net radiation (R_n) for the homogeneous area (Cell 9) for 18 June 97.

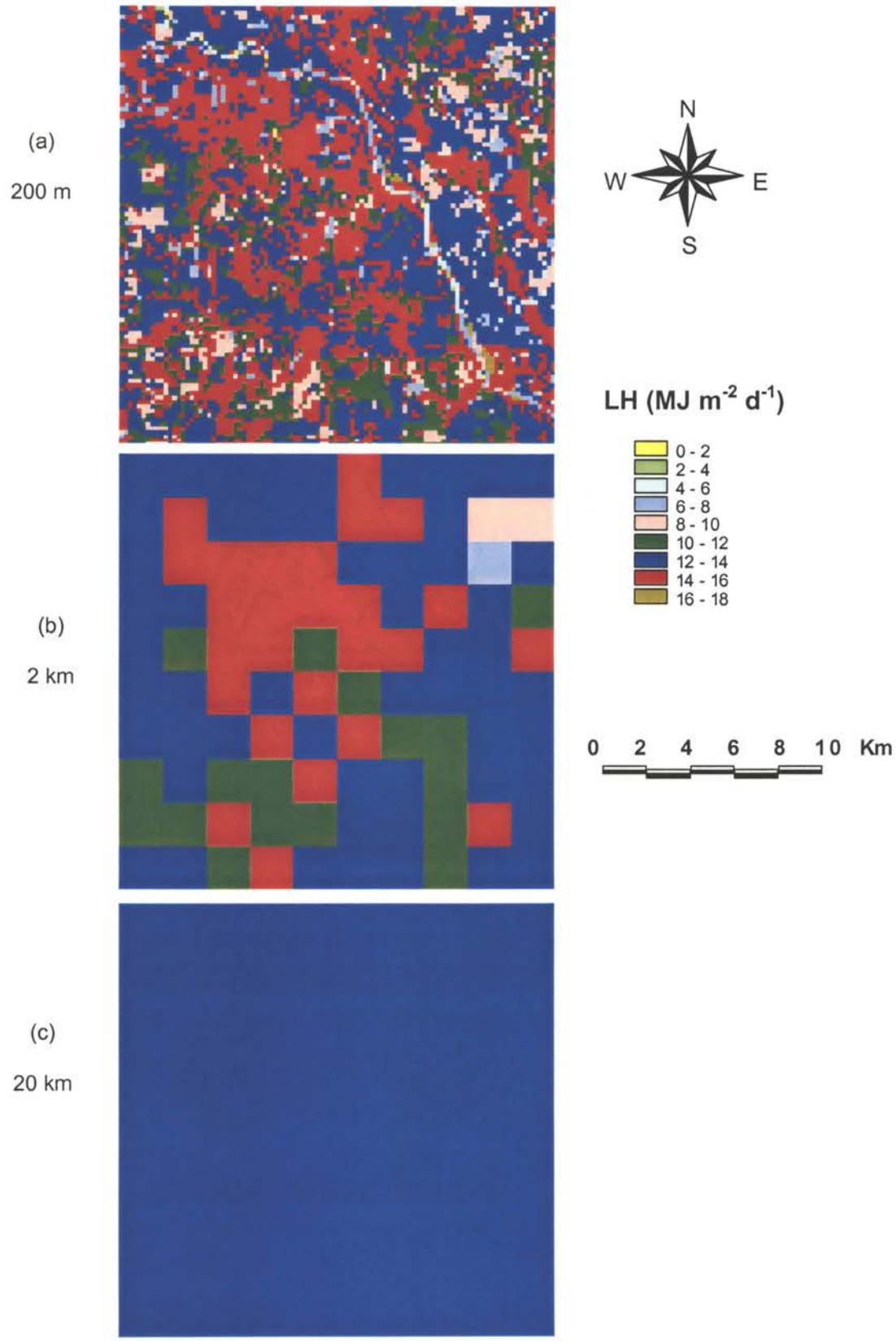

Figure 5-8. Scale comparisons of modeled latent heat flux (LH) for the heterogeneous area (Cell 21) for 18 June 97.

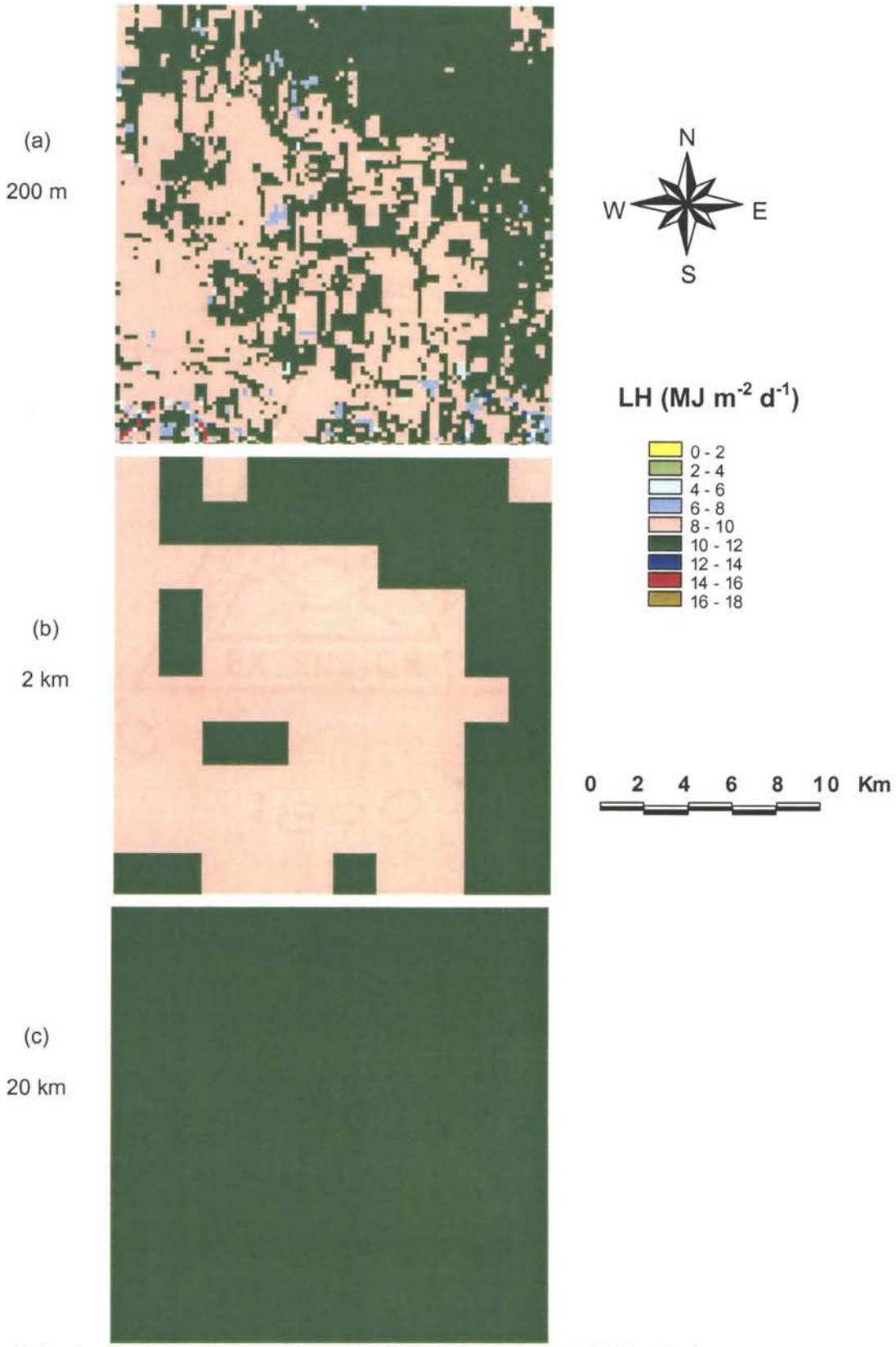

Figure 5-9. Scale comparisons of modeled latent heat flux (LH) for the homogeneous area (Cell 9) for 18 June 97.

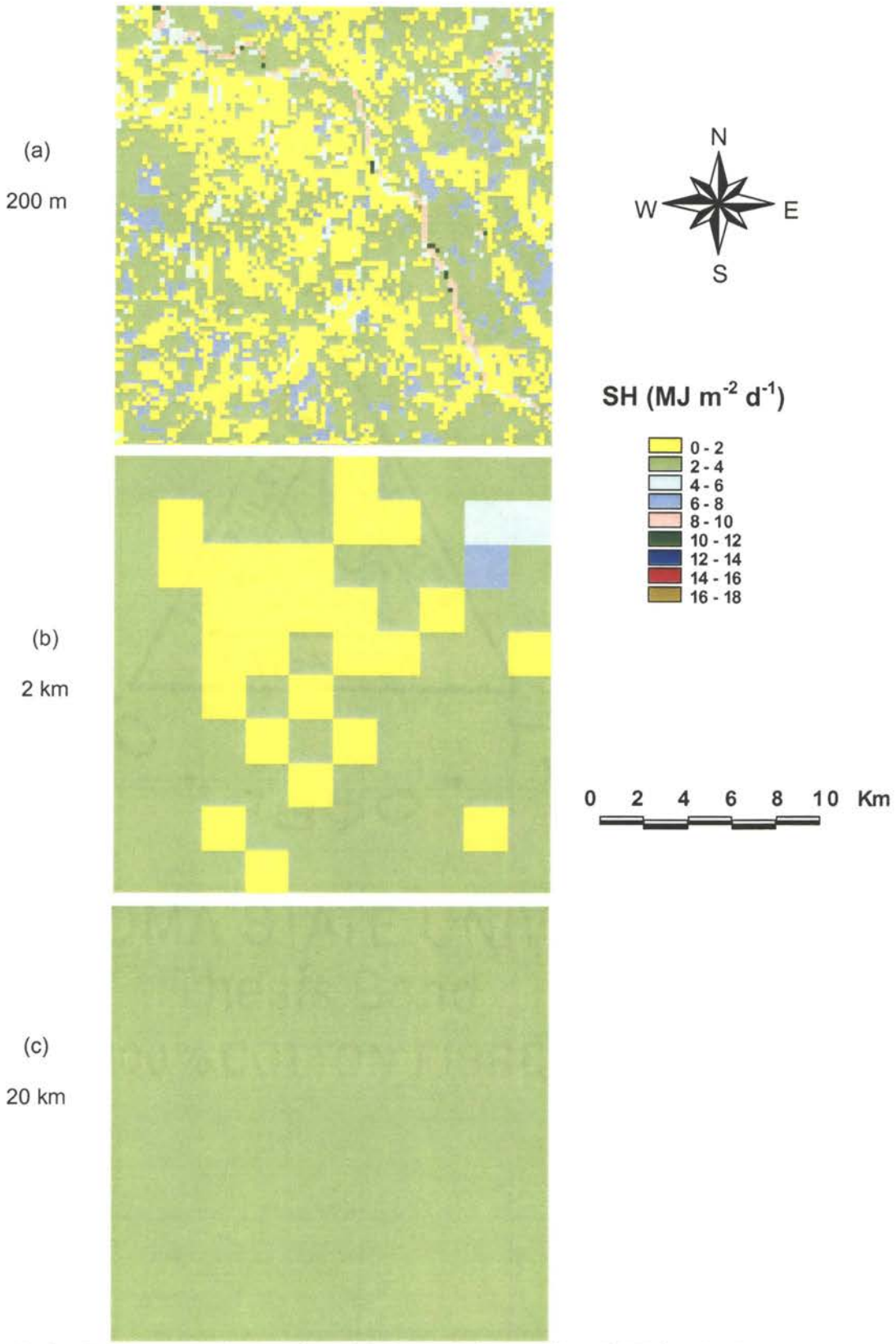

Figure 5-10. Scale comparisons of modeled sensible heat flux (SH) for the heterogeneous area (Cell 21) for 18 June 97.

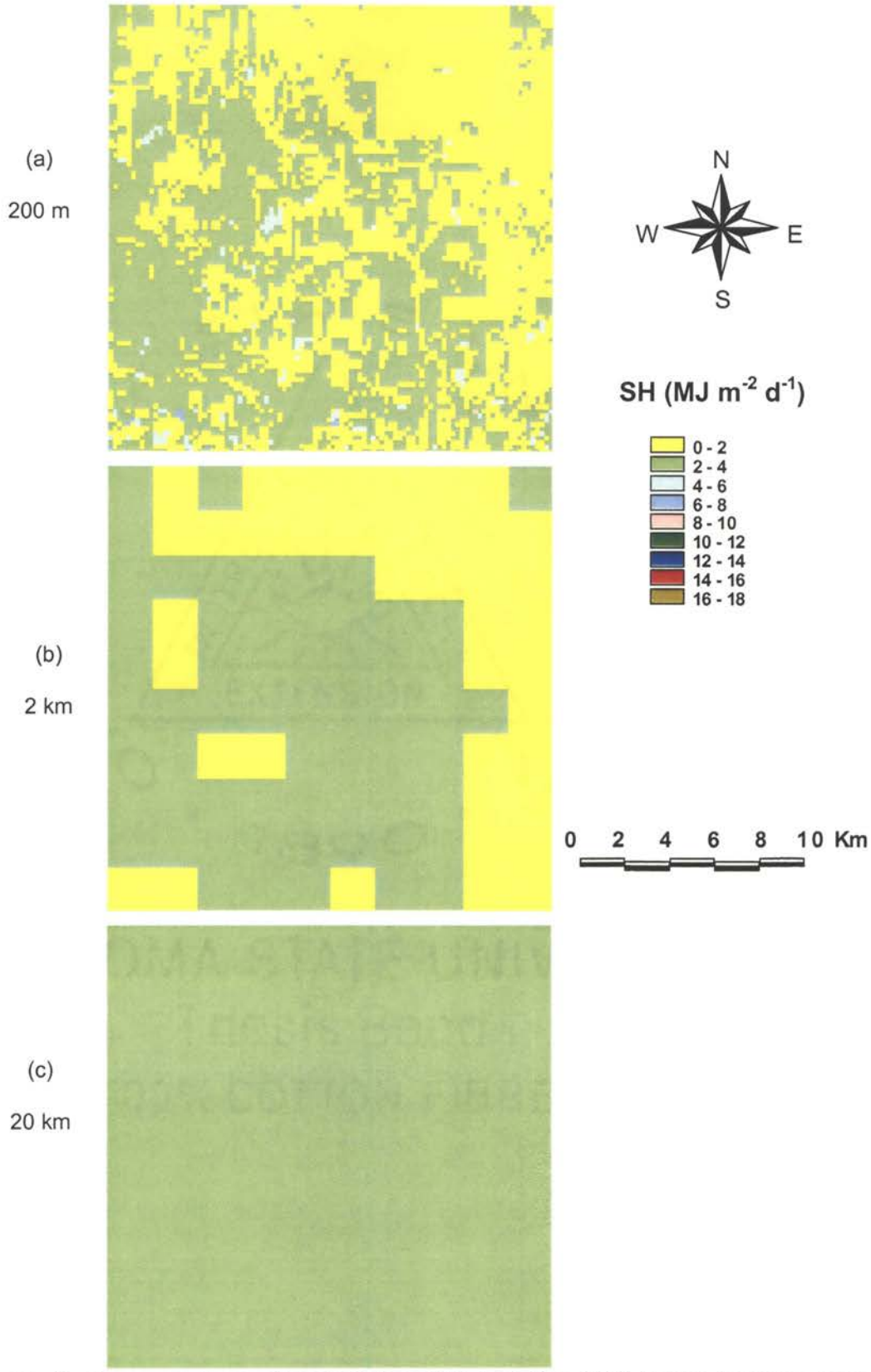

Figure 5-11. Scale comparisons of modeled sensible heat flux (SH) for the homogeneous area (Cell 9) for 18 June 97.

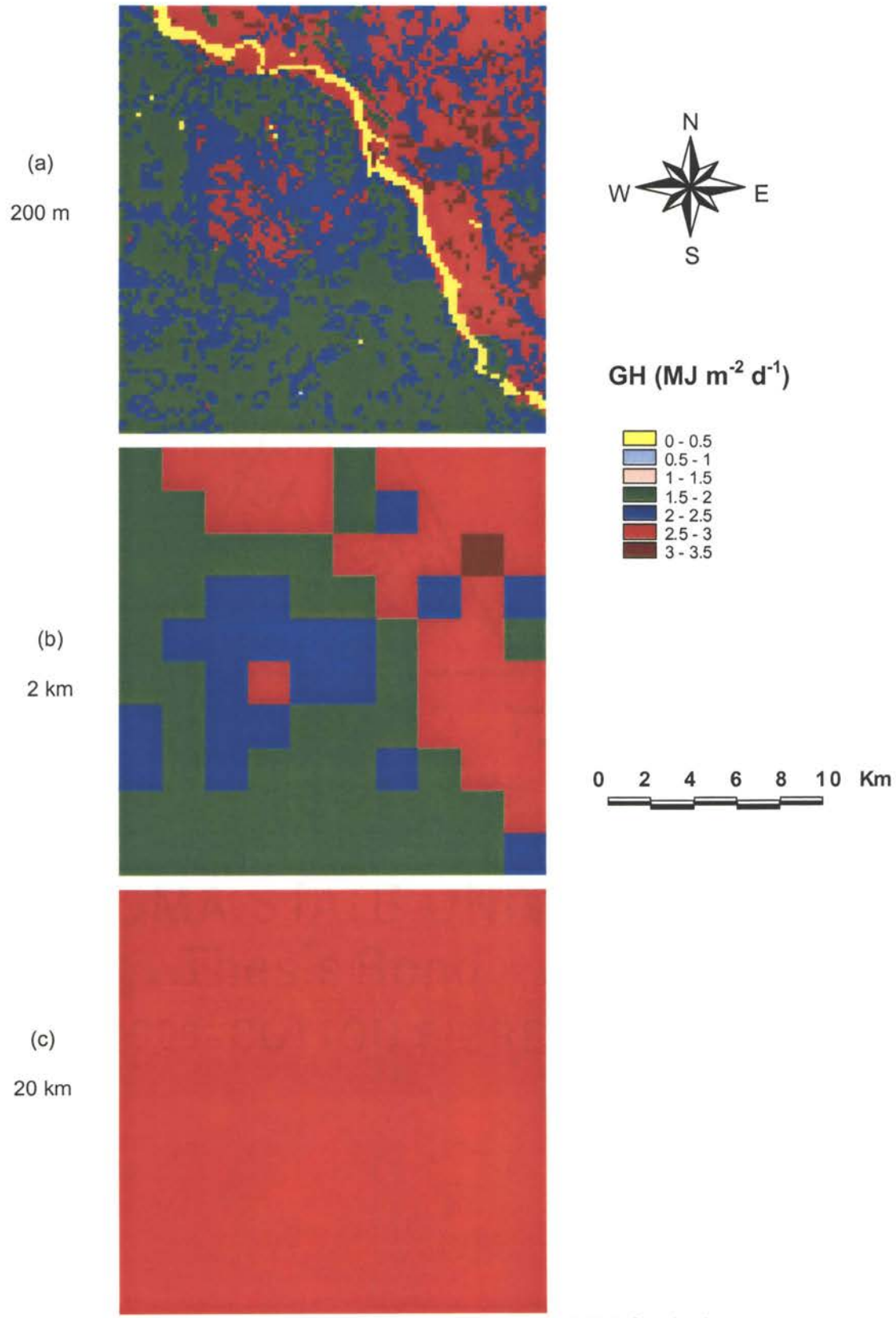

Figure 5-12. Scale comparisons of modeled ground heat flux (GH) for the heterogeneous area (Cell 21) for 18 June 97.

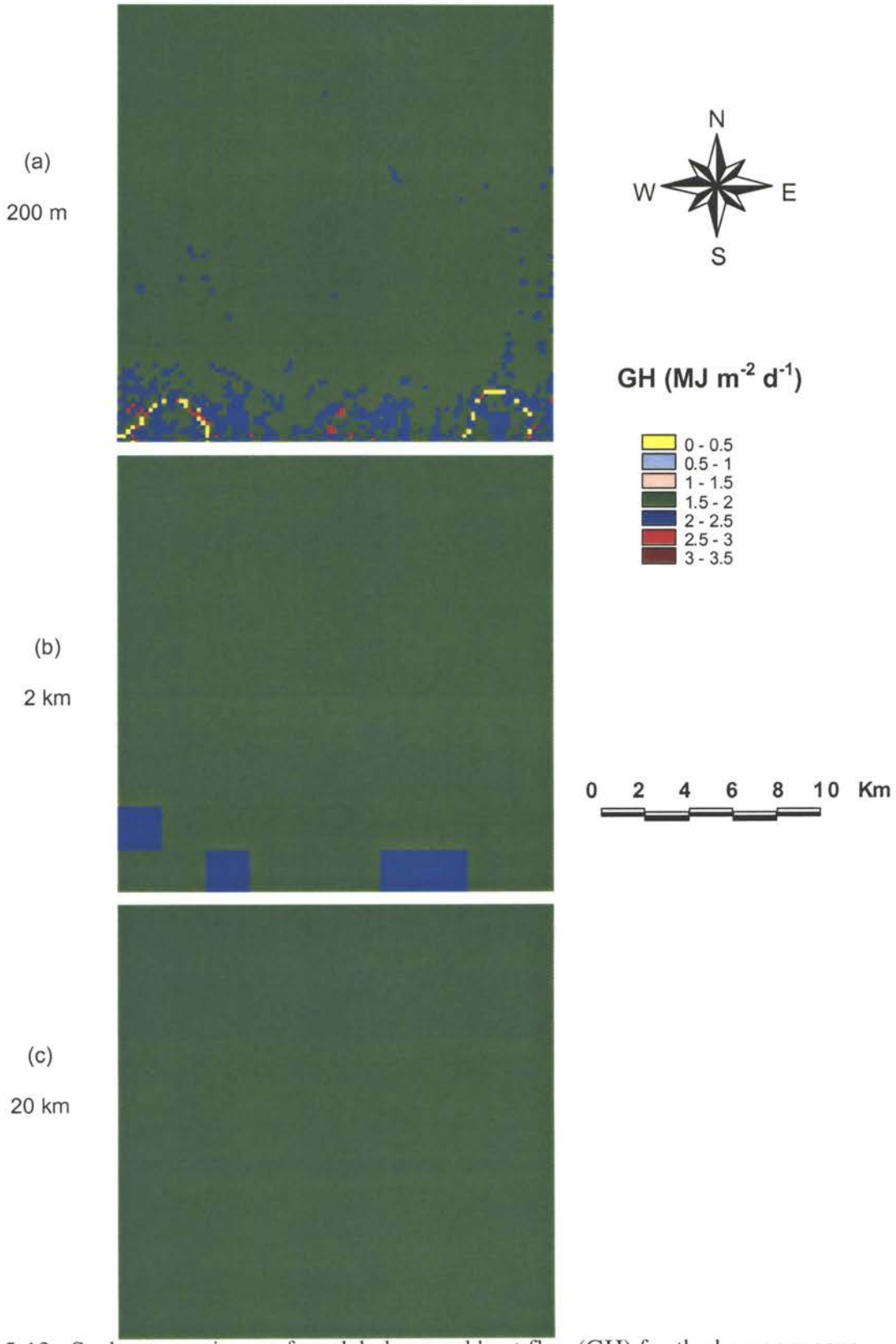

Figure 5-13. Scale comparisons of modeled ground heat flux (GH) for the homogeneous area (Cell 9) for 18 June 97.

magnitude of difference was similar to that for the latent heat flux estimation. Finally, the residual energy in the energy budget (the ground heat flux), as shown in Figure 5-14d, tended to be predicted slightly higher at the 20-km resolution than at the 200-m and 2-km resolution. Thus, scaling effects were manifested in the partitioning of the energy, especially latent and sensible heat. These differences became evident at the 20-km scale.

The modeling results for the homogeneous area (Cell 9) were studied in a similar way. Figure 5-15 represents the time series plots of simulated surface energy-balance components for all three scales. The results of the simulated net radiation for 200 m, 2 km and 20 km again agreed very well as shown in Figure 5-15a. Both latent heat flux (Figure 5-15b) and sensible heat flux (Figure 5-15c) showed slight deviations at the coarsest scale, i.e., 20 km, but overall the results for the three scales agreed closely. Ground heat flux matched very well at all three scales as shown in Figure 5-15d. As expected, the aggregation of input data had less impact on the model output when the variability in surface conditions was less.

Comparison of the bias in the model output for the three scales

This section discusses equal-value plots of all surface energy-balance components for the three possible scale intercomparisons (2 km vs. 200 m, 20 km vs. 200 m and 20 km vs. 2 km) (Figures (5-16)–(5-19)). This is, in fact, another approach to visualizing details of the scaling effects. Figure 5-16 (net radiation for the heterogeneous area) clearly shows that there was no bias in the estimated net radiation across the three scales. Figure 5-17 indicates that the estimation of latent heat flux at 200 m and 2 km agreed very well while there was a negative bias in the estimation as the scale moved to 20 km. Sensible heat flux predictions (Figure 5-18) again indicated a bias at the 20 km scale, but

in this case it was positive. The patterns for ground heat flux (Figure 5-19) were quite similar to those for sensible heat flux. Thus, energy partitioning at the 20-km scale became biased toward sensible heat and ground heat fluxes, and away from latent heat flux. This trend is consistent with the soil and land use at the 20-km scale for Cell 21. The sub-grid variability which was preserved at the 200-m and 2-km scales becomes non-existent when a single soil type (sand) and single vegetation type (grassland) are assigned for the entire domain of the 20-km resolution analysis. Obviously, the combination of sand and grassland resulted in reduced latent heat flux at 20 km when compared with the other two scales. More of the available energy was then partitioned into sensible and ground heat fluxes.

Figures (5-20)- (5-23) are similar equal-value plots for Cell 9. All of these plots confirm that, for the homogeneous cell, the scaling-up of input data had very little impact on modeled surface energy-balance components. In other words, the results for Cell 9, a homogeneous area in terms of soil and vegetation when compared with Cell 21, validated the hypothesis that aggregating the surface conditions such as soil and vegetation when there was less variability, would have less impact in the simulation of net radiation, latent, sensible and ground heat fluxes.

Deflections in the model output at 20-km scale

Appendix D (Figures (D-17)-(D-20)) contains the deflection plots of modeled surface energy-balance components for both Cell 21 and Cell 9. This is another way of looking at the scale dependency of the model output. Although this analysis was done using only three scales, the plots are somewhat analogous to a semivariogram analysis. For both Cell 21 and Cell 9, no significant deviation was observed among the three

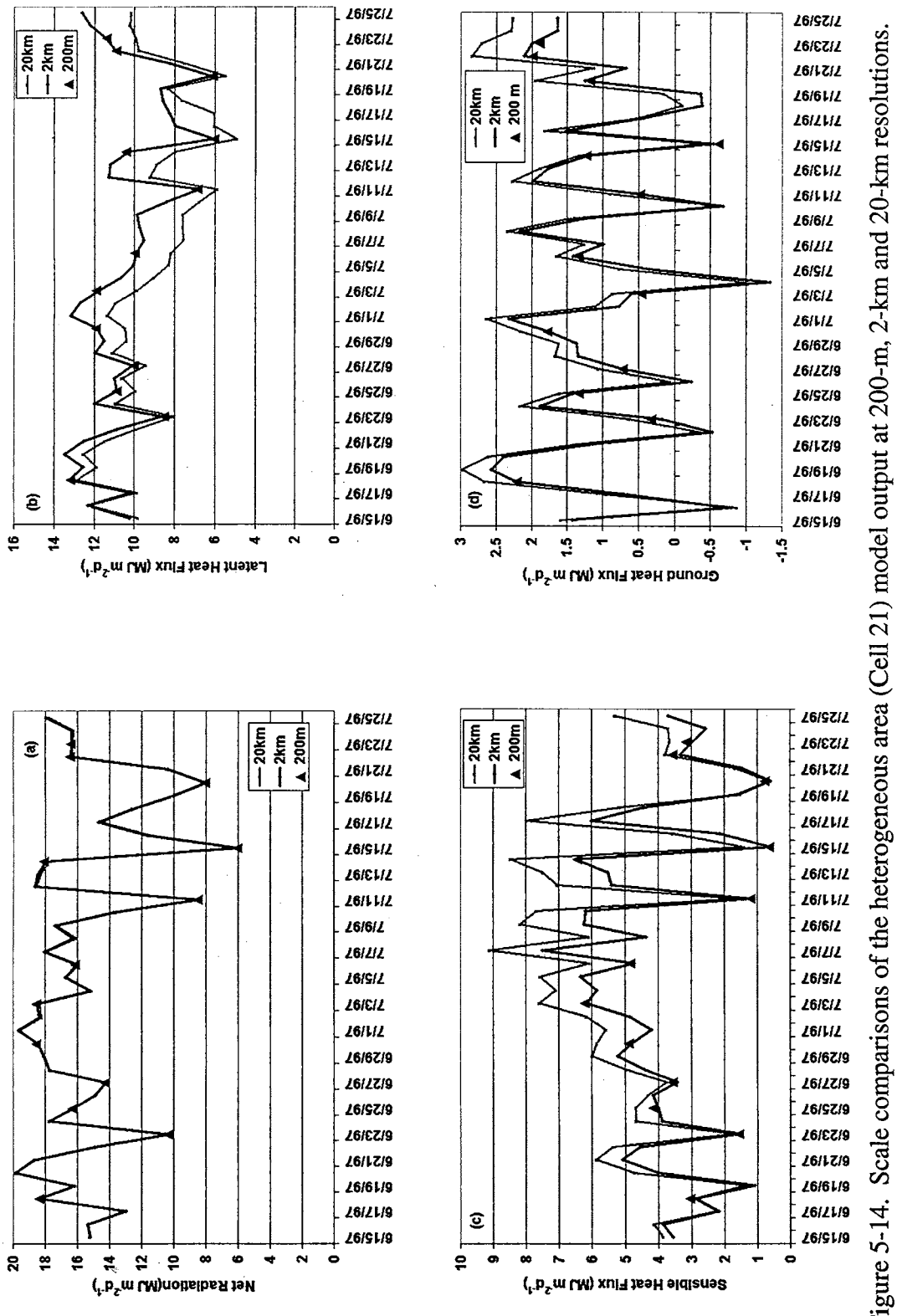

Figure 5-14. Scale comparisons of the heterogeneous area (Cell 21) model output at 200-m, 2-km and 20-km resolutions.

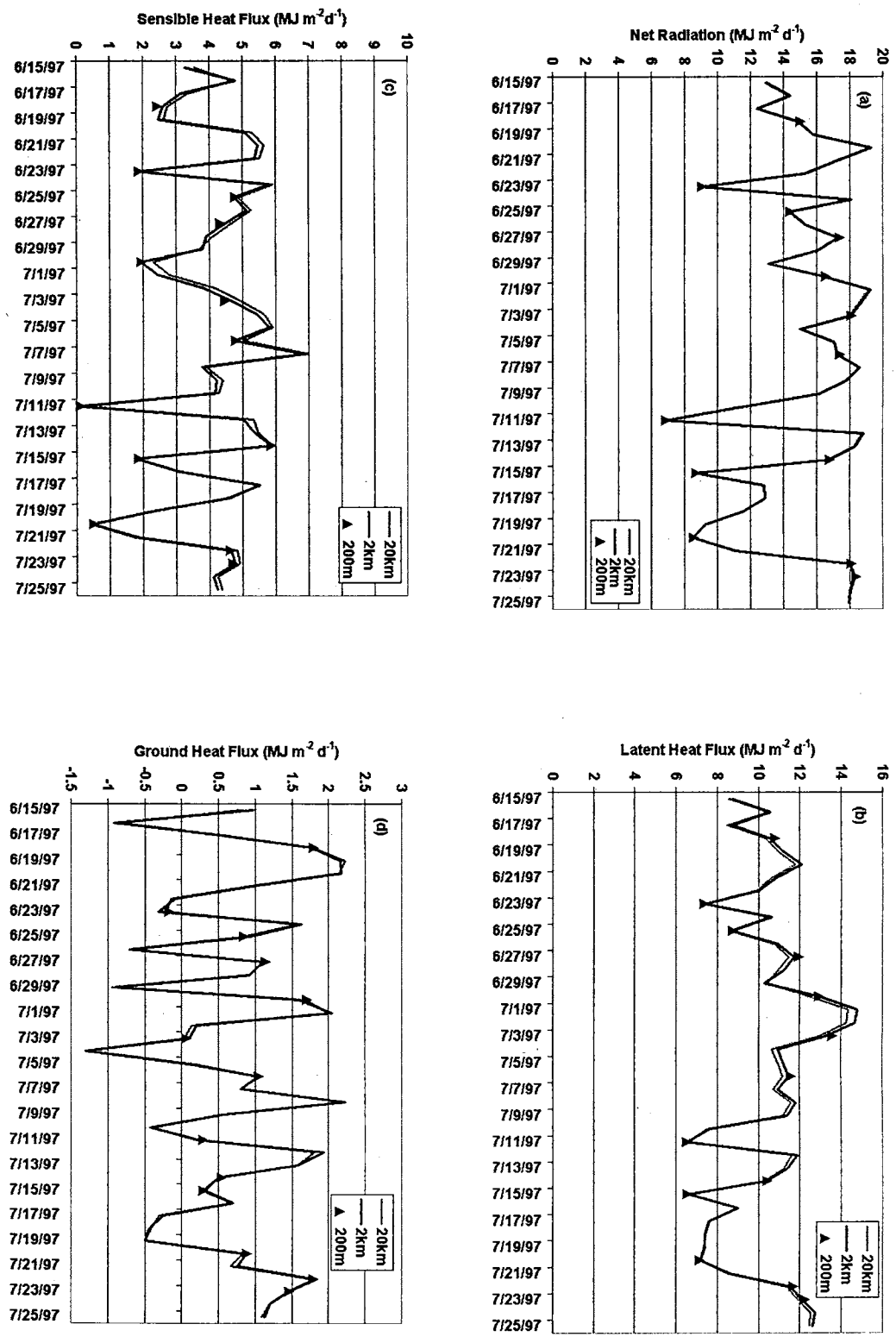

Figure 5-15. Scale comparisons of the homogeneous area (Cell 9)model output at 200-m, 2-km and 20-km resolutions.

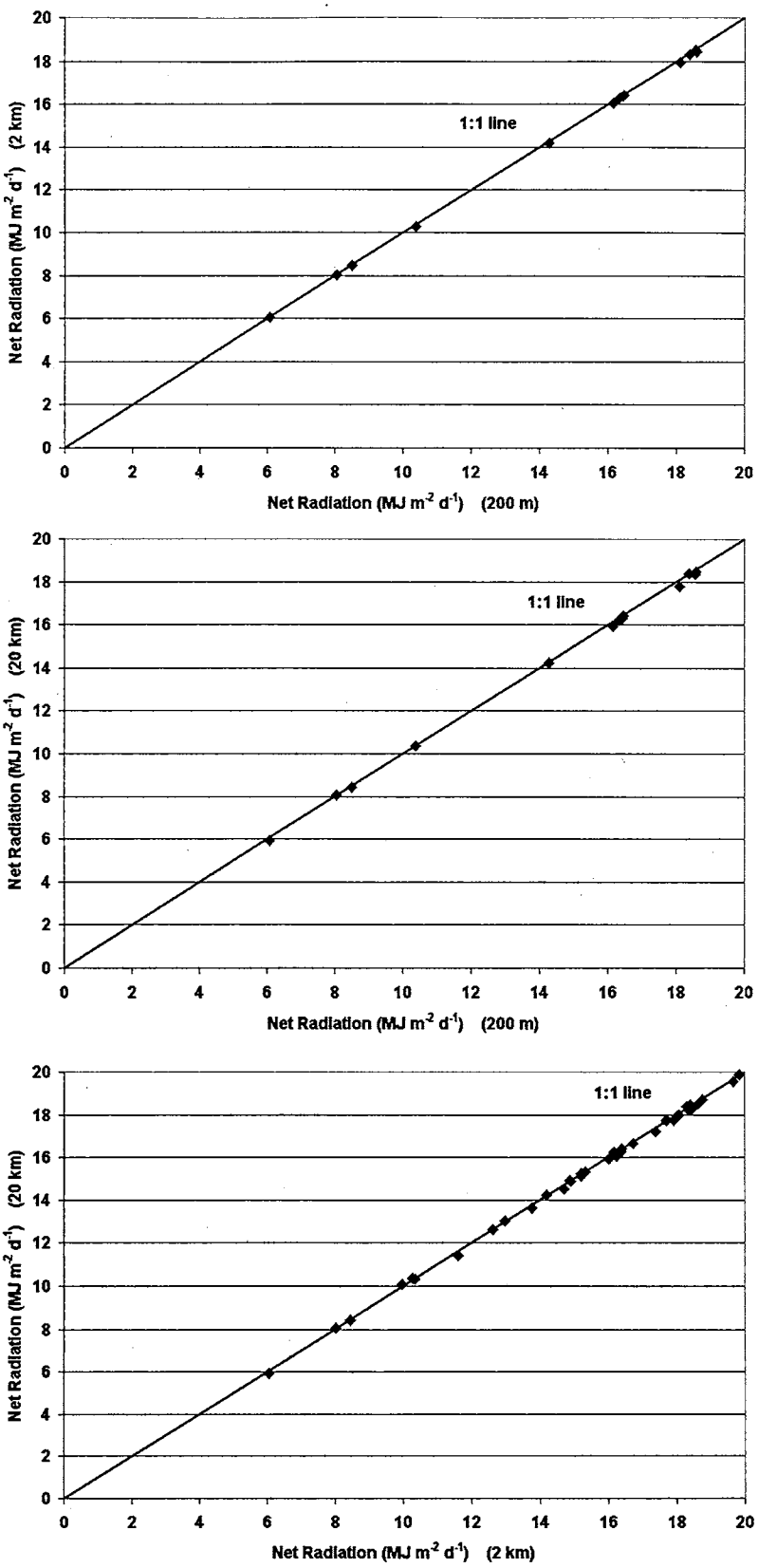

Figure 5-16. Equal-value plots of modeled net radiation for the three scales in the heterogeneous area (Cell 21).

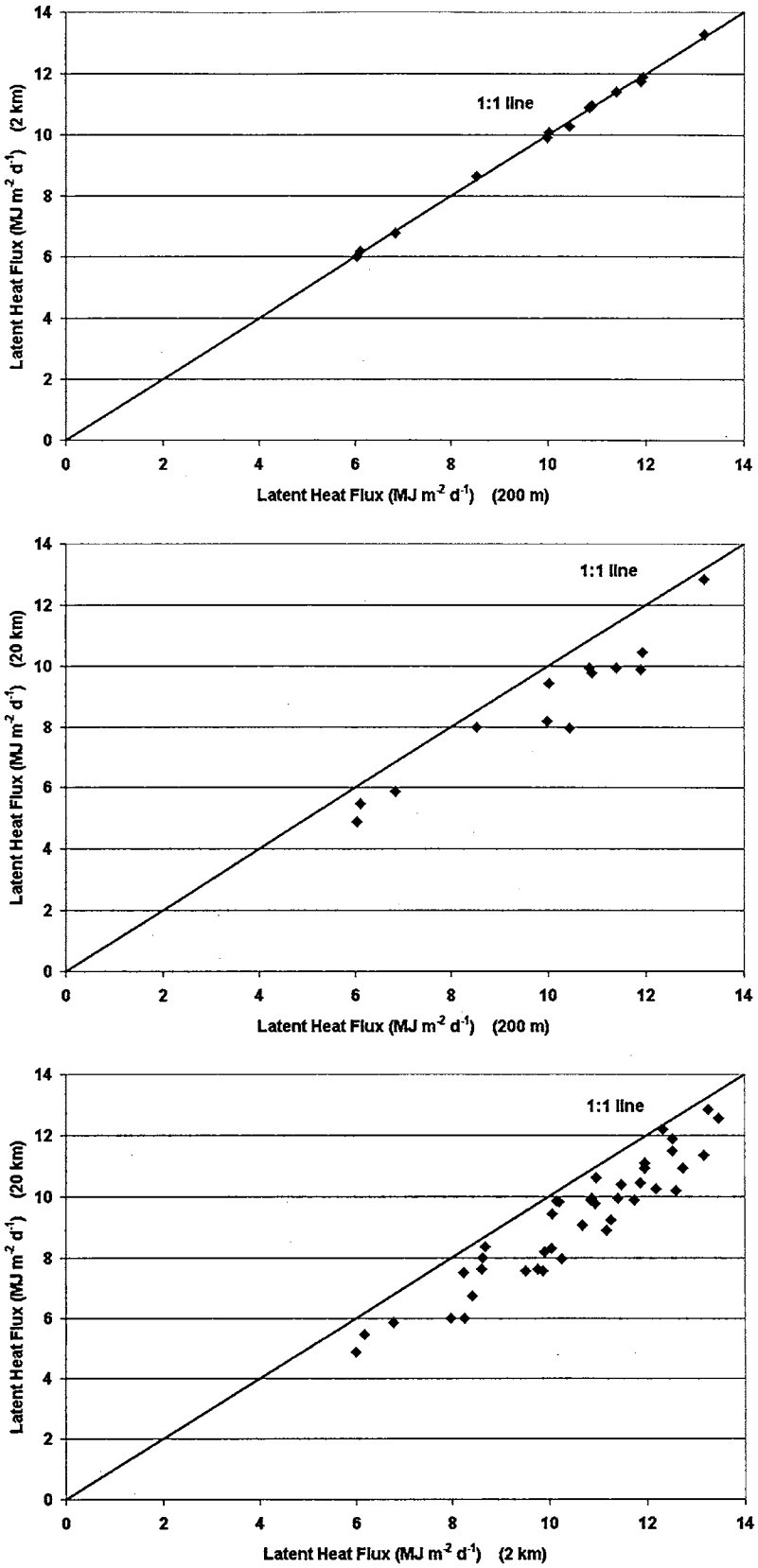

Figure 5-17. Equal-value plots of modeled latent heat flux for the three scales in the heterogeneous area (Cell 21).

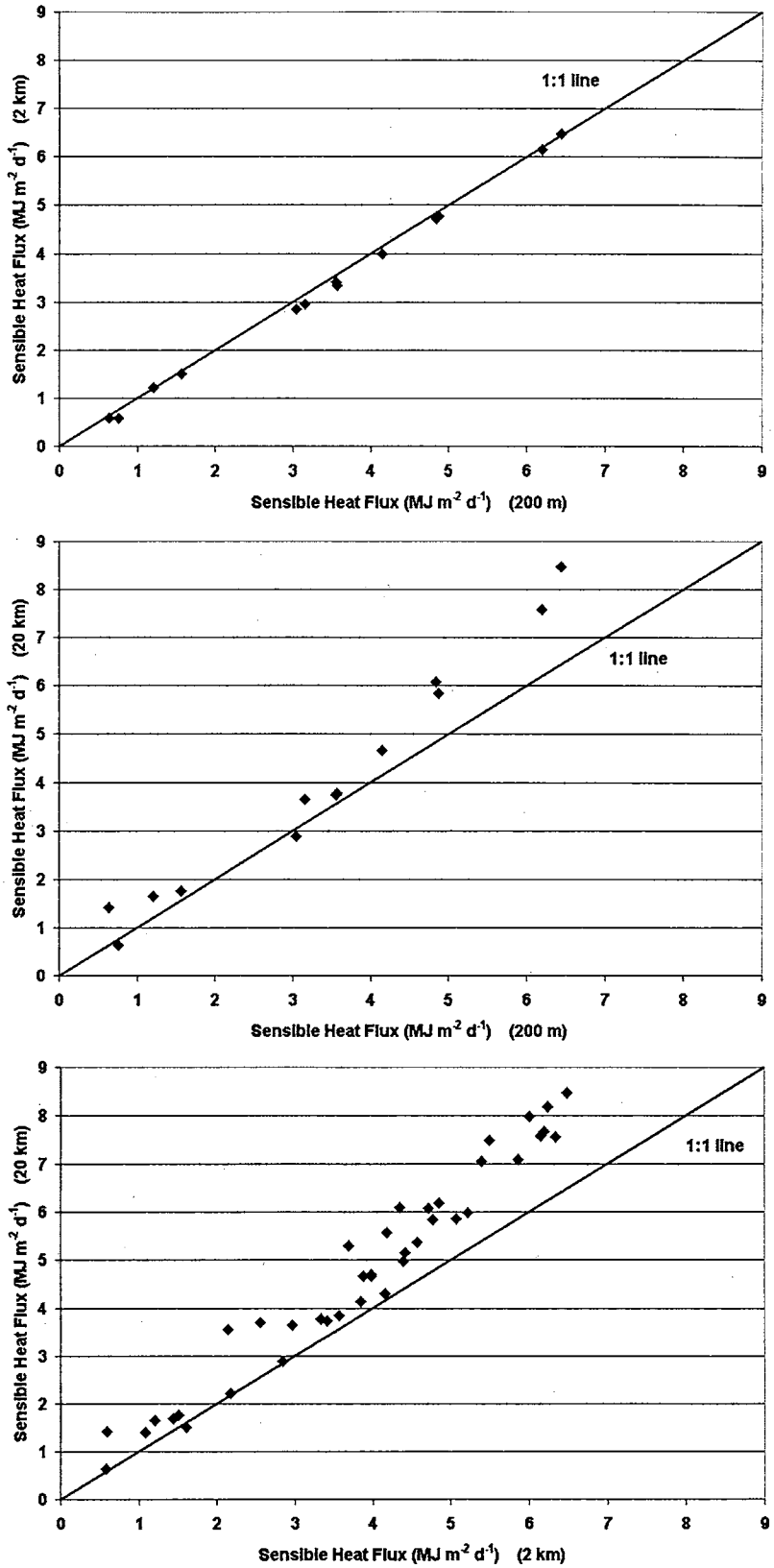

Figure 5-18. Equal-value plots of modeled sensible heat flux for the three scales in the heterogeneous area (Cell 21).

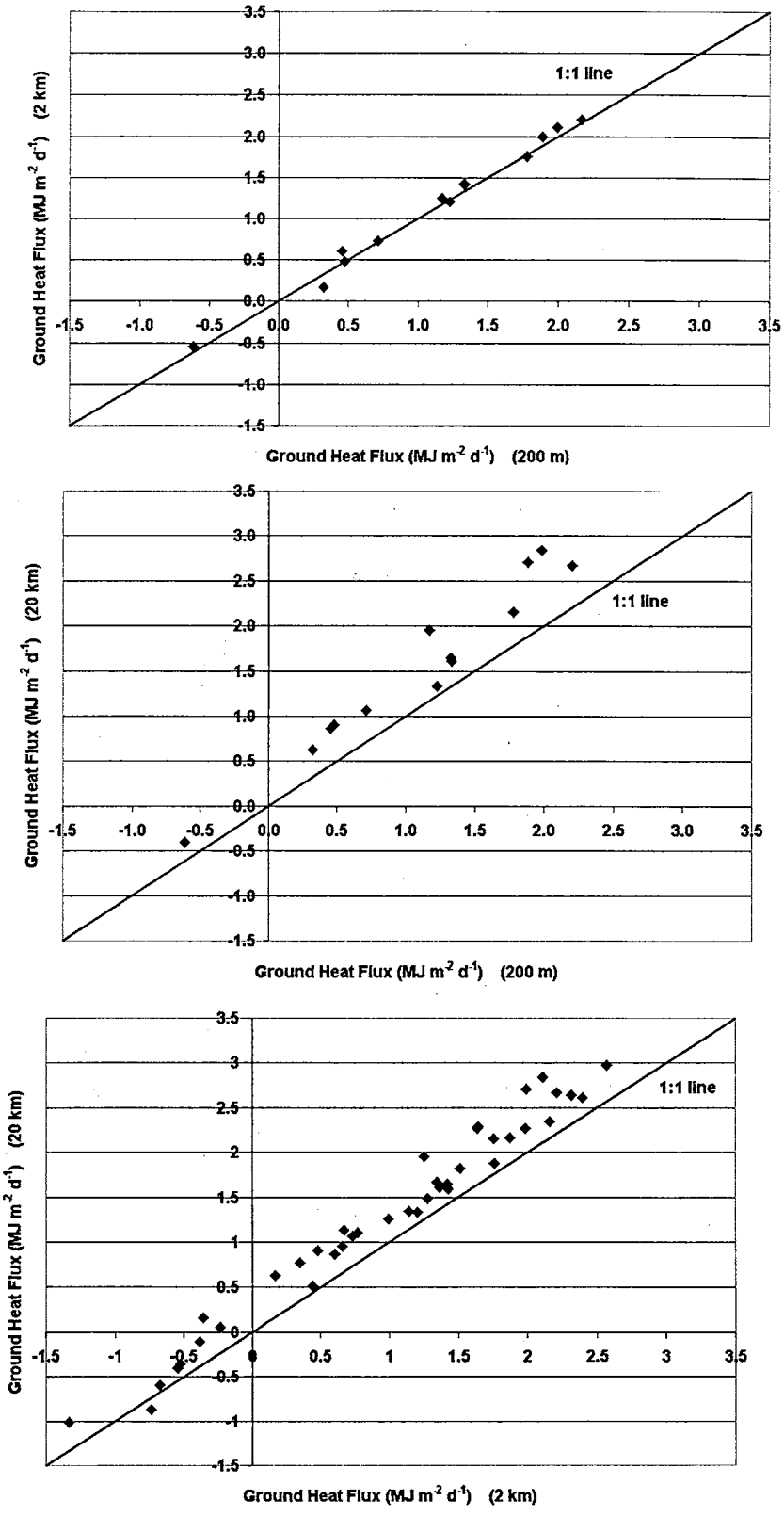

Figure 5-19. Equal-value plots of modeled ground heat flux for the three scales in the heterogeneous area (Cell 21).

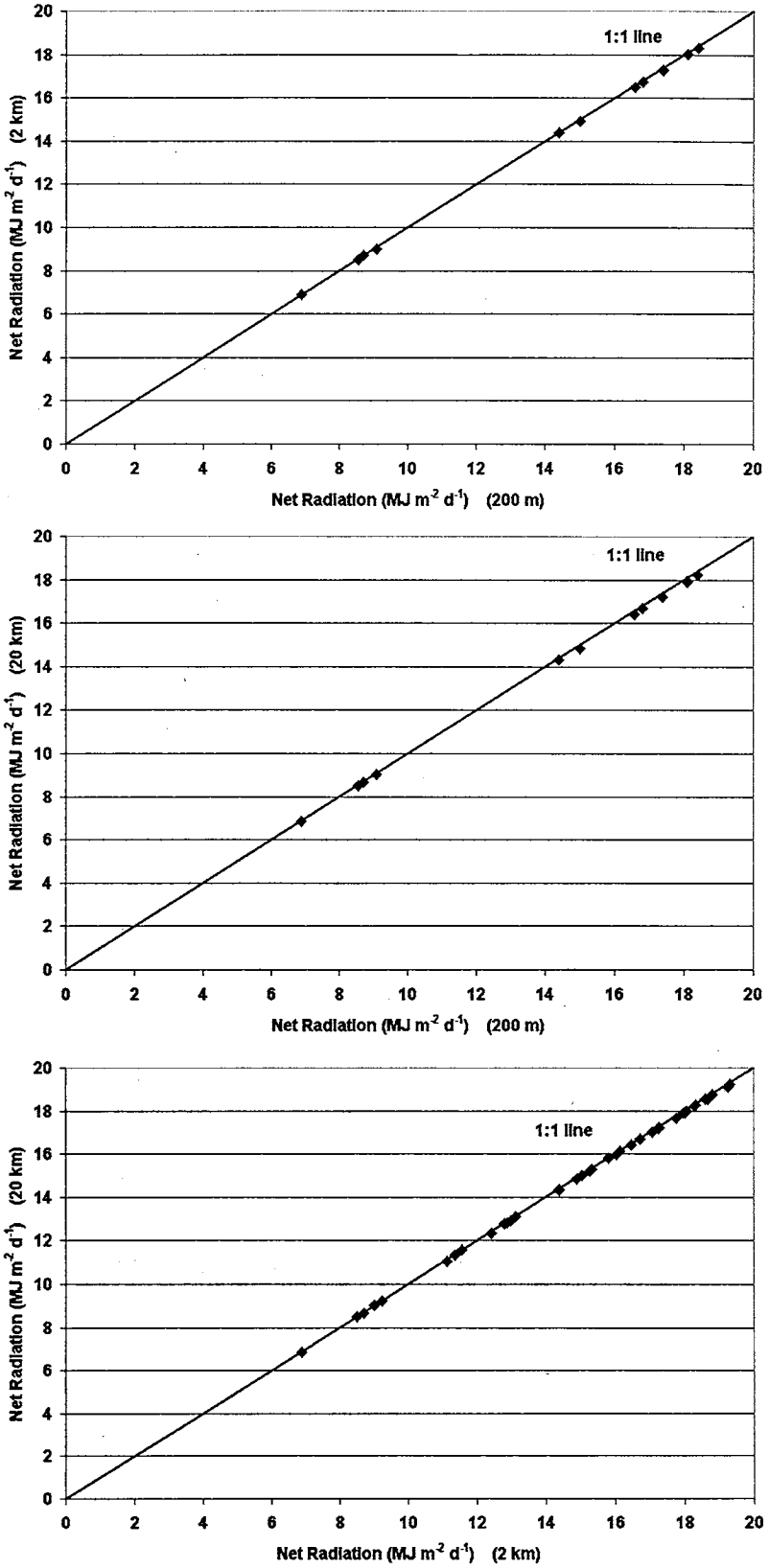

Figure 5-20. Equal-value plots of modeled net radiation for the three scales in the homogeneous area (Cell 9).

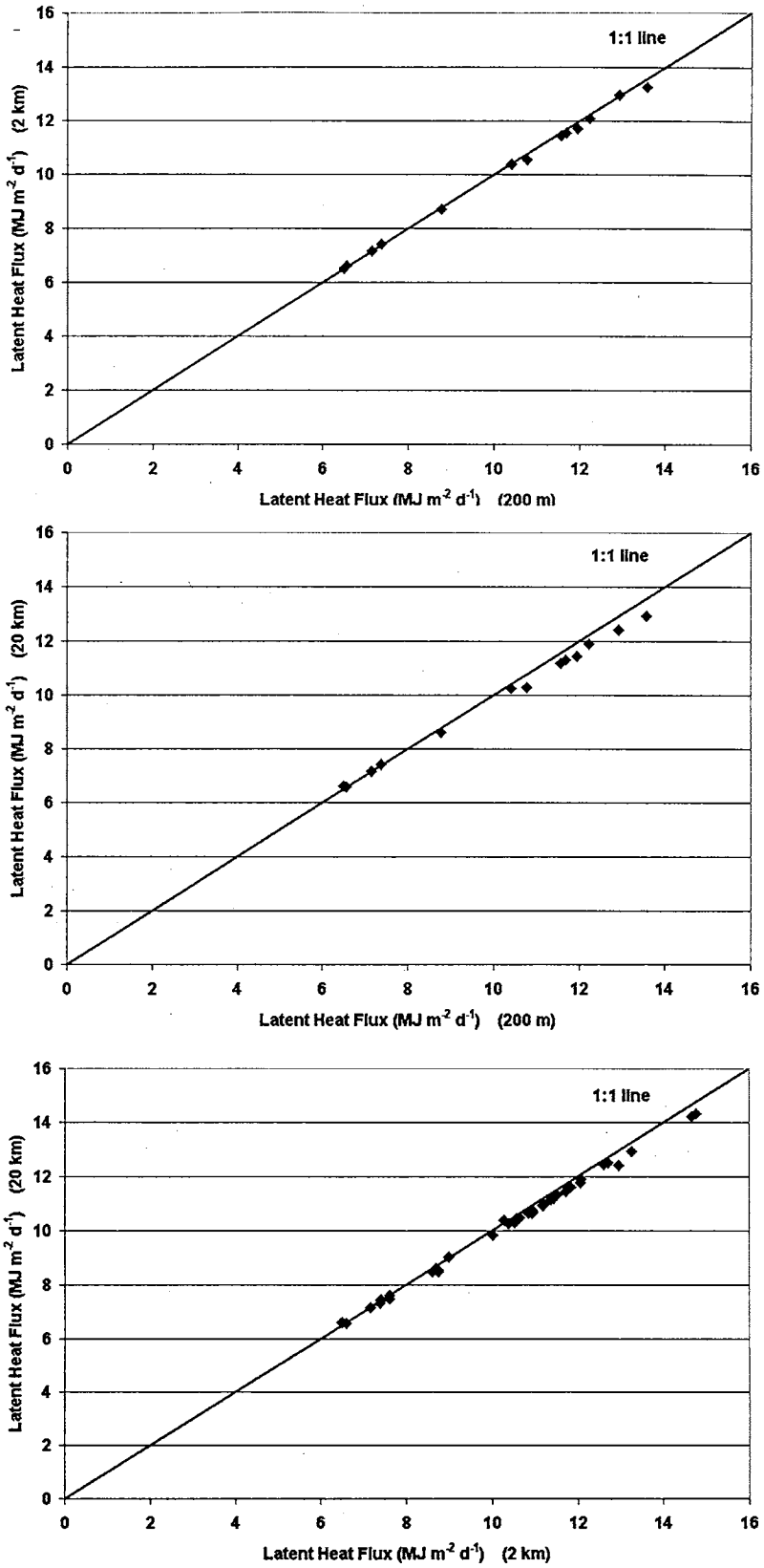

Figure 5-21. Equal-value plots of modeled latent heat flux for the three scales in the homogeneous area (Cell 9).

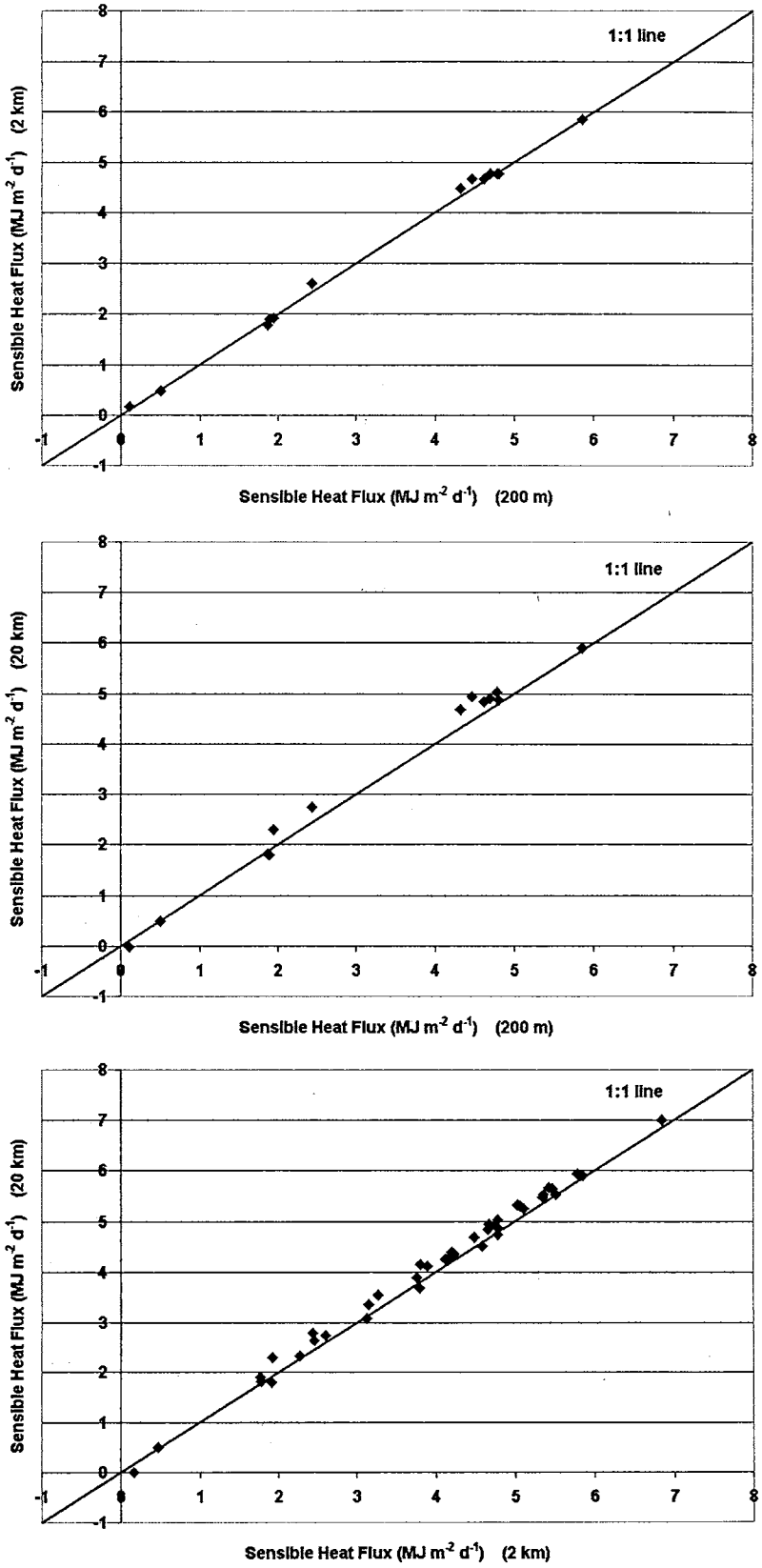

Figure 5-22. Equal-value plots of modeled sensible heat flux for the three scales in the homogeneous area (Cell 9).

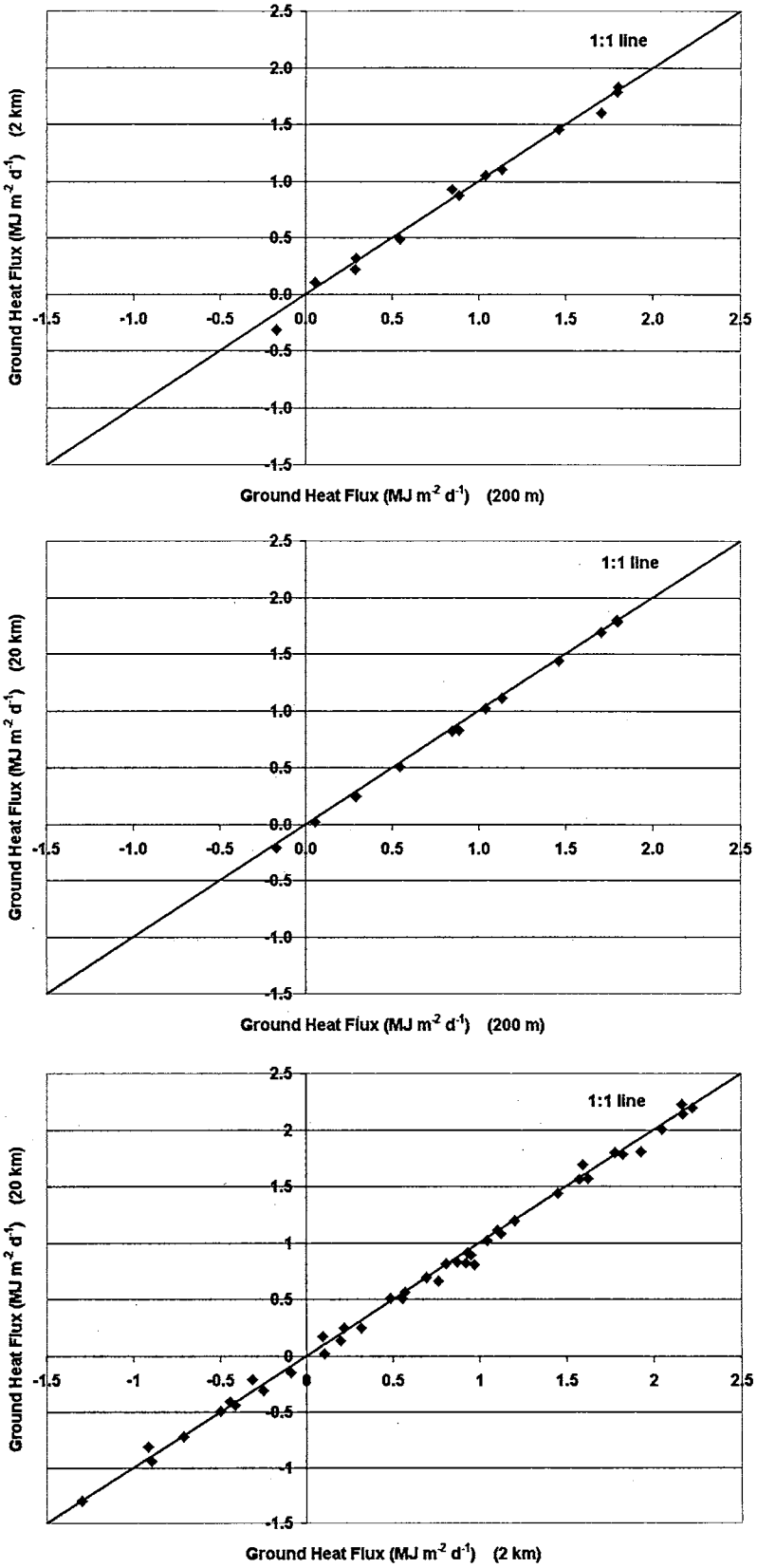

Figure 5-23. Equal-value plots of modeled ground heat flux for the three scales in the homogeneous area (Cell 9).

different scales for the estimation of net radiation, suggesting that its modeling scale is independent. The latent heat flux comparisons implied that this energy-balance component became scale dependent between 2 km and 20 km. This was predominantly observed in Cell 21. The sensible heat flux also exhibited scale dependency beyond 2 km, but only for Cell 21. Ground heat flux estimation showed a slight scale dependency for Cell 21.

Summary and Conclusions

Large scale modeling of land surface processes is made more complex by sub-grid scale heterogeneity. This research was focused on first identifying the variability in vegetation and soil for the SGP97 region, secondly on quantifying modeled surface energy-balance components at various spatial scales by aggregating certain input data, and finally on analyzing the scale effects at a sub-grid level for better understanding of land-atmosphere interactions. The well tested NOAH-OSU Land Surface Model (LSM) was used for this study.

Starting with a 280 km x 100 km area in central Oklahoma, a statistical procedure was followed to characterize the variability of soil and vegetation within 70 cells, each 20 km x 20 km. Cell 21 and Cell 9 were identified as the most heterogeneous and the most homogeneous cell, respectively. These areas were found to be heterogeneous and homogeneous in the context of the SGP97 region and not necessarily at regional or continental scales.

The scaling study was performed at 200 m, 2 km and 20 km using each of these two cells as a modeling domain. Soil and vegetation input data at the 200-m resolution

were aggregated to the coarser scales and model results were analyzed for the following surface energy-balance components: net radiation, latent, sensible and ground heat fluxes.

The sensitivity analysis of the model to the vegetation fraction derived based on area-averaged and dominant-landuse-based NDVI showed that there was essentially no difference in the model outputs.

The domain average net radiation, latent, sensible, and ground heat fluxes estimated for Cell 21 and Cell 9 at 200 m , 2 km and 20 km were compared individually. The results indicated that the heterogeneous cell exhibited considerable differences in latent and sensible heat fluxes when soil and vegetation data were aggregated from 200 m to 20 km. The variations in the estimations were insignificant between 200 m and 2 km, however. Though the magnitude of net radiation and thereby other fluxes tended to be less for cloudy days, differences in the estimation of latent and sensible heat fluxes were found to exist between the two coarser scales. Cell 9, the homogeneous cell, responded differently to the aggregation process. For both clear and cloudy days, it was evident that the quantification of domain average net radiation, latent, sensible and ground heat fluxes showed no significant difference at the 200-m, 2-km and 20- km resolutions.

The results suggested that the aggregation of spatially variable soil and vegetation inputs has a greater impact on the quantification of latent and sensible heat fluxes than net radiation and ground heat flux. The change in model response occurred between the 2-km and 20-km scales; model output for the 200-m scale was very similar to that for the 2-km scale. Not surprisingly, scaling-up of input had much less impact for relatively homogeneous land areas. Earlier studies implied that improper modeling of land surface processes would impact the land-atmosphere exchange processes. This investigation

supported the argument that sub-grid variability should be considered for proper quantification and partitioning of surface energy-balance components.

CHAPTER 6

SUMMARY, CONCLUSIONS AND RECOMMENDATIONS

Summary

Recent years have witnessed a dramatic increase in modeling of land-atmospheric interactions. Factors influencing this trend include improved model physics, enhanced computer capability, and the availability of high-resolution data sets including remotely sensed data for larger areas and longer times. Convergence of land surface hydrology with the atmospheric science discipline has energized scientific research efforts aimed at improved weather forecasting and better energy, agriculture and natural resource management.

Hydrological processes at the surface of the earth assume significance in the context of soil-vegetation-atmosphere exchange modeling. Land-atmosphere exchange processes include net radiation (R_n), latent heat (LH), sensible heat (SH) and ground heat (GH) fluxes. Their interdepedence and non-linear behavior provide challenges, especially when large scale modeling is attempted. Despite the recognition of the feedback between the land and the atmosphere, and its impact on physically based modeling, many issues are unresolved. Scaling is one of those key issues.

The main objective of this research was to examine the effects of different spatial scales of input data on modeled net radiation, latent, sensible and ground heat fluxes, and thereby understand the resolution needed for the realistic modeling of large-scale land

atmosphere interaction. For this investigation, the NOAH-OSU (Oregon State University) Land Surface Model (LSM) was chosen because it is used operationally in weather prediction and is widely recognized by the hydrology and atmospheric science research community. Field measurements were available from the Oklahoma Mesonet and the accompanying Oklahoma Atmospheric Surface-layer Instrumentation (OASIS) project. There are 10 OASIS "Super sites" equipped with instrumentation for measuring surface energy-balance components (R_n, LH, SH and GH).

The LSM needed downwelling longwave radiation as one of its forcing inputs, and it is rarely measured. There are several downwelling longwave radiation models available and no single technique has emerged as the most appropriate one to use. This led to developing a methodology for estimating downwelling longwave radiation during nighttime and daytime conditions and clear and cloudy sky conditions, as a function of vapor pressure and air temperature.

Using a simple linear regression procedure, Brutsaert's model for incoming longwave radiation (LW_{in}) was calibrated for four sites (ALVA, FORA, GRAN and IDAB) individually. The resulting coefficients ranged in value from 1.30 to 1.32, with an average of 1.31. The resulting expression was

$$LW_{in} = 1.31\left(\frac{10e_d}{T}\right)^{1/7}\sigma T^4 \qquad (6\text{-}1)$$

where T is the air temperature (K), e_d is the vapor pressure (kPa) at screen height, σ is the Stefan- Boltzmann constant (5.675×10^{-8} J m^{-2} K^{-4} s^{-1}) and LW_{in} has units of Wm^{-2}. The model was tested for five independent sites (BESS, BURN, MARE, NORM and STIG). These validation sites represent different regions of the state of Oklahoma and fall under

different climatic regimes. The calibrated model predictions consistently agreed well with the measurements, suggesting that the scheme could be used for any site in this region during daytime and nighttime as well as clear and cloudy sky conditions.

In order to employ the uncoupled LSM for large-scale simulations, it was first prudent to assess the performance of the model at point sites. So, validation of the LSM using data from seven OASIS sites (ALVA, BOIS, BURN, FORA, GRAN, MARE and NORM) was performed. The duration of this validation period was one year (June 1999 through May 2000). The 5-minute average observations of surface energy-balance components were further averaged over one-hour periods. The field data set was filtered for good energy-balance closure using the criterion that the daily (hourly) sum (R_n-LH-SH-GH) was within the range of -10 W m^{-2} to $+10$ W m^{-2}. Model simulations were performed with an hourly time step.

The sensitivity of the model to vegetation fraction was analyzed. Vegetation fractions were estimated from Advanced Very High Resolution Radiometer (AVHRR) Normalized Difference Vegetation Index (NDVI) data, using two different methods, Gutman-Ignatov (G-I) and Carlson-Ripley (C-R). At BOIS and BURN, the computed vegetation fractions from these two schemes showed significant differences, with the G-I method estimating lower values than the C-R method. The simulated surface energy-balance components, especially latent and sensible heat fluxes using the two approaches showed some differences. This suggested that the model was sensitive to the variations in vegetation fraction. However, further analysis was carried out using only the G-I vegetation fraction scheme.

Each of the four modeled surface energy-balance components was analyzed for both daily and hourly time scales. The overall results showed that the model predicted well for the long period of time. The energy balance in the LSM is formulated in a such a way that the excess net radiation is redistributed into latent, sensible and ground heat fluxes:

$$R_n = LH + SH + GH \tag{6-2}$$

The seven-site average results indicated that the model tended to slightly overestimate R_n . Most of this excess radiant energy was assigned to LH as opposed to SH. This is because the LSM first computed potential evaporation and then actual evaporation, which was used to determine the skin temperature at equilibrium state, and subsequently SH was computed. As the LSM computed LH first, it tended to distribute excess energy to that term. The model showed a positive bias in LH estimation and a slight negative bias in SH estimation. The trends observed in hourly and daily estimates for all energy-balance components were similar except for GH, which had a slight positive bias for the daily analysis.

Following the validation analysis, the effects of scaling on modeled surface energy-balance components were examined. The Southern Great Plains 1997 (SGP97) Hydrology Experiment area was chosen for this study.

First, a 280 km x 100 km area in central Oklahoma was divided into 70 cells, each 20 km x 20 km. A statistical procedure was followed to characterize the variability of soil and vegetation in these cells. Cell 21 and Cell 9 were identified as the most heterogeneous and the most homogeneous cell, respectively. However, the

heterogeneity/homogeneity in this study region may not reflect that found over larger areas.

The scaling analysis was carried out at 200-m, 2-km and 20-km resolutions using each of the two cells as a modeling domain. Soil and vegetation input data at the high spatial resolution (200 m) were aggregated to obtain the data sets for the 2-km and 20-km resolutions. In order to study the effect of area-averaged vs. dominant-landuse-based vegetation on the model output at 2 km and 20 km, simulations were performed using vegetation fraction derived from NDVI by these two methods. There was essentially no difference between the two vegetation fraction methods in the model estimation of R_n, LH, SH and GH.

The simulations for the scaling analysis were carried out with proper initialization of the model and a reasonable 'spin-up' period to remove any instability caused in the beginning of the simulation. The SGP97 study period was between 18 June and 25 July 1997. For Cell 21, the heterogeneous cell, there was no appreciable difference between the model simulations at the 200-m and 2-km resolutions but there were differences between the 2-km and 20-km resolutions, especially for LH and SH. Similar trends were evident for both clear and cloudy days. On the contrary and as expected, Cell 9, the most homogeneous cell, showed very little difference in the model output across all three resolutions.

Conclusions

Investigations of available downwelling longwave radiation schemes suggested that a simple technique was needed to estimate downwelling longwave radiation for input to the LSM. This technique would need to rely on readily available data, and should

perform well under both daytime and nighttime and clear and cloudy conditions. A simple approach based on the Brutsaert equation and using near-surface vapor pressure and air temperature was developed and presented. The predictions by this method showed good agreement with field measurements and paved the way for its application in the validation and scaling studies to follow.

As verification of the performance of the NOAH-OSU LSM for Oklahoma conditions, model testing was done with the measurements from OASIS sites. Hourly simulation results for a one-year period were compared with the observations. It was found that the model slightly over predicted net radiation and this excess energy was directed to latent heat flux as opposed to sensible heat flux. Ground heat flux estimations were reasonably close to the field observations.

The effects of three different scales of input data on modeled net radiation, latent, sensible and ground heat fluxes were analyzed for the heterogeneous area (Cell 21) and the homogeneous area (Cell 9). The aggregation process undertaken for these two cells resulted in fewer classes as the scale increased from 200 m to 2 km and a single class at the 20-km resolution. The comparison of domain average net radiation, latent, sensible and ground heat fluxes estimated for Cell 21 across the three scales showed that there was good agreement between the 200-m and 2-km resolution model output. However, the simulation results at the 20-km resolution showed appreciable differences for all four components, especially latent and sensible heat fluxes for both clear and cloudy days. The results for Cell 9 exhibited the expected trend. For all three scales, the estimated net radiation, latent, sensible and ground heat fluxes were closely matched across all three scales.

The results suggested that the aggregation of spatially variable soil and vegetation inputs has a greater impact on the quantification of surface energy-balance components and partitioning of latent, sensible heat fluxes. It was confirmed that the effects of scaling-up of input data on model estimates are more pronounced for heterogeneous areas than for homogeneous areas.

Recommendations

The objectives of this dissertation were accomplished as described in previous chapters and summarized and concluded in the earlier sections of this chapter. However, in continuing to address some of these issues, improvements could be made in the following areas:

1. Although the soil hydrology model conceptually encompasses four soil layers, all of the layers are considered to have the same soil texture in the current version of the model formulation. This is considered to be an important limitation as the soil layers could have different soil textures and hence different properties. Thus, consideration of the individual textures for each layer is needed, should it be supported by the available data.
2. In order to make the model more specific, it is necessary to include a greater number of vegetation classes with reasonable parameters for each of them, and some effort should be spent in testing those parameters as well.
3. The spatial variability in atmospheric forcing should also be considered, especially for precipitation. Differences in the partitioning of latent and sensible heat fluxes would be amplified by variability in precipitation and its impact on soil moisture.

Radar estimates of precipitation could provide a vehicle for incorporating this variability into the modeling.

4. Model outputs were viewed using a Geographic Information System (Arc/Info). However, a real-time user-friendly graphical interface could simplify the display of the model output and increase the efficiency of modeling studies.

REFERENCES

Aase, J.K., and Idso, S.B. (1978). A comparison of two formula types for calculating long-wave radiation from atmosphere. Water Resources Research, 14, 623-625.

Anderson, E.R. (1954). Energy-budget studies, Water-loss investigations: Lake Hefner studies. U.S. Geological Survey Professional Paper 269, 71-119.

Avissar, R. (1992). Conceptual aspects of a statistical dynamical approach to represent landscape subgrid-scale heterogeneities in atmospheric models. Journal of Geophysical Research, 97(D3), 2729-2742.

Avissar, R. (1992). Conceptual aspects of a statistical dynamical approach to represent landscape subgrid-scale heterogeneities in atmospheric models. Journal of Geophysical Research, 97(D3), 2729-2742.

Benjamin, S.G., and Carlson, T.N. (1986). Some effects of surface heating and topography on the regional severe storm environment, I, Three-dimensional simulations, Monthly Weather Review, 114, 307-329.

Betts, A.K., Ball, J.H., Beljaars, A.C.M., Miller, M.J., and Viterbo, P. (1996). The land-surface-atmosphere interaction: a review based on observational and global modelling perspectives. Journal of Geophysical Research, 101, 7209-7225.

Betts, A.K., Chen, F., Mitchell, K., and Janjic, Z.I. (1997). Assessment of the land surface and boundary layer models in two operational versions of the NCEP Eta model using FIFE data. Monthly Weather Review, 125, 2896-2916.

Bloschl. G and Sivapalan, M. (1995). Scale issues in hydrological modelling: A review. In: Scale Issues in Hydrological Modelling. (eds.) J.D. Kalma and M. Sivapalan. John Wiley & Sons Ltd., England, 9-48.

Braud, I. (1998). Spatial variability of surface properties and estimation of surface fluxes of a savannah. Agricultural and Forest Meteorology, 89, 15-44.

Brock, F.V., Crawford, K.C., Elliott, R.L., Cuperus, G.W., Stadler, S.J., Johnson, H.L., and Eilts, M.D. (1995). The Oklahoma Mesonet: A technical overview. Journal of Atmospheric Ocean.Technology, 12(1), 5-19.

Brotzge, J.A. (2000). Closure of the surface energy budget. Ph.D. Dissertation. Univ. of Oklahoma, Norman, OK, 208pp.

Brotzge, J.A., Richardson, S.J., Crawford, K.C., Horst, T.W., Brock, F.V., Humes, K.S., Sorbjan, Z., and Elliott, R.L. (1999). The Oklahoma Atmospheric Surface-layer Instrumentation System (OASIS) Project. Thirteenth Conf. on Boundary-Layer Turb., Am. Meteorol. Soc., Dallas, TX, Jan.10-15.

Brunt, D. (1932). Notes on radiation in the atmosphere. Quart. J. Roy. Meteor. Soc., 58, 389-418.

Brutsaert, W. (1975). On a derivable formula for long-wave radiation from clear skies. Water Resources Research, 11(5), 742-744.

Carlson, T.N., and Ripley, D.A. (1997). On the relation between NDVI, fractional vegetation cover and leaf area index. Remote Sensing of Environment, 62, 241-252.

Chen, D., and Brutsaert, W. (1995). Diagnostics of land surface spatial variability and water vapor flux. Water Resources Research, 100(D12), 25,595-25,606.

Chen, F., and Dudhia, J. (2001). Coupling an advanced land-surface/hydrology model with the Penn State-NCAR MM5 modeling system. Part I: Model implementation and sensitivity. Monthly Weather Review, 129, 569-585.

Chen, F., and Mitchell, K. (1999). Using the GEWEX/ISLSCP forcing data to simulate global soil moisture fields and hydrological cycle for 1987-1988. Journal of the Meteorological Society of Japan , 77, 1B, 167-182.

Chen, F., Janjic, Z.I., and Mitchell, K. (1997). Impact of atmospheric surface-layer parameterization in the new land surface scheme of the NCEP mesoscale Eta numerical model. Boundary –Layer Meteorology, 85, 391-421.

Chen, F., Mitchell, K., Schaake, J., Xue, Y., Pan, H., Koren, V., Duan, Q.Y., Ek, M., and Betts, A. (1996). Modeling of land surface evaporation by four schemes and comparison with FIFE observations, Journal of Geophysical Research, 101, 7251-7268.

Chen, Z.-Q., Govindaraju, R.S., and Kavvas, M.L. (1994a). Spatial averaging of unsaturated flow equations under infiltration conditions over areally heterogeneous fields: 1. development of models. Water Resources Research, 30 (2), 523-533.

Chen, Z.-Q., Govindaraju, R.S., and Kavvas, M.L. (1994b). Spatial averaging of unsaturated flow equations under infiltration conditions over areally heterogeneous fields: 2. numerical simulations. Water Resources Research, 30 (2), 535-548.

Choudhury, B.J., Ahmed, N.U., Idso, S.B., Reginato, R.J., and Daughtry, C.S.T. (1994). Relations between evaporation coefficients and vegetation indices studied by model simulations. Remote Sensing of Environment, 50,1-17.

Cosby, B.J., Hornberger, G.M, Clapp, R.B., and Ginn, T. R. (1984). A statistical exploration of the relationships of soil moisture characteristics to the physical properties of soils. Water Resources Research, 20, 682-690.

Crawford, T.M., and Duchon, C.E. (1999). An improved parameterization for estimating effective atmospheric emissivity for use in calculating daytime downwelling longwave radiation. Journal of Applied Meteorology, 38, 474-480.

Cuenca, R.H., Ek, M., and Mahrt, L. (1996). Impact of soil water property parameterization on atmospheric boundary-layer simulation. Journal of Geophysical Research, 101, 7269-7277.

Culf, A.D., and Gash, J.H.C. (1993). Longwave radiation from clear skies in Niger: A comparison of observations with simple formulas. Journal of Applied Meteorology, 32, 539-547.

DeCoursey, D.G. (1996). Hydrological, climatological and ecological systems scaling: A review of selected literature and comments. Interim Progress Report. USDA-ARS-NPA. Fort Collins, CO.

Diak, G.R., Bland, W.L., Mecikalski, J.R., and Anderson, M.C. (2000). Satellite-based estimates of longwave radiation for agricultural applications. Agricultural and Forest Meteorology, 103, 349-355.

Dickinson, R.E., Henderson-Sellers, A., and Kennedy, P.J. (1993). Biosphere-Atmosphere Transfer Scheme (BATS) version 1e as coupled to the NCAR Community Climate Model. NCAR Technical Note. NCAR/TN-387+STR.

Dirmeyer, P.A. (1999). Assessing GCM sensitivity to soil wetness using GSWP data. Journal of the Meteorological Society of Japan, 77 (1B), 367-385.

Dirmeyer, P.A., Zeng, F.J., Ducharne, A., Morril, J.C., Koster, R.D. (2000). The sensitivity of surface fluxes to soil water content in three land surface schemes. Journal of Hydrometeorology, 1, 121-134.

Dooge, J.C.I. (1982). Parameterization of hydrologic processes. In: Land Surface Processes in Atmospheric General Circulation Models. (eds.) P.S. Eagleson. Cambridge University Press, London, 243-288.

Dooge, J.C.I. (1986). Looking for hydrologic laws. Water Resources Research, 22(9), 46S-58S.

Eagleson, P.S. (1978). Climate, soil and vegetation. 1. Introduction to water balance dynamics. Water Resources Research,14(5), 705-712.

Eagleson, P.S. (1986). The emergence of global-scale hydrology. Water Resources Research , 22(9), 6S-14S.

Ek, M., and Mahrt, L. (1991). OSU 1-D PBL model user's guide. Department of Atmospheric Sciences, Oregon State University, Corvallis, Oregon 97331-2209.

Elliott, R.L., Brock, F.V., Stone, M.L. and Harp, S.L. (1994). Configuration decisions for an automated weather station network. Applied Engineering in Agriculture, 10(1), 45-51.

Entekhabi, D., and Eagleson, P.S.(1989). Land surface hydrology parameterization for atmospheric general circulation models including subgrid scale spatial variability. Journal of Climate, 2,816-831.

Entekhabi, D., Rodriguez-Iturbe, I., Castelli, F. (1996). Mutual interaction of soil moisture state and atmospheric processes. Journal of Hydrology, 184, 3-17.

Esbensen, S.K., and Kushnir, Y. (1981). The heat budget of the global oceans: An atlas based on surface marine observations. *Rep. 29*, Clim. Res. Inst., Org. State Univ., Corvallis.

Famiglietti, J.S. and Wood, E.F.(1994). Multiscale modeling of spatially variable water and energy balance processes. Water Resources Research, 30(11), 3061-3078.

Famiglietti, J.S., Devereaux, J.A., Laymon, C.A., Tsegaye, T., Houser, P.R., Jackson, T.J., Graham, S.T., Rodell, M. and Van Oevelen, P.J. (1999). Ground-based investigation of soil moisture variability within remote sensing footprints during the Southern Great Plains 1997 (SGP97) Hydrology Experiment. Water Resources Research , 35(6), 1839-1851.

Fennessy, M.J., and Shukla, J. (1999). Impact of initial soil wetness on seasonal atmospheric prediction. Journal of Climate, 12, 3167-3180.

Francis, J.A. (1997). A method to derive downwelling longwave fluxes at the Arctic surface from TIROS operational vertical sounder data, Journal of Geophysical Research, 102, 1795-1806.

Gillies, R.R., and Carlson, T.N. (1995). Thermal remote sensing of surface soil water content with partial vegetation cover for incorporation into climate models. Journal of Applied Meteorology, 34, 745-756.

Guest, P.S. (1998). Surface longwave radiation conditions in the eastern Weddell Sea during winter. Journal of Geophysical Research, 103, NO. C13, 30761-30771.

Gutman, G., and Ignatov, A. (1998). Derivation of green vegetation fraction from NOAA/AVHRR for use in numerical weather prediction models. International Journal of Remote Sensing, 19(8), 1533-1543.

Hanks, R.J., and Aschcroft, G.L. (1986). Applied Soil Physics. Springer-Verlag, NY, 159pp.

Hatfield, J.L., Reginato, R.J., and Idso, S.B. (1983).Comparison of long-wave radiation calculation methods over the United States. Water Resources Research, 19, 285-288.

Hatzianastassiou, N., Croke, B., Kortsalioudakis, N., Vardavas, I., and Koutoulaki, K. (1999). A model for the longwave radiation budget of the Northern Hemisphere: Comparison with Earth Radiation Budget Experiment data. Journal of Geophysical Research, 104, NO. D8, 9489-9500.

Henderson-Sellers, A. (1996). Soil moisture: A critical focus for global change studies. Global and Planetary Change, 13: 3-9.

Hipps, L.E., Swiatek, E., and Kustas, W.P. (1994). Interactions between regional fluxes and the atmospheric boundary layer over a heterogeneous watershed. Water Resources Research, 30(5), 1387-1392.

Hu, Z., and Islam, S., (1997). Effects of spatial variabilities on the scaling of land surface parameterizations. Boundary-Layer Meteorology, 83, 441-461.

Idso, S.B. (1981). A set of equations for full spectrum and 8-14 mm and 10.5-12.5 mm thermal radiation from cloudless skies. Water Resources Research, 17, 295-304.

Idso, S.B., and Jackson, R.D. (1969). Thermal radiation from atmosphere. Journal of Geophysical Research, 74, 3397-5403.

International GEWEX Project Office. (1998). Global Soil Wetness Project: Preliminary report on the pilot phase. IGPO Publication Series No. 29, 48pp.

Jackson, T.J. and Schiebe, F.R. (1993). Washita'92 data report. NAWQL Report 101, USDA National Agricultural Water Quality Lab, Durant, OK.

Jackson, T.J., Le Vine, D. M., Hsu, A.Y., Oldak, A., Starks, P.J., Swift, C.T., Isham, J.D., and Haken, M. (1999). Soil moisture mapping at regional scales using microwave radiometry: the Southern great plains hydrology experiment. IEEE Transactions on Geoscience Remote Sensing, 37 (5), 2136-2151.

Jackson, T.J., Le Vine, D.M., Swift, C.T., Schmugge, T.J. and Schiebe, F.R. (1995). Large area mapping of soil moisture using the ESTAR passive microwave radiometer in Washita'92. Remote Sensing Environment, 53, 27-37.

Jacquemin, B., and Noilhan, J. (1990). Sensitivity study and validation of a land surface parameterization using the HAPEX-MOBILHY dataset. Boundary-Layer Meteorology, 52, 93-134.

Jensen, K.H. and Mantoglou, A.(1992). Future of distributed modelling. Hydrological Processes, 6, 255-264.

Kalnay, E., and Kanamitsu, M. (1988). Time schemes for strongly nonlinear damping equations. Monthly Weather Review, 116, 1945-1958.

Kavvas, L.M. (1999). On the coarse-graining of hydrologic processes with increasing scales. Journal of Hydrology, 217, 191-202.

Kavvas, M.L. and Karakas, A. (1996). On the stochastic theory of solute transport by unsteady and steady groundwater flow in heterogeneous aquifers. Journal of Hydrology, 179, 321-351.

Kavvas, M.L., Chen, Z.Q., Tan, L., Soong, S. –T., Terakawa, A., Yoshitani, J., and Fukami, K. (1998). A regional-scale land surface parameterization based on areally-averaged hydrological conservation equations. Hydrological Sciences Journal, 43 (4), 611-631.

Koster, R.D. and Milly, P.C.D. (1997). The interplay between transpiration and runoff formulations in land surface schemes used with atmospheric models. Journal of Climate, 10,1578-1591.

Lanicci, J.M., Carlson, T.N., and Warner, T.T. (1987). Sensitivity of the great plains severe-storm environment to soil-moisture distribution, Monthly Weather Review, 115, 2660-2673.

Luxmoore, R.J., King, A.W. and Tharp, M.L. (1991). Approaches to scaling up physiologically based soil-plant models in space and time.

Mahrt, L., and Ek, K. (1984). The influence of atmospheric stability on potential evaporation. J. Clim. Appl. Meteor., 23, 222-234.

Mahrt, L., and Pan, H.L. (1984). A two-layer model of soil hydrology. Boundary-Layer Meteorology, 29,1-20.

Marshall, C. H. Jr., 1998. Evaluation of the new land-surface and planetary boundary layer parameterization schemes in the NCEP Mesoscale Eta model using Oklahoma Mesonet observations. M.S. Thesis., Univ. of Oklahoma. Norman, OK.,176pp.

McCumber, M.C., and Pielke, R. A. (1981). Simulation of the effects of surface fluxes of heat and moisture in a mesoscale numerical model soil layer. Journal of Geophysical Research, 86, 9929-9938.

McGarigal, K and Marks, B.J.(1995). FRAGSTATS: spatial pattern analysis program for quantifying landscape structure (version 2.1). Gen.Tech.Rep. PNW-GTR-351. Portland, OR: U.S. Department of Agriculture, Forest Service, Pacific Northwest Research Station. 122p.

Meentemeyer, V. (1989). Geographical perspectives of space, time and scale. Landscape Ecology, 3,163-173.

Mintz, Y. (1981). The sensitivity of numerically simulated climates to land surface boundary conditions. Proc. JSC Study Conf. On Land Surface Processes in Atmospheric GCM, Greenbelt, MD.

Mintz, Y. (1984). The sensitivity of numerically simulated climates to land-surface boundary conditions, in Global Climate, edited by. J.H. Houghton, 79-105, Cambridge University Press, Cambridge, England.

Morill, J.C., Dickinson, R.E. and Hahmann, A.N. (1999). Sensivity of a land surface model to the diurnal distribution of downward longwave radiation. Journal of Meteorological Society of Japan, 77, 265-279.

Noilhan, J., and Planton, S. (1989). A simple parameterization of land surface processes for meteorological models. Monthly Weather Review, 117, 536-549.

Oglesby, R.J. (1991). Springtime soil moisture variability, and North American drought as simulated by the NCAR Community Climate Model I, Journal of Climate, 4, 890-897.

Pan, H-L., and Mahrt, L. (1987). Interaction between soil hydrology and boundary-layer development. Boundary-Layer Meteorology, 38, 185-202.

Peters-Lidard, C.D., Blackburn, E., Liang, X., and Wood, E.F. (1998). The effect of soil thermal conductivity parameterization on surface energy fluxes and temperatures. Journal of Atmospheric Science, 55, 1209-1224.

Pielke, R.A. (1989). Influence on severe storm development of irrigated land. National Weather Digest, 24(2), 16-17.

Robock. A., Schlosser, C.A., Vinnikov, K.Ya., Speranskaya N.A., and Entin, J.K. (1998). Evaluation of AMIP soil moisture simulations. Global and Planetary Change. Global and Planetary Change, 19, 181-208.

Rodriguez-Iturbe, I. (2000). Ecohydrology: A hydrologic perspective of climate-soil-vegetation dynamics. Water Resources Research, 36(1), 3-9.

Rodriguez-Iturbe, I., Vogel, G.K., Rigon, R., Entekhabi, D., Castelli, F. and Rinaldo, A. (1996). On the spatial organization of soil moisture fields, Geophysical Research Letters, 22(20), 2757-2760.

Rowntree, P.R., 1983. Sensitivity of GCM to land surface processes. Proc. Work. in Intercomparison of Large Scale Models for extended Range Forecasts, ECMWF, Reading, England, 225-261.

Schaake, J.C., Koren, V.I., Duan, Q.Y., Mitchell, K., and Chen, F. (1996). A simple water balance model (SWB) for estimating runoff at different spatial and temporal scales. Journal of Geophysical Research, 101, 7461-7475.

Schneider, J.M., Fisher, D.K. (1997). Meeting GEWEX/GCIP measurement needs by adding automated measurements of soil water and temperature profiles to the DOE ARM/CART Southern Great Plains Site, Preprints AMS 13th Conf. on Hydrology, 265-268.

Sellers, P.J., Heiser, M.D., Hall, F.G., Verma, S.B., Desjardins, L.R., Schuepp, M.P., and MacPherson, J.I. (1997). The impact of using area-averaged land surface properties-topography, vegetation condition, soil wetness-in calculations of intermediate scale (approximately 10 km2) surface-atmosphere heat and moisture fluxes. Journal of Hydrology, 190, 269-301.

Silberstein, R.P., Sivapalan, M., and Wyllie, A. (1999). On the validation of a coupled water and energy balance model at small catchment scales. Journal of Hydrology, 220, 149-168.

Sivapalan, M. and Woods, R.A. (1995). Evaluation of the effects of general circulation models' subgrid variability and patchiness of rainfall and soil moisture on land surface water balance fluxes. Scale issues in Hydrological Modeling (eds.) J.D. Kalma and M. Sivapalan. John Wiley & Sons Ltd., England, 453-473.

Southern Great Plains 1997 (SGP 97) hydrology experimental plan. (1997). USDA Agricultural Research Service, Beltsville, Maryland. 178 pp.

Swinbank, W.C. (1963). Long-wave radiation from clear skies. Quart. J. Roy. Meteor. Soc., 89, 339-348.

Viterbo, P., and Beljaars, A.C. (1995). An improved land surface parameterization scheme in the ECMWF model and its validation. Journal of Climate, 8, 2716-2748.

Wood, E.F. (1991). Land surface-atmospheric interactions for climate modeling: observations, models and analysis, Reprints from surveys in Geophysics, Vol. 12, Nos. 1-3, 1991. Kluwer Academic Publishers, Dordrecht, Boston and London.

Wood, E.F. (1994). Scaling, soil moisture and evapotranspiration in runoff models. Advances in Water Resources, 17, 25-34.

Wood, E.F., Lettenmaier, D.P., and Zartarian, V.G. (1992). A land-surface hydrology parameterization with subgrid variability for general circulation models. Journal of Geophyscial Research, 97, 2717-2728.

Yan, H., and Anthes, R. A. (1988). The effect of variations in surface moisture on mesoscale circulations. Monthly Weather Review, 116, 192-208.

Yucel, I., Shuttleworth, W.J., Washburne, J., and Chen, F. (1998). Evaluating NCEP Eta model derived data against observations. Monthly Weather Review, 126, 1977-1991.

APPENDIX A

THE SOIL AND VEGETATION-RELATED PARAMETERS IN THE LAND SURFACE MODEL

Table A-1. Soil-related parameters in the land surface model.

	MAXSMC	SATPSI	DRYSMC	SATDK	BB	REFSMC	WLTSMC	SATDW	F11	QUATZ
Sand	0.339	0.069	0.07	1.07E-06	2.79	0.236	0.01	6.08E-07	-0.472	0.92
Loamy Sand	0.421	0.036	0.14	1.41E-05	4.26	0.283	0.028	5.14E-06	-1.044	0.82
Sandy Loam	0.434	0.141	0.22	5.23E-06	4.74	0.312	0.047	8.05E-06	-0.569	0.6
Silt Loam	0.476	0.759	0.08	2.81E-06	5.33	0.36	0.084	2.39E-05	0.162	0.25
Silt	0.476	0.759	0.18	2.81E-06	5.33	0.36	0.084	2.39E-05	0.162	0.1
Loam	0.439	0.355	0.16	3.38E-06	5.25	0.329	0.066	1.43E-05	-0.327	0.4
Sandy Clay Loam	0.404	0.135	0.12	4.45E-06	6.66	0.314	0.067	9.90E-06	-1.491	0.6
Silty Clay Loam	0.464	0.617	0.1	2.04E-06	8.72	0.387	0.12	2.37E-05	-1.118	0.1
Clay Loam	0.465	0.263	0.07	2.45E-06	8.17	0.382	0.103	1.13E-05	-1.297	0.35
Sandy Clay	0.406	0.098	0.2	7.22E-06	10.73	0.338	0.1	1.87E-05	-3.209	0.52
Silty Clay	0.468	0.324	0.2	1.34E-06	10.39	0.404	0.126	9.64E-06	-1.916	0.1
Clay	0.468	0.468	0.2	9.74E-06	11.55	0.412	0.138	1.12E-05	-2.138	0.25
Organic Materials	0.439	0.355	0.2	3.38E-06	5.25	0.329	0.066	1.43E-05	-0.327	0
Water										
Bedrock	0.2	0.069	0.2	1.41E-04	2.79	0.108	0.006	1.36E-04	-1.111	0.1
Other(land-ice)	0.421	0.036	0.2	1.41E-05	4.26	0.283	0.028	5.14E-06	-1.044	0.82

Note: MAXSMC - Maximum soil moisture content (Porosity), SATPSI - Saturation soil suction (-ve), DRYSMC - Air dry soil moist content limits, SATDK - Saturation soil conductivity/diffusivity, BB - Soil conductivity/diffusivity coeff., REFSMC - Reference soil moisture (Field capacity), WLTSMC - Wilting point soil moisture content, SATDW - Saturation soil conductivity/diffusivity coeff., F11 - Soil conductivity/diffusivity coeff., Quartz - Soil quartz content.

Table A-2. Vegetation-related parameters in the land surface model.

	Albedo	Roughness length	Shade factor	Minimum stomatal resistance	Radiation stress function parameter	Vapor pressure deficit function parameter
Urban and Built-Up Land	0.25	1	0.1	200	999	999
Dryland Cropland and Pasture	0.19	0.07	0.8	40	100	36.25
Irrigated Cropland and Pasture	0.15	0.07	0.8	40	100	36.25
Mixed Dryland/Irrigated Cropland and Pasture	0.17	0.07	0.8	40	100	36.25
Cropland/Grassland Mosaic	0.19	0.07	0.8	40	100	36.25
Cropland/Woodland Mosaic	0.19	0.15	0.8	70	65	44.14
Grassland	0.19	0.08	0.8	40	100	36.35
Shrubland	0.25	0.03	0.7	300	100	42
Mixed Shrubland/Grassland	0.23	0.05	0.7	170	100	39.18
Savanna	0.2	0.86	0.5	70	65	54.53
Deciduous Broadleaf Forest	0.12	0.8	0.8	100	30	54.53
Deciduous Needleleaf Forest	0.11	0.85	0.7	150	30	47.35
Evergreen Broadleaf Forest	0.11	2.65	0.95	150	30	41.69
Evergreen Needleleaf Forest	0.1	1.09	0.7	125	30	47.35
Mixed Forest	0.12	0.8	0.8	125	30	51.93
Water Bodies	0.19	0.01	0	100	30	51.75
Herbaceous Wetland	0.12	0.04	0.6	40	100	60
Wooded Wetland	0.12	0.5	0.6	100	30	51.93
Barren or Sparsely Vegetated	0.12	0.01	0.01	999	999	999
Herbaceous Tundra	0.16	0.04	0.6	150	100	42
Wooded Tundra	0.16	0.06	0.6	150	100	42
Mixed Tundra	0.16	0.05	0.6	150	100	42
Bare Ground Tundra	0.17	0.03	0.3	200	100	42
Snow or Ice	0.8	0.01	0	999	999	999

APPENDIX B

HOURLY OBSERVED AND PREDICTED DOWNWELLING LONGWAVE RADIATION FOR FIVE SITES

(Supplement to Chapter 3)

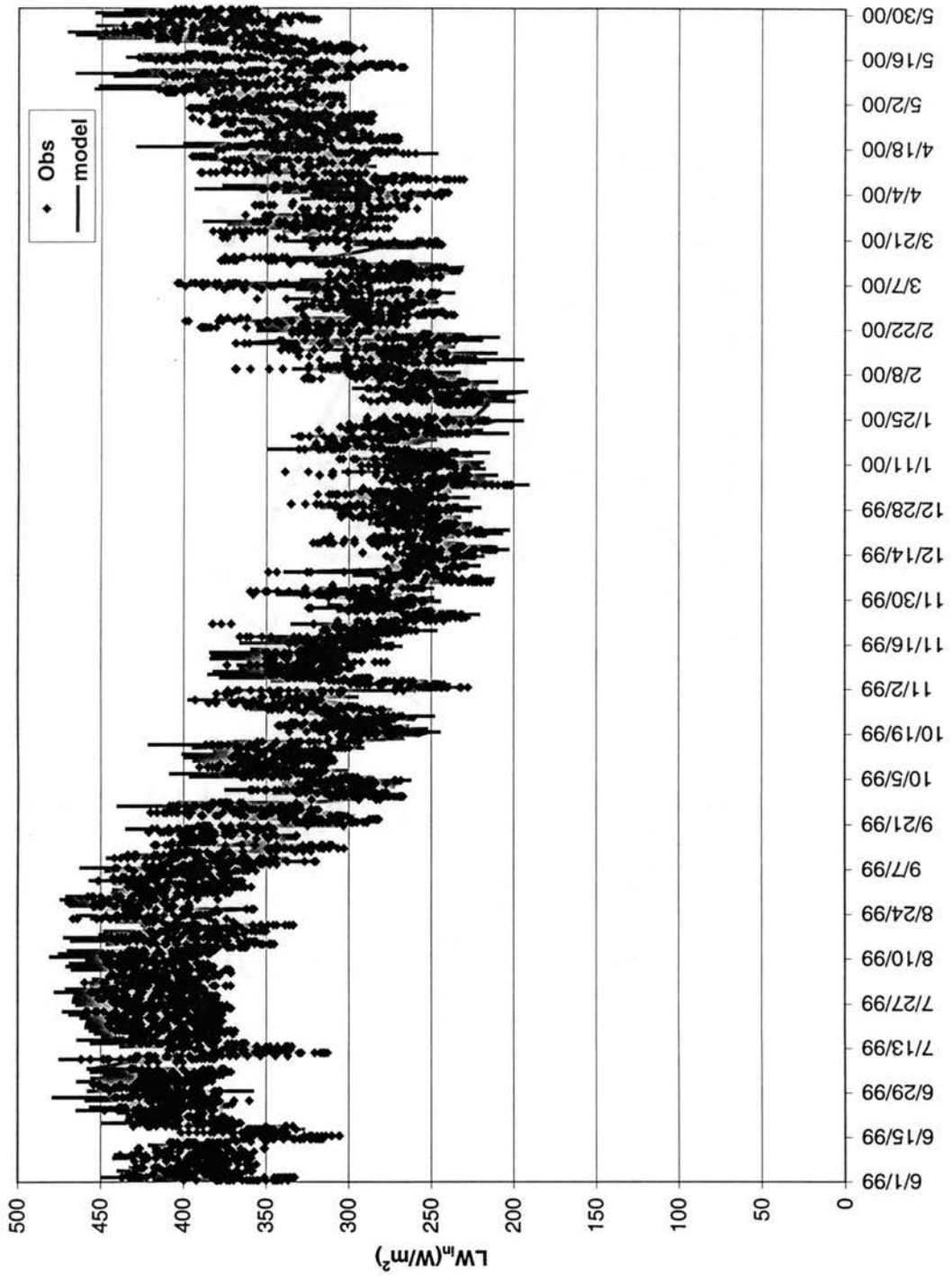

Figure B-1. Comparison of hourly observed and predicted downwelling longwave radiation for the BESS site.

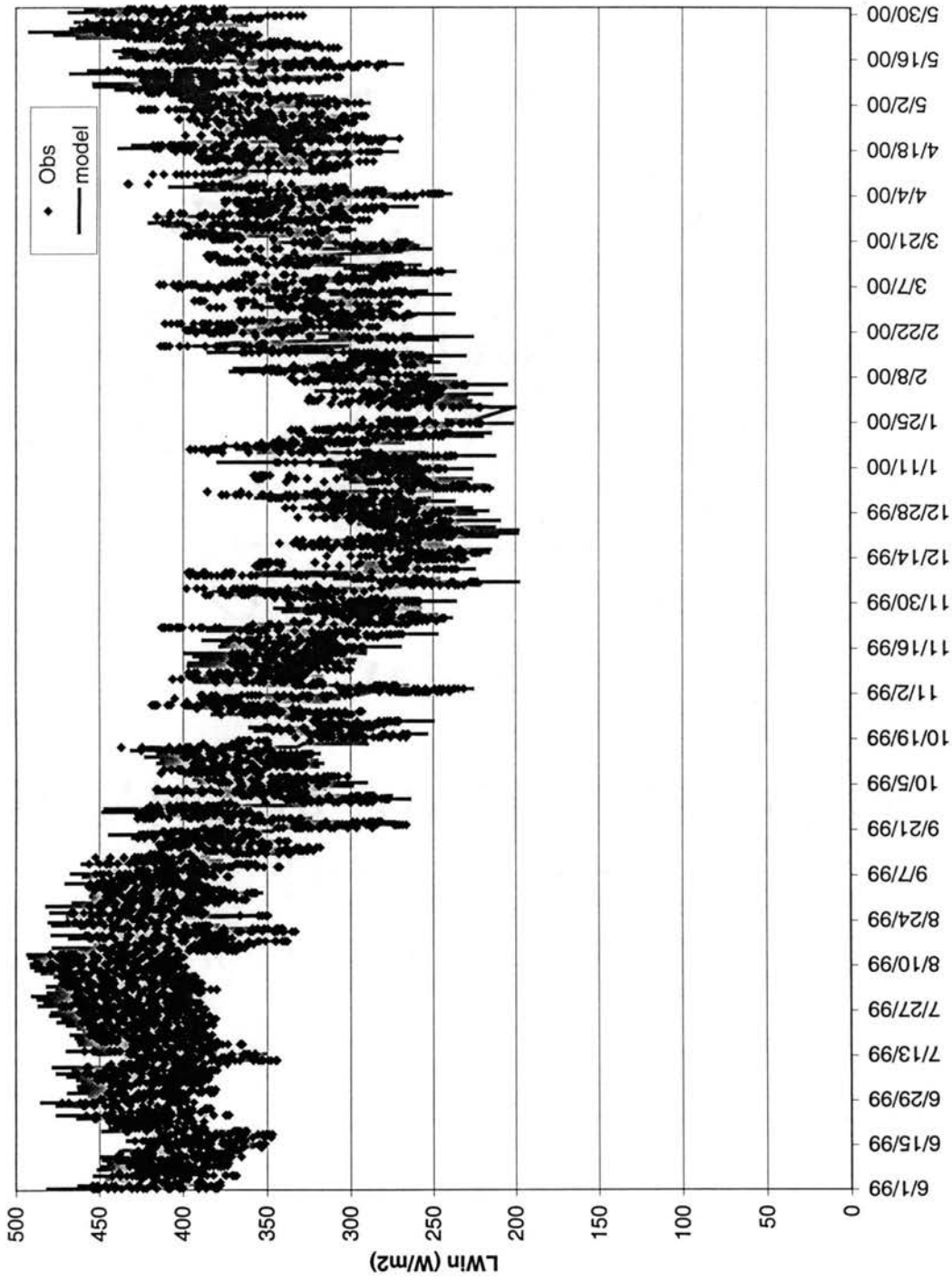

Figure B-2. Comparison of hourly observed and predicted downwelling longwave radiation for the BURN site.

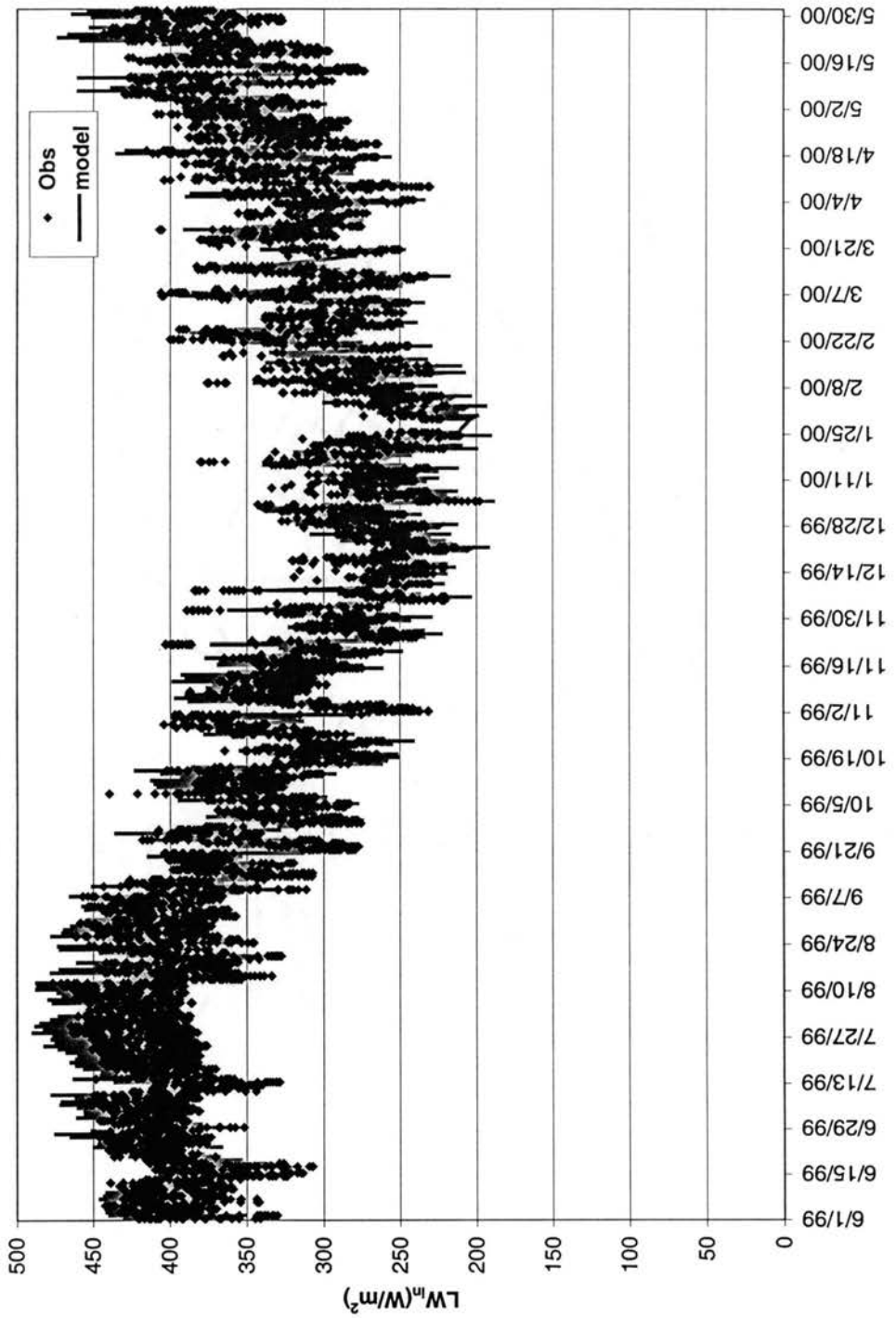

Figure B-3. Comparison of hourly observed and predicted downwelling longwave radiation for the MARE site.

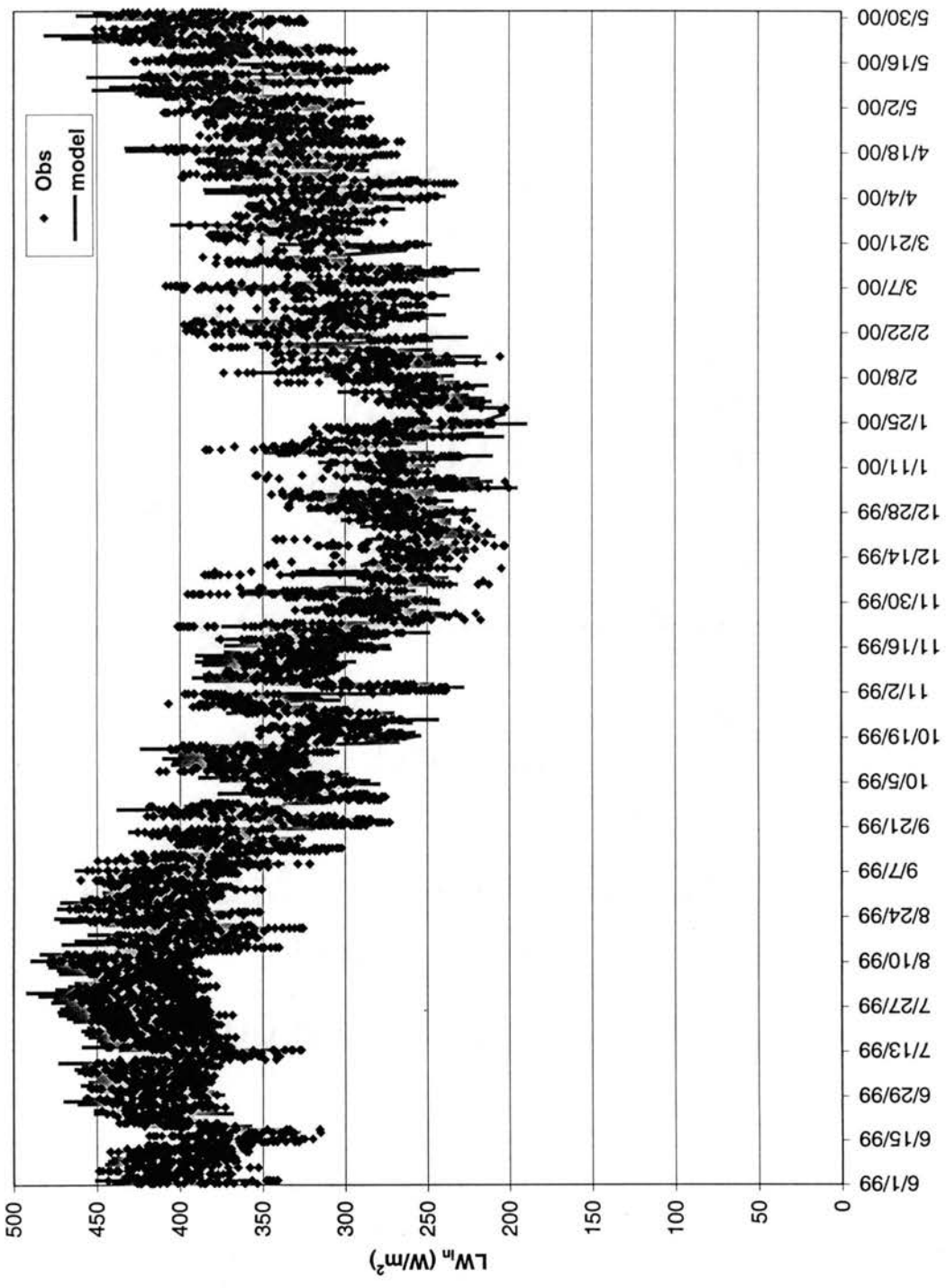

Figure B-4. Comparison of hourly observed and predicted downwelling longwave radiation for the NORM site.

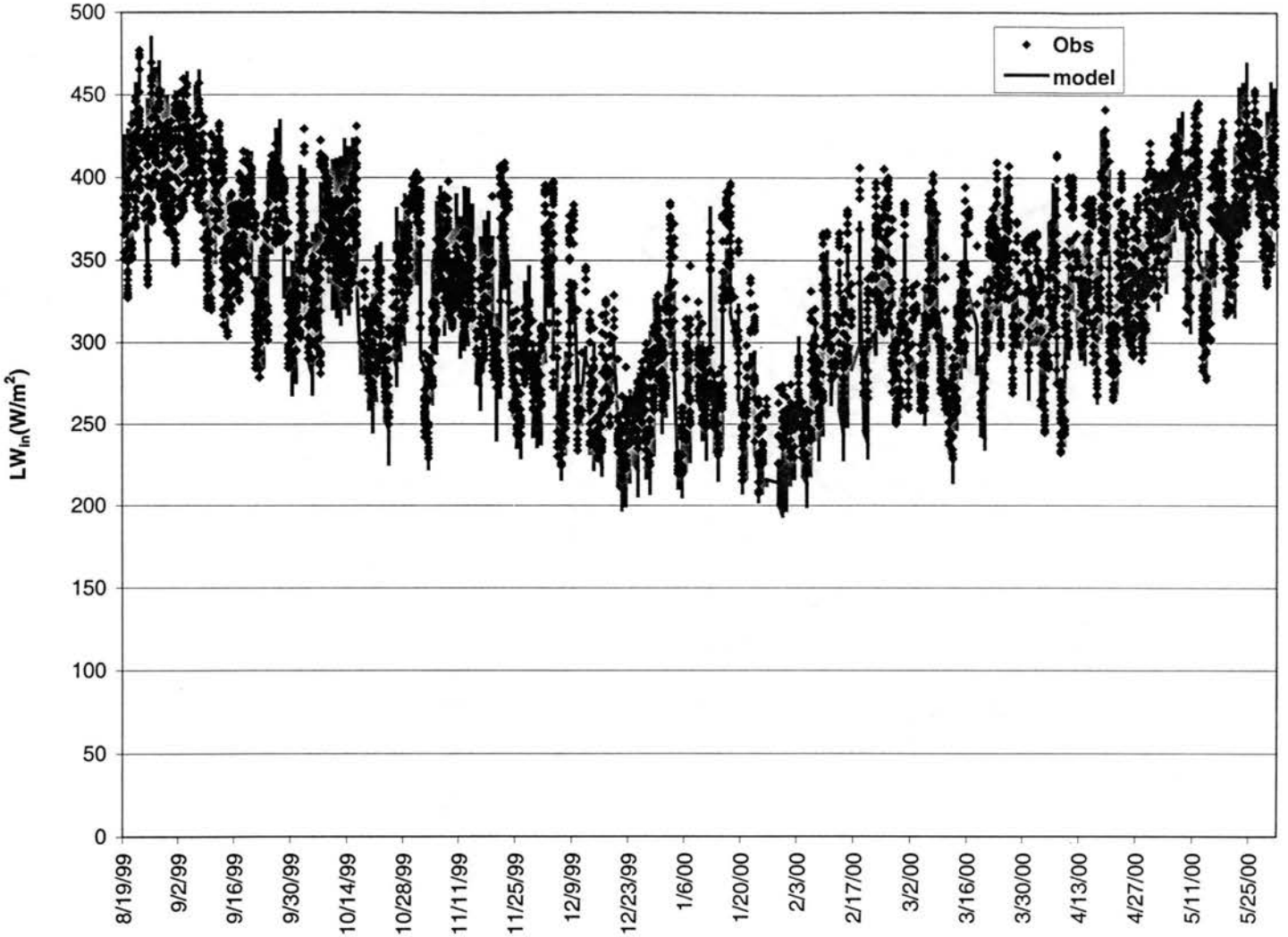

Figure B-5. Comparison of hourly observed and predicted downwelling longwave radiation for the STIG site.

APPENDIX C

COMPARISON OF OBSERVED AND MODELED ENERGY-BALANCE COMPONENTS FOR SEVEN SITES

(Supplement to Chapter 4)

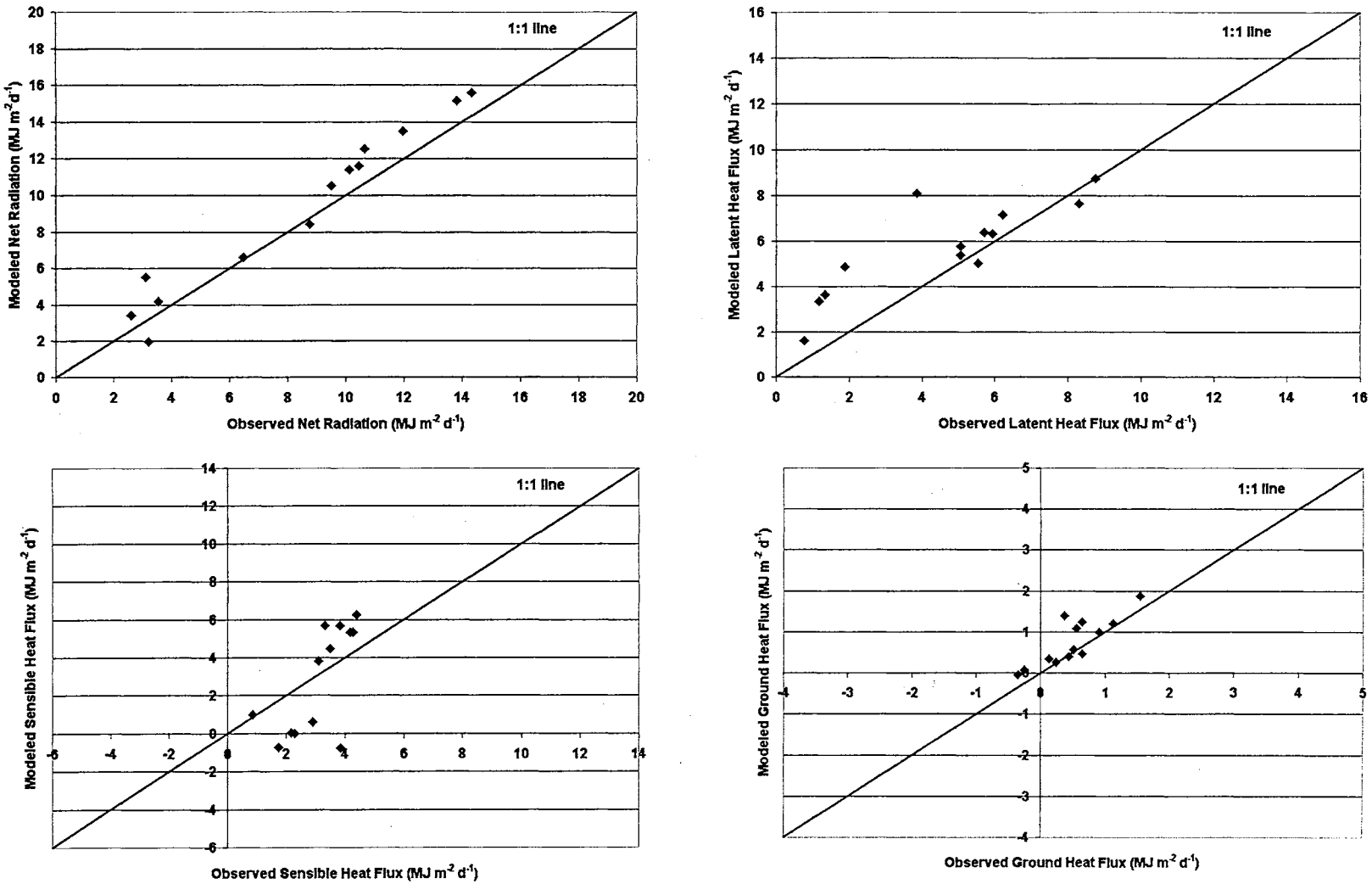

Figure C-1. Comparison of daily average observed and modeled R_n, LH, SH and GH for the ALVA site.

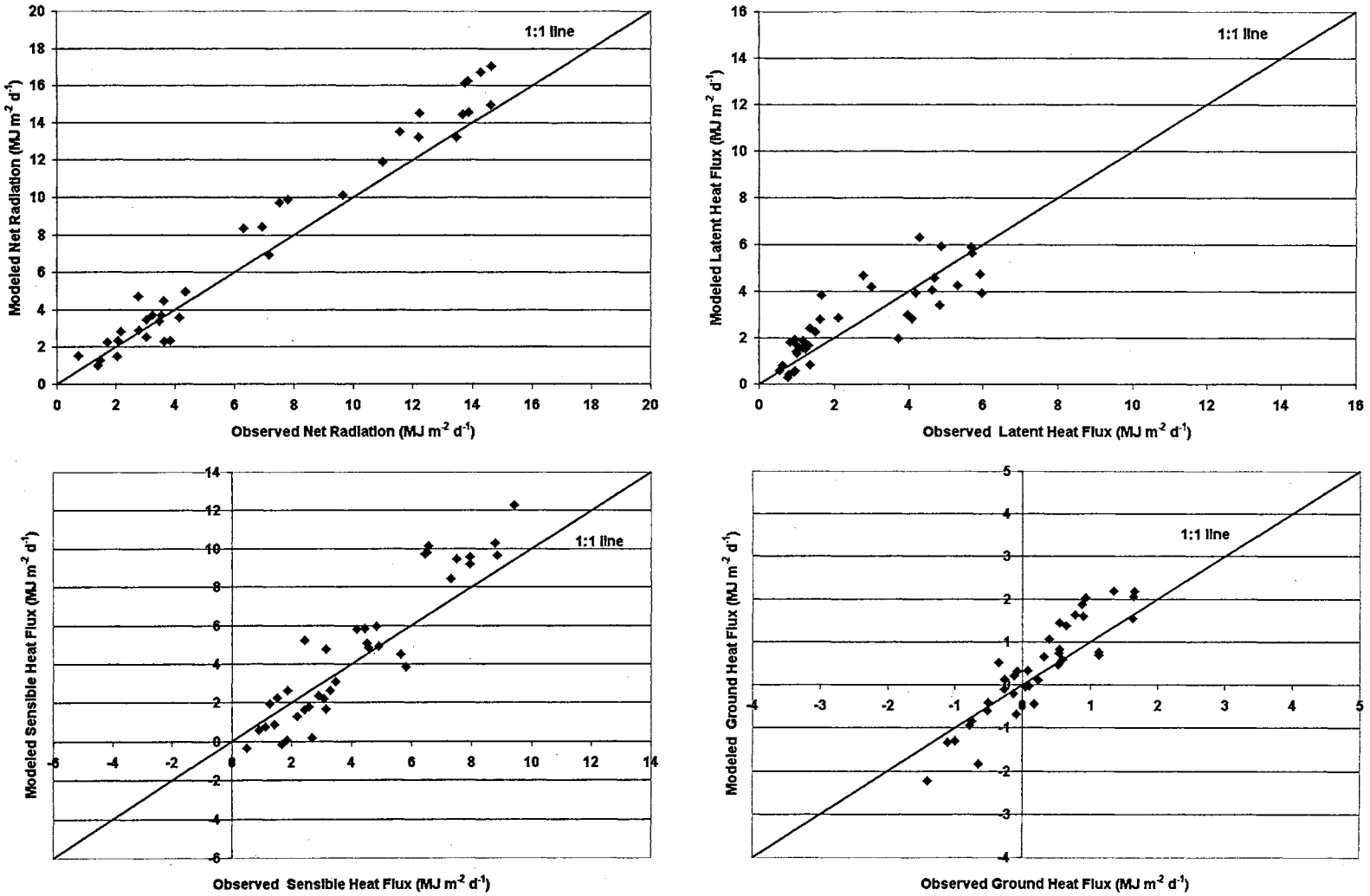

Figure C-2. Comparison of daily average observed and modeled R_n, LH, SH and GH for the BOIS site.

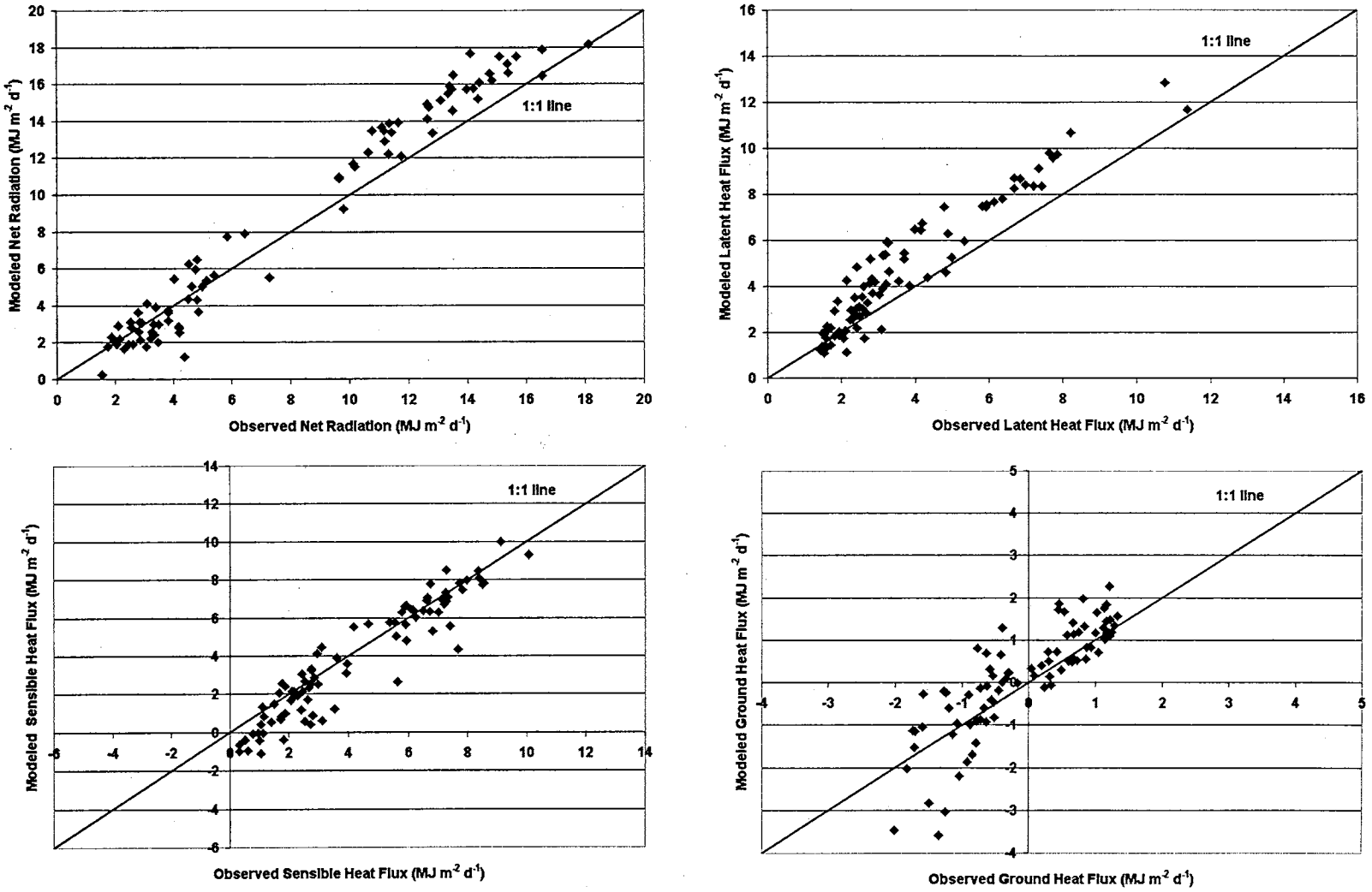

Figure C-3. Comparison of daily average observed and modeled R_n, LH, SH and GH for the BURN site.

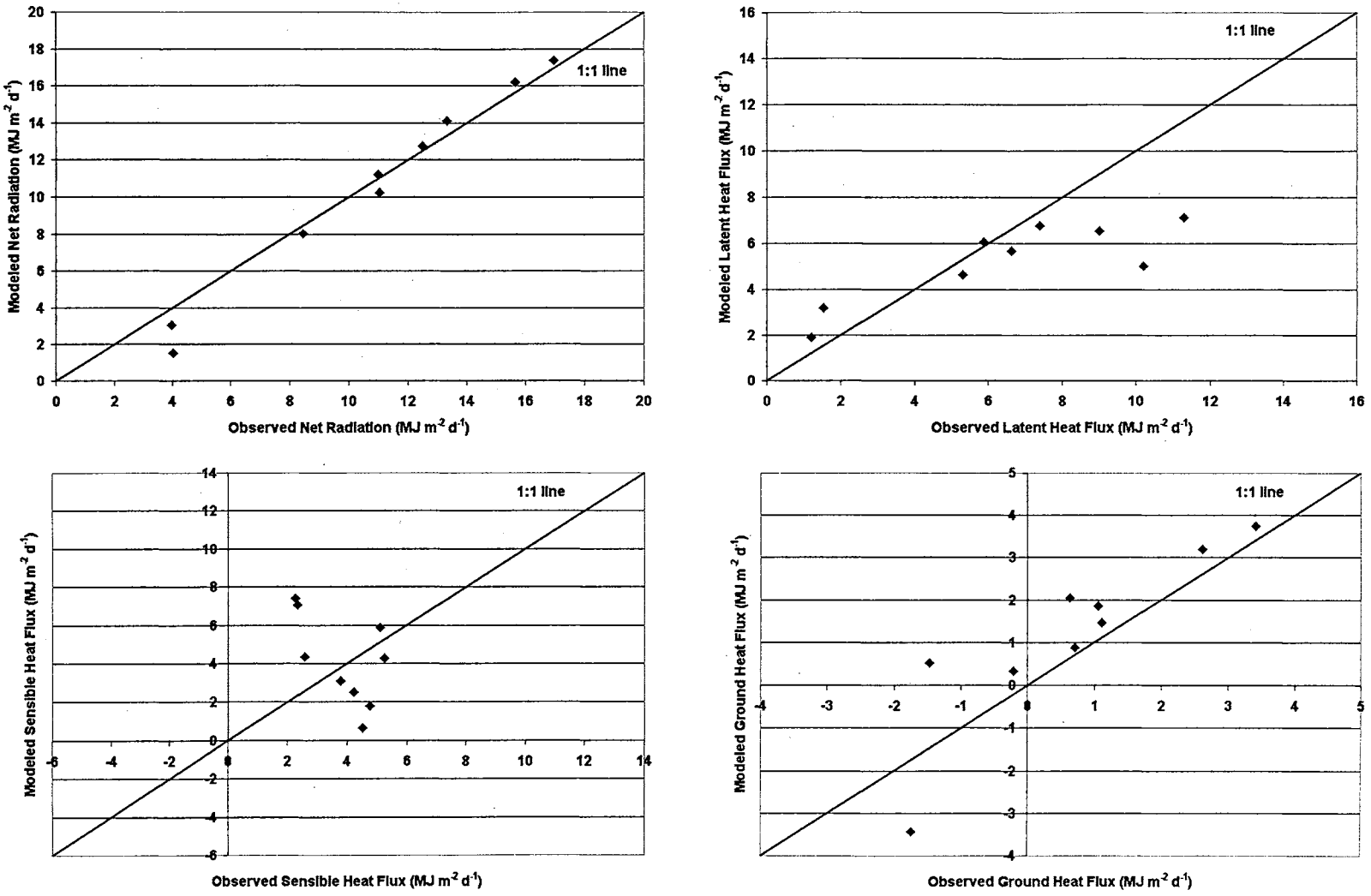

Figure C-4. Comparison of daily average observed and modeled R_n, LH, SH and GH for the FORA site.

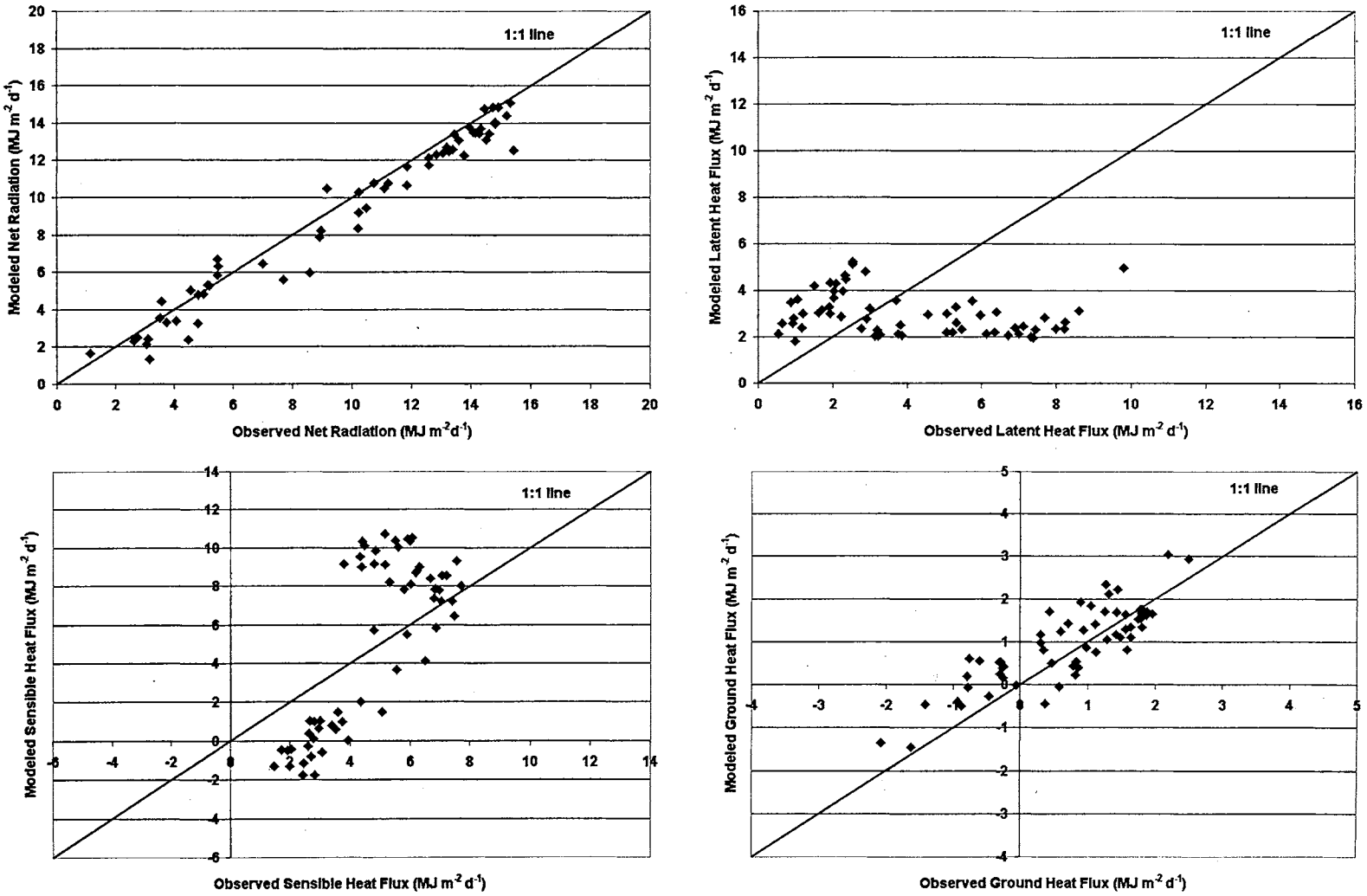

Figure C-5. Comparison of daily average observed and modeled R_n, LH, SH and GH for the GRAN site.

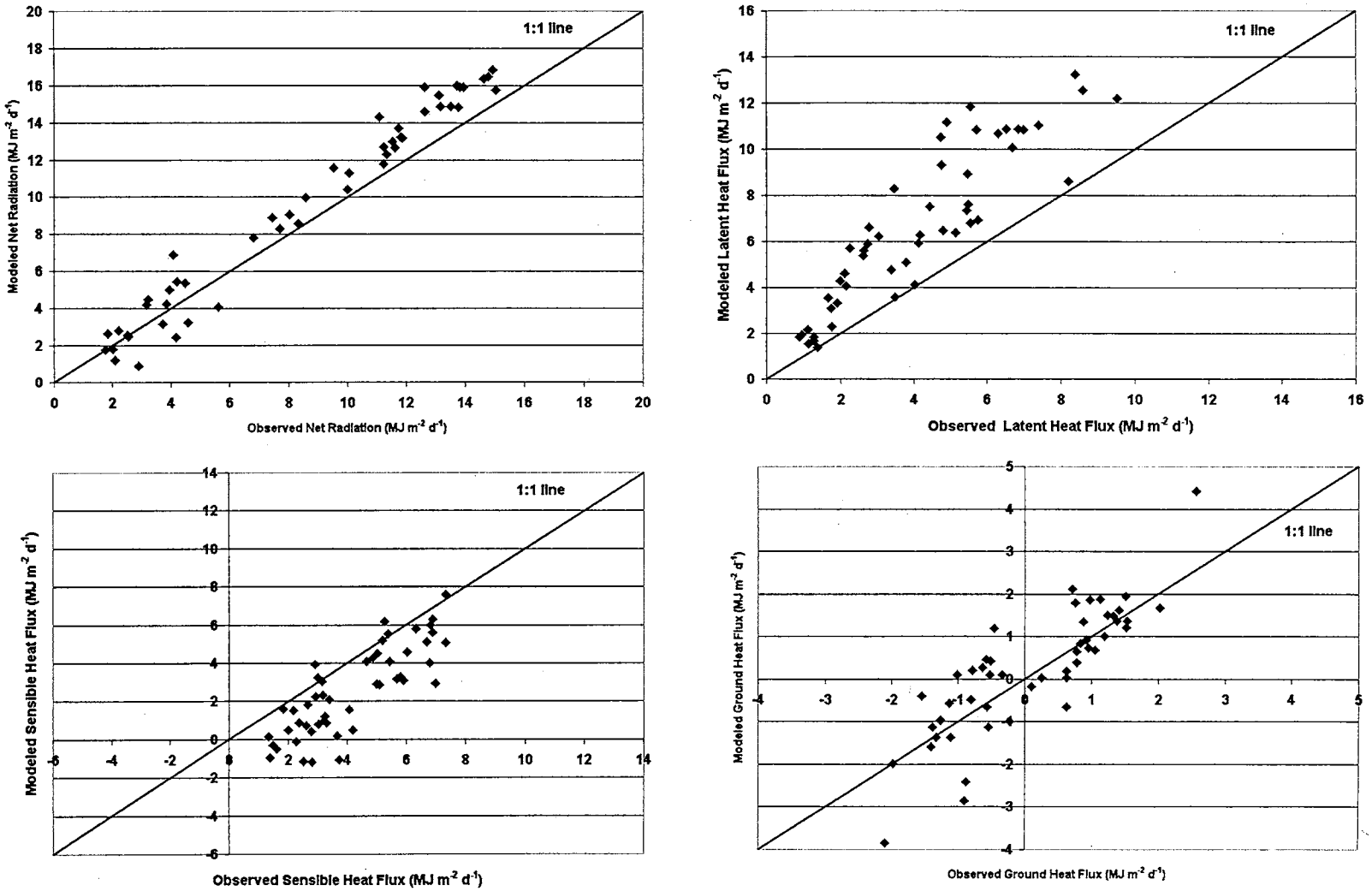

Figure C-6. Comparison of daily average observed and modeled R_n, LH, SH and GH for the MARE site.

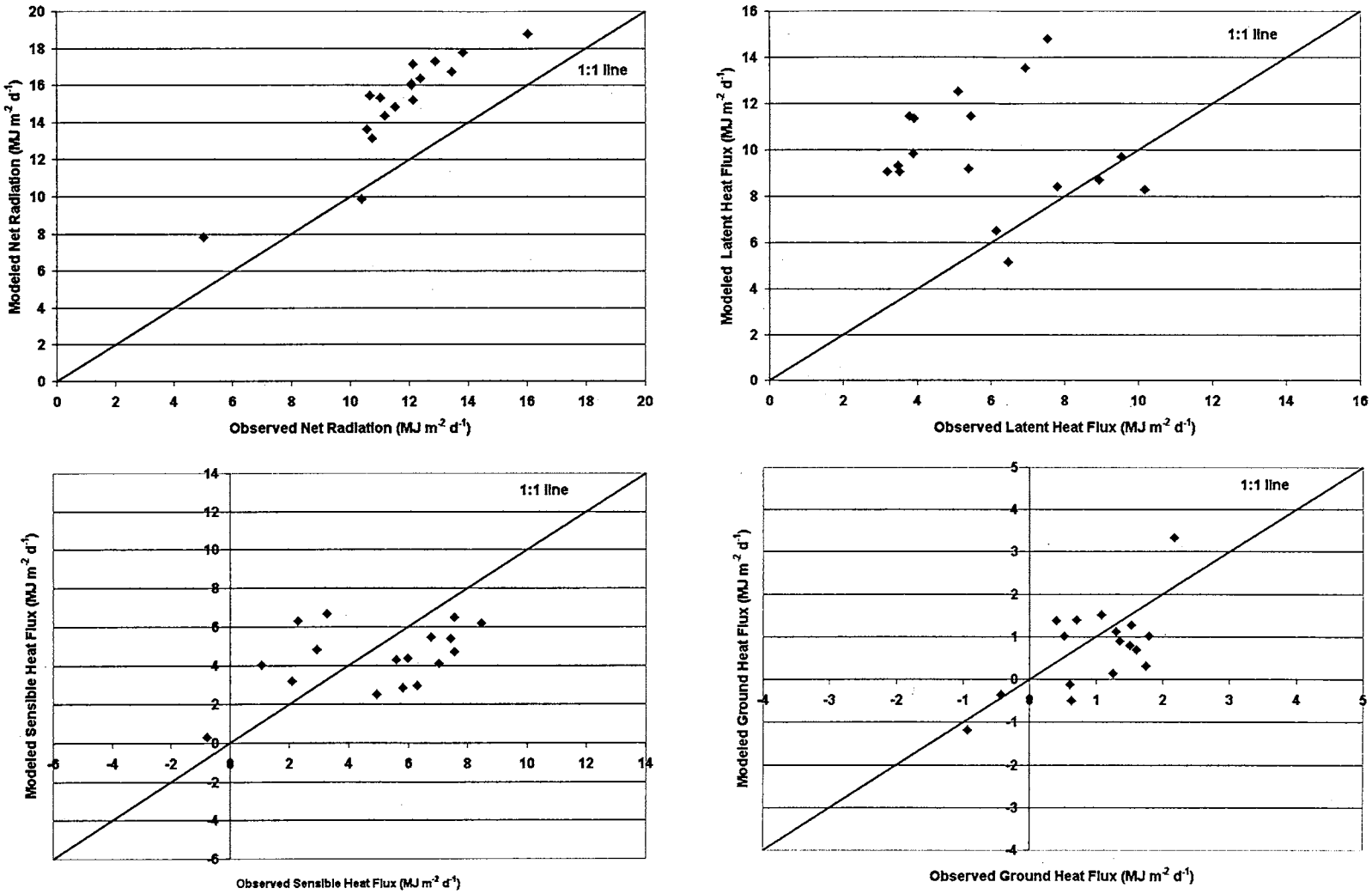

Figure C-7. Comparison of daily average observed and modeled R_n, LH, SH and GH for the NORM site.

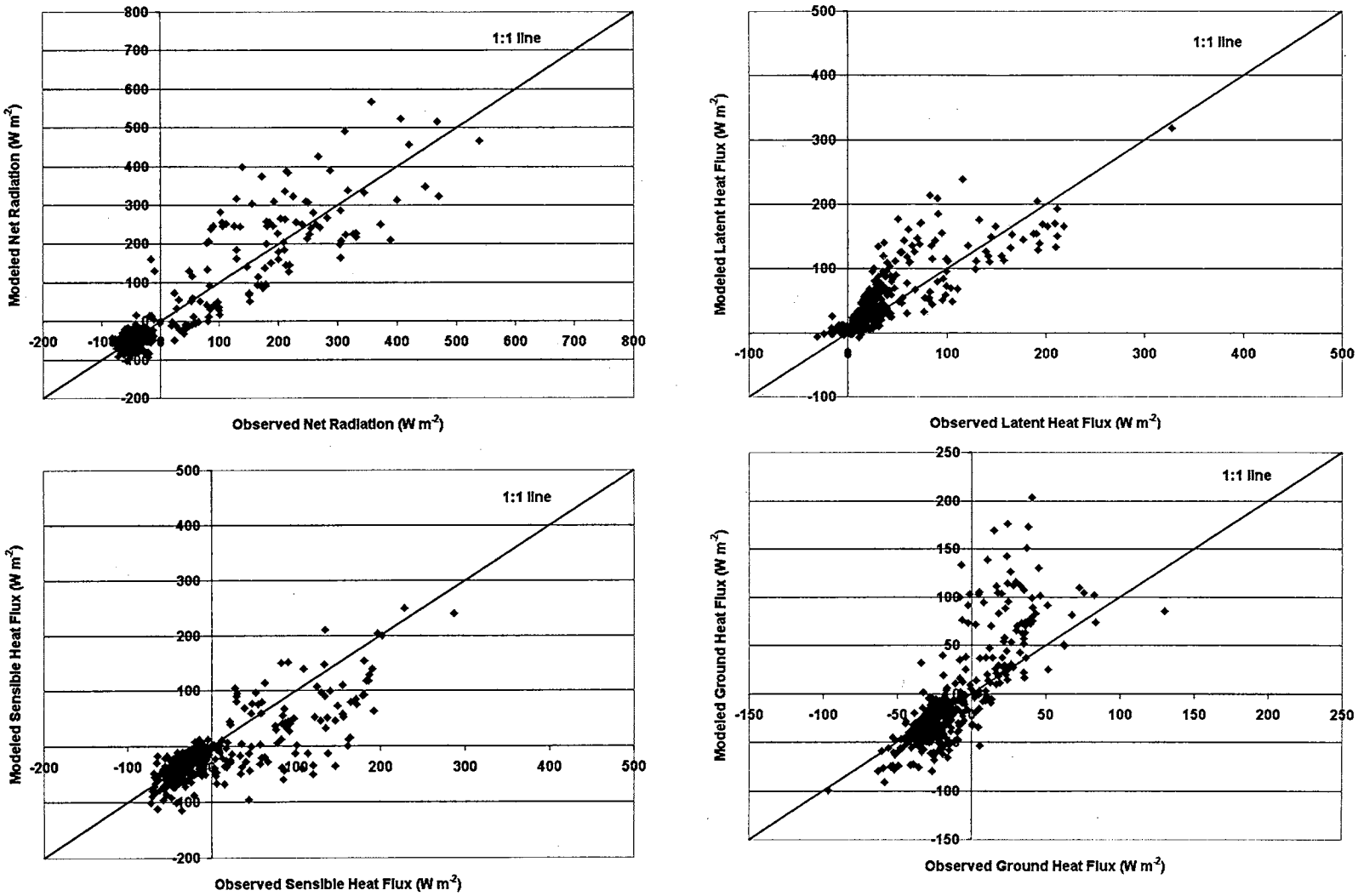

Figure C-8. Comparison of hourly average observed and modeled R_n, LH, SH and GH for the ALVA site.

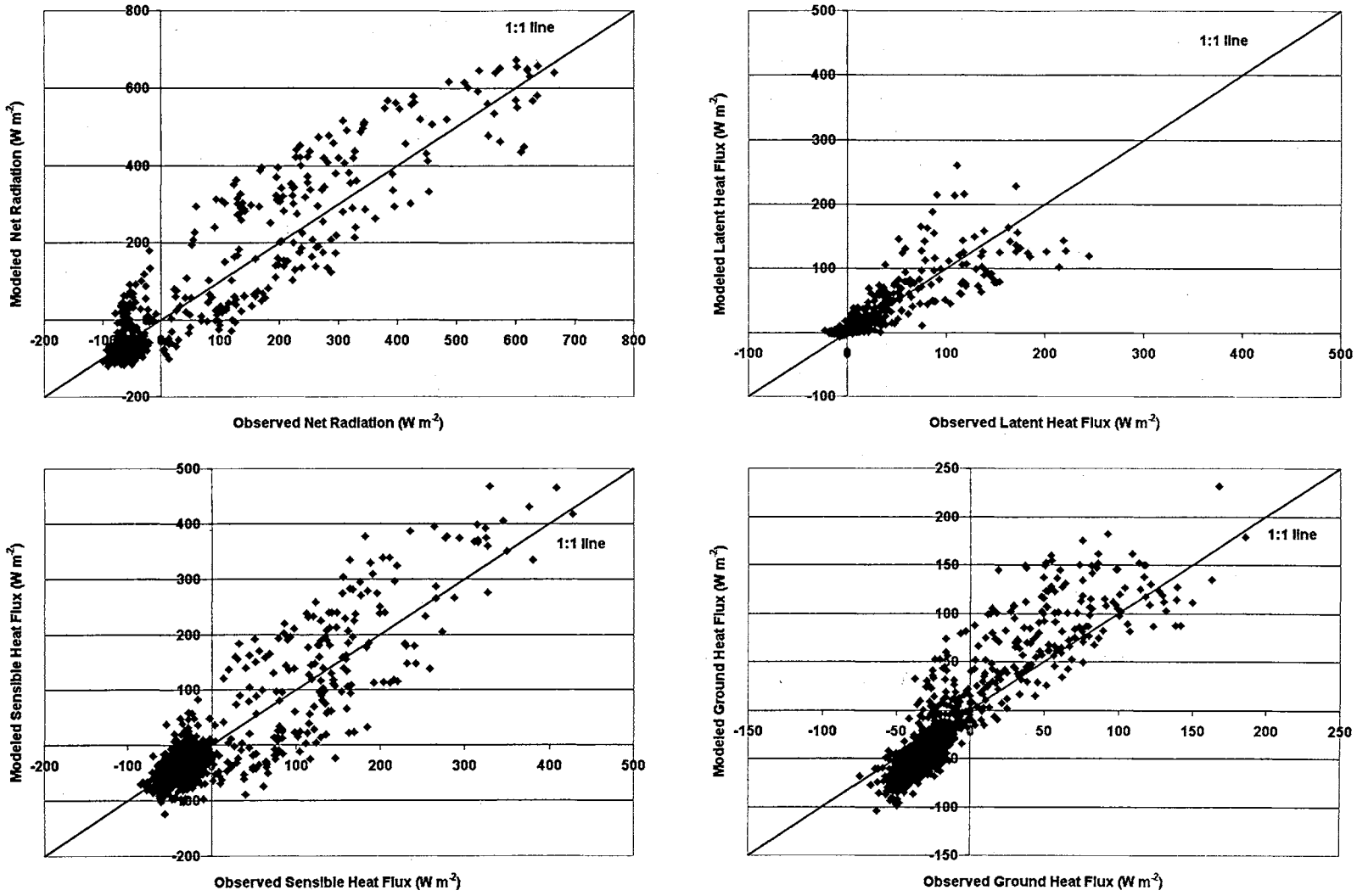

Figure C-9. Comparison of hourly average observed and modeled R_n, LH, SH and GH for the BOIS site.

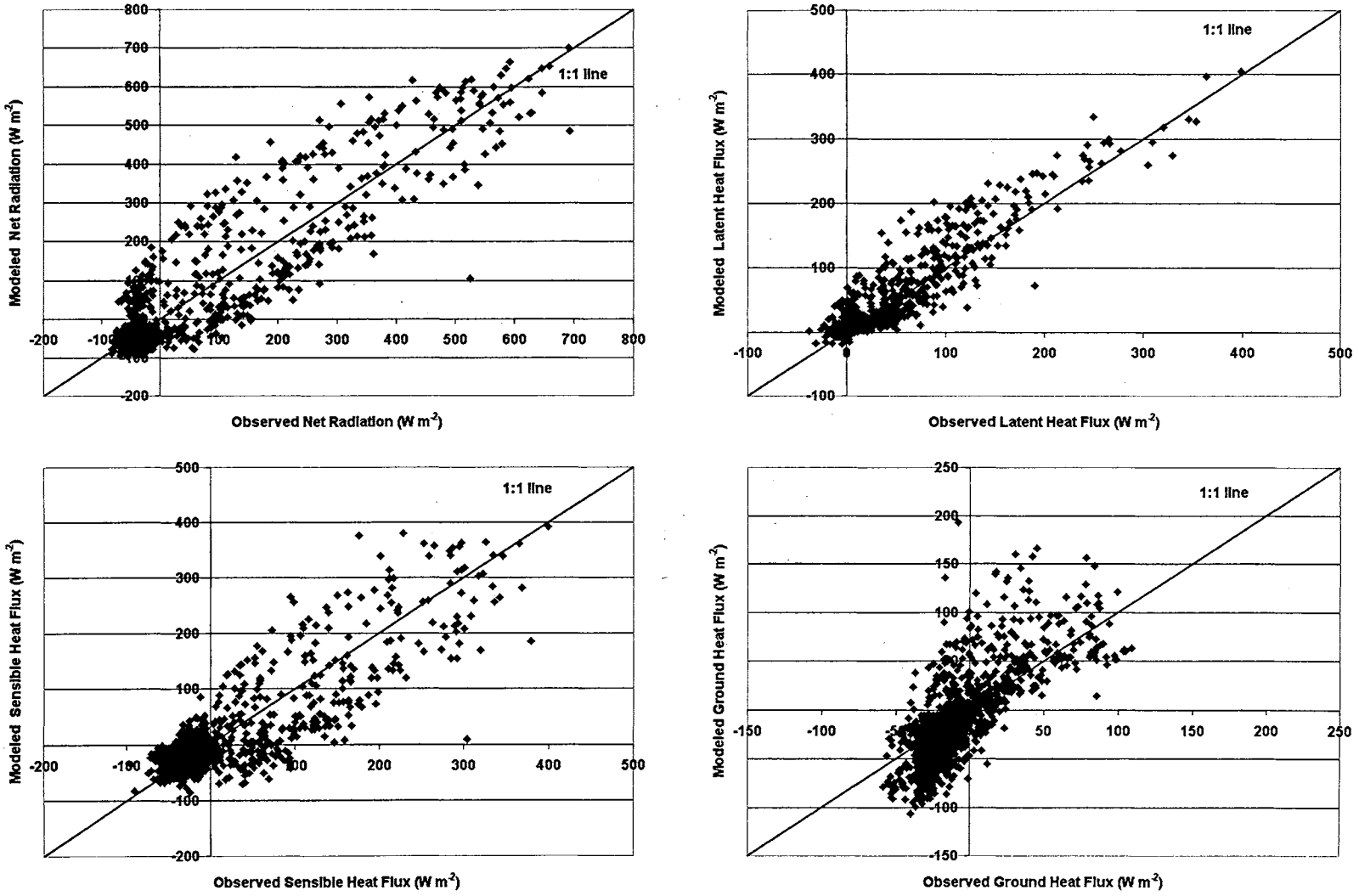

Figure C-10. Comparison of hourly average observed and modeled R_n, LH, SH and GH for the BURN site.

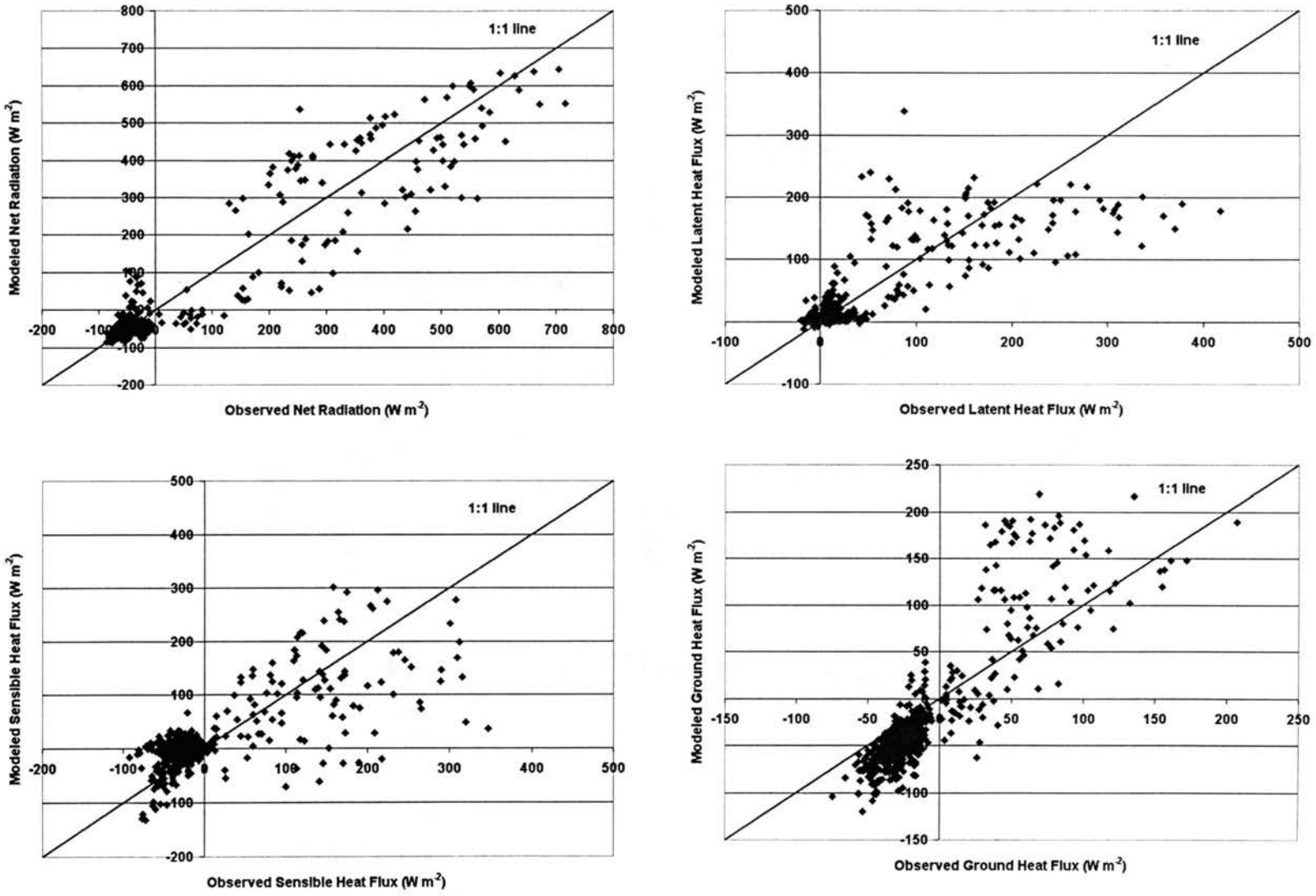

Figure C-11. Comparison of hourly average observed and modeled R_n, LH, SH and GH for the FORA site.

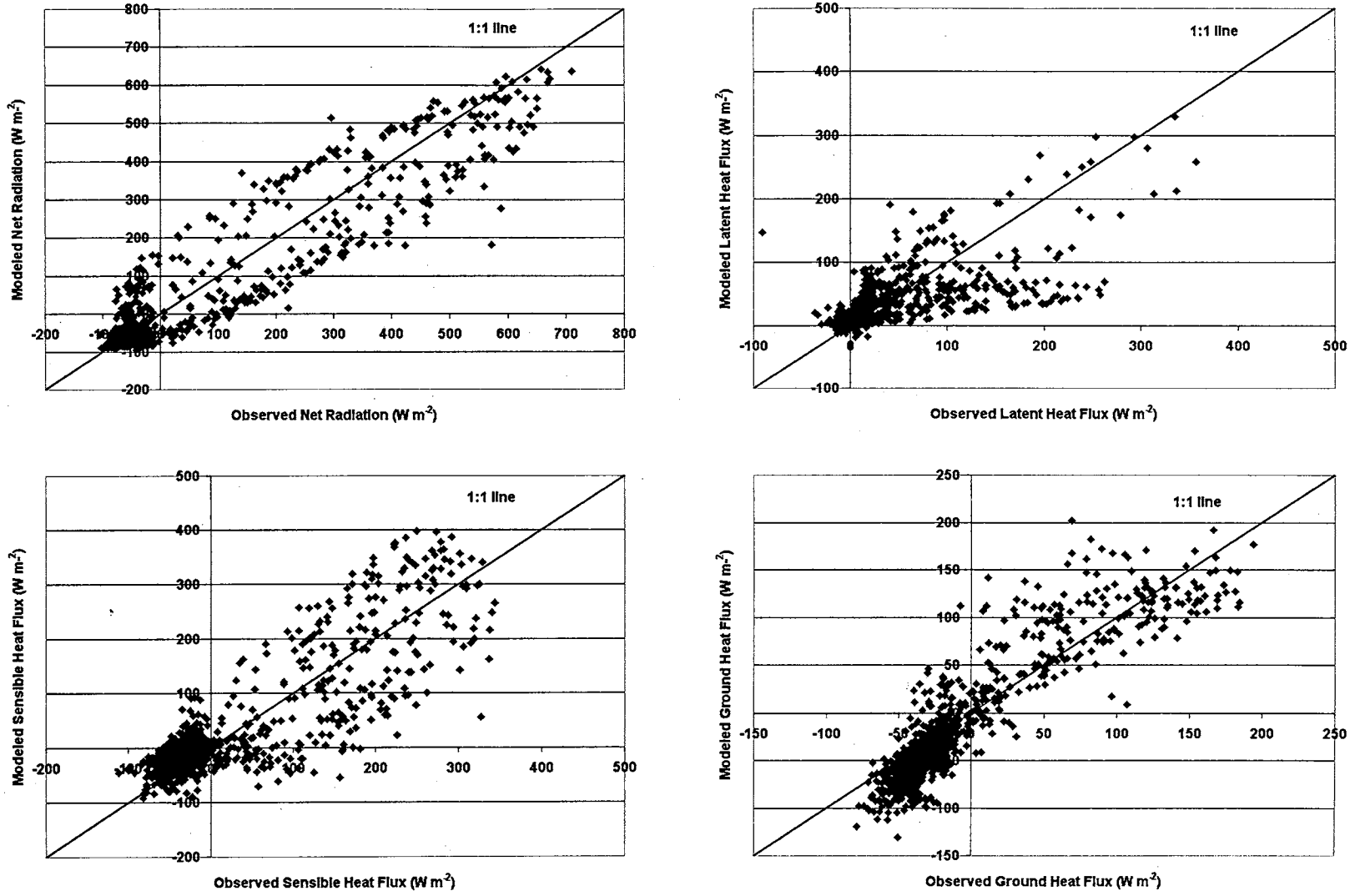

Figure C-12. Comparison of hourly average observed and modeled R_n, LH, SH and GH for the GRAN site.

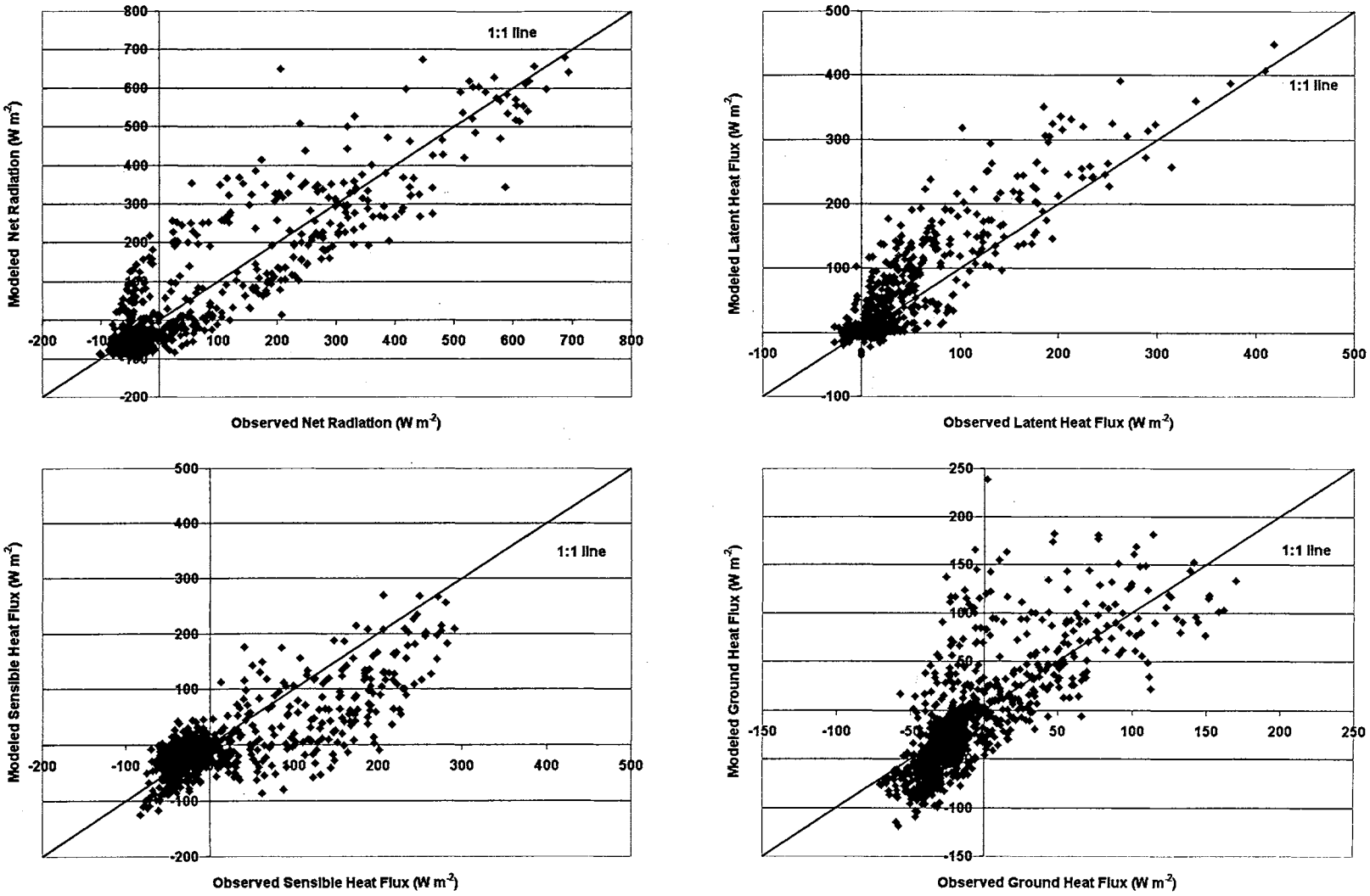

Figure C-13. Comparison of hourly average observed and modeled R_n, LH, SH and GH for the MARE site.

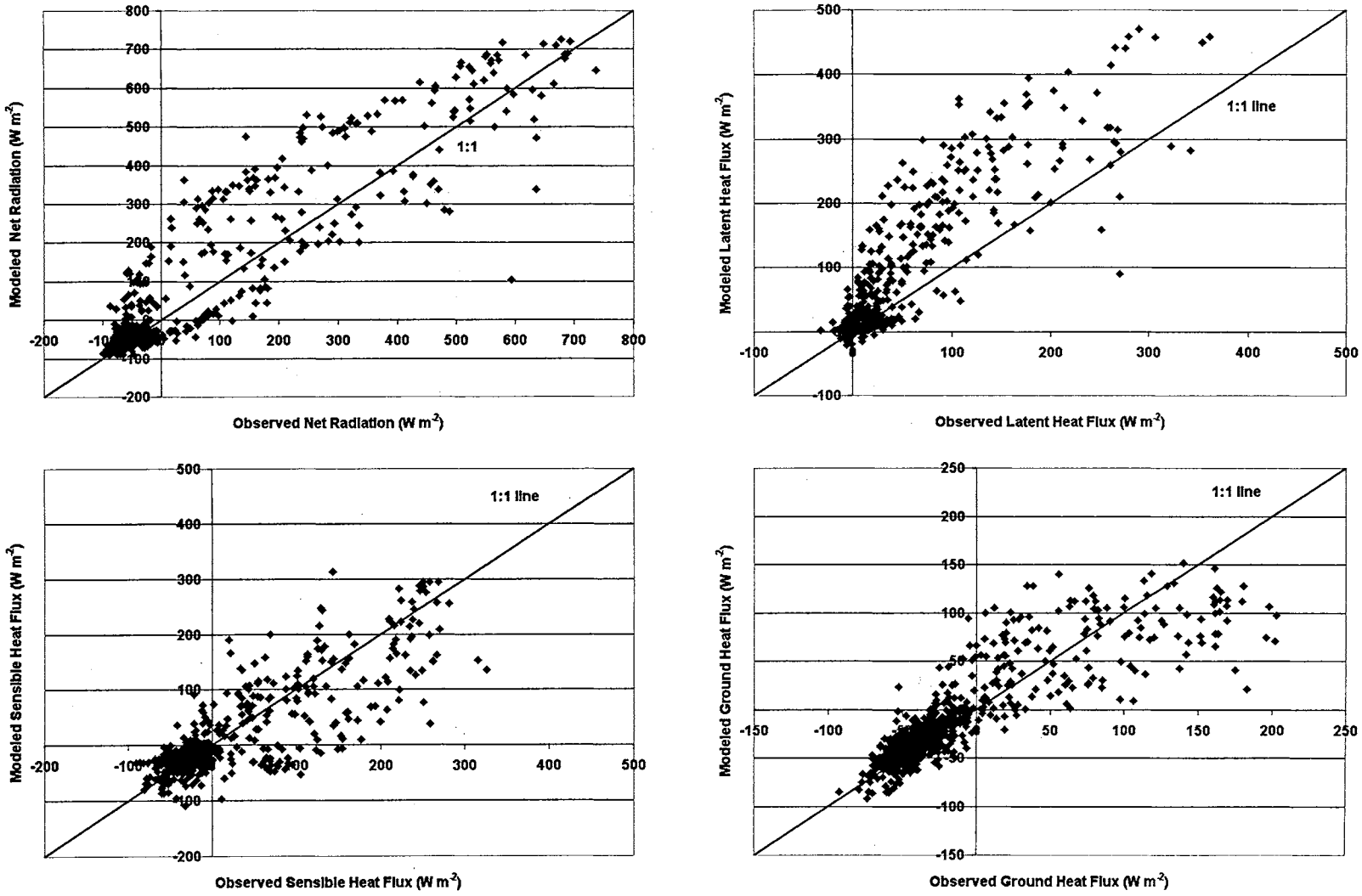

Figure C-14. Comparison of hourly average observed and modeled R_n, LH, SH and GH for the NORM site.

APPENDIX D

SCALE COMPARISONS OF MODELED SURFACE ENERGY-BALANCE COMPONENTS FOR THE HETEROGENEOUS AND THE HOMOGENEOUS AREA

(Supplement to Chapter 5)

Table D-1. The heterogeneous area (Cell 21) model output using area-averaged vegetation fraction.

Date		2 km				20 km			
		R_n ($MJm^{-2}d^{-1}$)	LH ($MJm^{-2}d^{-1}$)	SH ($MJm^{-2}d^{-1}$)	GH ($MJm^{-2}d^{-1}$)	R_n ($MJm^{-2}d^{-1}$)	LH ($MJm^{-2}d^{-1}$)	SH ($MJm^{-2}d^{-1}$)	GH ($MJm^{-2}d^{-1}$)
18-Jun-97	MAX	19.56	15.95	7.96	3.10				
	MIN	17.75	8.50	1.06	1.70				
	AVE	18.31	13.24	2.86	2.21	18.39	12.83	2.89	2.67
23-Jun-97	MAX	11.25	9.70	3.92	0.49				
	MIN	10.06	7.28	0.73	-0.06				
	AVE	10.28	8.65	1.50	0.17	10.35	8.00	1.75	0.63
25-Jun-97	MAX	17.40	13.31	8.09	2.12				
	MIN	15.81	7.19	2.29	1.11				
	AVE	16.29	10.89	3.98	1.42	16.21	9.94	4.67	1.61
27-Jun-97	MAX	15.20	11.85	7.20	1.13				
	MIN	13.81	6.87	2.12	0.45				
	AVE	14.21	10.05	3.43	0.73	14.22	9.42	3.73	1.07
30-Jun-97	MAX	19.74	14.83	9.56	2.48				
	MIN	17.91	7.70	2.64	1.37				
	AVE	18.41	11.87	4.79	1.75	18.45	10.45	5.85	2.15
03-Jul-97	MAX	19.79	15.08	10.98	1.19				
	MIN	17.94	7.62	3.67	0.27				
	AVE	18.52	11.80	6.12	0.60	18.33	9.88	7.59	0.87
06-Jul-97	MAX	17.20	12.41	8.38	2.12				
	MIN	15.51	6.70	2.87	1.10				
	AVE	16.05	9.97	4.66	1.42	15.91	8.18	6.09	1.65
11-Jul-97	MAX	9.26	7.64	3.17	0.90				
	MIN	8.27	5.53	0.58	0.17				
	AVE	8.46	6.77	1.22	0.48	8.42	5.88	1.65	0.90
14-Jul-97	MAX	19.29	12.95	10.18	1.96				
	MIN	17.46	7.14	4.40	0.97				
	AVE	17.96	10.29	6.47	1.20	17.77	7.96	8.47	1.33
15-Jul-97	MAX	6.63	7.10	2.32	-0.26				
	MIN	5.86	4.80	-0.25	-0.75				
	AVE	6.06	6.03	0.58	-0.54	5.91	4.89	1.41	-0.40
20-Jul-97	MAX	8.76	6.80	2.04	1.93				
	MIN	7.87	4.93	0.30	0.72				
	AVE	8.01	6.17	0.59	1.25	8.06	5.47	0.64	1.95
22-Jul-97	MAX	17.63	12.45	6.14	3.18				
	MIN	16.05	8.31	2.41	1.50				
	AVE	16.40	10.94	3.34	2.11	16.39	9.78	3.78	2.84
23-Jul-97	MAX	17.51	13.21	6.34	2.95				
	MIN	15.94	8.22	1.82	1.40				
	AVE	16.37	11.41	2.97	1.99	16.29	9.93	3.65	2.71

Table D-2. The homogeneous area (Cell 9) model output using area-averaged vegetation fraction.

Date		2 km				20 km			
		R_n ($MJm^{-2}d^{-1}$)	LH ($MJm^{-2}d^{-1}$)	SH ($MJm^{-2}d^{-1}$)	GH ($MJm^{-2}d^{-1}$)	R_n ($MJm^{-2}d^{-1}$)	LH ($MJm^{-2}d^{-1}$)	SH ($MJm^{-2}d^{-1}$)	GH ($MJm^{-2}d^{-1}$)
18-Jun-97	MAX	15.36	12.19	3.28	2.24				
	MIN	14.74	9.28	1.26	1.64				
	AVE	14.91	10.54	2.60	1.78	14.85	10.33	2.73	1.80
23-Jun-97	MAX	9.18	7.98	2.51	-0.18				
	MIN	8.91	6.76	1.38	-0.36				
	AVE	9.00	7.41	1.91	-0.31	9.02	7.44	1.79	-0.21
25-Jun-97	MAX	14.79	10.16	5.31	1.24				
	MIN	14.25	7.74	3.68	0.82				
	AVE	14.40	8.69	4.78	0.92	14.30	8.62	4.86	0.82
27-Jun-97	MAX	17.70	13.24	5.29	1.73				
	MIN	17.10	10.55	3.26	1.00				
	AVE	17.30	11.72	4.48	1.11	17.24	11.47	4.66	1.11
30-Jun-97	MAX	16.92	14.63	2.68	2.12				
	MIN	16.31	11.99	0.70	1.40				
	AVE	16.49	12.97	1.92	1.60	16.41	12.43	2.28	1.69
03-Jul-97	MAX	18.55	15.33	5.64	0.42				
	MIN	17.83	12.11	3.02	0.07				
	AVE	18.04	13.26	4.67	0.10	17.90	12.95	4.92	0.02
06-Jul-97	MAX	17.80	13.34	5.18	1.45				
	MIN	17.14	10.92	3.29	0.96				
	AVE	17.27	11.44	4.78	1.05	17.22	11.19	5.01	1.02
11-Jul-97	MAX	7.03	6.80	0.81	0.46				
	MIN	6.84	5.73	-0.09	0.18				
	AVE	6.89	6.51	0.16	0.21	6.86	6.63	-0.03	0.25
14-Jul-97	MAX	17.17	12.03	6.86	0.83				
	MIN	16.62	9.15	4.60	0.40				
	AVE	16.72	10.39	5.85	0.49	16.68	10.28	5.89	0.51
15-Jul-97	MAX	8.96	7.39	2.59	0.60				
	MIN	8.65	5.56	1.14	0.26				
	AVE	8.70	6.61	1.78	0.32	8.66	6.60	1.81	0.25
20-Jul-97	MAX	8.70	7.45	0.64	1.34				
	MIN	8.46	6.86	0.21	0.83				
	AVE	8.51	7.17	0.47	0.87	8.50	7.18	0.49	0.83
22-Jul-97	MAX	18.48	12.89	4.95	2.47				
	MIN	17.91	11.08	3.53	1.68				
	AVE	18.02	11.53	4.66	1.83	17.96	11.34	4.84	1.78
23-Jul-97	MAX	18.73	13.69	5.12	2.08				
	MIN	18.18	11.50	3.75	1.29				
	AVE	18.31	12.09	4.76	1.45	18.24	11.90	4.91	1.44

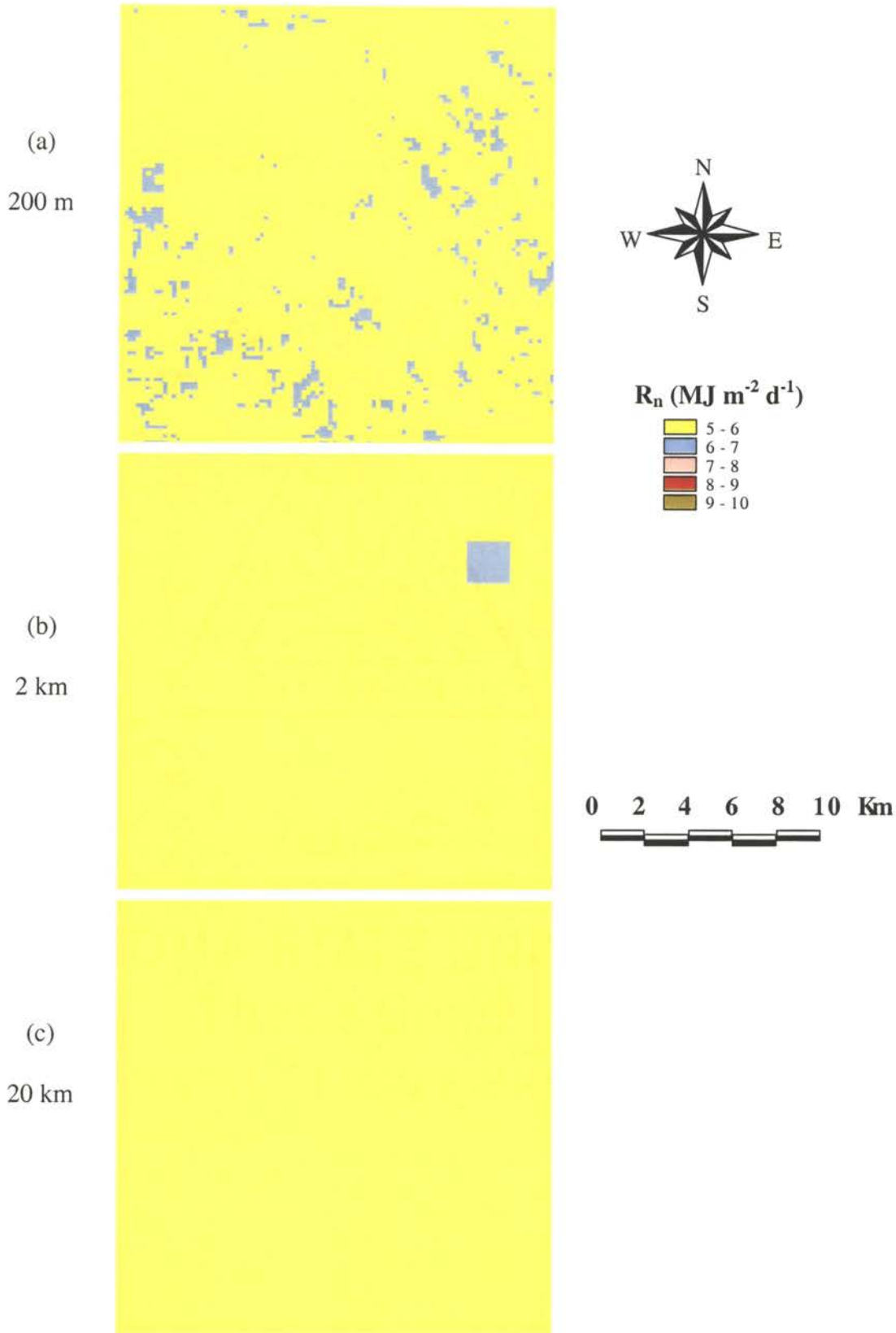

Figure D-1. Scale comparisons of modeled net radiation (R_n) for the heterogeneous area (Cell 21) for 15 July 97.

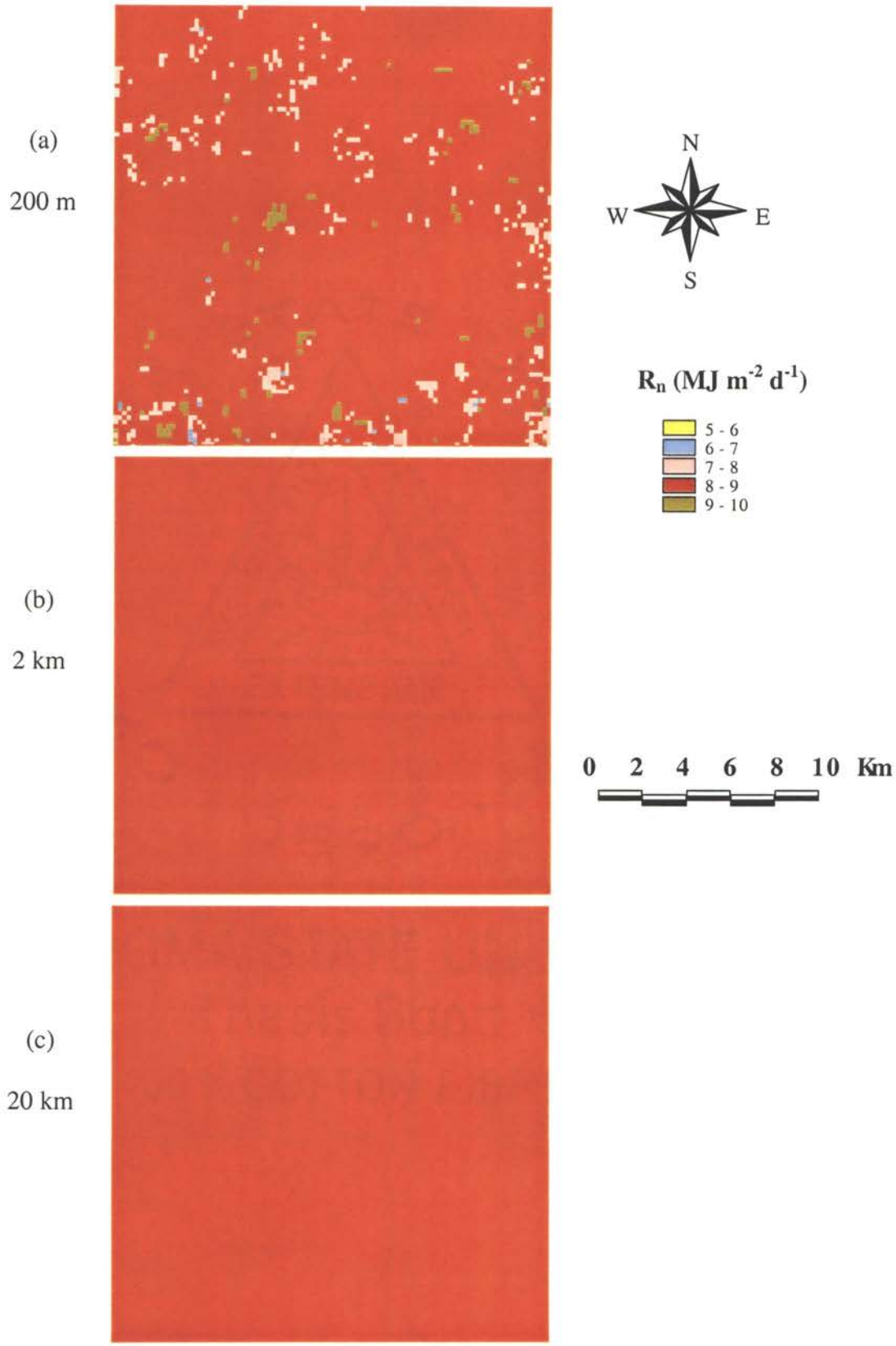

Figure D-2. Scale comparisons of modeled net radiation (R_n) for the homogeneous area (Cell 9) for 15 July 97.

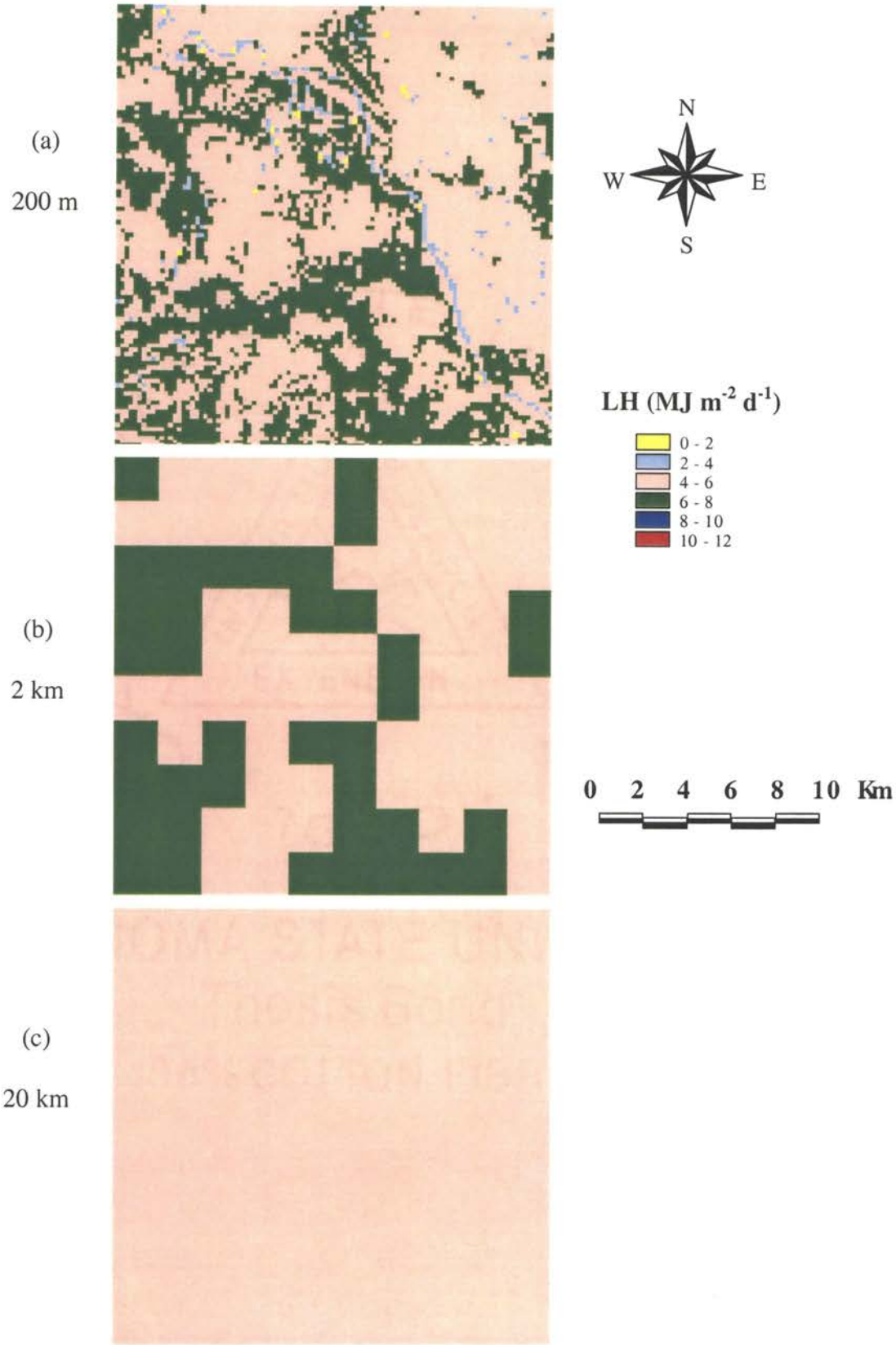

Figure D-3. Scale comparisons of modeled latent heat flux (LH) for the heterogeneous area (Cell 21) for 15 July 97.

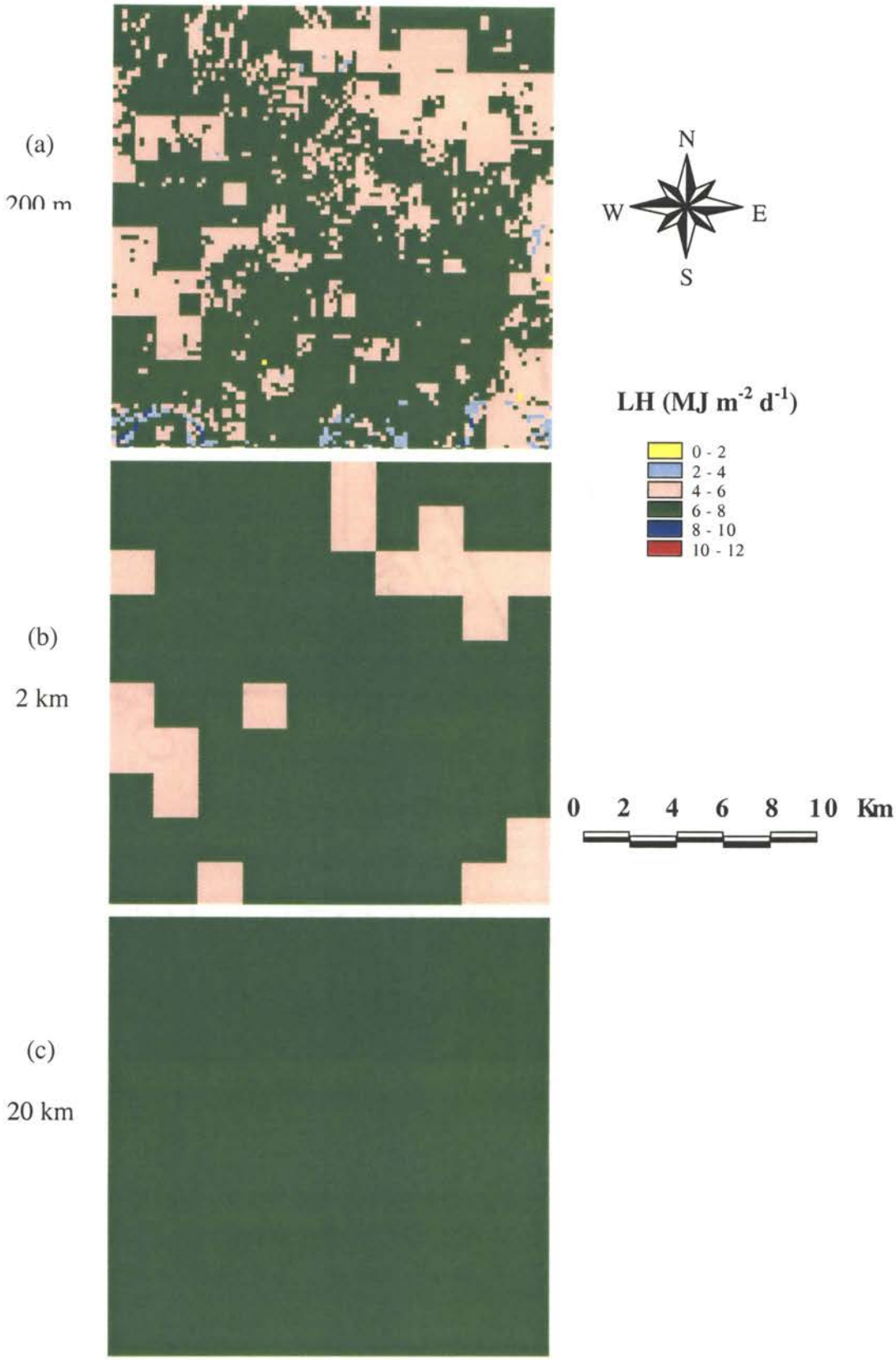

Figure D-4. Scale comparisons of modeled latent heat flux (LH) for the homogeneous area (Cell 9) for 15 July 97.

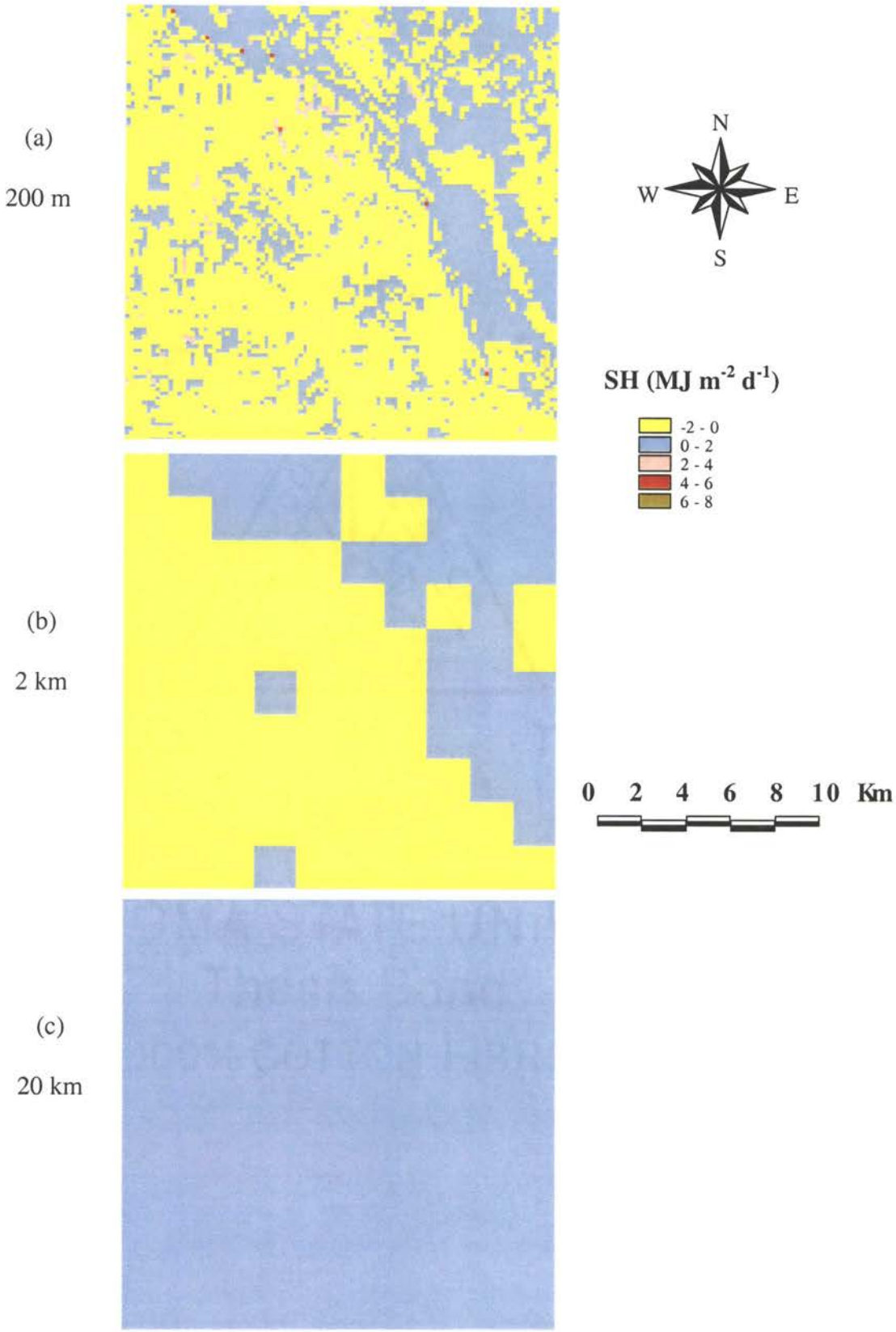

Figure D-5. Scale comparisons of modeled sensible heat flux (SH) for the heterogeneous area (Cell 21) for 15 July 97.

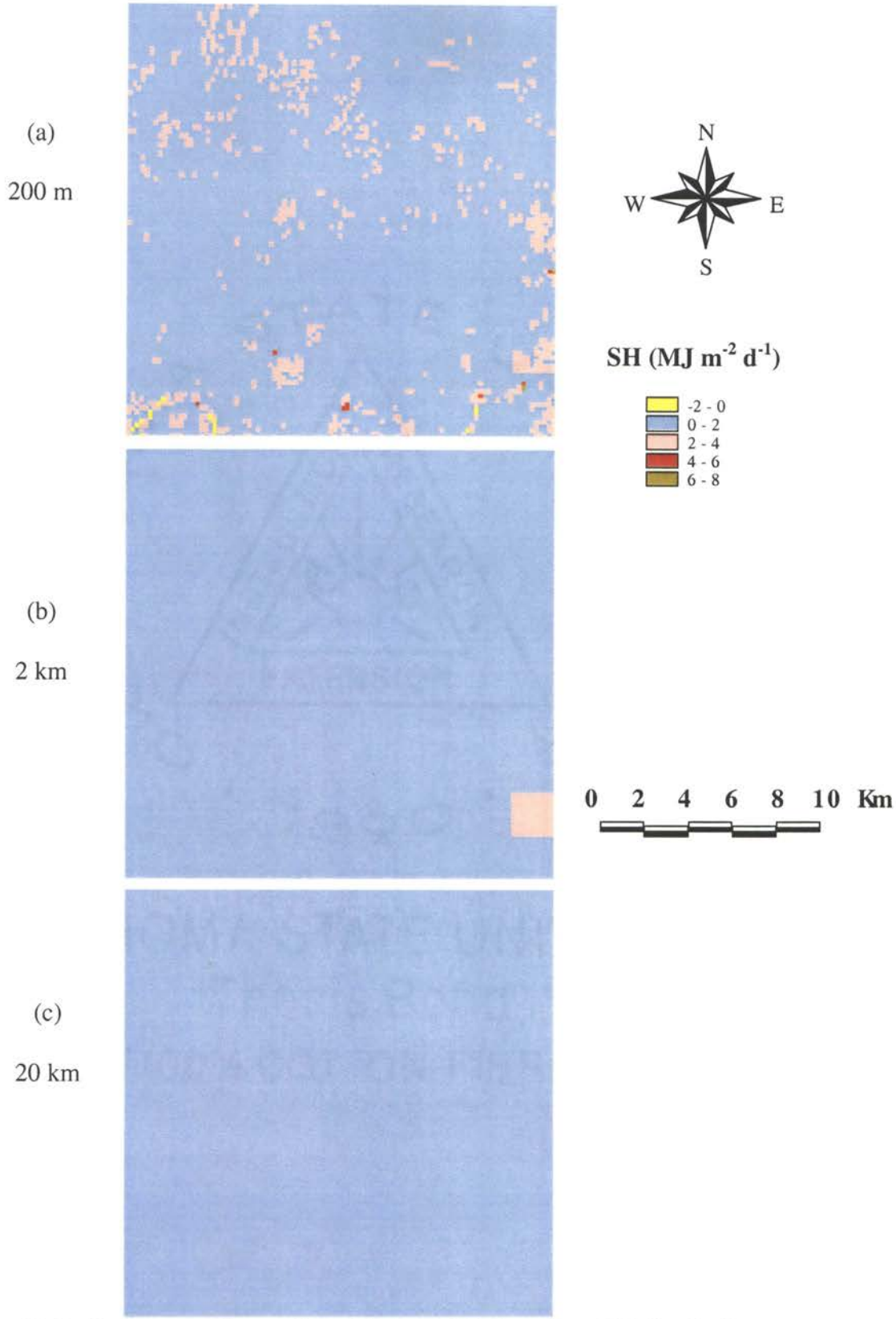

Figure D-6. Scale comparisons of modeled sensible heat flux (SH) for the homogeneous area (Cell 9) for 15 July 97.

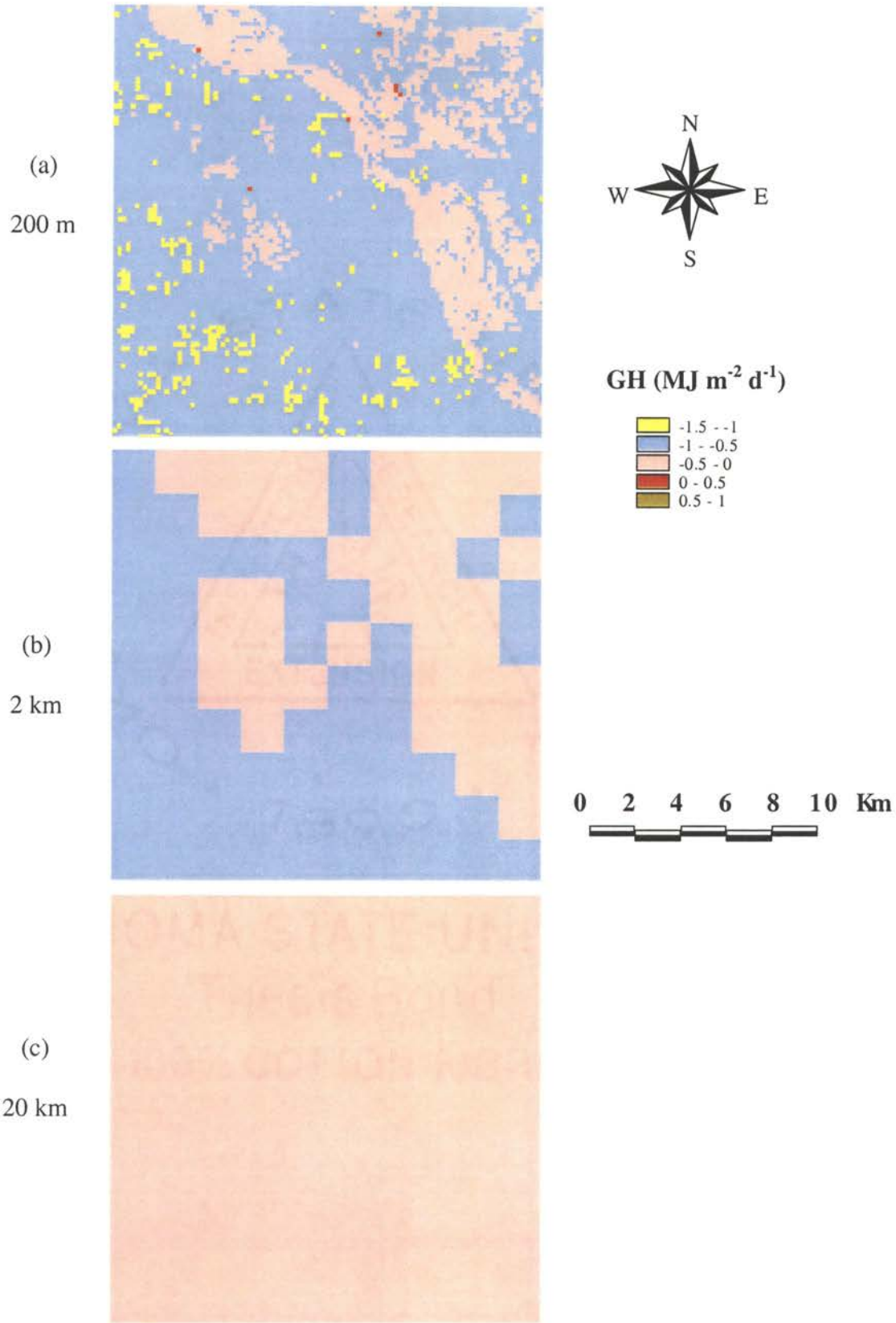

Figure D-7. Scale comparisons of modeled ground heat flux (GH) for the heterogeneous area (Cell 21) for 15 July 97.

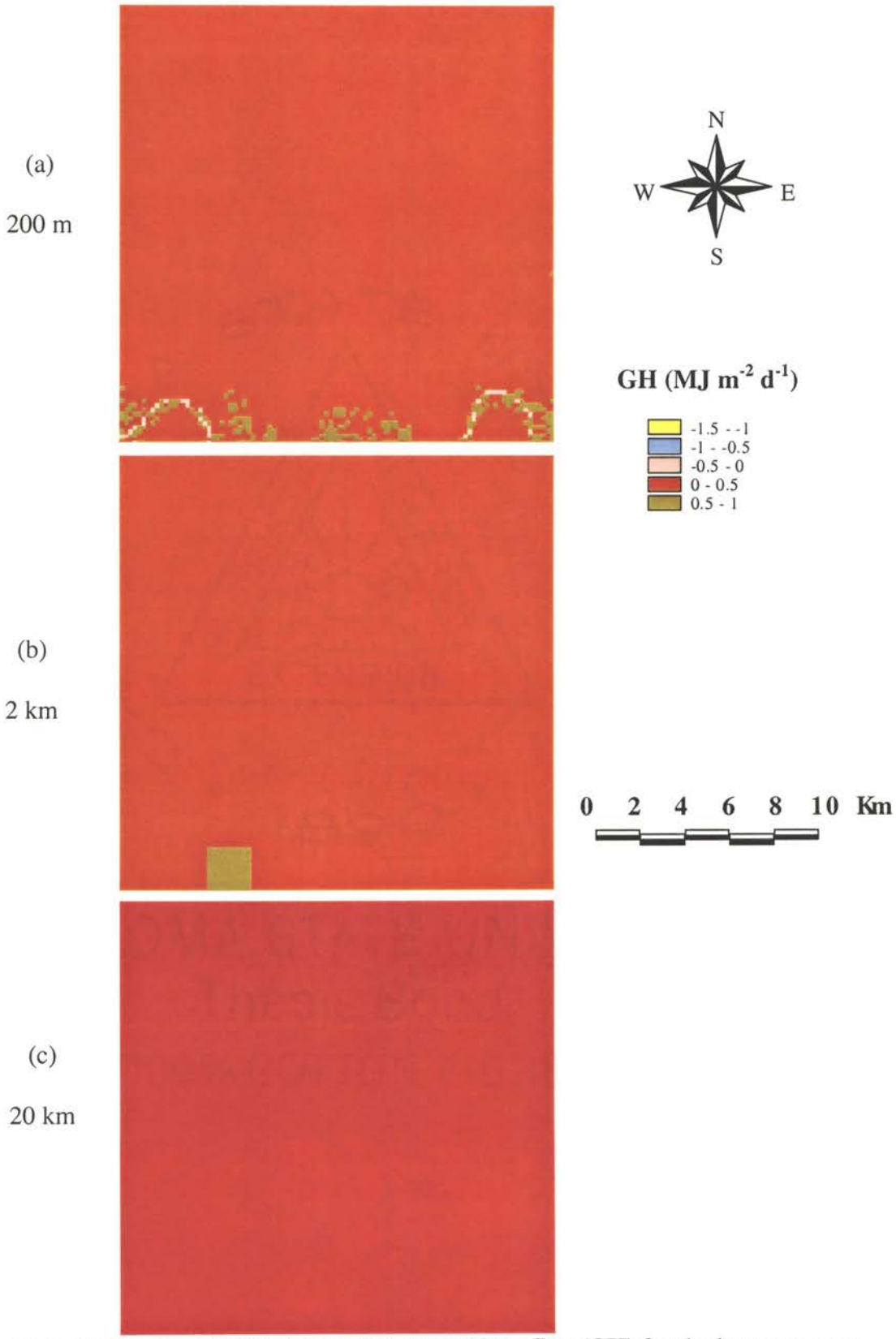

Figure D-8. Scale comparisons of modeled ground heat flux (GH) for the homogeneous area (Cell 9) for 15 July 97.

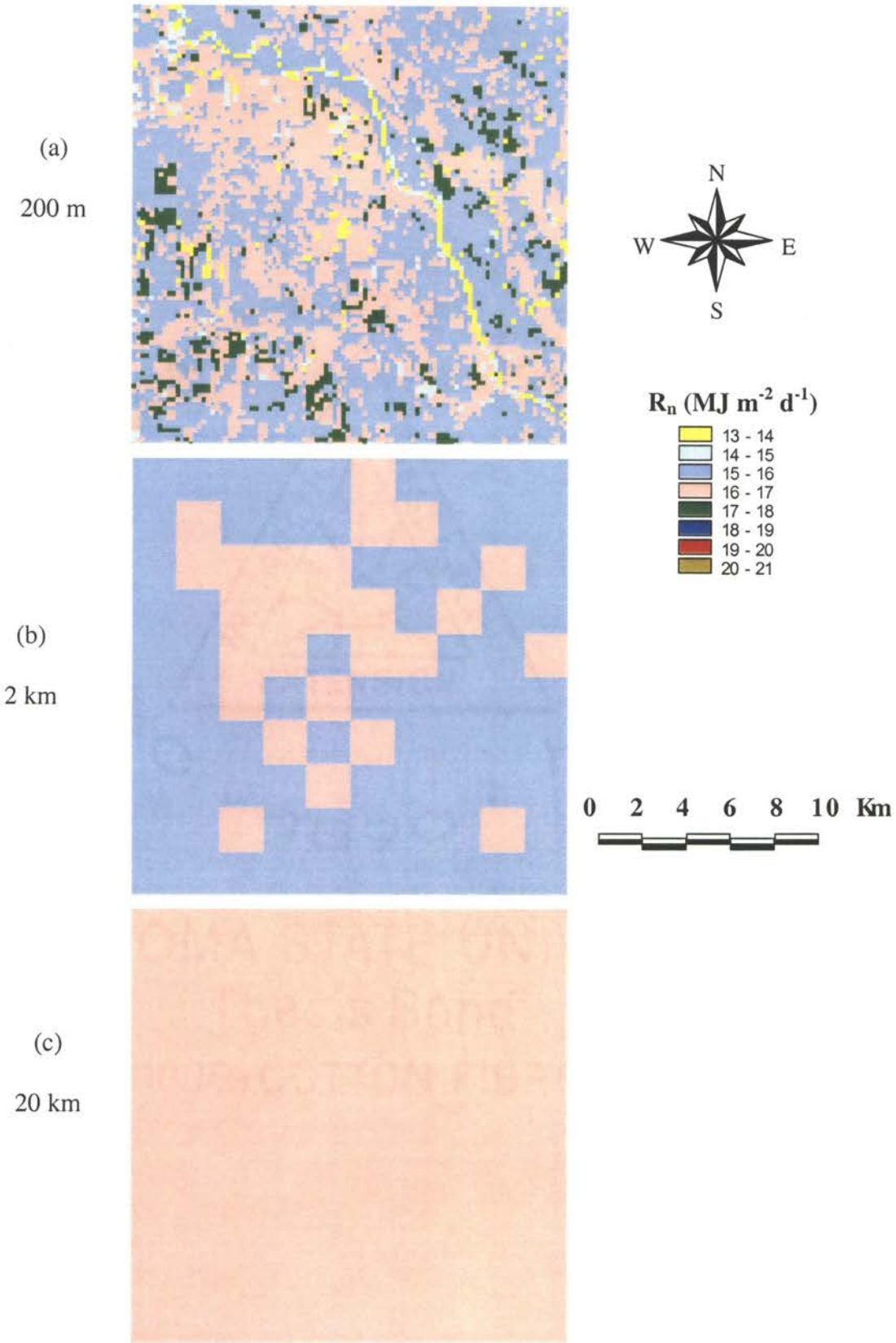

Figure D-9. Scale comparisons of modeled net radiation (R_n) for the heterogeneous area (Cell 21) for 23 July 97.

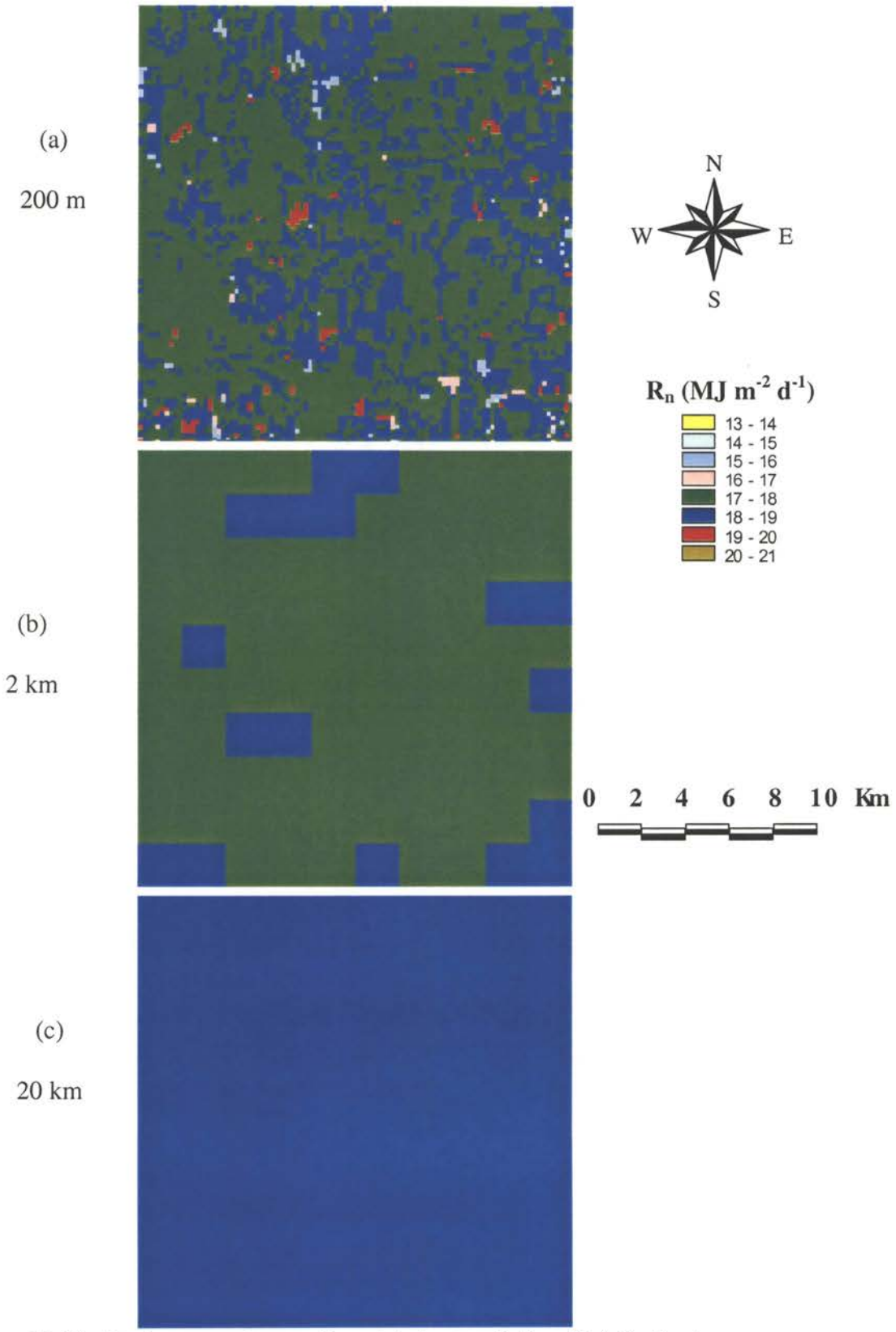

Figure D-10. Scale comparisons of modeled net radiation (R_n) for the homogeneous area (Cell 9) for 23 July 97.

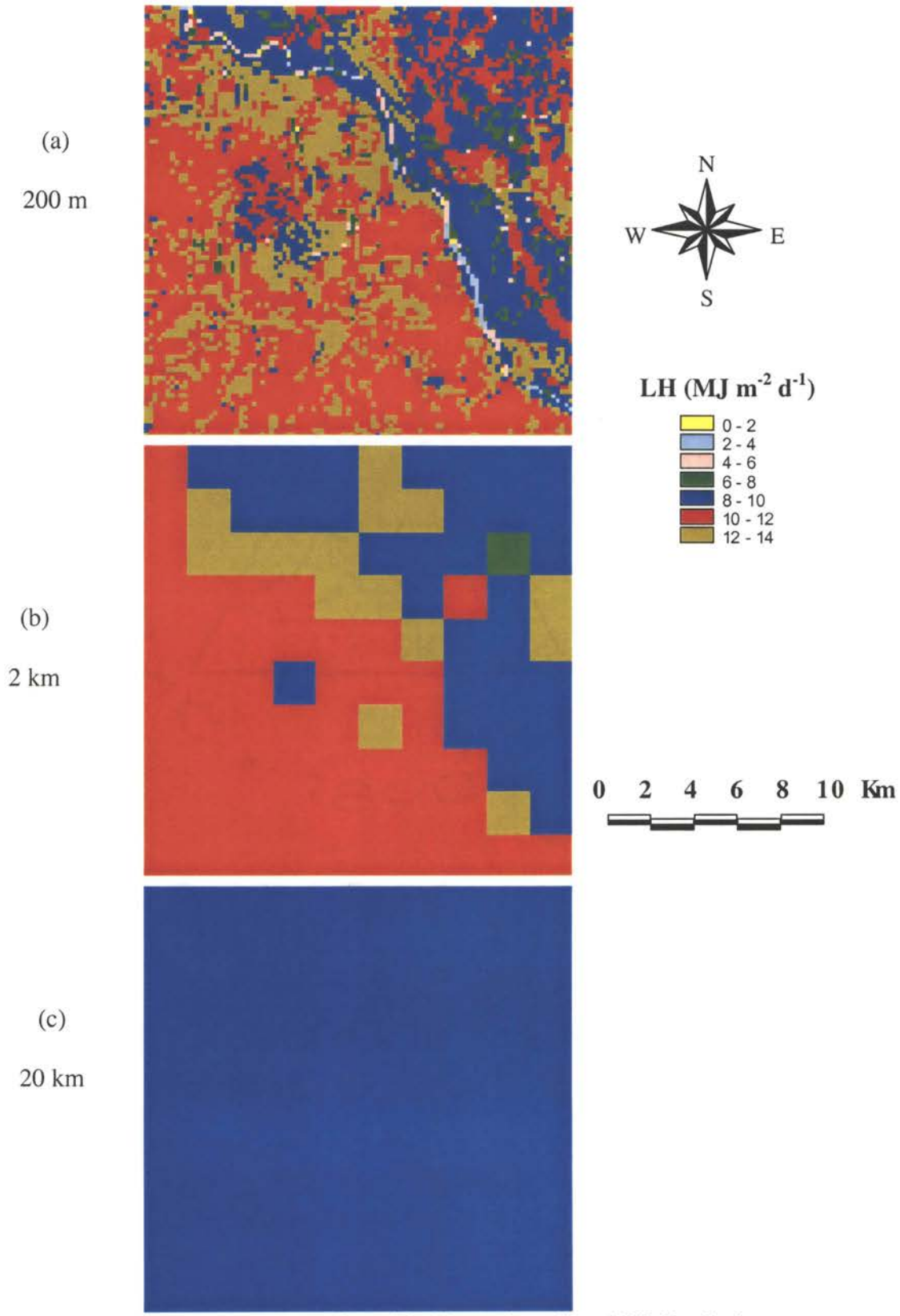

Figure D-11. Scale comparisons of modeled latent heat flux (LH) for the heterogeneous area (Cell 21) for 23 July 97.

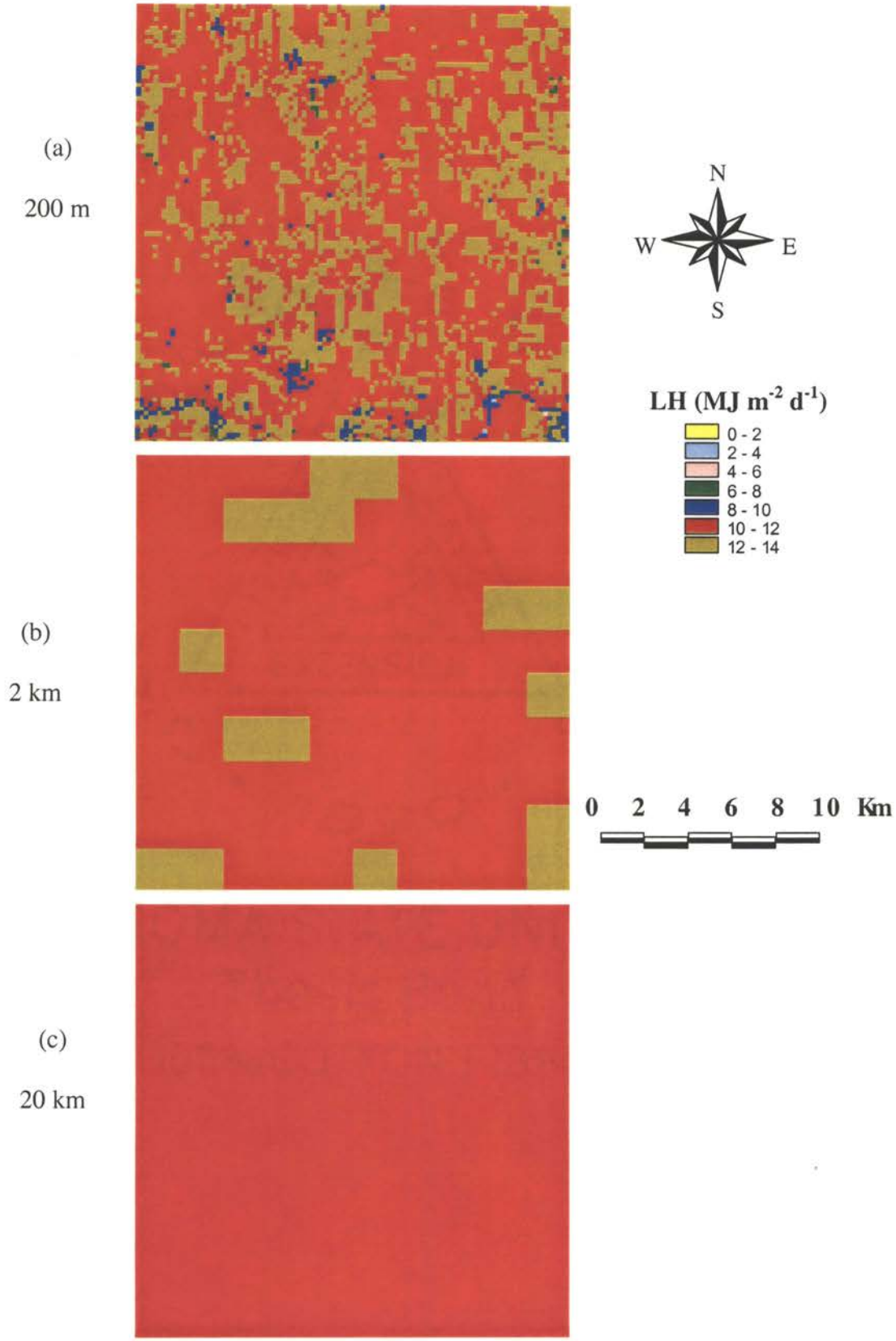

Figure D-12. Scale comparisons of modeled latent heat flux (LH) for the homogeneous area (Cell 9) for 23 July 97.

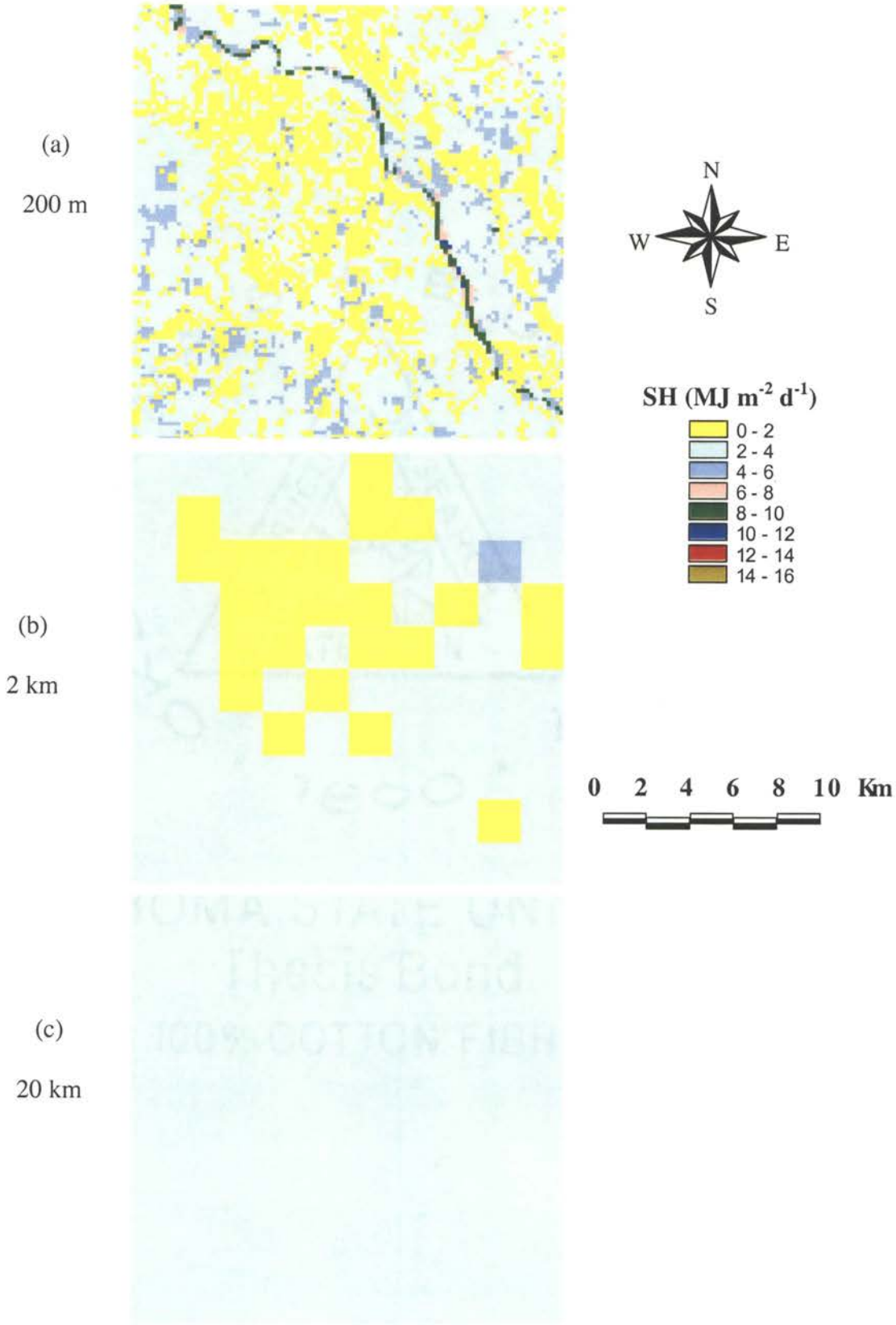

Figure D-13. Scale comparisons of modeled sensible heat flux (SH) for the heterogeneous area (Cell 21) for 23 July 97.

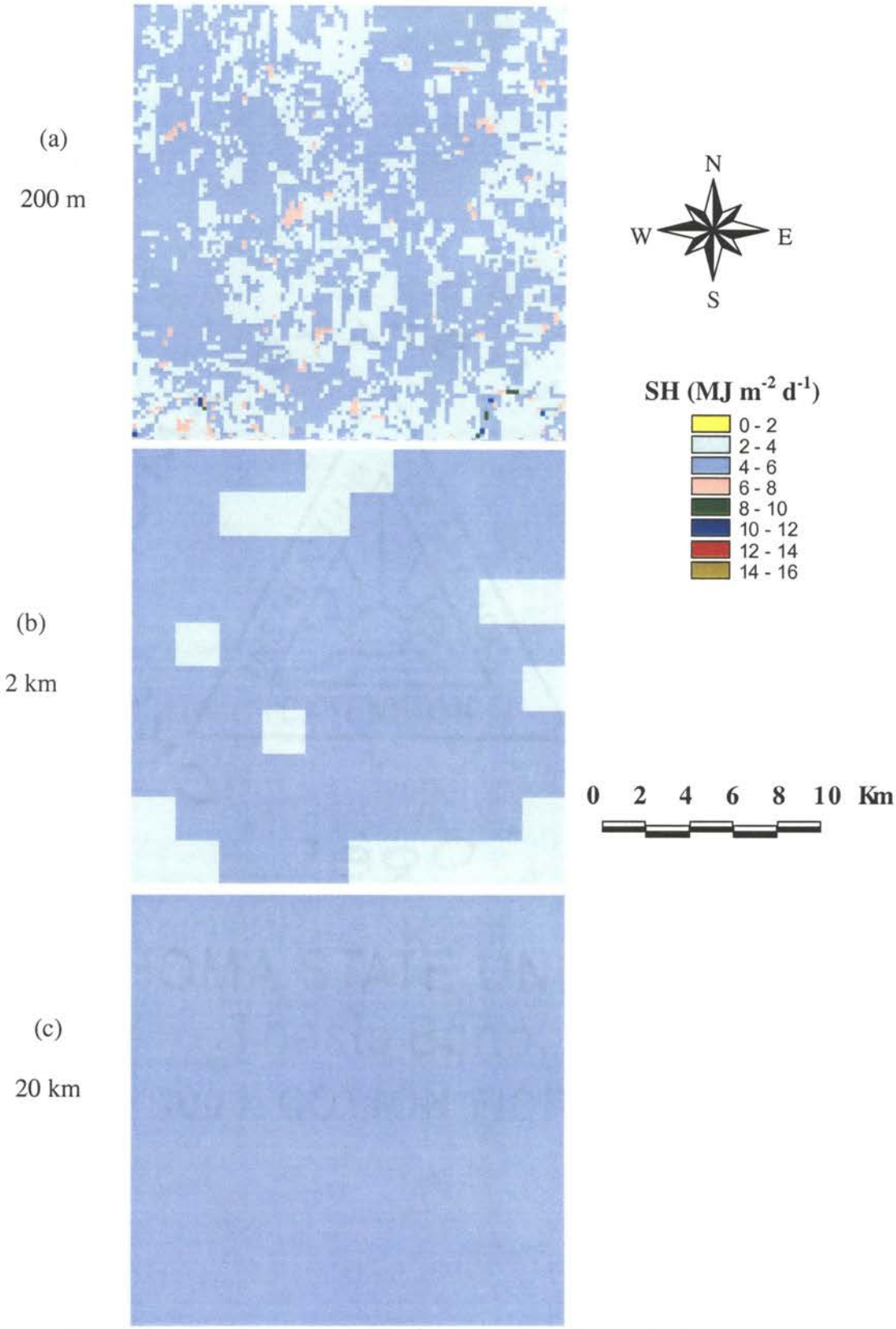

Figure D-14. Scale comparisons of modeled sensible heat flux (SH) for the homogeneous area (Cell 9) for 23 July 97.

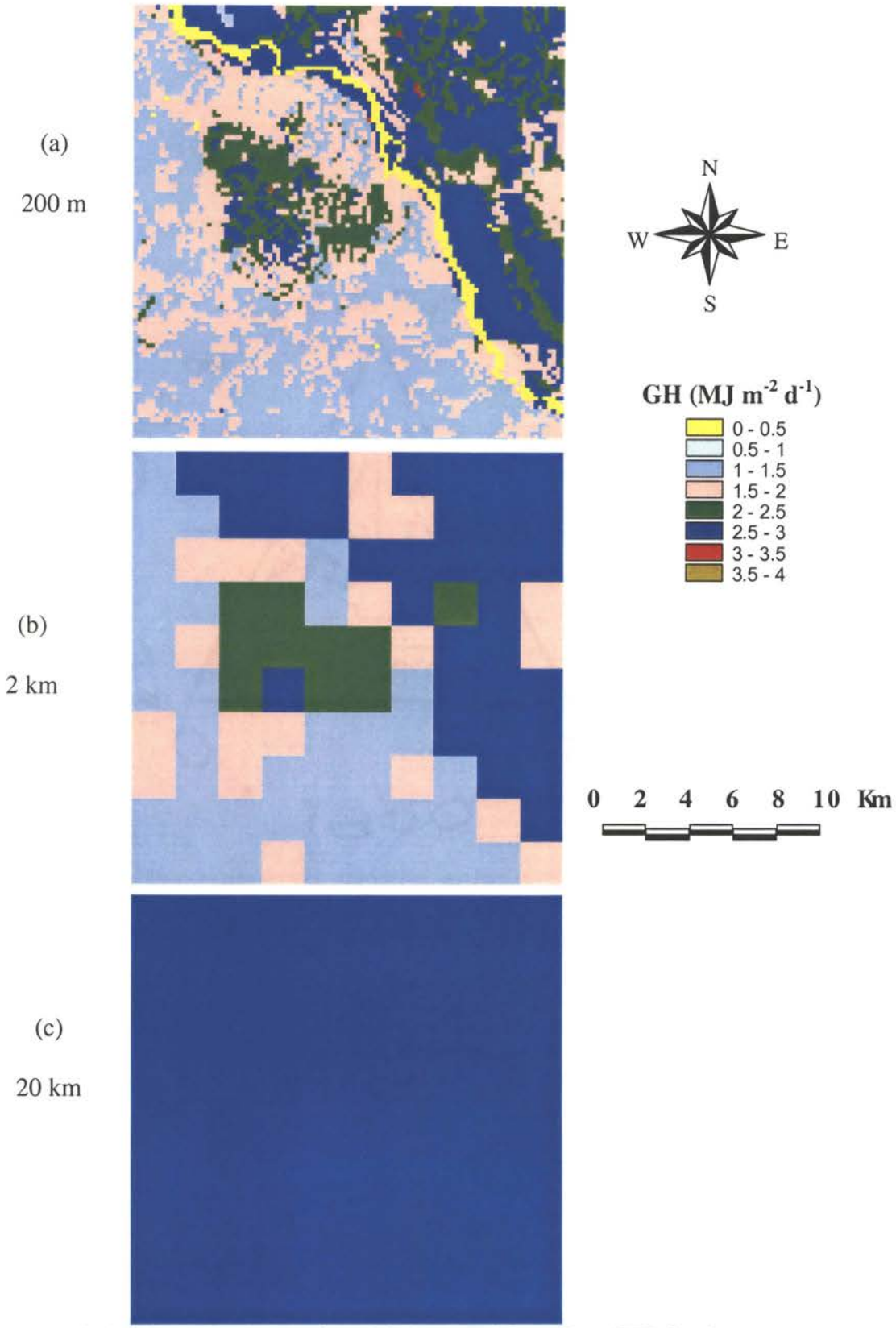

Figure D-15. Scale comparisons of modeled ground heat flux (GH) for the heterogeneous area (Cell 21) for 23 July 97.

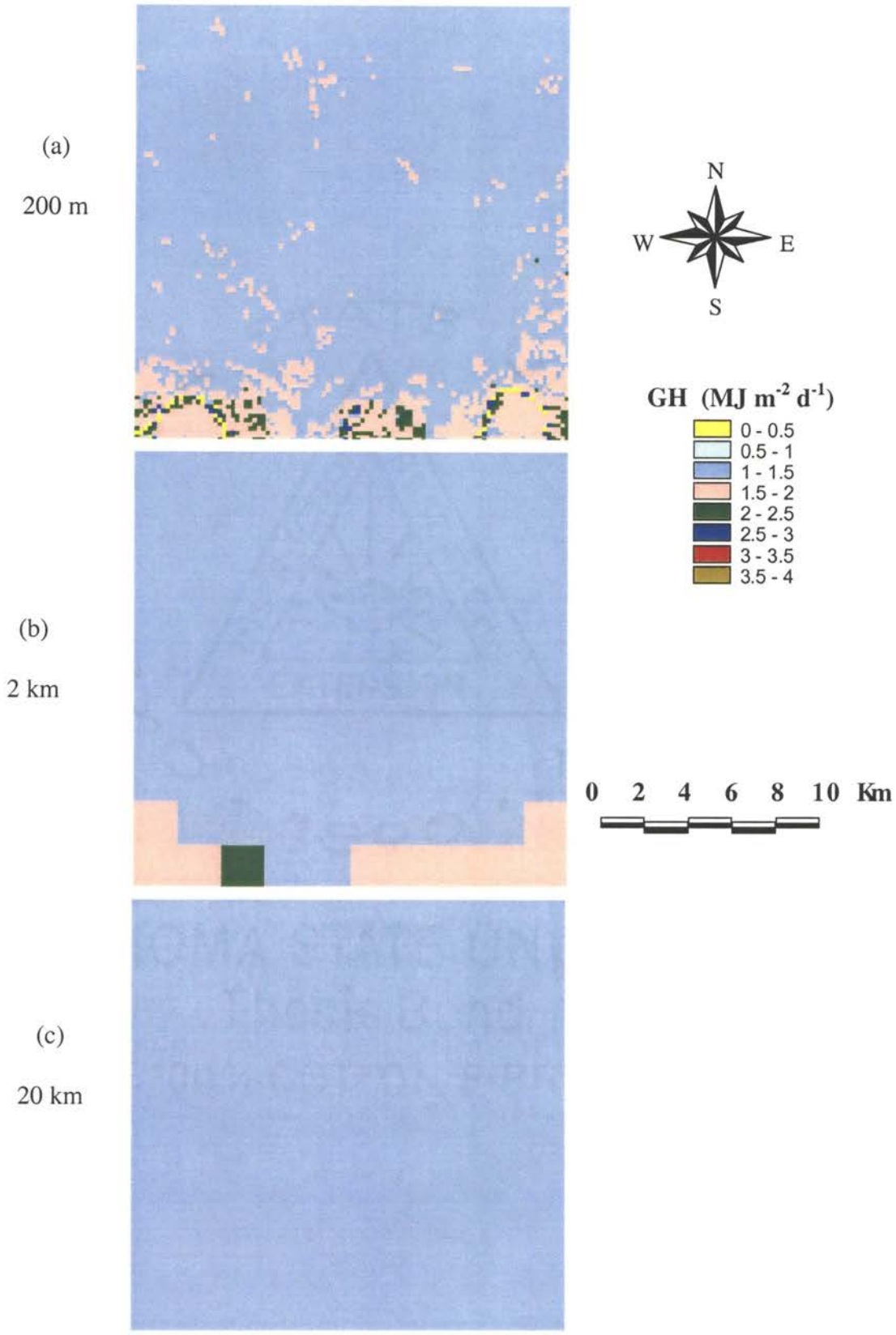

Figure D-16. Scale comparisons of modeled ground heat flux (GH) for the homogeneous area (Cell 9) for 23 July 97.

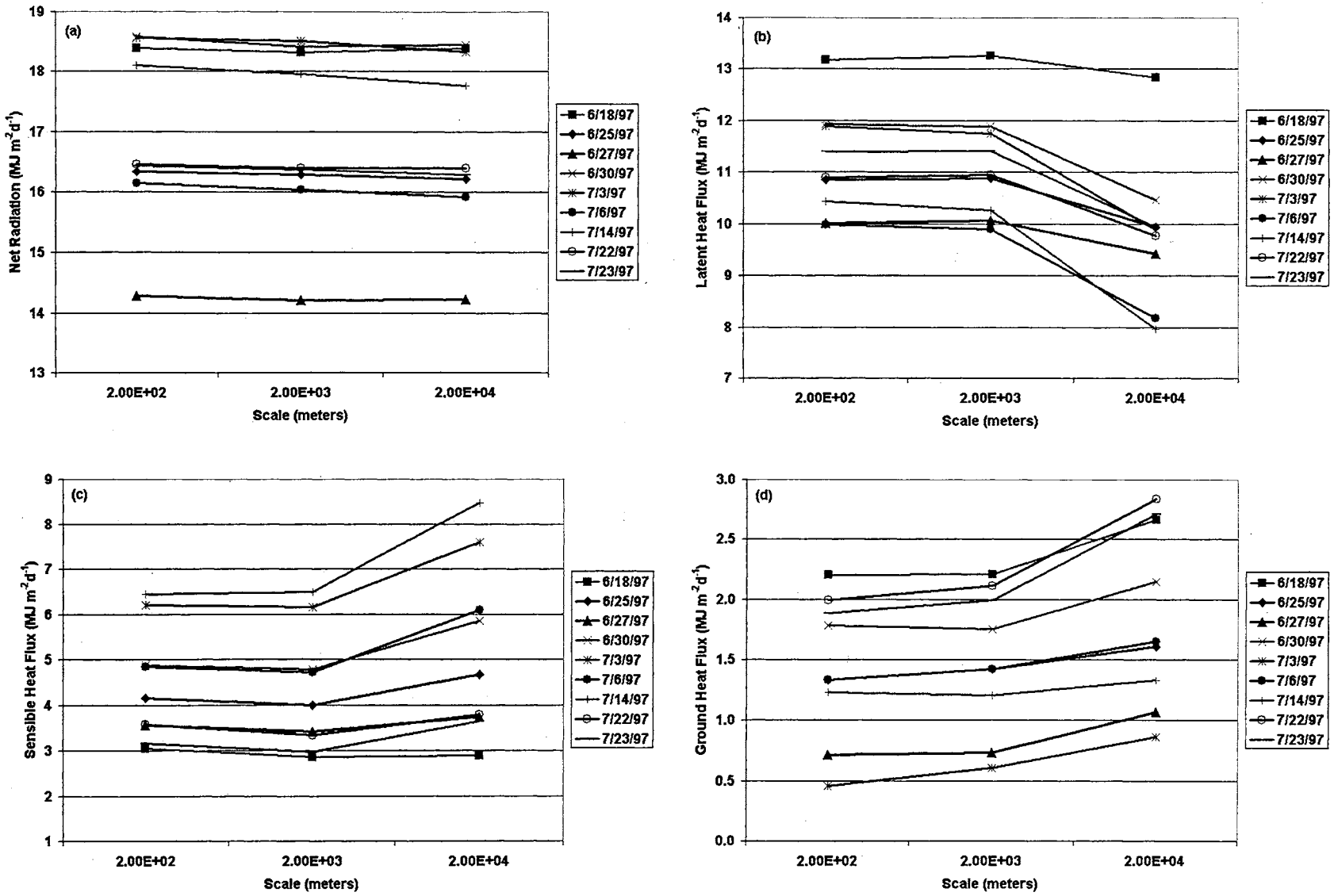

Figure D-17. Scale deviations observed from the heterogeneous area (Cell 21) clear-day model output.

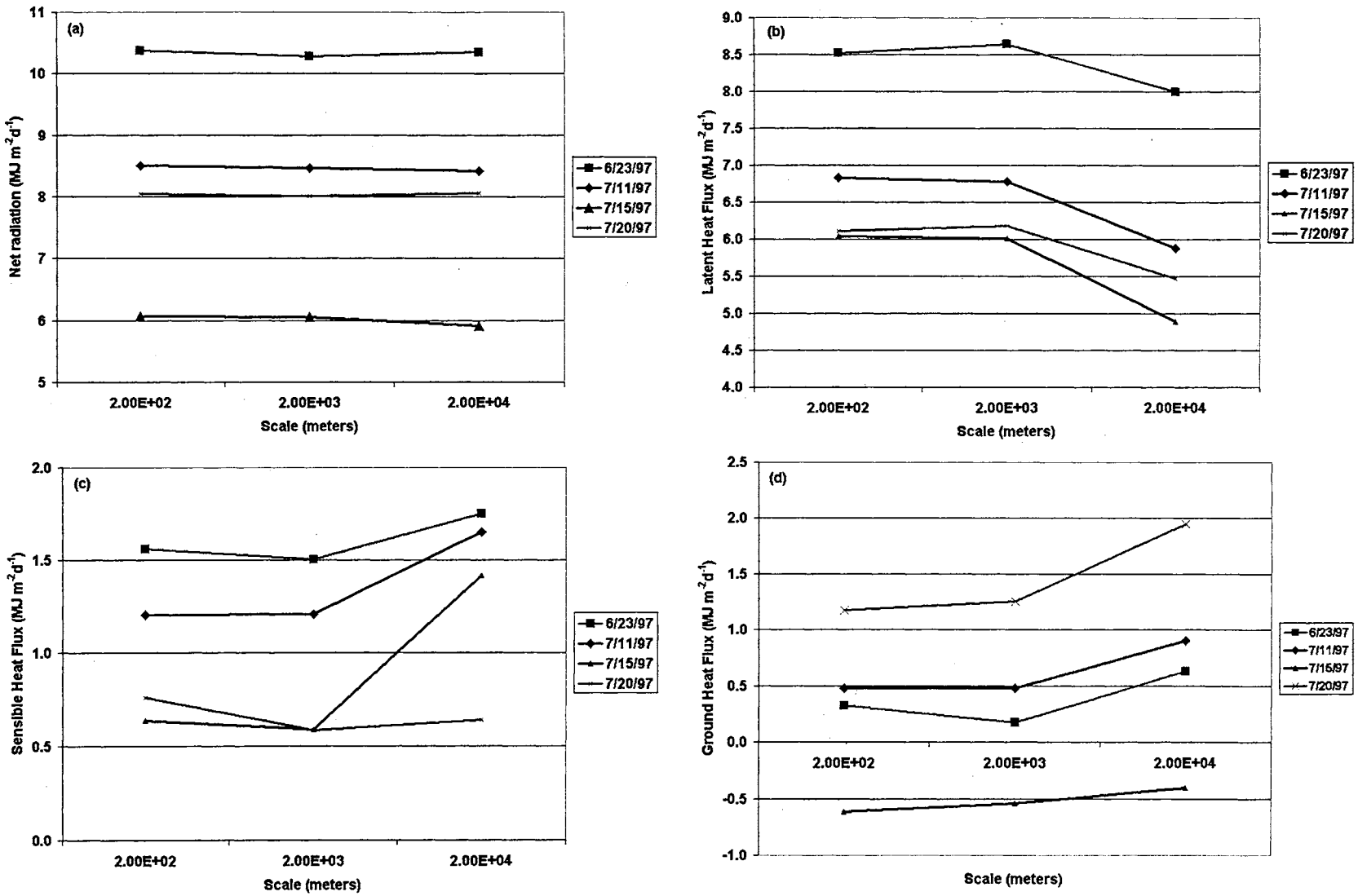

Figure D-18. Scale deviations observed from the heterogeneous area (Cell 21) cloudy-day model output.

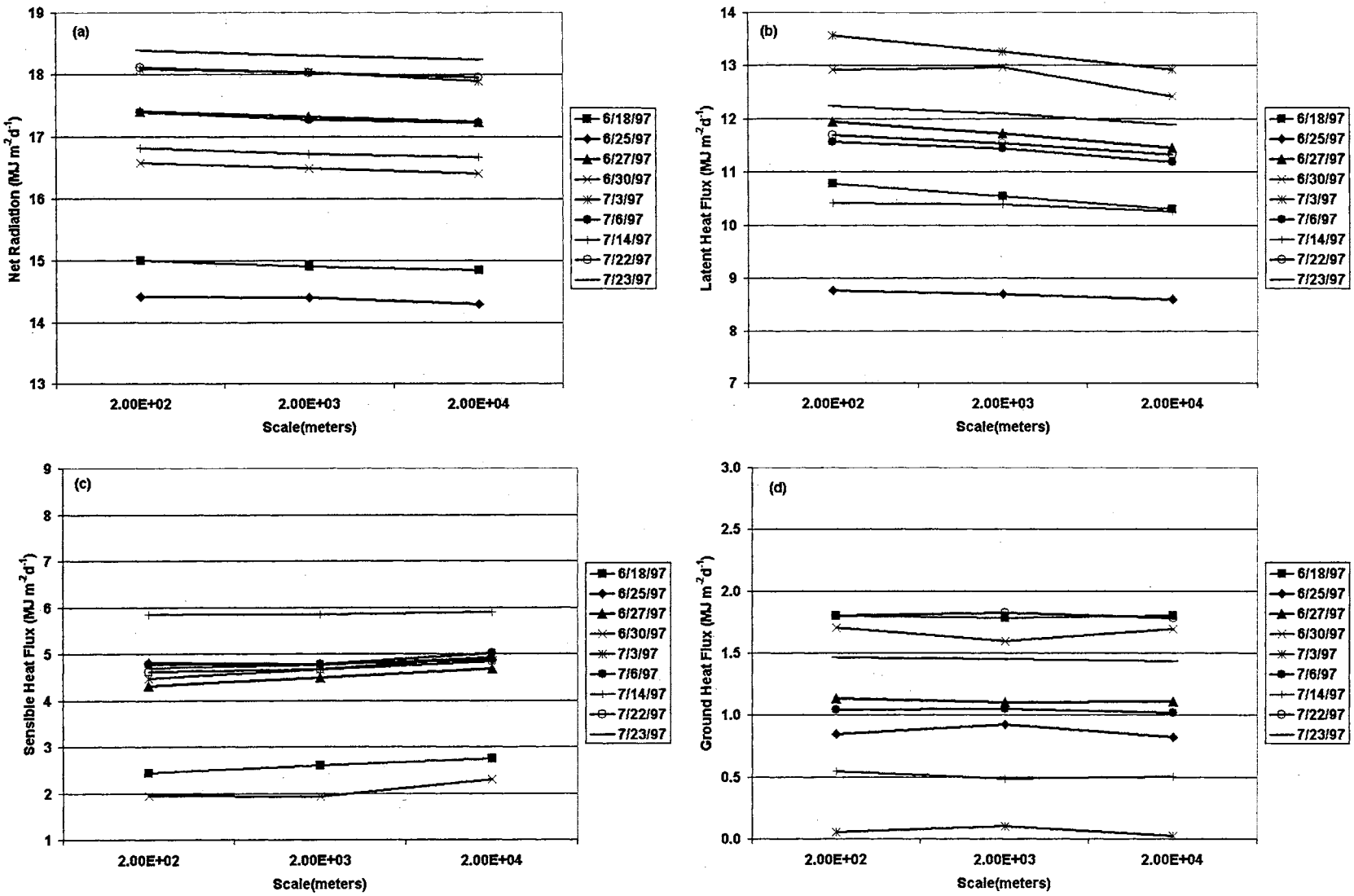

Figure D-19. Scale deviations observed from the homogeneous area (Cell 9) clear-day model output.

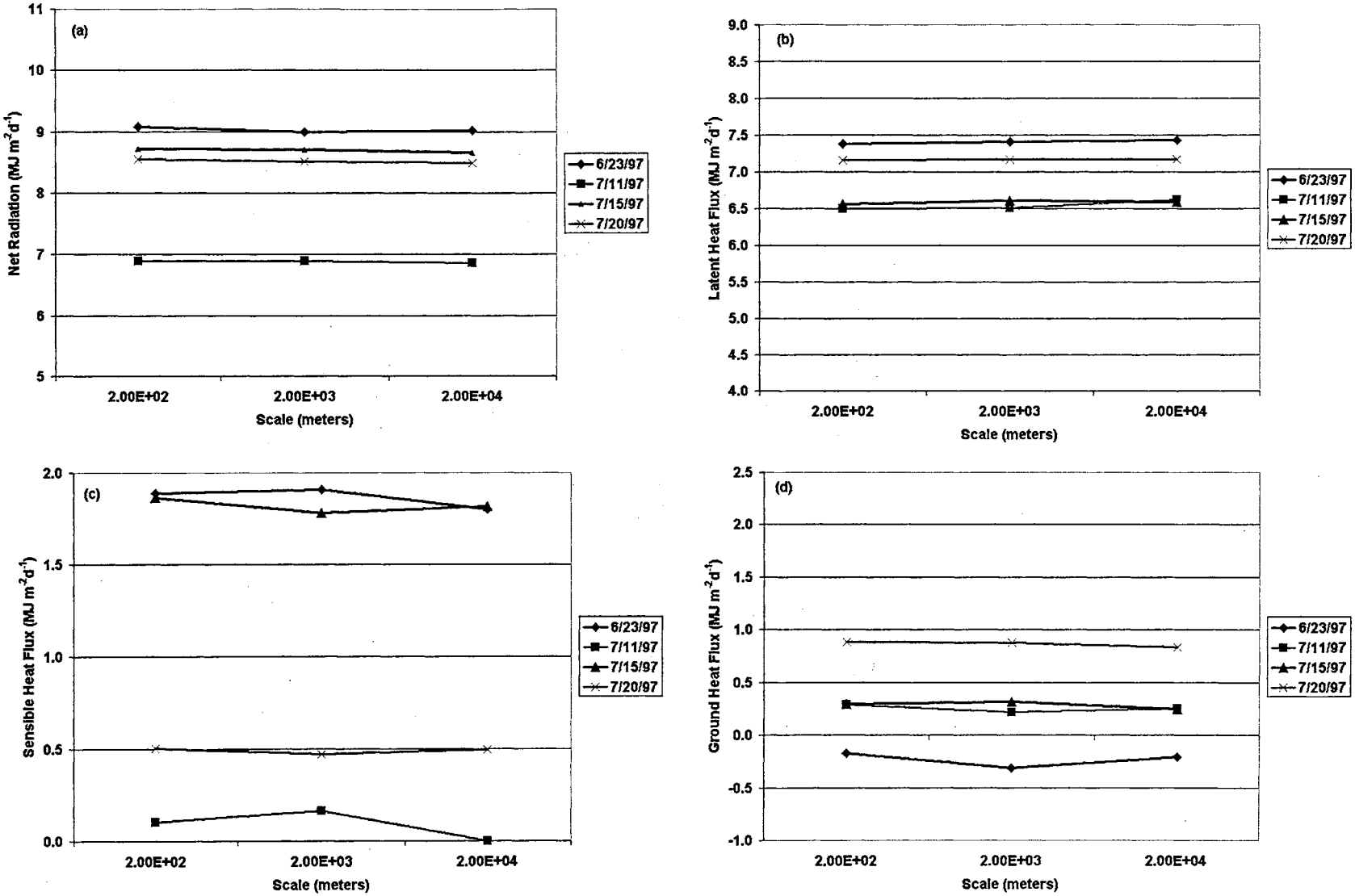

Figure D-20. Scale deviations observed from the homogeneous area (Cell 9) cloudy-day model output.

VITA

Venkataramana Rao Sridhar

Candidate for the Degree of

Doctor of Philosophy

Thesis: LAND SURFACE MODELING OF ENERGY-BALANCE COMPONENTS: MODEL VALIDATION AND SCALING EFFECTS

Major Field: Biosystems Engineering

Biographical:

Personal Data: Born in Tirukoilur, Tamil Nadu, India, On July 24, 1969.

Education: Graduated (12^{th}) from St. Joseph's Higher Secondary School, Cuddalore, India in June 1986; received Bachelor of Engineering in Agricultural Engineering from the Tamil Nadu Agricultural University, Coimbatore, India in March 1991; received Master of Engineering in Irrigation Engineering and Management from the Asian Institute of Technology, Bangkok, Thailand in August 1994; completed the requirements for the Doctor of Philosophy with a major in Biosystems Engineering at Oklahoma State University in August 2001.

Experience: Employed as a Service Engineer by Tractor and Farm Equipment Ltd., Madras, 1992; employed as a Consultant Engineer by Environmental Technologic Thai Co. Ltd., Bangkok, Thailand, 1994-95; employed as a Water Resources Engineer by STS Engineering Consultants Co. Ltd., Bangkok, Thailand, 1995-96; employed by the Department of Biosystems and Agricultural Engineering as a Graduate Research Assistant, Oklahoma State University, 1997 to present.

Professional Memberships: ASAE (The Society for Engineering in Agricultural, Food and Biological Systems); American Geophysical Union, Asian Association for Agricultual Engineering; American Water Resources Association; American Society of Civil Engineers; Alpha Epsilon (The Honor Society of Agricultural Engineering); Gamma Sigma Delta (The Honor Society of Agriculture); Sigma Xi (The Scientific Research Society).